Studies on Spinal Fusion from Computational Modelling to 'Smart' Implants

Author:
Ramakrishna, Vivek

Publication Date:
2023

DOI:
https://doi.org/10.26190/unsworks/25053

Studies on Spinal Fusion from Computational Modelling to 'Smart' Implants

by

Vivek Ramakrishna

A thesis in fulfilment of the requirements for the degree of Doctor of Philosophy

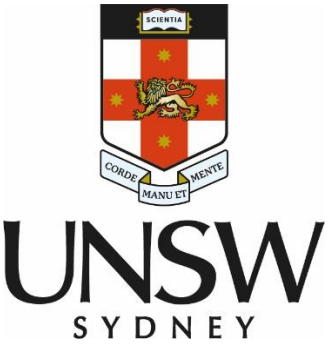

UNIVERSITY OF NEW SOUTH WALES

School of Mechanical and Manufacturing Engineering

Faculty of Engineering

(February 2023)

ORIGINALITY STATEMENT

☑ I hereby declare that this submission is my own work and to the best of my knowledge it contains no materials previously published or written by another person, or substantial proportions of material which have been accepted for the award of any other degree or diploma at UNSW or any other educational institution, except where due acknowledgement is made in the thesis. Any contribution made to the research by others, with whom I have worked at UNSW or elsewhere, is explicitly acknowledged in the thesis. I also declare that the intellectual content of this thesis is the product of my own work, except to the extent that assistance from others in the project's design and conception or in style, presentation and linguistic expression is acknowledged.

COPYRIGHT STATEMENT

☑ I hereby grant the University of New South Wales or its agents a non-exclusive licence to archive and to make available (including to members of the public) my thesis or dissertation in whole or part in the University libraries in all forms of media, now or here after known. I acknowledge that I retain all intellectual property rights which subsist in my thesis or dissertation, such as copyright and patent rights, subject to applicable law. I also retain the right to use all or part of my thesis or dissertation in future works (such as articles or books).

For any substantial portions of copyright material used in this thesis, written permission for use has been obtained, or the copyright material is removed from the final public version of the thesis.

AUTHENTICITY STATEMENT

☑ I certify that the Library deposit digital copy is a direct equivalent of the final officially approved version of my thesis.

UNSW is supportive of candidates publishing their research results during their candidature as detailed in the UNSW Thesis Examination Procedure.

Publications can be used in the candidate's thesis in lieu of a Chapter provided:

- The candidate contributed **greater than 50%** of the content in the publication and are the "primary author", i.e. they were responsible primarily for the planning, execution and preparation of the work for publication.
- The candidate has obtained approval to include the publication in their thesis in lieu of a Chapter from their Supervisor and Postgraduate Coordinator.
- The publication is not subject to any obligations or contractual agreements with a third party that would constrain its inclusion in the thesis.

☑ The candidate has declared that **some of the work described in their thesis has been published and has been documented in the relevant Chapters with acknowledgement**.

A short statement on where this work appears in the thesis and how this work is acknowledged within chapter/s:

Elements of Chapter 2 are published in the following peer-reviewed journal article:
V.A.S. Ramakrishna, U. Chamoli, G. Rajan, S.C. Mukhopadhyay, B.G. Prusty and A.D. Diwan. "Smart orthopaedic implants: A targeted approach for continuous postoperative evaluation in the spine," Journal of Biomechanics, vol. 104, May 7 2020, doi: 10.1016/j.jbiomech.2020.109690.

The findings in Chapter 3 are published in the following peer-reviewed journal article:
V.A.S. Ramakrishna, U. Chamoli, A.G. Larosa, S.C. Mukhopadhyay, B.G. Prusty and A.D. Diwan, "Finite element modelling of temporal bone graft changes in XLIF: Quantifying biomechanical effects at adjacent levels," Journal of Orthopaedic Research, vol. 22, no. 6, pp. 1420-1435, Jun 2022, doi: 10.1002/jor.25166.

The findings in Chapter 4 are published in the following peer-reviewed journal article:
V.A.S. Ramakrishna, U. Chamoli, A.G. Larosa, S.C. Mukhopadhyay, B.G. Prusty and A.D. Diwan, "A biomechanical comparison of posterior fixation approaches in lumbar fusion using computed tomography based lumbosacral spine modelling," Proc IMechE Part H: Journal of Engineering in Medicine, Jan 2023, doi: 10.1177/09544119221149119.

The findings in Chapter 5 are published in the following peer-reviewed journal article:
V.A.S. Ramakrishna, U. Chamoli, S.C. Mukhopadhyay, A.D. Diwan and B.G. Prusty, "Measuring compressive loads on a 'smart' lumbar interbody fusion cage: Proof of concept," Journal of Biomechanics, Jan 2023, doi: 10.1016/j.jbiomech.2023.111440.

Candidate's Declaration

I declare that I have complied with the Thesis Examination Procedure.

ABSTRACT

Low back pain, the worldwide leading cause of disability, is commonly treated with lumbar interbody fusion surgery to address degeneration, instability, deformity, and trauma of the spine. Following fusion surgery, nearly 20% experience complications requiring reoperation while 1 in 3 do not experience a meaningful improvement in pain. Implant subsidence and pseudarthrosis in particular present a multifaceted challenge in the management of a patient's painful symptoms. Given the diversity of fusion approaches, materials, and instrumentation, further inputs are required across the treatment spectrum to prevent and manage complications.

This thesis comprises biomechanical studies on lumbar spinal fusion that provide new insights into spinal fusion surgery from preoperative planning to postoperative monitoring. A computational model, using the finite element method, is developed to quantify the biomechanical impact of temporal ossification on the spine, examining how the fusion mass stiffness affects loads on the implant and subsequent subsidence risk, while bony growth into the endplates affects load-distribution among the surrounding spinal structures. The computational modelling approach is extended to provide biomechanical inputs to surgical decisions regarding posterior fixation. Where a patient is not clinically pre-disposed to subsidence or pseudarthrosis, the results suggest unilateral fixation is a more economical choice than bilateral fixation to stabilise the joint.

While finite element modelling can inform pre-surgical planning, effective postoperative monitoring currently remains a clinical challenge. Periodic radiological follow-up to assess bony fusion is subjective and unreliable. This thesis describes the development of a 'smart' interbody cage capable of taking direct measurements from the implant for monitoring fusion progression and complication risk. Biomechanical testing of the 'smart' implant demonstrated its ability to distinguish between graft and endplate stiffness states. The device is prepared for wireless actualisation by investigating sensor optimisation and telemetry. The results show that near-field communication is a feasible approach for wireless power and data transfer in this setting, notwithstanding further architectural optimisation required, while a combination of strain and pressure sensors will be more mechanically and clinically informative. Further work in computational modelling of the spine and 'smart' implants will enable personalised healthcare for low back pain, and the results presented in this thesis are a step in this direction.

ACKNOWLEDGEMENTS

The PhD journey is not one that can be completed without a network of support, be it technical, mental, or emotional. Beyond the degree itself, it was a period of immense personal growth and learning that I owe to the people around me.

Firstly, I would like to express my deepest gratitude to my supervisor, Prof. Ganga Prusty. You somehow always found time for me over a busy 4 years, guiding me in so many different ways. It has been a privilege to be part of your distinguished group. The way you coordinate your vast range of research activities and team members is an inspiration and something I aspire to.

I would also like to thank Dr. Ashish Diwan, Prof. Subhas Mukhopadhyay, and Dr. Uphar Chamoli. I am extremely grateful for your guidance and presence along the journey. To work under such an involved supervisory team is an incredibly enriching experience and I was lucky to have a group of supervisors so invested in my learning and growth. Uphar, I am especially thankful for your mentorship. I am blessed to have worked with someone so selfless and caring in all aspects beyond the PhD. Every student needs a supervisor with your calmness and wisdom; I will always look up to you.

There are many others who invested their efforts in me and ensured I strived for the best quality research possible. Vasu, I would not have accomplished any of the last year's work without your help. I leant on you a lot and you were always there to support me – no matter the hour, or day of the week. Seetha, you found solutions to many problems I thought unsolvable, your efforts were tireless, and you showed so much patience with me. You were an integral part of my work throughout. To the ARC Training Centre for Automated Manufacture of Advanced Composites (AMAC) team, thank you for your invaluable support during the course of my PhD. It was great to meet you all and share so many cakes and celebrations. I would also like to thank Alessandro – your efforts were crucial to all my FEA work. Thank you for the time you put in. I am very grateful for the support I received through the UNSW Scientia PhD Scholarship program. It provided me with world-class career development opportunities throughout my candidature that have boosted my post-PhD credentials.

I feel blessed to have had the emotional support from so many friends I have made along the way. To the group at Macquarie – I am lucky to have worked with such a friendly group of people who were so willing to give up their time to help me with my research. I would also like to

thank everyone at Spine Labs for all the fun times we had and for putting up with my FEA presentations.

A massive thank you to Nikhil, Prashanth, Jerrin, Nimal, Faisal, and Othman. I am so fortunate to have made such close friendships with you all. You made this such a fun experience. You made UNSW feel like a second home, you know exactly what the journey is like, and I am so lucky to have had you with me – I can not thank you enough. To the team at Merunova; Kyle, Manon& Josh, I am so grateful for your support. Kyle, at the hardest times, you knew exactly what to do to lighten the mood. Kyle & Nikhil – I am immensely thankful to have had the guidance of both of you, just ahead of me in your PhDs, to answer all my thesis-related questions and share your sage advice.

My closest friends – Orin, Will, Sam, Luca; you were the best distraction I could ask for. You may not feel like you did much, but I really can not express the impact your friendship has on me. It has been a busy 4 years but we still managed to eat a lot of good food. You have supported me in more ways than you know, and I am grateful to have you in my life.

Lastly, but most importantly, I would like to thank my family for their love, affection, and moral support. I know I have not been the most valuable household contributor in the recent years, and I am not really look forward to doing that again, but I promise I will anyway. Mum & Dad – you knew when I wanted space, you knew when I wanted a hug, and your mere presence was enough to make me feel better. You have showered me with love, blessings, and spiritual guidance. To my family in India and abroad – you have never felt distant, nor will you ever. Thank you for your constant encouragement and support.

Thatha, you have blessed my studies and my life every step of the way, and I know this milestone will be no different. Thank you for watching over me.

TABLE OF CONTENTS

LIST OF FIGURES

LIST OF TABLES

NOMENCLATURE

List of Acronyms

Abbreviation	Description
ADC	Analogue to digital converter
AF	Annulus fibrosus
ALIF	Anterior lumbar interbody fusion
ALL	Anterior longitudinal ligament
Ant.	Anterior
ASD	Adjacent segment degeneration
ASK	Amplitude-shift keying
ASTM	American Society for Testing and Materials
BL	Bilateral pedicle screw fixation
BMP-2	Bone morphogenetic protein two
CL	Capsular ligament
CNC	Computer numerical control
CNT	Carbon nanotubes
CSF	Cerebrospinal fluid
CSV	Comma-separated values
CT	Computed tomography
DEXA	Dual-energy X-ray absorptiometry
DICOM	Digital Imaging and Communications in Medicine
EEPROM	Electrically Erasable Programmable Read Only Memory
Ex	Extension
FDA	Food and Drug Administration
FE	Finite element
FF	Full fusion
FSK	Frequency-shift keying
Fx	Flexion
GPIO	General purpose input/output
IC	Integrated circuit
ILL	Iliolumbar ligament

ISL	Interspinous ligament
ISO	International Organisation of Standardisation
ITL	Intertransverse ligament
Lat.	Lateral
LBP	Low back pain
LF	Ligamentum flavum
LIF	Lumbar interbody fusion
LLIF	Lateral lumbar interbody fusion
LLIF-P	Lateral lumbar interbody fusion with posterior fixation
LSL	Lumbosacral ligament
MCID	Minimum clinically important difference
MRI	Magnetic resonance imaging
NF	No fixation
NFC	Near-field communication
NP	Nucleus pulposus
OLIF	Oblique lateral interbody fusion
OLIF-P	Oblique lateral interbody fusion with posterior fixation
OOK	On-off keying
PAM/FM	Pulse amplitude modulation / frequency modulation
PCB	Printed circuit board
PDMS	Polydimethylsiloxane
PEEK	Polyether ether ketone
PF	Partial fusion
PI	Polyimide
PLIF	Posterior lumbar interbody fusion
PLIF-P	Posterior lumbar interbody fusion with posterior fixation
PLL	Posterior longitudinal ligament
PMMA	Poly(methyl methacrylate)
PSK	Phase-shift keying
RAM	Random access memory
RFID	Radiofrequency identification
ROM	Range of motion
SC	Soft callus

SD	Secure Digital
SG	Solid graft
S/H	Sample and hold
SHM	Structural health monitoring
SLM	Selective laser melting
SLS	Selective laser sintering
SPI	Serial Peripheral Interface
SSL	Supraspinous ligament
STEP	Standard for the Exchange of Product Data
STL	Stereolithography
St1	Temporal stiffness stage one
St2	Temporal stiffness stage two
St3	Temporal stiffness stage three
TCP	Transmission Control Protocol
TLIF	Transforaminal lumbar interbody fusion
TLIF-P	Transforaminal lumbar interbody fusion with posterior fixation
UL	Unilateral pedicle screw fixation
USB	Universal Serial Bus
VBR	Vertebral body replacement
WiFi	Wireless Fidelity
XLIF	Extreme lateral interbody fusion
YLD	Years lived with disability
2D	Two-dimensional
3D	Three-dimensional

List of Symbols

Abbreviation	Description
A	Area
C	Neo-Hookean constant
C_1, C_2	Mooney-Rivlin constants
d	Distance
⌀	Diameter
Δ	Change
E, E_{xx}, E_{yy}, E_{zz}	Young's modulus in local coordinate system
ε	Strain
ϵ_0	Permittivity in vacuum
ϵ_r	Relative permittivity
F	Force
G, G_{xy}, G_{yz}, G_{xz}	Shear modulus in local coordinate system
GND	Ground
K	Bulk modulus
k	Stiffness
L	Length
N	Number
ν, ν_{xx}, ν_{yy}, ν_{zz}	Poisson's ratio in local coordinate system
P	Pressure
Σ	Sum
T	Tension
t_m	Measurement period; Duration of measurement
t_{off}	Minimum turn-off duration
t_r	Read duration
t_0, t_1, t_2, t_3, t_4	Time point zero, one, two, three, four
V_{DD}	Input voltage
V_{ref}	Reference voltage
V_{th}	Threshold voltage
(x, y, z)	Local nodal coordinates
XX, YY, ZZ	Local coordinate system directions

1. Introduction

1.1 Research Rationale

1.1.1 Burden of Low Back Pain

Low back pain (LBP) is a physically debilitating condition that, in Australia, affects almost 80% of individuals at some point in their life [1-5]. According to the Global Burden of Diseases study in 2019, LBP is the worldwide leading cause of years lived with disability (YLD) amongst men and women combined [6, 7]. From 2007 to 2017, the group reported a 17.5% increase in YLD due to LBP, representing a larger increase than the next two highest contributors; headache disorders (15.4%) and depressive disorders (14.3%) [8]. The combined mental and physical aspects of LBP tend to reduce the individual's workforce productivity and quality of life [9]. The annual cost of back pain to the Australian healthcare system is $2.8b, with wider economic impacts as the leading cause for early retirement and reduced productivity [10-12]. Similarly in the UK, the annual economic cost across the workforce equates to £998m [1].

LBP has a complex biomechanical foundation and considerable variation in its presentation between individuals. The source of pain is not often clear, complicating decisions regarding treatment options. A wide scope of conservative and operative approaches complicates the assessment of clinical outcomes. Underpinning the poor outcomes from treatment and a high risk of adverse events is a lack of research into their biomechanical origins, presenting a complex challenge to clinicians in preoperative planning and postoperative monitoring.

1.1.2 Overview of Spinal Fusion Surgery

Spinal fusion is a surgical technique for treating LBP, which was originally developed for the treatment of tuberculosis and deformity [13]. Since the first operation, indications have broadened to include trauma, tumours, infection, and degenerative conditions [14-16]. Currently, fusion surgery is most commonly performed to treat disc degeneration

[15, 17]. The aim of fusion surgery is to immobilise spinal segments through the ossification of surgically implanted bone graft into native bone between adjacent levels.

Fusion surgery was first developed without instrumentation; bone graft placed between the laminae of adjacent spinal segments promotes ossification of those regions and eventual fusion of the adjoining levels into one bony mass over a period of 6-12 months [13]. A variety of pedicle screw fixation techniques and devices have evolved to improve the efficacy of the procedure, reduce instrumentation failure, and optimise the biomechanical rigidity of the stabilised segments (Figure 1.1) [13].

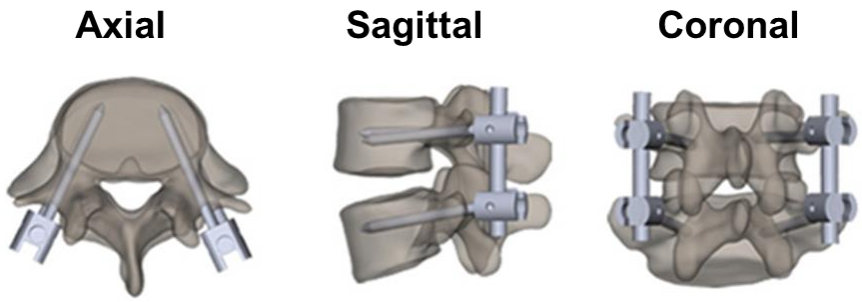

Figure 1.1: Pedicle screw fixation viewed from axial, sagittal, and coronal planes [CC BY 4.0] [18].

Interbody fusion was devised to restore intervertebral height, decompress nerve roots, and treat stenosis. The method requires the removal of the native intervertebral disc and insertion of an interbody cage (or spacer) in the intervertebral space (Figure 1.2). The implant acts as a vessel for the bone graft that promotes fusion between the vertebrae [19]. The cages are often made of polyether ether ketone (PEEK) or titanium [13], while common bone grafts include autograft, allograft, bone morphogenetic protein 2 (BMP-2), bone marrow aspirate, ceramics, demineralised bone matrix, and growth factors [20]. This thesis is only concerned with lumbar interbody fusion (LIF).

Between 400,000-450,000 spinal fusions are performed in the USA every year [15, 16, 21]. Further, the number of operations doubled between 1998 and 2008 [15]. The total cost of fusions to the US healthcare system was $33.9b in 2008 [15]; in Australia the annual direct cost of fusion operations reached $650m in 2013 [22]. At a conservative 5% annual growth estimate [23], the current projected costs of spinal fusion are $67b in the US and $1.1b in Australia. Approximately half of all spinal fusions are performed on the lumbar spine at an average cost of approximately $82,000 each [15].

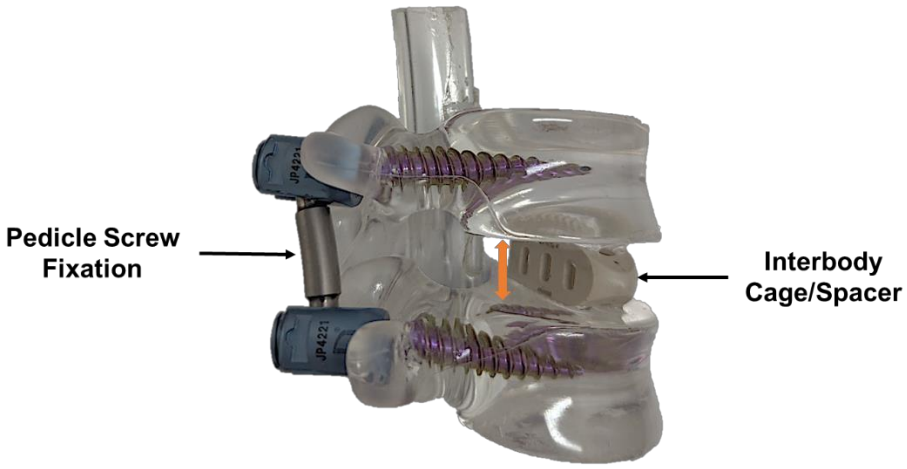

Figure 1.2: Example of transforaminal LIF demonstrating the positioning of the interbody cage between adjacent vertebrae.

The cage is packed with bone graft to facilitate bony fusion between the vertebrae indicated by the orange arrow. Lumbar fusion, depending on the approach, is performed with additional pedicle screw fixation, as depicted in Figure 1.2.

1.1.3 Lumbar Interbody Fusion: Complications and Outcomes

Despite the number of operations performed annually and the associated cost, fusion surgery is associated with several complications and poor outcomes. Adverse events occur in 17% of fusion operations; 22% for trauma indications and 15% when treating degenerative conditions [24]. Of these complications, 25% relate to mechanical failure of the instrumentation [24].

One in five patients require reoperation within four years following a lumbar fusion operation [25], while 6% of all lumbar fusions performed are revision surgeries [21]. Further, revision surgeries are associated with more operated spinal levels, higher costs, and longer in-hospital recovery [21]. The rate of revision in patients over 65 reaches 26% [21].

In a 2-year follow-up study following lumbar fusion, only 57% of patients achieved a minimum clinically important difference (MCID) in functionality compared to their preoperative scores [26]. Similar results were found for their experience of back (56%) and leg (57%) pain. In general, however, patients consider MCID to be a conservative measure of improvement post-surgery [27].

1.1.4 Underlying Biomechanical Issues with Lumbar Interbody Fusion

Lumbar fusion surgeries are expensive procedures with poor outcomes and high complication rates. The source of these failures has a complex biomechanical underpinning that has, to date, not been thoroughly examined. There are 3 key challenges to address with LIF:

I. The biomechanical impacts of fusion surgery on surrounding spinal structures are not well understood.
II. Pre-surgical planning lacks objective biomechanical inputs that can be used to construct an informed patient-specific treatment plan.
III. Current postoperative monitoring techniques have limited accuracy and reliability.

Performing a LIF procedure consists of numerous decisions, including at a minimum, the choice of access, implant design and material, graft type, and whether to use supplemental fixation for added stability. With such variation in surgical practice, it is difficult to investigate and understand the source of poor outcomes and complications. Consequently, the biomechanical impacts and correlates of LIF are not well understood for each specific cage material and design that a surgeon has access to. Despite an abundance of studies evaluating fusion implant designs using *in vitro* testing and computational modelling, the wider biomechanical impacts of these implants on spinal structures both proximate and distant to the operated region remain unclear.

Despite the number of factors surgeons must consider, their decisions continue to be under-informed from a biomechanical perspective. Surgeons do not have access to biomechanical rationales and inputs that can assist in pre-surgical planning and facilitate the provision of patient-specific treatment. Patients require treatment that is specific to their anatomy and stability requirements, which is difficult to assess using preoperative imaging techniques alone. Surgical failures and complications are likely to result, in part, from pre-surgical decision-making, where patients are over- or under-stabilised consequent to unsuitable instrumentation chosen by the surgeon.

Current methods of postoperative monitoring consist of radiological imaging (computed tomography (CT) or X-ray) at periodic intervals. These methods, however, are

subjective, with limited accuracy and reliability [28, 29]. As such, postoperative imaging fails to identify the risk factors that can lead to the avoidance of complications. Further, imaging often fails to detect existing complications early enough to instigate appropriate clinical management such that the patient does not become symptomatic or require revision surgery [30]. Unless detected by postoperative imaging, complications are uncovered at the onset of painful symptoms and often require surgical intervention.

1.1.5 Methods for Assessing the Biomechanics of Lumbar Fusion

The outlined challenges are evident contributors to the complication rate and poor outcomes associated with LIF surgery. A better understanding of LIF can be gained through biomechanics research, using information gathered therefrom to inform pre-surgical planning and develop more effective postoperative monitoring tools, ensuring patients benefit from a reduced likelihood of adverse outcomes.

The ideal approach to foster a holistic biomechanical understanding of lumbar fusion involves a combination of techniques. Finite element (FE) analysis is well-placed to investigate mechanical changes in the spine. A ligamentous multilevel lumbar spine model can quantify load-distribution changes arising from a LIF cage under bending loads. Studying the mechanics resulting from material changes, such as those of the interbody cage or occurring in the graft region, is practical with computational models. Further, the use of CT-based mesh generation enables accurate anatomical modelling to simulate the outcome of patient-specific surgical decisions. Thereafter, the detailed outputs are useful for the development of broad-based pre-surgical rationales that consider a patient's spinal biomechanical stability requirements.

Novel methods are required to gather *in vivo* data in the postoperative monitoring phase to replace imaging that does not proactively attempt to avoid complications or detect them early. The ideal approach uses direct measurement of mechanical information from the implant to provide more objective inputs to the postoperative management of a patient. Wireless data acquisition from sensors embedded in the interbody cage is less onerous to a patient and enables more frequent data collection. A sensor-enabled interbody cage can supply real-time patient-specific data to clinicians about alignment, surrounding bone quality, and the ongoing ossification of the graft. Equipped with this information, surgeons can proactively assess complication risk and take appropriate

actions to avoid the occurrence thereof, without relying on the onset of symptoms to prompt an investigation. With widespread adoption, wireless sensor-embedded implants will consolidate the approach to assessing surgical outcomes, regardless of approach, design, and material.

1.2 Research Aims

The collection of work contained in this thesis aims to enhance biomechanical perspectives on the impacts of LIF, addressing complications and poor outcomes by providing quantifiable inputs to preoperative planning and developing objective methods for postoperative monitoring. This thesis specifically takes the example of extreme lateral interbody fusion (XLIF).

Chapter 2 examines the available literature that is within the scope of this thesis. Approaches to LIF, implant designs, and materials are briefly described. Computational modelling approaches relevant to spine research are also outlined. Subsequently, the literature review discusses the body of research in 'smart' orthopaedic implants, highlighting challenges and opportunities for improvement. Sensing and wireless telemetry methods applicable to implantable devices are also examined to identify suitable approaches to wirelessly enable a 'smart' interbody cage.

Chapter 3 uses FE analysis to understand the biomechanical changes occurring *in vivo* after performing LIF surgery. This chapter describes the development of a FE model representing a L4-L5 XLIF, which quantifies load-distribution changes at the instrumented level and in adjacent spinal structures. The computational model describes how lumbar spine biomechanics changes according to the maturity of the fusion mass. The ensuing analysis describes the behaviour of the preserved spinal structures with respect to their intended stabilising capacity following XLIF, such that surgeons can improve surgical outcomes by considering treatment options cognisant of a patient's anatomy and condition.

Chapter 4 extends the scope of computational modelling work, using FE analysis to develop a preoperative biomechanical rationale for decisions regarding the use of posterior supplemental fixation alongside XLIF. This chapter simulates the outcomes of surgical decisions, comparing three levels of stability (no fixation, unilateral and bilateral pedicle screw fixation) to provide an objective biomechanical perspective for surgeons

to examine during pre-surgical planning in addition to the clinical factors they currently consider. Chapter 4 highlights the importance of providing patient-specific guidance to prevent postoperative complications in addition to the feasibility of FE analysis as a means to achieve this.

Chapter 5 describes the design, development, and testing of a proof-of-concept 'smart' interbody cage. The pressure-sensing implant is a novel alternative to traditional postoperative imaging that gathers real-time mechanical data under physiological loads. The designed 'smart' cage is tested under compression loads to assess its ability to distinguish between different graft and endplate stiffnesses. In doing so, the effectiveness of the 'smart' implant approach to monitor fusion progression and complications related to bone quality is determined. Design inputs are specified, and optimisation is discussed.

Chapter 6 investigates multidirectional strain as an alternative measurand to pressure for the purpose of optimising the sensor configuration in preparation for wireless integration. The interbody cage, affixed with strain gauges, is subjected to compressive loads, ultimately aiming to identify the most efficient combination of pressure and strain sensors for maximum clinical utility. Subsequently, this chapter describes the design and validation of a proof-of-concept near-field communication (NFC) telemetry module. The clinical feasibility of the integrated wireless 'smart' cage is discussed. This chapter aims to provide the necessary direction to advance the concept towards clinical adoption, providing surgeons with an objective tool to prevent adverse outcomes from LIF surgery.

Chapter 7 summarises the main findings of the thesis, demonstrating how complications can be avoided and managed using computational modelling and 'smart' implants. This chapter concludes on results of immediate relevance to LIF surgery and highlights how the methods can be extended beyond the scenario investigated in this thesis. Limitations of the research methods are presented. Future work is outlined to address these shortcomings and further their adoption as techniques for improving surgical low back pain treatment.

1.3 Research Outputs

1.3.1 Journal Publications

1) V.A.S. Ramakrishna, U. Chamoli, S.C. Mukhopadhyay, A.D. Diwan and B.G. Prusty, "Measuring compressive loads on a 'smart' lumbar interbody fusion cage: Proof of concept," *Journal of Biomechanics*, vol. 147, Jan 2023, doi: 10.1016/j.jbiomech.2023.111440.
2) V.A.S. Ramakrishna, U. Chamoli, A.G. Larosa, S.C. Mukhopadhyay, B.G. Prusty and A.D. Diwan, "A biomechanical comparison of posterior fixation approaches in lumbar fusion using computed tomography based lumbosacral spine modelling," *Proc IMechE Part H: Journal of Engineering in Medicine*, Jan 2023, doi: 10.1177/09544119221149119.
3) V.A.S. Ramakrishna, U. Chamoli, A.G. Larosa, S.C. Mukhopadhyay, B.G. Prusty and A.D. Diwan, "Finite element modelling of temporal bone graft changes in XLIF: Quantifying biomechanical effects at adjacent levels," *Journal of Orthopaedic Research*, vol. 22, no. 6, pp. 1420-1435, Jun 2022, doi: 10.1002/jor.25166.
4) V.A.S. Ramakrishna, U. Chamoli, G. Rajan, S.C. Mukhopadhyay, B.G. Prusty and A.D. Diwan. "Smart orthopaedic implants: A targeted approach for continuous postoperative evaluation in the spine," *Journal of Biomechanics*, vol. 104, May 7 2020, doi: 10.1016/j.jbiomech.2020.109690.

1.3.2 Conference Presentations

1) 4th Annual Sydney Spinal Symposium. 9th September 2022. Oral. 'Smart orthopaedic implants: A targeted approach for continuous postoperative evaluation in the spine'. Sydney, Australia.
   *Awarded Best Basic Science Oral Presentation
2) Spine Society of Australia 33rd Annual Scientific Meeting. 27th - 29th May 2022. Oral. 'Biomechanically rational pre-surgical planning using CT-based lumbosacral spine modelling'. Darwin, Australia.
3) Spine Society of Australia 32nd Annual Scientific Meeting. 26th - 28th November 2021. Top 10 Poster. 'Quantifying biomechanical effects of XLIF at adjacent levels'. Virtual.

4) 2nd Annual Workshop of IEEE Sensors Council NSW Chapter & 5th Annual Workshop of IEEE IMS NSW Chapter. 16th April 2021. Oral. 'Towards the development of smart implants in orthopaedic spinal applications'. Macquarie University, Sydney, Australia.

1.3.3 Invention Disclosure

1) V.A.S. Ramakrishna, B.G. Prusty, A.D. Diwan and S.C. Mukhopadhyay, WO 2022/232861 A1, "A surgical implant". Filed 7th May 2021. PCT/AU2021/050423.

2. Literature Review

2.1 Literature Review Outline

The relevant literature is reviewed under 4 pillars (Figure 2.1). The various approaches to lumbar interbody fusion (LIF) and their corresponding implant designs are briefly examined, providing context for the prominent complications and challenges associated with surgical outcomes, surgical decision-making, and postoperative monitoring. The failures of LIF are considered from a biomechanical perspective to elicit engineering approaches to improve treatment outcomes. Computational modelling methods are reviewed, highlighting how finite element (FE) analysis can be used to address complications in LIF through a detailed biomechanical analysis of surgical approaches and implant designs. Implantable sensor-enabled devices for orthopaedic applications, referred to as 'smart' orthopaedic implants, are reviewed for their performance in hip, knee, shoulder, spine, and fracture fixation implants. The architecture and clinical utility of the reported designs is discussed, highlighting potential development directions in the area of 'smart' interbody cages to address the identified clinical challenges. Finally, sensing modalities are compared and suitable wireless telemetry approaches are briefly explored to identify potential avenues for the development of a 'smart' interbody cage.

Elements of this chapter are published in the following peer-reviewed journal article:

> V.A.S. Ramakrishna, U. Chamoli, G. Rajan, S.C. Mukhopadhyay, B.G. Prusty and A.D. Diwan. "Smart orthopaedic implants: A targeted approach for continuous postoperative evaluation in the spine," *Journal of Biomechanics*, vol. 104, May 7 2020, doi: 10.1016/j.jbiomech.2020.109690.

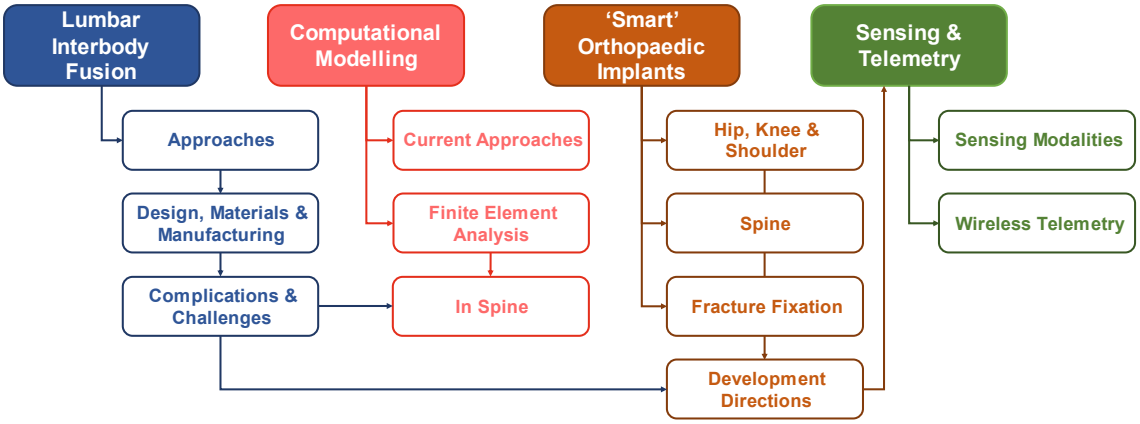

Figure 2.1: Literature review structure.

2.2 Lumbar Interbody Fusion

2.2.1 Lumbar Interbody Fusion Approaches

The high uptake of spinal fusion may be, in part, influenced by improvements in technology and materials, or the development of new techniques [16]. As the scope of surgical practice widens, decisions regarding the choice of approach and instrumentation become more complex. During LIF surgery planning, there are numerous decisions surgeons make based on their preference, the surgical indication, and the patient's clinical presentation, including anterior, lateral, or posterior access (Figure 2.2); standalone fusion or supplemental fixation; cage design, material, and size [16]. Examining the diversity of approaches provides insights into the complications associated with LIF.

Posterior LIF (PLIF) is one of the most established and common interbody fusion approaches [16]. The posterior approach provides good height restoration and access to the nerve roots to perform decompression [16, 31, 32]. Conversely, the approach comes with a higher risk of neural and dural injury, excessive endplate damage, and paraspinal muscle injury [16, 32-34]. The anterior LIF (ALIF) technique preserves the posterior elements of the spine, reduces the risk of neural and muscle injury, and provides access for a larger implant with greater stability, height restoration, and lordosis correction [32]. ALIF, however, has a higher risk of vascular injury and damage to organs due to its anterior retroperitoneal approach [35, 36]. While visualisation of the intervertebral space is limited and lordosis correction is more challenging, transforaminal LIF (TLIF) also preserves posterior ligaments and musculature for improved postoperative stability of

the instrumented levels, with a lower risk of neural and dural injury [16, 32, 37-39]. Lateral LIF (LLIF) and extreme lateral interbody fusion (XLIF) are both transpsoas retroperitoneal approaches that split the muscle fibres of the psoas muscle to access the intervertebral space [16]. While not suitable for the L5-S1 level, LLIF and XLIF provide access for a large footprint interbody cage while maintaining the natural stabilising structures of the spine, such as facets, ligaments, and musculature [16, 40]. LLIF and XLIF can be performed using a standalone interbody cage without additional fixation [16, 40]. Lateral approaches are not suitable for some high deformity conditions [16]. Evidently, there are several access options for a surgeon to consider, each with associated advantages and limitations. There is no conclusive evidence to suggest superiority of one approach over another [16].

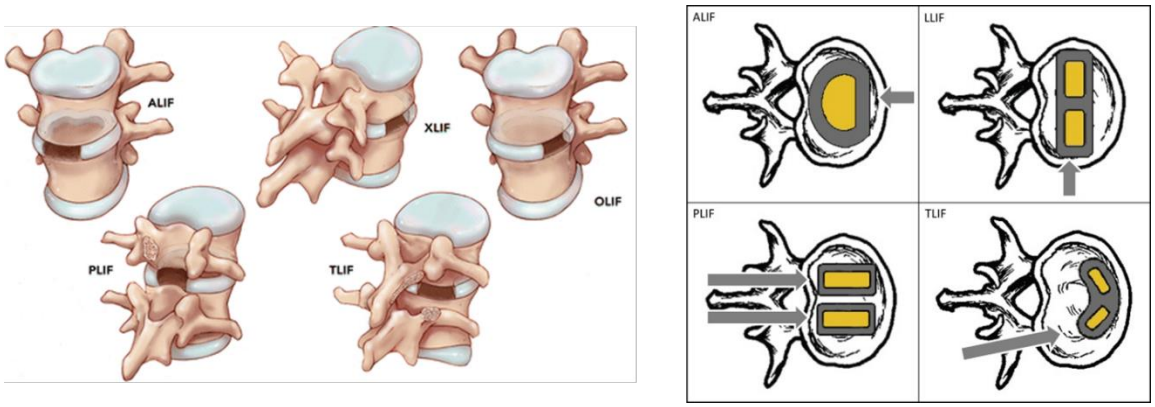

ALIF: Anterior lumbar interbody fusion; XLIF: Extreme lateral interbody fusion; OLIF: Oblique lateral interbody fusion; PLIF: Posterior lumbar interbody fusion; TLIF: Transforaminal lumbar interbody fusion; LLIF: Lateral lumbar interbody fusion.

Figure 2.2: Lumbar fusion approaches and associated cage designs [41, 42].

Standalone LIF, without supplemental fixation constructs, is generally only performed with lateral and anterior approaches. Screws, rods, and plates are commonly instrumented with interbody fusion cages to increase the stability of the spinal segment, or integrated with the cage design for ALIF, LLIF, and XLIF (Figure 2.3) [43, 44]. Lateral approaches can be combined with lateral vertebral body screws and plates or pedicle screw fixation (Figure 2.4), whereas PLIF and TLIF are most commonly performed with posterior fixation (Figure 2.5a). Conversely, ALIF is performed with integrated fixation, anterior plate fixation, or posterior fixation [45]. Posterior fixation includes a variety of techniques, including translaminar facet screw fixation and transfacet screw fixation,

however unilateral and bilateral pedicle screw fixation are the most common constructs [44].

Figure 2.3: An ALIF interbody cage with integrated fixation that allows screws to penetrate the superior and inferior vertebrae.

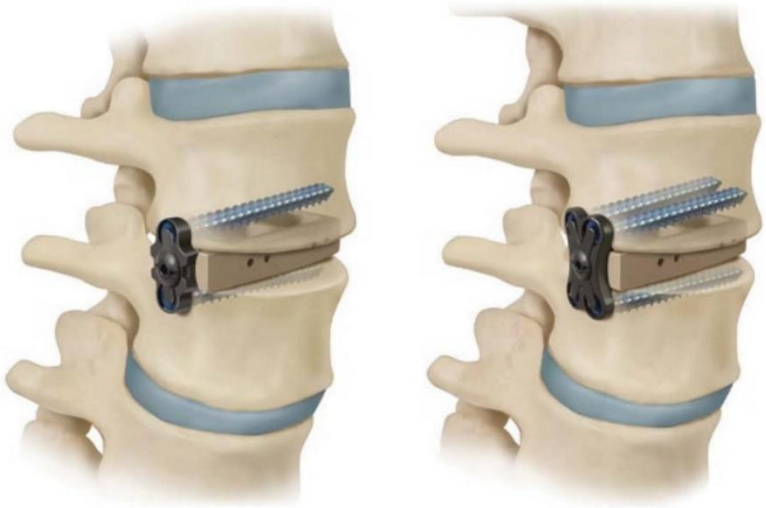

Figure 2.4: Lateral vertebral screw fixation for LLIF and XLIF approaches [46] [CC BY-NC-ND 4.0].

Increasing the extent of fixation undoubtedly increases the rigidity of the implanted region and restricts motion [44, 46], lowering the likelihood of implant migration and the overall loads on the fusion cage. Concurrently, it introduces risks associated with instrumentation failure, such as screw loosening and breakage [47-49], and increases operating time, cost, and blood loss [50-52]. There is currently no clear evidence on the clinical impact of fixation on surgical outcomes apart from complications relating to the

fixation construct itself. Posterior fixation approaches are further compared in Chapter 4.

The high complication rate and poor outcomes from LIF surgery may be, in part, related to the range of approaches used by surgeons. The biomechanics of each specific approach and fixation construct must be understood from a biomechanical perspective to ensure the right procedure is selected for a patient based on their anatomy and condition.

2.2.2 Interbody Cage Design, Materials & Manufacturing

Each lumbar fusion approach has associated interbody cage designs and sizes depending on the access afforded and preparation required by the technique. The design, material, and size of the cage produce substantive differences in the resultant biomechanics of the joint, at least until the point of full fusion. The links between such parameters, biomechanics, and clinical outcomes are not completely understood.

Cylindrical titanium threaded screw cages achieve high fusion rates, though also have an increased tendency to subside and do not provide stability in bending [53]. The modern conventional box-shaped design was developed to provide more stability in bending and rotation [53, 54]. This traditional design, however, has evolved into kidney, bullet, trapezoidal, and cylindrical shaped cages [55]. Trapezoidal cages are more common in ALIF and are effective at restoring sagittal balance, while bullet and kidney shaped cages are more common in posterior and transforaminal approaches, which also facilitate the insertion of two interbody cages for improved stability [55]. Larger rectangular cages are used in LLIF and XLIF. There is no biomechanical evidence to suggest the superiority of one cage design over another [56]. Supplemental fixation, particularly for TLIF and PLIF, structurally supports the instrumented segments, however, some interbody cages have been designed with integrated anchors and/or screws into the adjacent vertebrae to improve the stability of the standalone construct (Figure 2.5b) [36, 53].

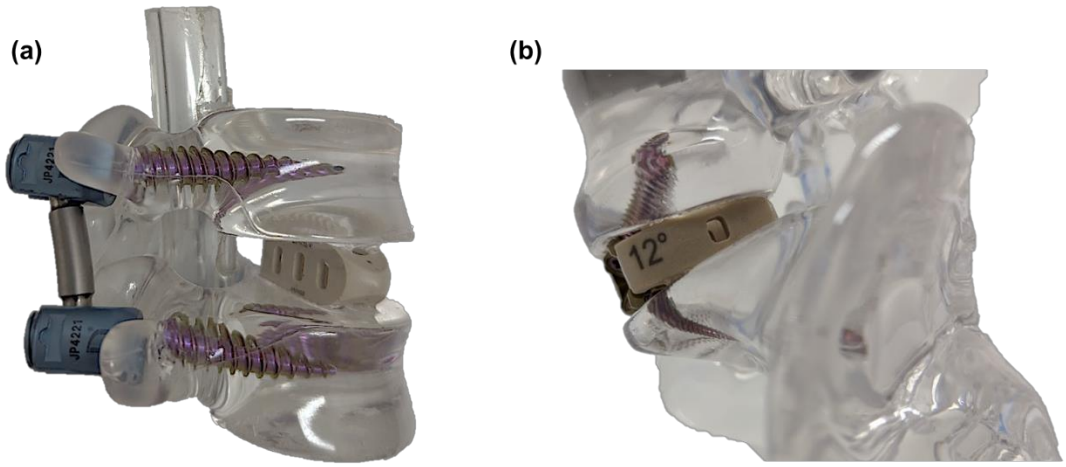

Figure 2.5: Models depicting the different designs for a (a) bullet TLIF cage with pedicle screw fixation and (b) trapezoidal ALIF cage with integrated fixation.

An interbody cage with ideal stiffness properties would provide sufficient joint stability without damaging the adjacent endplates while enabling load-transfer to the graft in a manner that promotes ossification [55]. Stress-shielding occurs when the elastic modulus of the interbody cage is higher than the graft to the extent that load is borne by the cage and not transferred to the graft in a manner that promotes bone healing. There is an evident trade-off between elastic modulus, stress-shielding, and damage to the articulating bone due to modulus incongruence, whereby a high elastic modulus provides rigidity for joint stability while increasing subsidence risk and stress-shielding effects [55]. Matching the elastic modulus of the cage to natural bone is the established approach to preventing subsidence, however radiolucency, osteoconductivity, and biocompatibility are similarly important material considerations [55].

Interbody cage materials have evolved over time to address limitations in strength, osseointegration, and subsidence (Figure 2.6). Due to its poor mechanical integrity, the use of bone graft alone as an interbody spacer is no longer common practice [13, 57]. Subsequently, machined metals provided the required strength while causing subsidence, and polymer cages had superior stiffness with poor osseointegration [57]. Both metal and polymer cages continue to be used in clinical practice, with ongoing development aimed at overcoming their associated limitations.

Polyether ether ketone (PEEK) and titanium are the two most utilised cage materials [53]. The theoretical advantage of titanium over PEEK is its superior bone adhesion qualities

and corrosion-resistance, however PEEK is MRI compatible, biologically inert, and has a similar elastic modulus to bone [53, 58]. Titanium prevent the postoperative assessment of bone fusion with traditional imaging due to its high radio-density [59]. While Lingutla et al. found no difference between PEEK and titanium with regards to disc space height restoration [60], Chen et al. reported better long-term outcomes and height restoration with PEEK [58]. Meng et al. suggest that interbody cage material may have an influence on the fusion rate due to the relative stiffness and osteoconductivity of PEEK and titanium [61]. With the substantial stiffness discrepancy between titanium (110GPa) and bone (2.1-2.4GPa) [36], titanium cages are generally associated with higher subsidence rates [62, 63], although Campbell et al. reported the opposite trend [64]. The modulus of PEEK is similar to bone and has demonstrated superior load-share and stress distribution compared to titanium, theoretically lowering subsidence risk and improving fusion rate [65, 66]. Fogel et al. reported conflicting fusion rates and subsidence results across several meta-analyses, demonstrating that it is still unclear whether titanium or PEEK produce more desirable outcomes [62].

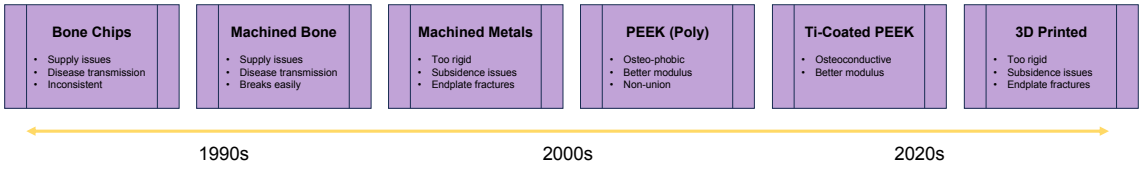

Figure 2.6: Evolution of interbody cage materials, addressing their limitations over time [57] [CC].

Silicon nitride interbody cages are being investigated as an alternative to PEEK implants, aiming to overcome the poor osseointegration of PEEK while maintaining similar mechanical properties [53]. Studies on carbon-fibre reinforced PEEK have demonstrated its similar mechanical performance with superior wear characteristics compared to pure PEEK [67]. Both materials are yet to reach clinical practice. Hybrid titanium-coated PEEK cages have been developed to combine the superior stiffness properties of PEEK with the osseointegration of titanium [55, 67]. The commercially-available titanium-PEEK hybrids are associated with increased fusion bone volume and similar clinical outcomes compared to pure PEEK [67, 68]. Titanium-coated PEEK, however, is significantly stiffer particularly in flexion-extension and lateral bending, highlighting that it has not

replicated the mechanical properties of pure PEEK [68]. Further investigation is required to determine whether this results in higher subsidence rates.

Altering the microstructure of the cage is a current area of research, aiming to reduce interface bone stresses. Porous tantalum cages mimic the trabecular structure of cancellous bone with a desirable elastic modulus and high coefficient of friction for improved stability [69]. As a relatively new material for interbody cages with supply issues and lacking in definitive evidence of its osseointegration, there are few devices on the market in porous tantalum [69]. More recently, the favourable response of porous titanium to mechanical loading has shown it may reduce the risk of subsidence and pseudarthrosis [62]. The stiffness of the porous titanium cage developed by Fogel et al. is 30% lower than solid titanium and only 8% higher than solid PEEK [62]. Under histological examination, the porous cage supported bony in-growth that is not compatible with solid cage designs [62]. Torstrick et al. described how the surface topography of porous PEEK improves contact between the cage and the articulating bone, due to their similar stiffness properties, increasing the *in vivo* fixation of the implant compared to pure PEEK and titanium-coated PEEK [70]. There are clear advantages to porous interbody cages in terms of elastic modulus and osseointegration, however reproducible manufacturing of the required microstructures relies on techniques such as additive manufacturing.

Interbody cages are generally manufactured by injection moulding or machining from bulk material [71], however additive manufacturing is becoming more prevalent in both research settings and commercial applications, particularly for titanium cages [71-73]. Additive manufacturing enables fine control over strut positions and widths to produce porous cages [74]. 3D-printed titanium implants have shown favourable fusion outcomes owing to their trabecular structure [75], however there are few studies assessing subsidence in comparison to conventional interbody cages [76]. Additive manufacturing of PEEK remains in its infancy. There are ongoing challenges in managing its high melting temperature, crystallinity, and delamination with fused filament printing methods [77]. Further, PEEK is not suitable for the higher-resolution selective laser melting (SLM) printing methods used for metallic implants. Nonetheless, it is not within the scope of this work to assess the performance of implants with relation to their manufacturing process.

2.2.3 Clinical Complications and Issues

Lumbar interbody fusions are expensive procedures with high complication rates and poor outcomes. It is not the intention of this thesis to thoroughly investigate the clinical sources of adverse events and outcomes in lumbar fusion, but rather to address such complications through a biomechanical lens. One such approach is to consider complications associated with instrumentation failure and diagnosis. This thesis focuses primarily on pseudarthrosis and subsidence in their association with the interbody cage.

There are several challenges associated with LIF that are poorly understood due to the technological limitations of *in vivo* data collection. Risk of delayed union, pseudarthrosis (non-fusion), implant migration into the vertebra (subsidence), screw loosening (1–15%) [47], and screw breakage (0–3%) [48, 49] are undesirable complications with adverse biomechanical and clinical implications that require revision surgery and present a challenge to the postoperative management of the patient. Without biomechanically-informed surgical decision-making and suitable monitoring approaches, timely diagnosis and preventative management of these adverse events is difficult.

Pseudarthrosis is the incomplete bony union between the adjoining vertebrae following LIF surgery, characterised by persistent pain and associated with several other complications [61]. Rates of pseudarthrosis at least one year after LIF surgery range from 3-20% in patients with healthy bone [61, 78-80]. Non-union is a higher risk for patients with poor bone quality, occurring in 20-30% of patients with osteoporosis [49, 81, 82].

There is a considerable degree of ambiguity in the assessment of the bony fusion mass following a spinal fusion surgery that makes the diagnosis of pseudarthrosis challenging [30, 81]. Surgeons currently rely on different imaging measures to assess bone maturity in the fusion mass, including the absence of radiolucent gaps, increasing opacification, indications of trabecular bone bridging (Figure 2.7), and negligible motion on flexion-extension radiographs [30, 83, 84]. Routine radiology exposes patients to regular ionising radiation, which can be dangerous if the dose accumulates. Furthermore, there is no clear standard for the determination of radiologically-assessed 'negligible' motion [81]. Plain radiographs have been shown to be ineffective at detecting pseudarthrosis [85] and it is evident that radiologically determined solid fusion may not correlate with biomechanically solid fusion. The two standards for assessing fusion, plain radiographs

and fine-cut computed tomography (CT), were previously classified as fair to moderate for interobserver and intraobserver reliability [28, 29]. Furthermore, agreement on fusion grade between the two imaging modalities was only 46-59% [28]. A high false-positive rate has also been reported using CT to determine solid fusion of the bridging mass [29].

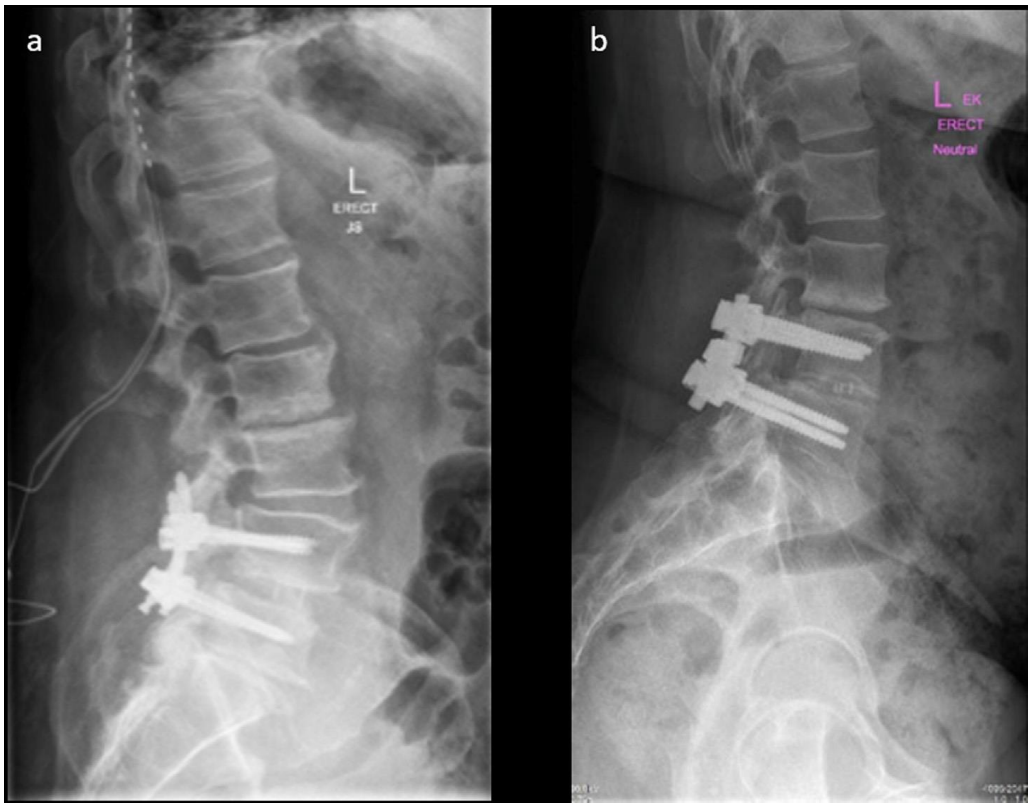

Figure 2.7: Lateral X-Rays of the lumbar spine demonstrating (a) non-union at L4-L5 with no evidence of bridging bone and (b) solid fusion at L4-L5.

While the onset of subsidence alone can be considered an adverse event, it may in turn cause non-union, deformity, or adjacent segment degeneration, all of which may result in leg pain and radiculopathy due to nerve root compression from loss of foraminal height [86, 87]. Rates of subsidence vary by fusion type, implant design, use of supplemental fixation, and bone quality (Table 2.1) [88]. Based on the meta-analysis performed by Parisien et al. (2022), subsidence is a notable risk with all LIF approaches regardless of posterior fixation [88]. Management of subsidence is complex with no standard practice for treatment. In cases where subsidence is symptomatic and has caused a considerable loss of intervertebral height, the cage may be removed and replaced with a larger interbody cage if the fusion mass has not matured. Alternatively, surgeons may instrument additional fixation by way of screws, rods, and plates to

reduce load on the interbody cage. In any case, managing symptomatic subsidence is invasive and challenging.

Table 2.1: Maximum and minimum rates of subsidence occurrence by lumbar fusion approach obtained from a meta-analysis by Parisien et al. (2022) [CC BY-NC-ND] [88].

Subsidence Occurrence			
LIF Approach	**Minimum**	**Maximum**	**Number of Studies**
ALIF	6%	23%	6
LLIF	9%	40%	11
LLIF-P	3%	21%	8
OLIF-P	4%	37%	7
PLIF-P	7%	32%	5
TLIF-P	0%	51%	14

ALIF: Anterior lumbar interbody fusion, LLIF: Lateral lumbar interbody fusion, LLIF-P: Lateral lumbar interbody fusion with posterior fixation, OLIF-P: Oblique lateral interbody fusion with posterior fixation, PLIF-P: Posterior lumbar interbody fusion with posterior fixation, TLIF-P: Transforaminal lumbar interbody fusion with posterior fixation.

As previously highlighted, titanium interbody cages have a higher risk of subsiding [62, 63]. Stress concentrations on the cage surface are likely to increase the risk of subsidence and, as such, fusion cages aim to maintain a uniform stress distribution on the endplates [89]. This has resulted in the recent development of porous cage interfaces, and patient-specific cage designs that conform to the curvature of the endplate, both aiming to reduce stresses at the endplate-prosthesis junction [62, 90]. Similarly, cages occupying a larger footprint result in lower rates of subsidence [91].

Subsidence, however, is largely related to bone quality. While the stiffer, denser peripheral endplate region is less susceptible to fracture and implant subsidence, global bone quality may degrade with age following fusion surgery [92]. Low bone density, characteristic of osteoporosis, is a subsidence risk factor which has a high prevalence in populations that undergo LIF surgery [87, 93, 94]. Bone mineral density is assessed using CT or dual-energy X-ray absorptiometry (DEXA) scans [87, 93]. Traditional postoperative follow-up, therefore, may not necessarily uncover the degradation of bone quality which increases subsidence risk.

2.2.4 Challenges in Lumbar Interbody Fusion Treatment

There are 3 aspects to investigate when aiming to address LIF complications and outcomes from a biomechanical perspective; understanding of *in vivo* biomechanical changes, quantifiable patient-specific pre-surgical planning, and effective postoperative monitoring.

The diversity of surgical approaches, implant designs and materials, and fixation configurations has resulted in clinical practice where surgeons do not have a clear understanding of the biomechanical consequences of each decision. The links between preoperative decisions, biomechanics, and complications are not evident. It is pertinent to examine the impacts of a LIF surgery on lumbar spine mechanics at the operated level and at adjacent segments to elicit a holistic perspective of *in vivo* changes following the procedure. Thereafter, biomechanics can be used as an input to pre-surgical planning, enabling surgeons to provide patient-specific treatment. Computational modelling is well-placed to quantify the biomechanical impacts of LIF surgery and simulate the effects of clinical scenarios.

Postoperative monitoring currently relies on imaging periodically or at the onset of pain. If not detected by periodic imaging, diagnosis of subsidence will only occur with the development of symptoms. If not identified during routine follow-up, subsidence may worsen over time and result in symptoms with further migration into the vertebra and consequent reduction in intervertebral height [95]. There is no diagnostic method for the early detection, risk assessment, or prevention of subsidence. Further, there is an evident need to investigate more sensitive and specific measures for the monitoring of bony growth in the fusion mass after LIF surgery. The poor outcomes and high complication rate from LIF surgery must be considered in the context of currently unreliable postoperative monitoring techniques cognisant of the multitude of surgical approaches and diversity in instrumentation design. Direct measurement from embedded sensors in implanted devices will yield more objective measures for postoperative evaluation that account for patient and practice variability.

2.3 Computational Modelling Approaches

2.3.1 Current Approaches in Computational Biomechanics

Computational methods in orthopaedic research provide tools to understand the mechanisms and biomechanical impacts of pathologies and complications. Further, they provide the means to develop, test, investigate, and optimise novel surgical techniques and orthopaedic prostheses with respect to their mechanical performance. Experimental mechanical testing is expensive and time-consuming, while not always providing the appropriate outputs to examine contact forces, stress distributions, and failure mechanisms [96]. Moreover, it is difficult to make efficient parametric changes and re-evaluate results when conducting mechanical testing [96]. Conversely, computational simulations rely heavily on the quality and validity of the input parameters, often obtained from experimental data. Computational biomechanics, as a field, provides the means to quantify loads in different orthopaedic joints, tissues, and structures in detail. Computational techniques are one of the three key approaches to understanding a clinical problem; where experimental data provides validity to simulation findings and clinical data confirms generalisability across patient populations.

Accurate modelling of orthopaedic joints requires consideration of their material, boundary, and geometric non-linearities. Orthopaedic joints are irregular in shape and often consist of multiple material components, such as cartilage, ligament, tendon, synovial fluid, and bone. Consideration of orthotropic and non-linear elastic material behaviour is critical to the quality of the output results. With different degrees of freedom at each orthopaedic joint, applying appropriate constraints and loads is similarly important.

Static rigid body modelling is a simplistic technique for assessing mechanical loads, often between bones and implants, where the bodies are assumed to be motionless [96]. Interactions are modelled with a single point of contact. As such, the contact forces are often over-estimated and the purpose of the models is, rather, to accurately represent the geometry of the bodies. The most obvious application of this tool is in prosthetic sizing and comparisons, which have utility in preoperative planning, whereby different prosthesis sizes or designs may be compared to each other in terms of the contact forces

they produce [96-99]. Ultimately, static rigid body modelling is an efficient tool for simple contact force comparisons.

Dynamic musculoskeletal models are often larger-scale models accounting for multiple joints and anatomical features, capable of modelling kinematics [96]. Similarly, the constituent bodies are rigid and reaction forces are simplified to allow for computation of body dynamics [96]. Upper-body models, such as those created in OpenSim [100], simultaneously simulate the influence of musculature and multiple joint interactions. Muscles are modelled as string or beam elements with tension. OpenSim models are scalable, providing the capability to manipulate muscle attachments and force interactions, and study the effects of different patient anatomies. Further, the models can be efficiently adapted to adjust for age, size, sex, and pathology [101, 102] – a benefit not often associated with computational models, but rather investigated in clinical cohort studies. Dynamic musculoskeletal models generally aim to account for kinematics and do not possess the ability to assess contact forces and model material behaviour in detail.

Inverse and forward dynamic models are less common computational techniques used in biomechanics. Inverse dynamics uses position, velocity, and acceleration inputs to calculate muscle forces and joint torques [96]. The inputs, however, are often taken from experimental setups, such as gait analysis, whereby the measures may be specific to the subject who was analysed. Alternatively, the kinematic input may be obtained from cadaveric testing. Inverse dynamics simulations are conducted by solving equations at discrete time points across the induced motion, which may last seconds to minutes [96]. The simulations are computationally inexpensive. Inverse dynamics is subject to several limitations, including simplified reaction forces and material modelling, and ideal conditions for simulating joint movement [96]. Further, the results are heavily dependent on the quality of the input kinematic parameters. Inverse dynamic models are suitable for studying clinical scenarios such as the mechanical causes of rotator cuff injury [100]. Forward dynamic models rely on the reverse process, using muscle forces and external loading as inputs to calculate the resultant kinematics [96]. The technique requires the calculation and minimisation of 'musculoskeletal cost' through algorithms run at each time point [96]. While input parameters can be more readily adjusted in forward dynamics, the simulation is more computationally expensive [96]. Studies using forward dynamics simulations have highlighted the activation and control of certain

shoulder muscles over others during common activities such as steering and turning a doorknob [103, 104]. Results from forward dynamics simulations have generally been accurate when provided with electromyography data inputs [96], however the computational cost is its largest drawback preventing widespread adoption. Forward dynamics simulations in biomechanics are best suited to addressing clinical questions of muscle pattern optimisation and motor control [96].

FE analysis is the most commonly used computational tool in biomechanics research [96]. The geometry of the model is divided into 3D blocks known as 'elements', where each vertex is considered a 'node'. The elements are assigned material properties and external loads are applied. The output is a detailed distribution of force and displacement throughout the model. Though computationally expensive, FE analysis provides the widest breadth of options to expend computational resources where desired – whether in modelling complex nonlinearities or in capturing the geometry with a finer mesh. Of the aforementioned methods, FE analysis incorporates the greatest level of detail in contact and material modelling while providing force and kinematic outputs at a level commensurate to the mesh density. As such, FE analysis is the most suitable computational modelling approach to study the biomechanical impacts of LIF surgery on spinal structures, as it produces a level of detail that provides genuine insight into clinical complications.

2.3.2 Finite Element Analysis

CT scans of the spine may be used to accurately capture and segment the anatomical regions of interest prior to generating a volumetric mesh. Further, adaptive meshing tools allow critical interfaces, such as the endplate-prosthesis junction, to be modelled with a finer mesh, improving the accuracy and detail of the results extracted from this region. FE analysis allows different deformable material models to be applied to specific regions of the model. For example, cancellous bone may be modelled as orthotropic, while the cartilage may be modelled using Mooney-Rivlin, Neo-Hookean, or Fung material models. FE analysis accounts for geometric and material nonlinearities, and experimental data can be used to define material behaviour. Certain FE packages contain multi-physics tools that incorporate fluid dynamics and hydroelasticity, relevant to synovial joint modelling. FE analysis can handle multiple complex boundary constraints and loading conditions while providing better estimates of contact forces [96].

In this thesis, Strand7 (vers. 2.4.6, Strand7 Pty. Ltd, Australia) is used to conduct FE analysis due to its ability to import and simulate high-density, segmented volumetric meshes in the order of 1.5M tetrahedral elements. Further, Strand7 can simultaneously solve multiple solutions on a single software license, maximising the computational efficiency of the solver. In all other respects, Strand7 is similar to other commercially available software packages, such as Ansys or Abaqus.

FE analysis is traditionally deterministic, that is, the outputs are directly related to the input parameters. In contrast, probabilistic modelling predicts a likely output considering uncertainties in the input parameters [105]. A traditional FE model, for example, can calculate the response of an implant to different applied loads corresponding to the weight of a patient. There are, however, many more factors influencing the performance of an implant, such as bone and muscle quality, location, and alignment [105]. These may be considered as sources of uncertainty in the system, which can be accounted for using statistical methods. Each of these input parameters is no longer a single variable, but a probability distribution. Computational biomechanics is increasingly adopting this blend of statistical and mechanical techniques to improve the clinical applicability and generalisability of the simulation, which has often been its greatest drawback. While all analyses conducted in this thesis are deterministic, it is important to consider this trend for future modelling endeavours.

(a) Finite Element Analysis in Spine Biomechanics Research

FE analysis has consistently been used to study the biomechanics of spinal degenerative conditions [106], loading patterns [107, 108], and implants [109-113]. A summary of the FE models used to study the spine from eminent spinal modelling research groups is presented in Table 2.2 [114]. Apart from Shirazi-Adl (1994), all other studies used commercially available FE software packages (Ansys or Abaqus) [115]. The approaches to material modelling of bone are split between isotropic and orthotropic material models, while most studies used a Neo-Hookean or Mooney-Rivlin model to represent the bulk of the annulus fibrosus. Frictional contact in the facets was only modelled in one study [113]. Pure bending moments, regardless of compressive pre-load, were applied between 7.5Nm and 10Nm [106, 107, 110-113, 115, 116]. Despite the diversity of modelling approaches employed, every study provided a detailed representation of the annulus fibres, accounting for their criss-cross orientation and multiple lamellae. The

successful implementation of the FE method in distinct spine research domains demonstrates its strength as a technique for investigating the mechanics of spinal implants and associated load-distribution changes. While the aim of this work is not to develop new modelling protocols, the methods in this thesis build on the existing literature with more accurate geometric modelling of the spine and prosthesis using finer meshing in contact areas of interest. The FE analysis literature provides clear inputs for considered approaches to intervertebral disc and ligament modelling. Many other material modelling parameters adopted in this thesis fit within the bounds of the seminal FE studies in spine.

Table 2.2: Summary of FE models used in spine biomechanics studies by eminent groups.

	Element Type	Elements	Nodes	Cortical bone	Cancellous bone	Annulus ground substance	Annulus fibres	Nucleus pulposus	Ligaments	Facet contact
Kiapour et al. [110]	8-node	27,450	32,946	Isotropic	Isotropic	Hyperelastic Neo-Hookean	8 layers; criss-cross; linear	Incompressible fluid	2D nonlinear hypoelastic elements	Soft frictionless
Zander et al. [112]	8-node	60,000	-	Isotropic	Orthotropic	Hyperelastic Neo-Hookean	14 layers; criss-cross; nonlinear	Incompressible fluid	Nonlinear stress-strain curves	Soft frictionless
Shirazi-Adl [115]	8-node; rigid bodies	1080 8-noded; 11 rigid bodies	3020	Rigid	Rigid	Linear hypoelastic	8 layers; alternating orientation; nonlinear	Incompressible fluid	Uniaxial 2-noded nonlinear elements	Soft frictionless
Schmidt et al. [111]	8-node	Not reported	-	Orthotropic	Orthotropic	Hyperelastic Mooney-Rivlin	16 layers; criss-cross; nonlinear	Incompressible fluid	Nonlinear stress-strain curves	Hard frictionless
Little et al. [107]	8-node	Not reported	-	Isotropic	Isotropic	Hyperelastic Mooney-Rivlin	8 layers; alternating orientation	Incompressible fluid	Linear elastic	Finite-sliding frictionless
Liu et al. [113]	8-node	112,174	94,162	Orthotropic	Orthotropic	Hyperelastic Mooney-Rivlin	12 layers; criss-cross; nonlinear	Incompressible fluid	Linear stress-strain curves	Friction
Aytürk & Puttlitz [116]	8-node	88,536	184,646	Orthotropic	Unknown	Hyperelastic Yeoh	2 groups; nonlinear	Linear isotropic	Exponential force-displacement curves	Neo-Hookean
Park et al. [106]	8-node	139,322	51,653	Isotropic	Isotropic	Hyperelastic Mooney-Rivlin	6 layers; criss-cross; nonlinear	Incompressible fluid	Nonlinear stress-strain curve	Hard frictionless

With respect to LIF, surgical approaches and implant designs have been compared using FE analysis, examining interface stresses, ligament strain, and stability in terms of range of motion (ROM) [117-119]. The literature thoroughly compares the effects of each approach and implant, however the studies did not model the progressing ossification of the fusion mass or quantify changes in all the relevant stabilising spinal structures, such as the facets. Regardless, the studies illustrate how FE analysis can be used to predict implant failure and clinical complication risk. Fixation configurations have been extensively studied using FE analysis primarily to measure ROM and endplate stress [120-126], however it is worth noting that the range of available cage geometries necessitates studies for each specific design and fixation configuration. Practical adjustment of patient-specific anatomical and clinical parameters, such as lordosis and bone quality [127, 128], is achievable with FE analysis; surgical factors such as implant positioning can also be studied [129]. Similarly, the parametric approach lends itself to evaluating fusion cage materials [130-135]. As previously discussed, the increase in interface stress with elastic modulus has been quantified, highlighting its influence on implant subsidence [132-134]. Further, FE analysis enables optimisation of implant porosity by studying interface stresses, joint stability, and implant strains under physiological spine loading [130, 131, 135]. Such studies support that porous materials provide the ideal mechanical properties for interbody cages.

Evidently, spine biomechanics has been widely researched using FE analysis. The diversity of surgical practice and complication rate, however, demand further research in this area targeted towards patient-specific guidance and pre-surgical planning for the avoidance of pseudarthrosis and subsidence.

2.4 'Smart' Orthopaedic Implants

The prevention of complications can be addressed through better-informed pre-surgical planning and patient selection studied with computational modelling, however timely intervention and management of complications relies on effective postoperative monitoring. Novel methods are required to gather direct measurements from the implanted device, which can be used to assess the risk of adverse events.

'Smart' orthopaedic implants refer to implantable devices used for surgical treatment in orthopaedics, for example, joint reconstruction and fracture fixation, which contain

sensing elements for real-time or delayed feedback to patients or clinicians [136, 137]. The electronics are often wireless for remote monitoring and may contain actuating components for delivering therapy, such as drug release or electrotherapy for stimulating bone growth [136, 137]. The sensing features are broad, including force, pressure, strain, accelerometric, and gyroscopic measurement. A defining feature of 'smart' implants is their ability to take *in vivo* measurements and provide patient-specific data for consideration in clinical management, such as load monitoring during postoperative physiotherapy, identifying signs of infection, and assessing complication risk. Safe remote monitoring requires wireless powering and telemetry of the device, negating the need for percutaneous leads. This mostly relies on inductive coupling or energy harvesting, and radiofrequency telemetry [138]. As such, advances in 'smart' orthopaedic implants will transform and modernise clinical practice by generating a new source of patient-specific data for guiding postoperative decision-making, reducing ambiguity in such decisions, and improving the standard of care. This section discusses the literature on 'smart' implants in orthopaedic applications to identify potential avenues for adoption in LIF treatment and management.

2.4.1 Hip, Knee & Shoulder

The humerus is a common location for fracture and shoulder joint injuries that require reconstructive surgery and replacement with a prosthetic humeral head [139]. A detailed understanding of forces and moments acting on the glenohumeral joint assists in understanding normal and pathological shoulder biomechanics [140]. 'Smart' shoulder implants provide access to *in vivo* biomechanical measurements from the joint. Bergmann et al. described the development of an instrumented, telemetric shoulder implant measuring contact forces and moments, involving modifications to a commercially available shoulder prosthesis [140]. Hollowed sections of the implant head and shaft provided the requisite space for semiconductor strain gauges to be embedded, measuring deformations in the neck of the implant [140]. Cavities in the shaft provided housing for associated electronics [140, 141]. The implant integrated a programmable telemetry chip, inductively powered at 4kHz, with radiofrequency transmission of mechanical and temperature data at a rate of 125Hz [138, 141]. As a result, Bergmann et al. successfully measured contact forces and moments acting on the glenohumeral joint, recording normalised data from the implant over a 7-month period during daily

activities and physiotherapy exercises [140]. While the study demonstrates that 'smart' shoulder implants may be clinically applicable and durable, concerns remain over the single patient study design. Westerhoff et al. and Bergmann et al. expanded the number of participants to 4 and 6 respectively, collecting contact force data from the shoulder implant during daily activities and physiotherapy exercises [142, 143]. Bergmann et al. were able to measure the variability in shoulder loads amongst study participants and quantify the increased frictional force in patients without glenoid replacements [143]. Westerhoff et al. identified specific motions to be avoided by patients in the immediate weeks following a shoulder operation due to the high loads measured at the implant-host junction and the potential for subsequent complications [142]. Both studies highlight the ability of 'smart' orthopaedic implants to elicit patient-specific clinical insight from mechanical data resolved from a limited number of sensors.

Hip implants are more commonly instrumented with electronics for monitoring due to the implant space afforded and complications associated with the operation. Mann et al. detailed the development of inductively-coupled instrumented hip implants over a series of publications [144-151]. The 'smart' hip implants, developed from a modified Austin Moore endoprosthesis, measured pressure across the surface of the acetabular cartilage [144-151]. Measurements were derived from resistive Wheatstone bridge arrangements and PAM/FM (pulse amplitude modulation/frequency modulation) transmission [136]. The 'smart' implant collected clinically meaningful data over a 32-month period [150]. Contact pressures during gait correlated positively with post-mortem histology of the cartilage, and negatively with cartilage thickness, demonstrating the effectiveness of the *in vivo* pressure measures as a representation of histological and anatomical changes [150]. Drawing on these results, Givens-Heiss et al. and Krebs et al. aimed to examine the effects of daily activities and postoperative exercise regimes on interface stresses over a 5-year period, attempting to identify motions that cause increased loading indicative of cartilage degeneration [148, 152]. Krebs et al. documented variations in torque and rates of pressure rise during lower-limb exercises, also measuring the increase in peak pressures with exertion [148]. Further, Givens-Heiss et al. showed that peak pressures over the 5-year period were recorded 1 year after surgery, tending to decline or stabilise thereafter [152]. Pressures recorded during postoperative rehabilitative exercise suggested that acetabular interface stresses, linked to cartilage degeneration, may be reduced through improved control of

muscle force and velocity during the rehabilitation therapy [152]. Limitations of this data still include the single-patient study design. Mann et al., however, throughout their series of studies on the 'smart' hip implant, have established its capacity to gather clinically meaningful data over 3-5 years post-surgery.

Bergmann et al. expanded on this suite of studies with the development of their instrumented hip prosthesis by modifying various implant architectures in clinical use [153-160]. The focus of their later architectures, approved for human use, was to measure force, moment, and temperature data [136]. Bergmann et al. relied on resistive Wheatstone bridge arrangements optimised to resolve forces in 3 dimensions, and miniaturised radiofrequency transmission [136]. Bergmann et al. continued the trend of using instrumented implants to provide postoperative data for clinical guidance [153-156]. Their research firstly investigated risk factors for hip implant loosening and other complications, such as walking, jogging, climbing staircases, and stumbling [154, 155]. While staircase climbing was not identified as high-risk, stumbling produced a force twice as high as any other movement [154, 155]. Further, the group were able to examine inter- and intra-participant variation by conducting multi-patient studies. In a study of hip prosthesis loads in 4 patients, Bergmann et al. concluded that inter-participant variation was highest during stair climbing and that implants should be tested primarily based on loads during walking and stair climbing, as loads during most other tasks were comparatively low in this cohort [153]. Kotzar et al. developed a similar implant architecture, however relied on external excitation of an implanted battery to activate measurement [161]. In a comparison of 2 subjects, the results confirmed that contact forces on the hip implant are higher during uncharacteristic movements, requiring sophisticated balance, rather than daily activities [161]. In a larger cohort of 8 subjects, Damm et al. noted greater inter-participant variation in implant loads and friction, highlighting the importance of each individual's synovia in lubricating the joint [162]. While Bergmann et al. previously attempted to quantify the impact of joint friction on surrounding tissue through temperature measurement with limited success [163], Damm et al. more effectively captured inter-subject variation in gait by quantifying friction in terms of power loss, subsequently noting the associated risks of thermally-induced implant loosening [162]. Puers et al., however, integrated a capacitive accelerometer with inductively-powered radiofrequency transmission for vibration analysis to identify implant loosening [164].

This group of studies outlines the development of telemetric instrumented hip prostheses with a limited number of sensing elements, including a wide range of parameters, such as friction and moments. The complexity of measurement and multiparticipant studies (up to 8 patients) for extended periods (up to 9 years) establishes the utility of a 'smart' hip implant in clinical postoperative management, particularly for detecting implant loosening.

Forces through the knee following total knee arthroplasty are important to postoperative management and may uncover risk factors that increase the rate of implant wear, rate of breakage, or onset of other clinical complications [165]. Additionally, 'smart' knee implants find utility in intraoperative alignment and the monitoring of knee balance during surgery or postoperatively to gauge tensile loads on the ligaments [165]. Research headed by D'Lima et al. has led to the development of a 'smart' knee implant architecture for the measurement of tibiofemoral compressive forces [166]. Force transducers were inserted in the four corners of a tibial tray, which transmitted data through radiofrequency telemetry and was wirelessly powered with electromagnetic induction [166]. The micro-transmitter and antenna were housed in the stem of the implant. This proof-of-concept was optimised with cadaveric *in vitro* testing before implanting the 'smart' knee system in an 80-year-old subject [166, 167]. Axial forces on the tibial tray tended to increase during walking up to 12 months following the operation [167]. Measurements during exercise indicated that descending stairs placed less load on the implant and the force recorded during cycling was the least compared to walking, stair ascent, and stair descent [167]. These measurements provide indications of what may be considered 'safe' or 'high risk' activities in the immediate period following a total knee arthroplasty. The second-generation of D'Lima et al.'s implant was adapted to measure six components of force from load cells in the tibial tray [168]. The data recorded from the 83-year-old subject showed a minimal impact of shear forces on the tibial tray compared to axial forces during common lower-limb motions [168]. As such, D'Lima et al. derived that the surrounding soft tissue plays an active role in resisting tibial shear forces after surgery [168]. In a continuation of single-subject studies, D'Lima et al. adapted their instrumented knee system for remote monitoring of forces from the tibial tray during unsupervised activities over a 4-year period [169]. Novel methods were implemented to calculate knee kinematics from *in vivo* force data, the combination of which was an input to a neural network system that accurately classified activities such

as walking, stair-climbing, and sit-to-stand transitions [169]. The study highlights the importance of long-term data collection and clinical utility of 'smart' knee implants in patient monitoring, specifically for elderly patients with minimal supervision and care.

In a multi-subject study designed to assess the forces that contribute to implant wear and failure, D'Lima et al. measured tibial forces during daily activities and recreation in 3 patients [170]. Across the cohort, lower implant loads were recorded during elliptical exercise than jogging. Treadmill walking, tennis, and golf, however, produced higher peak tibial loads. The data from this study clearly identify activities that may place a tibial prosthesis at higher risk of failure or degradation in the early postoperative phase. 6 semi-conductor strain gauges were aligned to measure 6 components of force in an instrumented knee implant developed by Kutzner et al., which relied on wireless inductive power and customised telemetry [171]. The authors noted that the axial torque measured *in vivo* during daily activities across the cohort was higher than the testing requirements defined in ISO standards, which has clear implications for implant wear [171]. Other measurements of axial loads and shear were comparable to similar studies that used different instrumented knee architectures [168, 171]. While multi-subject studies improve the reliability of the presented data, the studies did not assess inter-subject variations in knee loads, which is pertinent to the discussion on delivering patient-specific care. Confidence in 'smart' knee implants would, however, be further improved given the similarity in results obtained from separate cohorts using unique instrumented tibial architectures.

'Smart' knee implants have been designed to provide therapeutic feedback to patients and clinicians. Real-time monitoring of *in vivo* forces during gait and other activities has been undertaken such that modified motions may reduce loading of the implant and lessen the likelihood of associated complications. High knee adduction moments are linked to pain severity and the rate of arthritis progression [172]. Real-time feedback can facilitate gait adjustments to reduce external knee adduction and improve the mediolateral balance of forces in a manner that delays the onset of degenerative disease in the knee. Fregly et al. reported that medialisation of the knee during the stance phase of gait reduces contact forces by 16% while the use of poles as walking aids reduces loads by 27% [173]. Data feedback to patients may allow them to reduce contact forces acting on the knee prosthesis by simple modifications in gait. Furthermore, the real-time

measured differences in tibial loads during assisted walking demonstrates the sensitivity of the 'smart' implant and its potential to provide guidance to clinicians and patients regarding the choice of walking aid and its proper use to avoid postoperative complications [172].

The extensive *in vivo* research into 'smart' knee implants has provided confidence to clinicians, and there are early indications of its adoption in clinical practice. Single-subject studies gathered extensive data on multidirectional knee loads during different activities and exercises over long follow-up periods [166-169]. The sensitivity and accuracy of the data collected allowed it to correctly classify a patient's movements [169]. While further multi-subject studies will increase confidence in the performance of instrumented knee prostheses, the evident clinical utility and provision of real-time therapeutic feedback are clear strengths and indications that widespread adoption in clinical practice is imminent. This is evidenced by the recent de novo clearance of Zimmer Biomet's 'smart' knee implant, by the USA's Food and Drug Administration (FDA), for remote monitoring and personalised operative and postoperative care [174].

2.4.2 Spine

The development of 'smart' orthopaedic implants for spinal applications is complicated firstly, by the size of the implants and, secondly, by the variety of geometries and materials used. While hip, knee, and shoulder implants retain some commonalities amongst their respective geometries and clinical rationales, spinal implants for orthopaedic applications may include interbody fusion cages, screws, rods, plates, and vertebral body replacements (VBRs). It is not immediately clear where the integration of sensing technology may produce the optimal clinical benefits. To date, 'smart' spinal implants for human use have generally taken the form of instrumented VBRs and fusion rods.

The development of the first instrumented VBR was reported by Rohlmann et al. in 2007 [175]. Rohlmann et al. modified a Synex VBR available for clinical use, integrating 6 semi-conductor strain gauges, for measuring 6 load components, with an inductively powered 9-channel telemetric unit operating pulse-interval-modulated radiofrequency transmission [175]. Rohlmann et al. implanted this instrumented VBR in two patients, measuring forces and moments acting on the implant during different movements [176].

While measurements were taken over a 6-month period, the highest forces were recorded in the first month after the operation. Upper-body flexion and stair climbing resulted in the highest loads on the implant. While both subjects reported a comparable reduction in load in the lying position, loads measured during sitting compared to standing were inconsistent between the two patients. Rohlmann et al. expanded their data collection and follow-up period, implanting their instrumented VBR in 5 patients with monitoring conducted over 5 years postoperatively [177]. High resultant forces were reported in activities involving the anterior relocation of the subject's upper body centre of mass. The authors, however, did not report any changes in load patterns over the postoperative follow-up period [177]. In a similar publication, the group reported the loads on the VBR during postoperative physiotherapy exercises [178]. In their study of 5 patients, Rohlmann et al. identify a group of safe exercises and those which place excessive loads on the implant that may compromise the surgical outcome [178]. In both studies, considerable inter- and intra-subject variation in force measurements demonstrated the influence of exercise technique on implant loads and, as such, the influence an individual or physiotherapist may have on a surgical outcome [177, 178]. In a detailed examination of load patterns from the VBR during upper body flexion and lifting exercises, Dreischarf et al. quantified how trunk support and the positioning of external loads influence implant mechanics [179, 180]. The accuracy and time-domain resolution of the data enabled a more detailed understanding of the force-patterns on the implant during each motion. Further, the authors highlighted the influence of anatomical, biological, and diurnal factors in causing inter- and intra-subject variability [179].

The design of instrumented posterior fixation rods for *in vivo* use in spinal fusion was first reported by Rohlmann et al. in 1994 [181]. 6 semi-conductor strain gauges were mounted to the inner walls of the fusion rods to measure multidirectional forces and moments [181]. An 8-channel radiofrequency telemetry unit and inductive coil were fit inside the rod cavities, wirelessly powered with electromagnetic induction. Thereafter, the instrumented fixation rods have been used to monitor patients in a variety of settings, including monitoring loads in cases of degenerative instability [182], assessing loads during walking and various body positions [183, 184], and determining the influence of muscle activation on resultant forces [185]. Rohlmann et al. gathered detailed load data before and after additional anterior fixation of a patient with

degenerative instability, reporting a clear change in load distribution, however only a minor reduction in load after the insertion of the anterior instrumentation [182]. The highest loads were recorded during the first month after surgery, with results suggesting that lifting, upper body flexion, and bending should be avoided to reduce the risk of postoperative complications arising from implant failure. Radiographic data obtained after 8 months confirmed that fusing bone was not present. Notwithstanding the limitations of a single-subject study, the data from the instrumented rods was not able to identify this complication. In a study of 2 subjects implanted with the instrumented rods, Rohlmann et al. documented higher loads during walking than lying, sitting, or standing [183]. Loads on the rods were highest during stair climbing, however considerable variation was reported between the participants. Rohlmann et al. expanded their investigation to 10 patients, monitoring forces in different body positions, however similar variability in results between participants was reported, potentially due to differences in surgical indications and approaches [184]. Consistently across the cohort, load distribution was altered following the insertion of an anterior interbody fusion cage and standing produced higher loads that sitting. The results allow for some substantiated suggestions about postoperative movements that may be considered safe and those that place excessive force on the fixation device. Muscle activation may be a further contributing factor to patient-specific spinal loading patterns and inter-subject variations, with Rohlmann et al. quantifying the influence of muscle tension on loads in the instrumented fixation device [185].

Windolf et al. recently described the development of posterior fusion rods integrated with a load-sensing unit [186, 187]. The battery-powered sensing units were designed to house resistive strain gauges configured to quantify bending and tensile loads, and a transmitter that sends data to a smartphone via Bluetooth [187]. In a single sheep study, Windolf et al. demonstrated a sensor-recorded reduction in load on the fusion rods as the fusion mass ossified in the facet joint gap [186]; a finding that was not produced by Rohlmann et al.'s design [182]. Szivek et al. attempted to integrate strain gauges with fusion rods to assess the progression of bony fusion over time *in vivo*, however were unable to record enough data to produce valid findings [188]. While the findings of Windolf et al.'s animal study may not be completely comparable to human studies, the results suggest achieving accurate monitoring of fusion progression may be possible with sensors embedded proximate to the fusion mass [186].

'Smart' orthopaedic implants for use in the human spine have so far been limited to VBRs and fusion rods. Detailed data has been captured for notable follow-up periods in individuals and in small cohort studies. Loads on the respective implants have been reliably documented, providing some basic indications of movements and activities that may compromise surgical outcomes based on the observed load patterns. The findings have clear and direct implications for postoperative physiotherapy. There were, however, considerable variations in measurements between subjects suggesting further study is required in larger cohorts. Accordingly, the research exemplifies the need for devices that enable patient-specific, individualised care during the postoperative phase in a manner that accounts for variability between patients.

It has not yet been reliably established that loads in fusion rods can be used to assess the maturation of the fusion mass. While instrumented spinal fusion cages are yet to be studied in humans, Ledet et al. recorded loads from an *in vivo* sensing interbody cage implanted in baboons [189]. The 6-week recording period, however, was not sufficient to demonstrate load changes with fusion progression. Demetropoulos produced a calibrated ALIF cage instrumented with strain gauges and a battery-powered telemetry unit, however were not able to demonstrate its clinical utility or record data *in vivo* [190]. Instrumented spinal implants have produced an array of meaningful data for understanding the mechanical influence of postures, movements, and muscle activation [191]. Nonetheless, they are yet to produce tangible results for the provision of clinically meaningful guidance and care, particularly in comparison to other 'smart' orthopaedic implants [191]. Complications, such as pseudarthrosis and subsidence, are common, painful, and difficult to avoid. 'Smart' spinal implants must be designed with consideration of how they may prevent these adverse outcomes or reduce their clinical impact.

2.4.3 Fracture Fixation

Internal fixation is required in some fracture cases, often in long bones, whereby a plate is affixed to stabilise the bony fragments and aid the healing process until bony union is achieved [191]. Non-union is a potential adverse outcome and the biomechanical indicators for this remain unclear. Furthermore, while radiological assessment of healing is the clinical gold-standard, such measures do not provide insight into the biomechanical changes at the site, as radiological, clinical, and mechanical union may

not necessarily be aligned [192]. Bone formation progresses through a mechanically soft phase during callus formation, early creeping substitution or endochondral ossification, fibrocartilaginous formation, or any combination of these histological stages. During this phase of bone healing, loading of the fracture site may cause excessive inter-fragmentary micromotions that inhibit proper ossification, or may stimulate ossification in accordance with Wolff's law [193]. In the absence of *in vivo* data, there are no objective parameters to accurately assess bone healing or guide the course of postoperative management to avoid complications and facilitate healthy and timely ossification. Several *in vivo* studies demonstrate the clinical applicability and effectiveness of sensors in assessing the extent of bone healing, while advances in osteoconductive stimulation provide the promise of a new generation of 'smart' implants with therapeutic actuation capabilities.

Burny et al. published the first design of a fracture fixation plate instrumented with percutaneously-wired strain gauges for *in vivo* use [194]. With data from large cohorts of more than 500 patients with long bone fractures, Burny et al. identified links between strain gauge measurements and 7 healing patterns, such as delayed union, non-union, and callus resorption [194]. The authors noted that complete healing at the fracture site was correlated with a plateau of force on the fixation plate at 50% of normal bone loads [194]. Similarly, loads from an instrumented intermedullary nail for femoral fracture fixation in a 33-year-old patient reduced by 50% following complete union of the segments 6 months after surgery [195]. The 8-channel telemetry system was inductively powered and resolved multidirectional strains from 4 gauges. Brown et al. measured loads from a battery-powered telemetric instrumented femoral fixation plate noting that peak bending moments were measured during walking in the 4-week period post-surgery [196]. Using a similar architecture, Seide et al. reported results from 54 patients with non-union of a femoral fracture [197]. Most notably, the results indicated that the mechanical effects of healing and union precede the radiological indications of healing onset. Further, the authors captured the high inter-subject variation in healing times ranging from 12 weeks to several months [198]. *In vivo* studies with sizeable cohorts confirmed the presence of the distinct healing patterns observed by Burny et al. [194, 197, 199]. Instrumented fixation implants for long bone fractures have clear promise and clinical utility. 'Smart' implants in this space are an evident alternative to radiological assessment and can inform postoperative management in patients to avoid over- or

under-loading the fracture site, safely assisting patients back to active states in the recovery period.

Capacitance-based stimulation systems have shown promising results in *in vitro* settings for improving osseointegration of orthopaedic implants [200, 201]. Optimisation of the capacitive electrodes led to osteoblastic proliferation and differentiation in the lab environment [201]. Soares dos Santos et al. documented a positive osteoconductive response at low frequencies, however also reported differences with electrode thickness and pattern [200]. Sensing modalities that utilise electric fields and capacitive principles are well-placed to capitalise on the osteoconductive properties of these signals to elicit the development of 'smart' orthopaedic implants with therapeutic actuation, which may reduce the risk of implant loosening, in the case of hip, knee, and shoulder prostheses, or reduce the likelihood of non-union, in the case of interbody fusion and fracture fixation. Nonetheless, there are challenges associated with surface-excitation, electrode exposure, and safety to be addressed as the field moves towards the clinical realisation of such devices.

2.4.4 Development Directions

The application of 'smart' implants has been studied in several orthopaedic joints, establishing their ability to quantify mechanical loads acting on the prosthesis for lengthy periods after surgery. Progressive load changes from the early to late postoperative phase, movement patterns, activities, and exercises were more successfully quantified in hip and knee implants than the other orthopaedic prostheses. A performance at this level indicates that these instrumented devices can guide postoperative physiotherapy and inform strategies to prevent the onset of adverse events associated with over-loading the implant.

Instrumented implants must produce clinically meaningful data and, preferably, real-time therapeutic feedback. While detailed analysis of loading patterns in different orthopaedic joints may be useful in research settings, clinical adoption requires the implant to promise an improvement in standards of care and clear indications of reduced adverse outcomes. Specifically, instrumented knee implants showed that changes in gait and the use of suitable walking aid can reduce loads on the knee in a manner that reduces pain and postoperative complications. Such findings led to higher clinical confidence

and subsequent commercialisation. Of similar clinical impact, instrumented fixation plates are a more accurate and objective measure than radiological assessment of bone healing. The real-time data can be used to adjust postoperative rehabilitation such that it facilitates bone healing and reduces the likelihood of non-union. Evidently, 'smart' orthopaedic implants, in any joint, must be designed to meet *specific* clinical challenges.

As of yet, 'smart' orthopaedic implants for the spine have been limited to fusion rods and vertebral body replacements. Their use as a device for postoperative monitoring in their current state has not shown sufficient clinical utility or the ability to produce meaningful change in postoperative patient care. There is a convergence between the domains of fracture fixation and spinal fusion, whereby spinal fusion represents an exaggerated case of fracture fixation. Sensors can be embedded in interbody fusion cages to create an instrumented, or 'smart', interbody fusion cage, designed for the primary purpose of tracking the progression of bone growth until complete fusion is achieved and eliminating the need for subjective and unreliable radiological assessment of the fusion mass. Addressing implant subsidence can be considered concurrently, while instability, misalignment, and targeted postoperative rehabilitation are secondary goals that can be achieved with the integration of a wider range of sensing modalities in next-generation architectures. Furthermore, given recent developments in therapeutic actuation, there is a role for the inclusion of electro-stimulation to improve osteoconductivity and reduce the rates of pseudarthrosis.

2.5 Sensing Modalities and Telemetry Considerations

Design of a functional 'smart' interbody cage requires identification of suitable sensing and telemetry technologies. The primary purpose of the 'smart' cage is to monitor fusion progression and assess subsidence risk; sensing modalities are compared in light of this. This section presents an overview of sensing modalities that have been used in orthopaedic biomechanical measurement and outlines their operating principles. Common wireless telemetry methods are also summarised relevant to the LIF context.

2.5.1 Sensing Modalities

Structural health monitoring (SHM) is a notion adapted from medicine, which is currently associated with civil and mechanical engineering disciplines [202]. Using real-time data from sensor arrays, SHM is an established strategy for damage detection in

large engineering structures [203]. Similarly, mechanical signals are of interest in orthopaedics to monitor the health of musculoskeletal joints, eliciting deeper insights into their biomechanical function and monitoring the onset of complications or mechanical failure.

Various sensing modalities are integrated with large civil and aviation structures at the macro and meso scale with limited size constraints, including optical fibre sensors [204], acoustic emissions sensors [205], and strain gauges [206], which are optimised for damage detection by measuring strain and high-frequency stress waves (Figure 2.8). In medical applications, sensors embedded within an implantable device measure the parameter of interest, transmitting it for external processing to reduce the extent of implanted electronics. Outputs from processing may be used as inputs for therapeutic actuation delivered by implanted components [136, 137]. Translating SHM from the macro and meso scale to orthopaedic applications at the micro scale requires sufficiently small sensors with suitable load limits and the potential for wireless actualisation. This thesis is not concerned with sensing at the molecular (nano) scale.

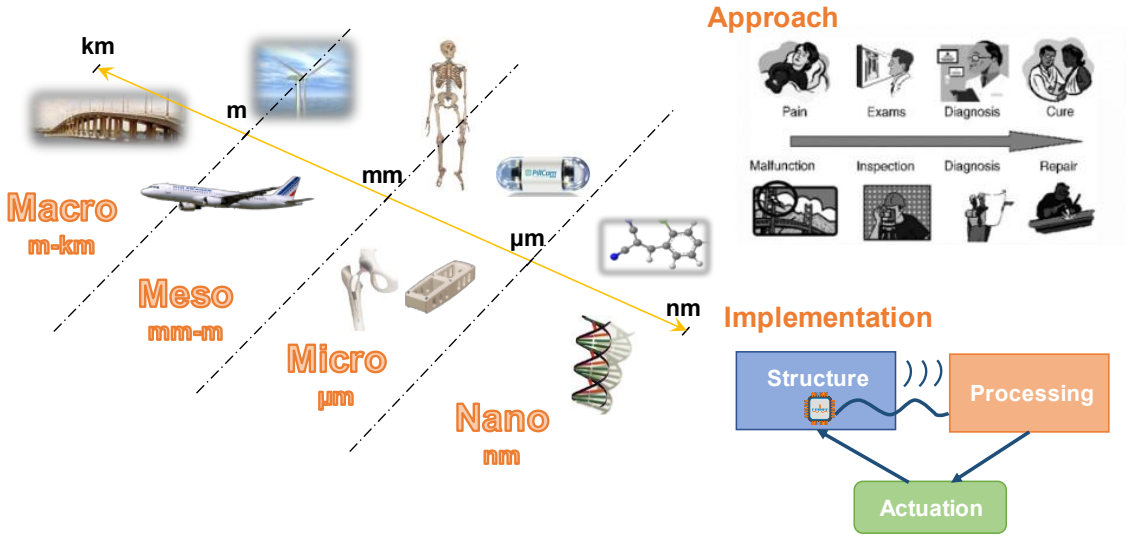

Figure 2.8: There are a range of sensing modalities available for SHM in large structures, aiming to monitor for mechanical failures.

Hip prostheses have been embedded with magnetic oscillators and ultrasound sensors for measuring vibrations indicative of implant loosening [165], however the progressive ossification of bone graft makes this measurand less relevant for monitoring LIF outcomes. Despite accurately mapping strains in bone, bone cement, dental composites,

and orthopaedic joints *in vitro* [207], the requirement for a coupled light source and reflectometry with optical fibre sensors is a significant impediment to wireless actualisation. Pressure, strain, and force measurements aid the primary goals of assessing fusion progression and subsidence risk by quantifying load-share with the graft and locating endplate stress concentrations. These sensors can be understood and compared for their utility in fusion implants under rigid and flexible classifications.

(a) Rigid Sensors

Rigid sensors can be defined as commercially available dies, which have mechanically stiff physical properties and operate on piezoelectric or piezoresistive principles; that is the sensors produce a proportional change in electrical potential or resistance, respectively, in response to an applied load. These sensors often require mounting on printed circuit boards (PCBs) for data extraction. A search of available rigid load sensors uncovers an abundance of sensors with unsuitably low load limits. There are limited examples of rigid sensors that would withstand 900-1200N of compressive load expected in the intervertebral space due to the fragility of their primary constituent materials; silicon and aluminium. As such, the durability of rigid sensors is questionable without appropriate encapsulation. Many are too large for an implantable medical device or comprise of irregular geometries, raising further challenges to integration. Despite the strict requirements for load limits, geometry, and size, Omron (2SMPB-02E, Japan), Murata (SCB10H-B012FB, Japan), and Amphenol (Novasensor P122, USA) are potential rigid sensor candidates for a load-sensing interbody cage, with operating limits up to 5MPa.

There are few examples of rigid sensors in 'smart' orthopaedic implants. Verasense for intraoperative knee prosthesis alignment has reached clinical adoption with embedded rigid electronics [208], however loads on the implant while the patient is supine are considerably lower than for everyday activities post-surgery. As such, durability of the sensors is not a principal consideration for that application. Conversely, the aforementioned sensors would require complete encasement and packaging to improve durability and prevent damage long-term for *in vivo* spine applications.

Rigid sensors have numerous advantages. The resolution of the system can be efficiently increased by mounting several spatially-distributed sensors on the same PCB within the implant. Further, PCB-mounting simplifies data collection and wireless integration,

enabling the required processing chips to be mounted on the same PCB as the sensors. Developments in the manufacturing of thin and flexible PCBs limit the space occupied within the implant. Lastly, the design of the sensors allows them to measure direct compression perpendicular to the applied load, increasing its sensitivity to changes in graft and endplate stiffness located proximate to the endplate-prosthesis interface (Figure 2.9). Strain gauges, often embedded under indirect loads, may be less effective under static compressive forces at the extremities of the implant.

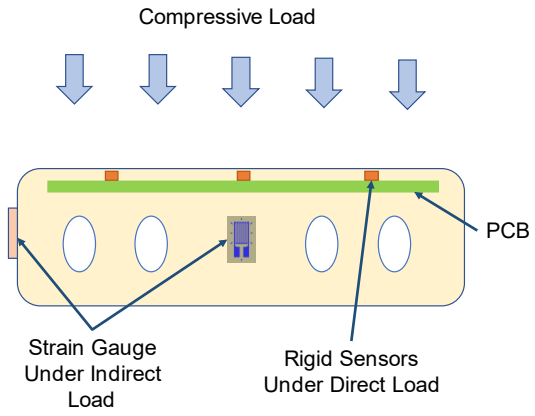

Figure 2.9: Anterior cross-sectional view example of an XLIF interbody cage embedded with rigid and flexible sensors.

(b) Flexible Sensors

Flexible sensors can be defined as conductive materials adhered to flexible substrates in patterns that cause a change in resistance, electrical potential, or capacitance in response to an applied load. A range of flexible sensors are available commercially and can be fabricated using techniques such as photolithography, aerosol or inkjet printing, sputtering, and screen printing [209-212]. Overall, flexible sensors are size-customisable, less susceptible to damage, and more sensitive to load due to their flexibility. Further advantages and drawbacks are sensor-specific.

Pressure-sensitive films (Sensor Products Inc., K-Scan, Tekscan) have previously been used to study loads in hip and knee joints [213, 214]. The films generally operate as force-sensing resistors, responding to load with a proportional decrease in resistance. The sensors have high spatial resolution and can map interface stresses; however, they are not suitable for dynamic loading [213-216]. Between loading cycles, the sensors do not adequately return to their rest state and are therefore more susceptible to drift. Further,

the film-based sensors have low load limits (~50N; Ohmite, Flexiforce USA) that are not suitable for use in postoperative monitoring [211], but rather suit intraoperative prosthesis alignment when the patient is supine [208, 214, 215]. These commercially available sensors are yet to be adapted for wireless telemetry and powering.

Strain gauges are the gold standard for measuring strain and operate most commonly using piezoresistive principles. Essentially, deformations in the plane of the resistive foil of the strain gauge induce an electrically measurable change from the rest state. The majority of the presented 'smart' implant research has used strain gauges hermetically sealed within the implant to assess loads on the prosthesis. Strain gauges were successfully used to monitor loads in spinal prostheses, however were generally more effective in larger implants such as VBRs [175-178, 181-185]. Strain gauges mounted on an interbody cage required subcutaneous housing of batteries and other electronics, while only successfully measuring loads from a baboon for 6 weeks [189]. Strain gauges are commercially available, reliable, sensitive, and accurate sensors for quantifying loads, however, they are more susceptible to damage compared to other sensors depending on the substrate. With strain limits of at least 5%, the load limits of a strain gauge are unlikely to be exceeded in the interbody cage under physiological loads. Further, multidirectional strain mapping may yield substantial clinical utility. Conversely, wired connections between the gauge and processor within the implant are susceptible to debonding. The spatial resolution of strain gauges is poor, and the sensors do not practically lend themselves to multiplexing. Increasing the number of sensors also increases the complexity of the associated electronics and power requirements.

Flexible capacitive sensors are a class of sensor consisting of a conductive material casted onto a polymeric substrate in an interdigitated structure. Common conductive materials include gold, silver, graphene, or carbon; polydimethylsiloxane (PDMS) and polyimide (PI) are common substrates [212]. PDMS and PI are typically inert, non-toxic, cheap, and hydrophobic, ensuring they will not swell in physiological conditions [211]. The sensors can be produced with a variety of techniques, however they generally involve a method for laser cutting the interdigitated structure into the substrate and a method for even coating of the conducting material [211, 212].

From Equation 2-1, it is clear that a strain-induced change in the effective sensing area (*A*) or inter-electrode distance (*d*) will cause a change in the measured capacitance. The capacitance is, therefore, a function of changes in length (*L*), width (*W*), and inter-electrode distance (*d*) (Figure 2.10) [211]. The sensor can be modified for biocompatibility, flexibility, durability, and sensitivity through changes in the substrate polymer and coating material.

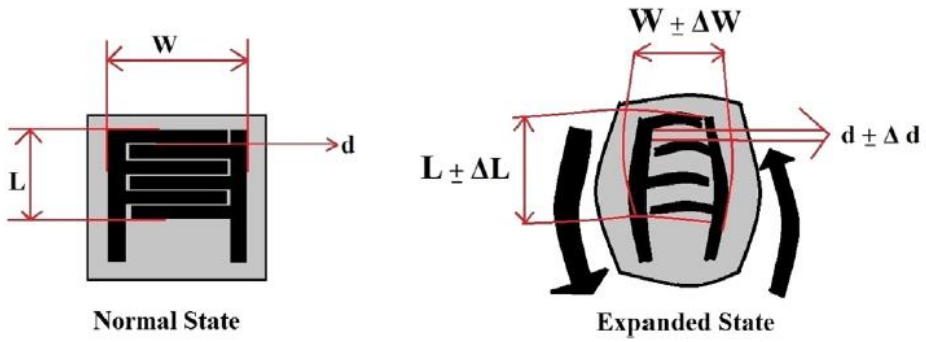

Figure 2.10: Interdigitated structure of the flexible sensor. Deformation causes changes in the effective sensing area, subsequently causing changes in the recorded capacitance [209].

The sensor detects strain through changes in capacitance. As described by Nag et al., the governing equation is derived from the capacitance for a parallel capacitive plate [211]:

$$C = \frac{\epsilon_0 \epsilon_r A}{d}$$

Equation 2-1

Where:

$$\epsilon_0 = Permittivity\ of\ vacuum$$
$$\epsilon_r = Relative\ permittivity$$
$$A = Effective\ sensing\ area$$
$$d = \ Distance\ between\ electrodes$$

Graphene coatings provide higher strain and pressure sensitivity than carbon nanotube (CNT), silver, or gold coatings [210, 217]. Nag et al. found graphene to be 60 times more conductive than CNTs [210]. There remain concerns over the biocompatibility of graphene, although further research is required into sensors utilising small volume

ratios of graphene in this specific application. Graphene has several distinct advantages apart from its conductivity and strength, including its homogeneity and dispersion characteristics [210]. It has been integrated with Radio-Frequency Identification (RFID) technology and in supercapacitors, highlighting its wireless and energy harvesting potential [210].

Due to their novelty and various typologies, flexible capacitive sensors have not been used to measure strain *per se*. To date, sensing applications for flexible sensors have been limited to external monitoring of limb movement and respiration [209, 211]. PDMS, polyurethane, and PI have suitable strain limits of 200%, 100%, and 5% respectively [217].

Flexible capacitive sensors and strain gauges have similar operating principles and limitations. Fabrication of flexible capacitive sensors may present a viable tailorable sensing modality in orthopaedic applications. Thicker, more deformable substrates, such as PDMS, may elicit a higher sensitivity to axial loads. Adopting the strain gauge or flexible sensor patterns to build a network of integrated sensors on a single substrate or PCB is a potential avenue to overcome their limited spatial resolution and reduce the complexity of signal processing.

Flexible capacitive sensors and strain gauges have evident advantages in terms of durability, sensitivity, and size. As per Figure 2.9, however, flexible sensors are not designed to measure direct load, but rather load-induced material deformations. Without PCB bonding, integration with processors and microcontrollers that control data extraction is more complex than for rigid sensors. Risk of debonding between the flexible sensor and PCB should also be considered. Notwithstanding the influence of substrate materials on sensor performance, etching capacitive flexible sensor or strain gauge patterns directly onto the PCB with conductive materials overcomes the debonding risk, and generates a spatially efficient and integrated implantable design with wireless telemetry potential.

2.5.2 Wireless Telemetry Methods

Wireless telemetry requires means for both wireless power transmission and data retrieval. While wireless data transmission in isolation is achievable with implantable batteries, subcutaneous wiring can lead to tissue scarring, battery leakage can cause

serious adverse events, and intervention is required for periodic battery replacement [218]. Modern implantable devices are trending away from implantable batteries as an energy source, relying primarily on inductive coupling and energy harvesting as an alternative (Figure 2.11).

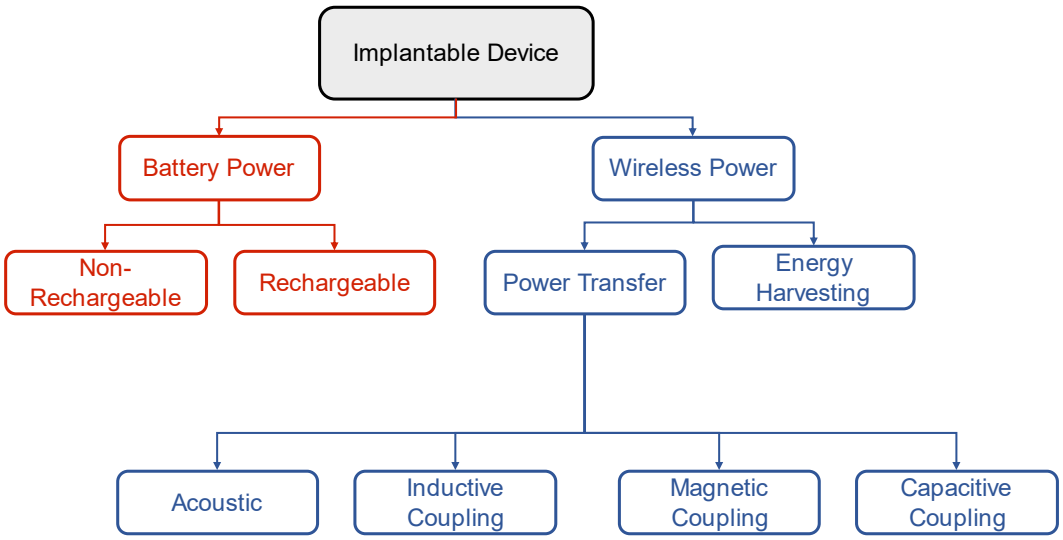

Figure 2.11: Overview of implantable device powering options.

Energy harvesting is a novel and evolving approach to continuous *in vivo* power generation, leveraging body movements and heat to produce energy. Periodic movements produce low levels of energy through frictional heat or deformations of a piezoelectric material. Previous research has established the applicability of electromagnetic, piezoelectric, and triboelectric energy harvesting in orthopaedic implants [219, 220]. Triboelectric generators are spatially efficient, however they are not yet able to produce the required power for sensors and telemetry [219]. Similarly, repetitive loading over time is required to produce continuous power for the 'smart' system and there is, therefore, a trade-off between the mechanical strength of piezoceramics, which produce more energy but are less deformable, and other piezoelectric materials that are more flexible but generate less power [219, 220]. In the absence of traditional energy storage or advancements in capacitive storage, energy harvesting for powering instrumented orthopaedic implants requires regular movement to produce deformations or friction that continuously power the device. Further research is required in this field to achieve those results.

Wireless power transfer in the context of implantable medical devices encompasses a system capable of transmitting power from an external source across a medium to an electrical load contained within the body that is without physical connection to the external power source. The power transmitted may be electromagnetic or non-electromagnetic energy, each with associated benefits depending on the application [218]. Electromagnetic energy transfer systems can be classified as near-field (up to 100mm distance) [221], mid-field (100mm to 500mm) [222], or far-field (greater than 500mm) [218]. Far-field systems are inappropriate for most biomedical applications, particularly owing to its high operating frequency [218]. Transmitting energy across wider fields results in energy spreading and poor transfer efficiency, such that the delivered power is insufficient, while increasing the power delivery would risk damage to tissue surrounding the implanted medical device [218, 223].

Near-field inductive coupling is the most established method for wireless power delivery in implantable medical devices. An external coil is powered with a high-frequency voltage to generate an alternating magnetic field that induces a current in the implanted receiver coil connected to a matched network. Generally, the size of the coils is proportional to the separation between them [218]. In contrast to energy harvesting, inductive powering is, in most cases, discontinuous, where a magnetic field induces current when measurements and data transmission are required, and removal of the field will prevent the system from recording data. Using continuous inductive coupling for constant real-time data retrieval may raise safety concerns [136, 137]. Inductive coupling systems, delivering power in the milliwatt range, have been integrated in brain implants [224], neurostimulators [225], ocular implants [226-228], capsule endoscopy [229], and shoulder [138, 141], hip [149, 164], knee [171], and spine prostheses [175, 182]. As a method for wireless power transfer through distances typically from 5mm to 50mm, inductive coupling has successfully translated from research to commercial implantable medical devices [218]. Near-field inductive coupling is the most common wireless power transfer mechanism for ‘smart’ orthopaedic implants, which are on the cusp of commercial translation. Being an established and reliable method, the literature presents clear protocols for design, optimisation, and testing of inductive power systems with well-defined architectures for different applications in implantable devices. Integrating such a system with a medical device is a matter of optimising the coil parameters against the distance and power requirements depending on the application [218]. Where the

device requires continuous power, ongoing alignment of the coils is required, which may be challenging to maintain in a mobile patient or with any migration of the implanted device [218]. Power transfer efficiency is an ongoing concern and research focus for inductive coupling systems, particularly with variable electrical load conditions on the receiver end [218]. Loading and displacement of the coil, of particular concern in orthopaedic applications, may induce power transmission fluctuations that must be appropriately addressed [230]. Further logistical issues with the location, size, fixation, and biocompatibility of the receiver coil remain application-dependent. Capacitive coupling is a novel approach to wireless power, whereby a pair of parallel conductive plates are placed on either side of the skin, generating a low current transferred through the skin to the implanted device [218]. Despite transferring power through 7mm of skin tissue, this technology remains in its infancy and requires further research into tissue safety [218].

Mid-field wireless power transfer is an emerging research focus within the wireless telemetry discipline, aiming to overcome limitations in power transfer at separation distances that are more reasonable for implanted medical devices. Magnetic coupling is achieved with transmitter and receiver antennas, and matching networks operating at high frequencies [218]. While commonly able to transfer power over the required distance, power delivery remains a concern in mid-field technologies. Applications in capsule endoscopy demonstrate the technology can be miniaturised for ingestible medical devices, however only 800μW was received by the conformal implanted antenna through a 5mm porcine tissue medium with 1W delivered from the transmitter antenna [231]. Applied in a neurostimulator with larger dimensions, the maximum power transfer measured was 180mW, however the maximum receiver power transfer efficiency ranged from 13-20% at a distance of 15mm [232]. Despite achieving transmission across 500mm of rabbit tissue, the received power in a 2mm x 4mm cardiac stimulator reached a maximum of 200μW from 500mW of transmission [233]. Evidently, the low output power of mid-field technology remains a concern for implantable medical devices. Compounding issues meeting tissue safety guidelines with high specific absorption rates at frequencies in the MHz and sub-GHz range, and alignment requirements between the antennas, raise further challenges in the broader adoption of mid-field wireless power systems [218].

Acoustic power transfer is the most promising alternative to electromagnetic coupling technologies, whereby piezoelectric transducers transfer ultrasound waves to the implanted device where it is converted to electrical energy [218]. Being an emerging technology, the cost and expertise required for acoustic power systems are substantial, while the effects of ultrasound on the body in power transfer applications are not fully understood at this point. Applications of acoustic power until now have generally been studied across simple soft-tissue mediums, achieving output power from 16μW to 3mW [234-236]. This is largely due to challenges in transmitting acoustic energy through tissues of different densities with attenuation increasing with distance [218, 237, 238]. Further, orthopaedic applications have not been well-studied due to the complete attenuation of acoustic signals by bone [218].

The data transmission aspect of wireless telemetry is simplified by the unidirectional flow of data from the implanted device to the external reader where closed-loop feedback and actuation features are excluded. Notwithstanding security concerns with medical data, Bluetooth and WiFi technologies would require separate protocols for handling power and data transfer, increasing the complexity of the implanted components and the required power. While multi-carrier telemetry improves power transfer efficiency by transmitting data and power as distinct signals, the added design features, *in vivo* space requirements, and cross-coupling between the signals are complex considerations for system design within the confines of an interbody cage [239]. Conversely, single-carrier telemetry transmits data through modulation of the power signal [239]. The use of a single link reduces the implantable hardware components and overall power consumption. Amplitude-shift keying (ASK) [240], frequency-shift keying (FSK) [241], and phase-shift keying (PSK) are common modulators for low-power single-carrier telemetric systems [239]. Binary data modulates the amplitude, frequency, or phase of the carrier signal (Figure 2.12), which is subsequently demodulated at the external receiver to recover the binary data. ASK is the most common modulation mode of the techniques due to its simple circuitry and minimal power requirements [239, 240]. In contrast, it is not robust to noise, interference, or coupling variation, resulting in a low data transfer rate [242]. On-Off keying (OOK) is a variation of ASK modulation that reduces sensitivity to noise [242]. In single-carrier systems using OOK, however, the low state is characterised by the absence of power delivery, preventing continuous powering of the device [242]. Further considerations, such as carrier frequency and transmission

distance, are intrinsically linked to those same parameters in the power domain and should be tested as an integrated system.

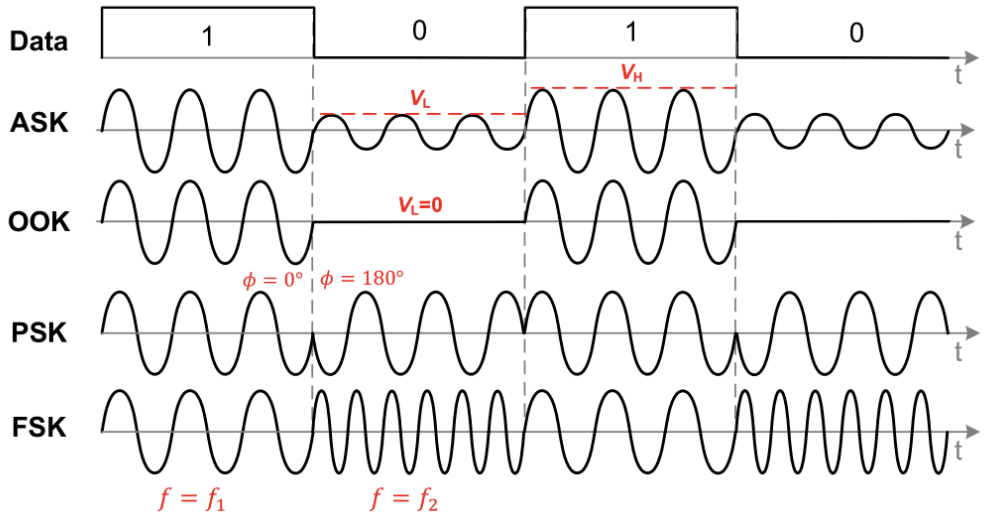

Figure 2.12: Depiction of binary data modulating the carrier signal in amplitude-, phase-, and frequency-shift keying modulation [242].

2.6 Summary

Finding the source of complications and poor outcomes from LIF surgery requires further biomechanical research. Issues relating to surgical decisions, such as implant design, material, and fixation configuration, can be practically investigated using FE analysis such that quantifiable inputs are used during pre-surgical planning to ensure patients receive targeted treatment. The techniques used to develop spine FE models are well-defined and can be adapted for this purpose. In the postoperative monitoring phase, quantified mechanical changes in the prosthesis and surrounding tissue can provide objective considerations for detecting and avoiding complications. The combination of computational modelling and 'smart' implant approaches can encourage objectivity in clinical management and patient-specific treatment in its truest sense.

Integrating the required electronics within the confines of an interbody cage is a greater challenge compared to the larger and more established instrumented hip, knee, and fixation plate implants. Further, interbody cages are implanted comparatively deeper within the body, which will require navigating the complexities of wireless telemetry over that distance. Discontinuous operation of the 'smart' implant system through

inductive coupling is a safe and power-efficient alternative to continuous measurement. It is fit-for-purpose in postoperative monitoring for spinal fusion, where continuous measurement provides limited additional clinical utility.

3. Development of a Computational Model to Assess the Biomechanics of Fusion

Preface

The previous chapters in this thesis have outlined the failures of lumbar interbody fusion and the need for a more detailed understanding of its impact from a biomechanical perspective. There are evident challenges with quantifying the mechanics of an *in vivo* process, however finite element analysis provides a means to analyse load patterns in spinal structures and uncover links with postoperative complications. This chapter presents a finite element analysis study into the biomechanical changes occurring in the lumbar spine following a L4-L5 extreme lateral interbody fusion. Load-distribution changes in surrounding spinal structures with fusion progression are quantified with implications for implant design, choice of graft, and complication risk up to the point of full fusion.

The findings in this chapter are published in the following peer-reviewed journal article:

> V.A.S. Ramakrishna, U. Chamoli, A.G. Larosa, S.C. Mukhopadhyay, B.G. Prusty and A.D. Diwan, "Finite element modelling of temporal bone graft changes in XLIF: Quantifying biomechanical effects at adjacent levels," *Journal of Orthopaedic Research*, vol. 22, no. 6, pp. 1420-1435, Jun 2022, doi: 10.1002/jor.25166.

3.1 Defining the Clinical Question and Translating to the Modelling Domain

Lumbar interbody fusion (LIF) is a common treatment for degeneration, instability, deformity, and trauma of the spine that encompasses a wide variety of surgical techniques and instrumentation aimed at immobilising spinal segments. Broadly, LIF involves the removal of the native intervertebral disc, insertion of an interbody spacer or cage with osteoconductive material, and in some cases, the addition of posterior instrumentation. Extreme lateral interbody fusion (XLIF) is a surgical fusion approach developed as an alternative to the more common anterior (ALIF), posterior (PLIF), and transforaminal (TLIF) LIF approaches [40, 243, 244]. In an XLIF procedure, access to the intervertebral space through a trans-psoas retroperitoneal approach prevents disruption to the existing natural stabilising elements of the spine, such as the facets, anterior longitudinal ligament, and posterior longitudinal ligament that are often excised or compromised in other LIF approaches [40, 244]. While ALIF, TLIF, and PLIF are often accompanied by posterior supplemental fixation by way of pedicle screws and rods, the abutment provided by the ligaments and maintained integrity of the facets allows XLIF to be performed with a standalone interbody cage [40, 243]. While the surgical approaches are distinct, most LIF surgeries include the insertion of bone graft or other synthetic osteoconductive material with the interbody cage to promote bone fusion between the two vertebrae until solid union is achieved. A common timeframe for achieving solid fusion is 6-12 months, however rates of non-union after 1 year, where complete fusion is not achieved, range from 3-20% [61, 78-80]. Given the process occurs entirely within the operated segment of the spine, the progression of fusion can only be monitored radiologically [30, 81]. As such, little is known about temporal stiffness changes in the graft region and their wider biomechanical impacts. Computational modelling lends itself to investigating the biomechanics of fusion progression, quantifying the impacts of temporal graft stiffness changes, where *in vivo* assessment is challenging.

The temporal mechanical features of biological bone growth following a LIF surgery have not been adequately modelled. During the healing process, the stiffness of the fusing bone is known to increase [245]. Depending on the type of bone graft used, the ossification process, rate, and histology may vary between patients, however the fusing

bone will progress from a mechanically soft to hard state [246]. Creeping substitution is one such mode of bone healing by which bone formation progresses from the endplates towards the centre of the intervertebral space [246]. In the early stages of bone formation or in the case of non-union, bonding of the newly formed bone to the endplates may be incomplete. At the point of complete fusion, however, the newly formed bone unites the two vertebrae between the endplates through the interbody cage cavities.

Load-share between the graft and cage has been investigated using finite element (FE) analysis, demonstrating polyether ether ketone (PEEK) cages promote loading of the graft more than titanium cages [133]. Further, computational modelling has shown stiffer bone grafts experience higher loads than softer grafts [245, 247]. These studies did not look at the wider biomechanical implications of graft stiffness changes on adjacent spinal elements that are structurally relevant to XLIF procedures. Published studies have investigated the impact of different types of bone graft [247] or contact area with the endplates [248], however they do not account for contact changes between the endplates and the cage-graft construct. This change in contact as part of the fusion process has not yet been modelled and, together with temporal graft stiffness changes, may have a considerable impact on load-distribution pathways.

This computational work describes the development of a FE model to quantify the effects of lumbar fusion in a L4-L5 XLIF, aiming to provide comprehensive biomechanical insights into clinically relevant questions about load-distribution changes that occur as fusion progresses *in vivo*. A holistic approach was taken to the assessment of load-distribution mechanisms, quantifying the changes that occur in the natural stabilising spinal elements, such as ligaments and facets, beyond the index level.

3.2 CT Image Segmentation

Anonymised computed tomography (CT) scans were obtained from an asymptomatic male subject (55 years old) from Southern Radiology Miranda (NSW 2228, Australia) in DICOM (Digital Imaging and Communications in Medicine) file format. The CT data were high-resolution (1291 axial cuts, 0.30mm slice thickness, 512 x 512 pixel resolution) and spanned the thoracolumbosacral region of the spine. Prior 'negligible risk research' ethics approval was obtained from the University of New South Wales (NRR-HC180027). The images were imported into Materialise Mimics (Materialise NV 2018b,

Belgium) for segmentation. Anatomical regions of interest were segmented for the L1-S1 region of the spine only.

3.2.1 Bony Structures

The *Thresholding* tool in Materialise Mimics allows pixels within anatomical regions to be automatically selected and grouped based on greyscale intensity. Using this tool, a mask was created that included all osseous structures. Subsequently, the pixels in the osseous mask were divided into cancellous and cortical segmented regions. Cancellous bone was only modelled in the vertebral body, encased by cortical bone with thickness 0.60mm (2 pixels) according to published literature (Figure 3.1) [249]. The posterior bony elements and sacrum were modelled as cortical bone only.

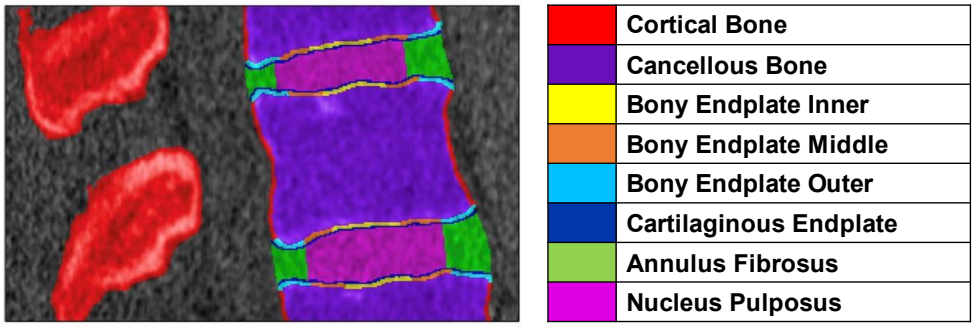

Figure 3.1: A segmented mid-sagittal CT slice showing the colour-coded 8 anatomical regions of interest.

3.2.2 Endplates

Given their distinct material properties [250], the endplates were divided into two regions: cartilaginous and bony endplates. Bony endplates were further divided into inner, middle, and outer regions with equal radial width and thickness of 0.60mm (2 pixels) (Figure 3.1, Figure 3.2) [251]. The adjacent cartilaginous endplate was segmented with a thickness of 0.30mm (1 pixel) across the superior and inferior vertebral body surfaces [252].

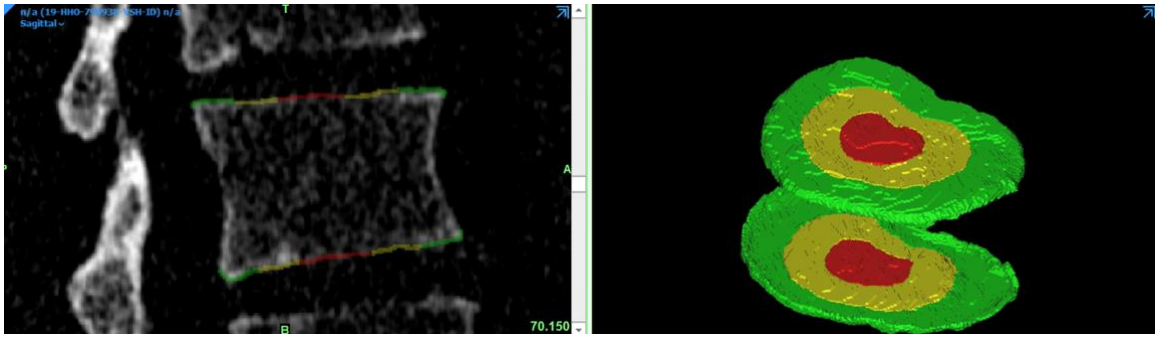

Figure 3.2: Sagittal view of a CT slice (left) and isometric reconstruction (right) showing the segmented bony endplates (Outer: green, Middle: yellow, Inner: red).

3.2.3 Intervertebral Discs

The intervertebral disc volume was assumed to occupy the space between the epiphyseal rings of the vertebrae. The disc was further divided into nucleus pulposus and annulus fibrosus regions. The nucleus was assumed to occupy 43% of the disc volume and was located slightly posterior relative to the centre of the intervertebral space [253]. The disc region was initially segmented as one region by selecting the area between the endplates using the *Multiple Slice Edit* tool (Figure 3.3). Subsequently, the *Rescale* function was used to scale the disc to 43% and assign it to the nucleus pulposus mask. Using the *Reposition* function, the mask was moved slightly posteriorly from the centre. A *Boolean Intersection* between the whole disc and the nucleus pulposus masks allowed for the creation of the annulus fibrosus mask in the remaining disc space (Figure 3.4). The properties of each mask were checked to ensure the volume proportions were accurately captured.

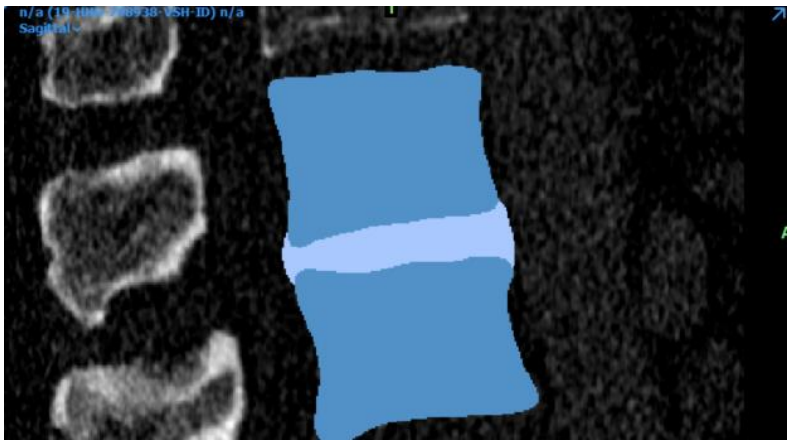

Figure 3.3: A sagittal slice of the CT scan showing the disc mask, initially selected as one whole region between the vertebral endplates.

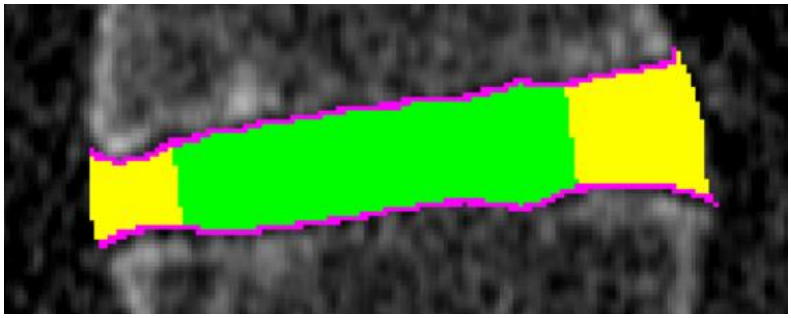

Figure 3.4: A sagittal slice of the CT scan showing the result of the Boolean operation between the whole disc mask in Figure 3.3 and the nucleus pulposus mask (green), resulting in the creation of the annulus fibrosus mask (yellow).

The annulus was segmented into five regions to allow modelling of its regional material stiffness variation using a combination of the *Boolean Intersection* and *Multiple Slice Edit* tools (Figure 3.5) [254].

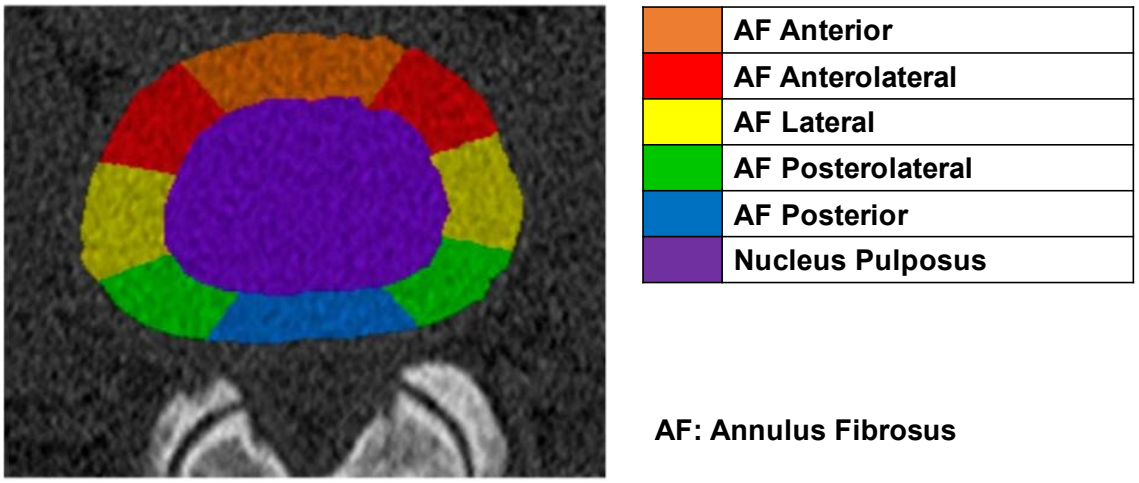

Figure 3.5: Axial view of the segmented intervertebral disc depicting the 5 stiffness regions of the annulus fibrosus (AF) in addition to the nucleus pulposus.

3.3 Surface and Volumetric Mesh Generation

3.3.1 Surface Mesh Generation

A *Non-manifold Assembly* was generated in Materialise Mimics comprising of all the segmented regions. No pre-smoothing was applied and the highest possible resolution was selected. The *Non-manifold Assembly* was exported from Materialise Mimics and imported into Materialise 3-Matic (Materialise NV 2018a, Belgium) for surface mesh generation. A uniform meshing was conducted to generate a basic surface mesh prior to

inserting the interbody cage model. Default parameters were used at this stage, as the surface mesh would require re-meshing following the insertion of the implant.

3.3.2 Inserting the Interbody Cage

A 3D model of an XLIF interbody cage was developed in SolidWorks (Dassault Systèmes SE, France) in accordance with the dimensions of commercially available Coroent XL implants from NuVasive (San Diego, USA) (22 x 50 x 10mm, 0° lordosis) [255, 256]. The CT scan and model were assessed by a practicing orthopaedic spine surgeon to ensure the dimensions of the implant were suitable for the spine anatomy. The implant model was imported into 3-Matic as a STEP (Standard for the Exchange of Product Data) file (Figure 3.6).

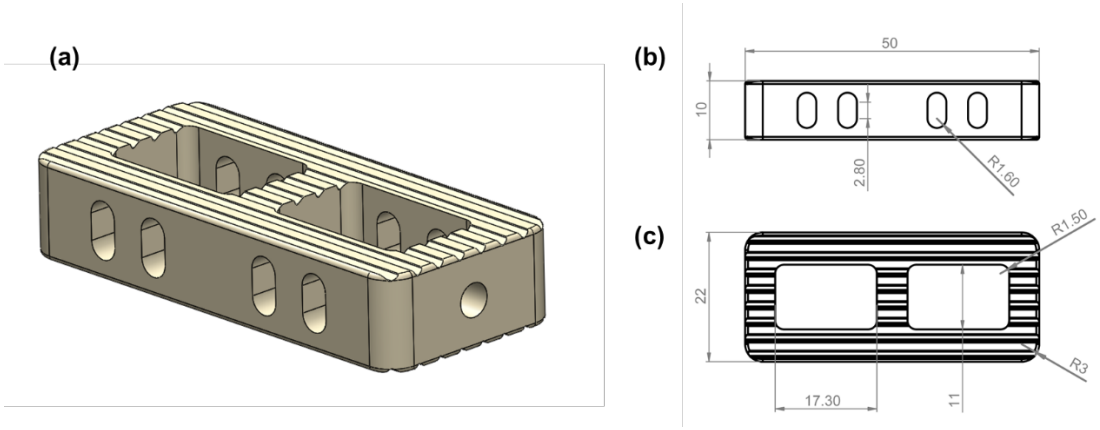

Figure 3.6: Isometric view (a) and dimensions of the interbody cage model imported into 3-Matic from side (b) and top (c) views. All dimensions in mm.

With guidance from a practicing orthopaedic spine surgeon, the implant model was positioned at the L4-L5 level of the meshed spine using the *Interactive Translate* and *Interactive Rotate* tools. The *N-Points Registration* tool was used to make finer adjustments to the positioning of the implant and ensure it was in contact with the L4 inferior and L5 superior endplates by selecting corresponding points on the endplates and the implant surfaces to co-locate (Figure 3.7).

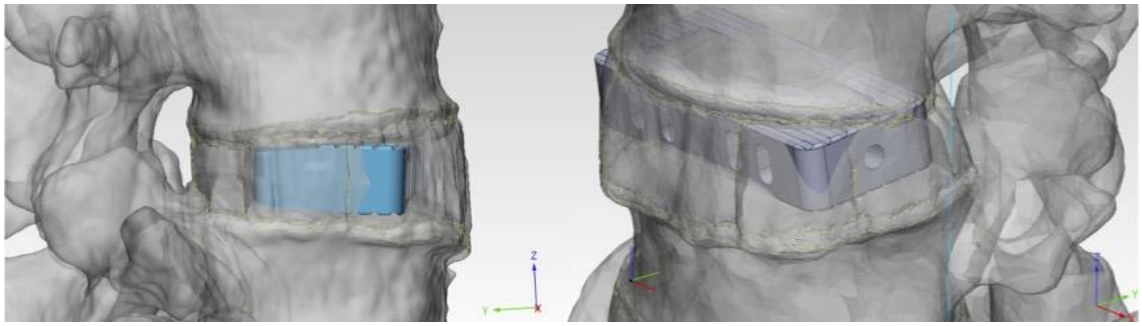

Figure 3.7: Positioning of the implant at the L4-L5 level of the meshed spine in Materialise 3-Matic prior to N-Points Registration.

3.3.3 Surface Mesh Re-Generation & Refinement

The *Non-Manifold Assembly* was split and re-assembled using the *Create Non-Manifold Assembly* tool to include the interbody cage within the assembly. The interbody cage was selected as the *Intersecting Entity*, such that the software performed a Boolean operation whereby the disc volume co-located with the interbody cage was replaced by the cage volume. A *Uniform Re-mesh* was then performed on the resulting *Non-Manifold Assembly* (Edge Length = 0.75mm). The fine meshing prevented geometrical losses.

Adaptive Re-mesh was performed to maintain high mesh density at the interface of the endplates and interbody cage, with a global edge length of 1.6mm, and local edge length of 1.0mm (Growth Rate = 50%**)** in the entities where the finer mesh was desired. Mesh projection was performed using the originally imported geometries to improve the geometric accuracy of the model. Another *Adaptive Re-mesh* was performed to reduce the mesh density in the posterior elements (Edge Length = 2.5mm), where detailed results would not be extracted and load transfer would only occur at the facets.

A perfect mesh would contain only equilateral triangles of the same size. The re-meshing process for such a complex and irregular geometry resulted in triangles of poor quality, double triangles, and intersecting triangles. Materialise 3-Matic contains several manual tools available that were used to improve surface triangle quality:

- *Flip Edge*
- *Collapse Edge*
- *Collapse Triangle*
- *Subdivide Triangle*
- *Add Point*
- *Add Point on Edge*
- *Move Point*
- *Create/Delete Triangle*

Table 3.1: Quality measures for surface mesh triangles in Materialise 3-Matic.

Parameter	Description	Value
Edge Ratio	Ratio of the largest edge length to the smallest edge length	≤ 5
Minimum Face Angle	Smallest angle in the triangle	≥ 5°
Maximum Face Angle	Largest angle in the triangle	≤ 170°
Abaqus Shape Factor	$\frac{Area}{Optimal\ Area}$ Where the optimal area is the area of an equilateral triangle with the same circumradius	≥ 0.01
Ansys Element Quality	$6.92820323 \times \frac{Area}{\Sigma(Edge\ Length^2)}$	≥ 0.01

All intersecting triangles were marked and rectified. Double triangles, with same or opposite directionality, were adjusted where the angle between the normal of the two triangles considered double was less than 10°. The *Analyse Mesh Quality* tool identified poor quality triangles according to the parameters in Table 3.1. Triangles that did not meet the quality criteria were adjusted with the aforementioned tools. The process was repeated until the software failed to identify any further intersecting, double, or poor quality triangles that may have been introduced in the process of manually modifying the surface triangles.

3.3.4 Volumetric Mesh Generation

The *Create Volumetric Mesh* tool was used to fill the surface mesh with 4-noded tetrahedral elements. Tetrahedral elements were preferred to hexahedral elements to improve the accuracy of the geometry captured. The volumetric mesh was exported as a .nas (Nastran) file and imported into Strand7 FE analysis software for further pre-processing, solving, and post-processing (Figure 3.8).

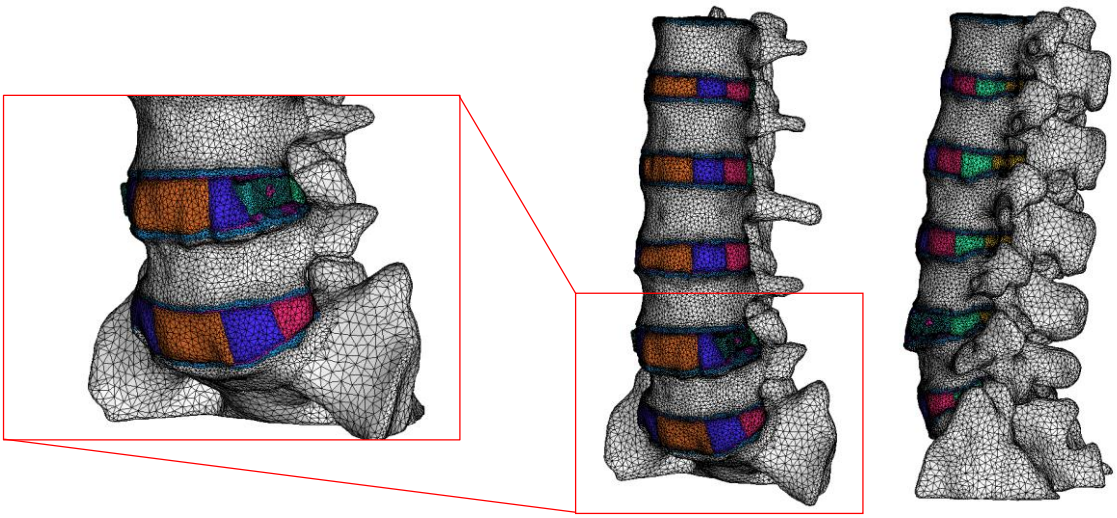

Figure 3.8: Volumetric mesh imported into Strand7.

3.4 Modelling Ligaments of the Lumbar Spine

Ligaments are fibrous connective tissue that attach bone to bone. They are critical load transfer components of the lumbar spine, particularly in tension. The seven primary ligaments; anterior longitudinal ligament (ALL), posterior longitudinal ligament (PLL), ligamentum flavum (LF), capsular ligament (CL), interspinous ligament (ISL), supraspinous ligament (SSL), and intertransverse ligament (ITL) in addition to the iliolumbar ligament (ILL) and lumbosacral ligament (LSL) were modelled as cylindrical beam elements in Strand7 (Figure 3.9). Modelling of ligaments and their attachment sites was performed in accordance with previously published protocols [257, 258].

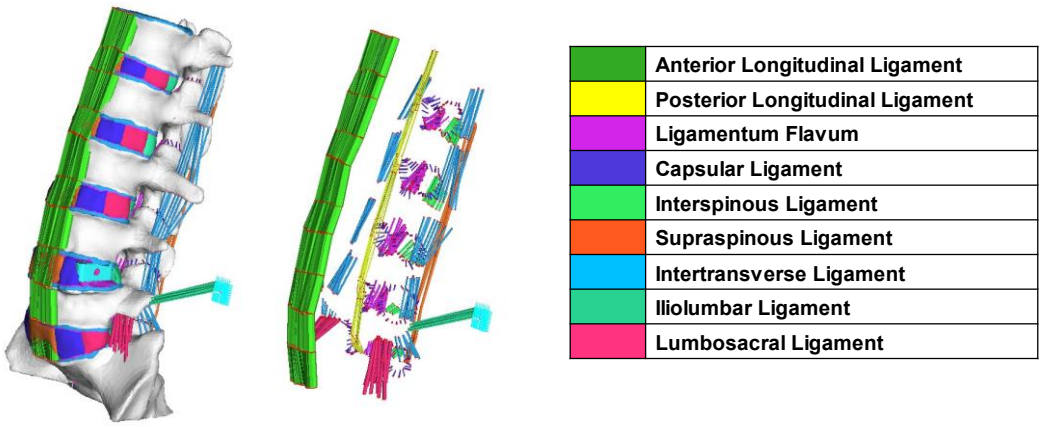

Figure 3.9: Modelling of ligaments and their attachments in the lumbar spine.

3.5 Modelling the Intervertebral Disc

The intervertebral disc consists of criss-cross collagen fibres embedded within a ground substance [257]. In accordance with the literature, four concentric layers of annulus fibres were modelled as cylindrical beam elements attached to the superior and inferior bony endplates [257, 259]. Cylindrical beams were also used to connect the criss-cross fibres within each layer and to model the interlamellar bridges between adjacent concentric layers at the superior and inferior nodes [259, 260]. The fibres were constructed to gradually increase in angle from ±24° at the ventral side to ±46° at the dorsal side relative to the transverse plane [254]. Annulus fibrosus material modelling protocols were in accordance with the eminent literature outlined in Table 2.2, while the nucleus pulposus was modelled as a Neo-Hookean material, as fluid modelling was met with software constraints in Strand7.

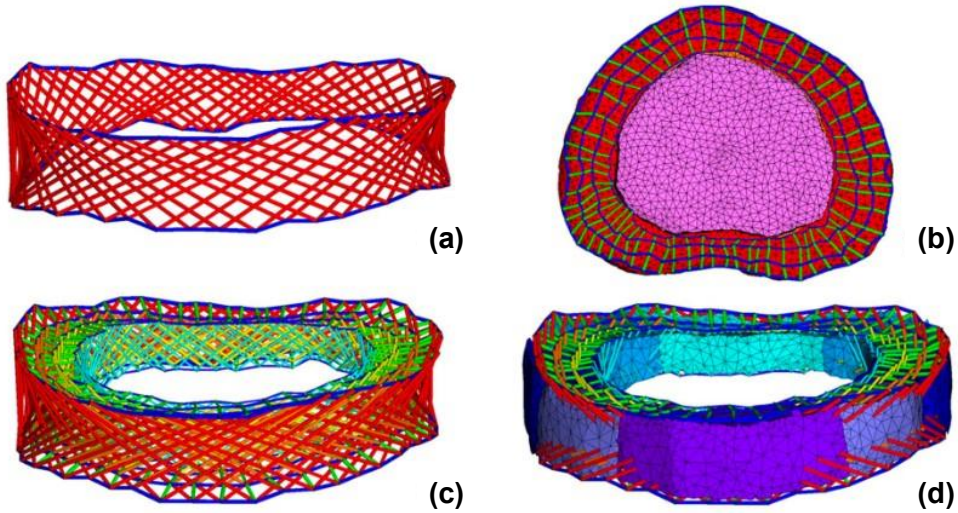

Figure 3.10: The criss-cross fibres (red) were connected with a lamellar ring at the superior and inferior nodes (blue) (a). Adjacent lamellae (layers) were connected with interlamellar bridges (green) (b). The complete fibre structure consisted of four concentric layers (c) embedded within a ground substance (d).

The fibre content of the annulus ground substance in each layer was 23% in layer 1 (outermost), 17% in layer 2, 11% in layer 3, and 5% in layer 4 (innermost) [260]. The diameter for each beam element representing a collagen fibre could then be calculated using the volume fraction of the fibre layer, total length of beams in that layer, number

of beams in that layer, and total annulus volume, as per previously published modelling protocols [257, 258].

3.6 Modelling Contact and Load Transfer at the Facets

The facets are a key structural component of the spine due to their role in load transfer. Load transfer through the facets was modelled using the CL and nonlinear *Point Contact* elements in Strand7. The CL provides resistance to tensile loads and is described in section 3.4. Conversely, the nonlinear *Point Contact* elements were evenly distributed on the articulating surfaces of the facets and were responsible for resisting compressive loads on the facets. The combination of *Point Contact* elements and CL were considered sufficient to model frictionless contact and load transfer in accordance with the current literature [114]. 5 *Point Contact* elements were modelled per joint as per previously published modelling protocols [257, 258].

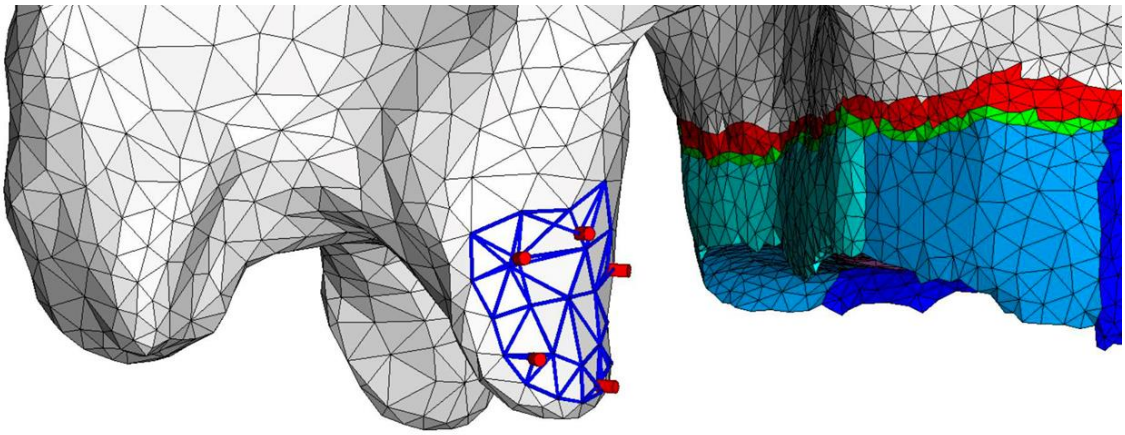

Figure 3.11: Modelling of facet articulation with nonlinear Point Contact elements (red) and a beam network (blue) for uniform load distribution on the facet face.

3.7 Modelling Temporal Graft Stiffness Changes

As previously discussed in section 3.1, the stiffness of the graft progresses from a mechanically soft to hard state during fusion, regardless of the histological process. Given fusion occurs *in vivo*, there is no reliable method to assess the stiffness progression of the fusion mass. As such, determining material properties for the same is challenging.

3.7.1 Obtaining Intermediate Material Properties Using a Modified Unit Cell Approach

Silicone was chosen to model the material behaviour of the graft in the mechanically soft state, known as soft callus (SC) formation, which forms in the early stages of ossification. Poly(methyl methacrylate) (PMMA) was used to model the material behaviour of the solid graft (SG) state, which is simultaneously representative of later-stage ossification and the use of stiff bone grafts in fusion surgery, such as allografts. Nonetheless, there were no clear means or insights from the literature to determine stiffness values between these points that would allow a complete study of temporal changes in graft stiffness. Therefore, a modified unit cell approach was employed to generate stress-strain curves for the intermediate stiffness points. The purpose of the unit cell was to produce stress-strain curves that characterise stiffness properties at ratios of 25:75, 50:50, and 75:25 of silicone to PMMA.

A 3D cube of 4x4x4mm (unit cell) was produced in Strand7 from 8-noded hexahedral elements. The unit cell was given Neo-Hookean properties for silicone (K = 20.7MPa, C = 0.207) (Kunovus, Australia), representing the SC graft material. The central node on the bottom surface of the unit cell was fixed in all degrees of freedom while remaining bottom surface nodes were constrained in the axial direction only. The cell was loaded with a uniform pressure using a steel cap until strains of greater than 4% were achieved.

Using subdivision of elements, a mesh convergence was performed from a starting element size of 1 x 1 x 1mm until the average axial strain results yielded a change of less than 1% between subdivisions. The resulting element size was 0.25 x 0.25 x 0.25mm.

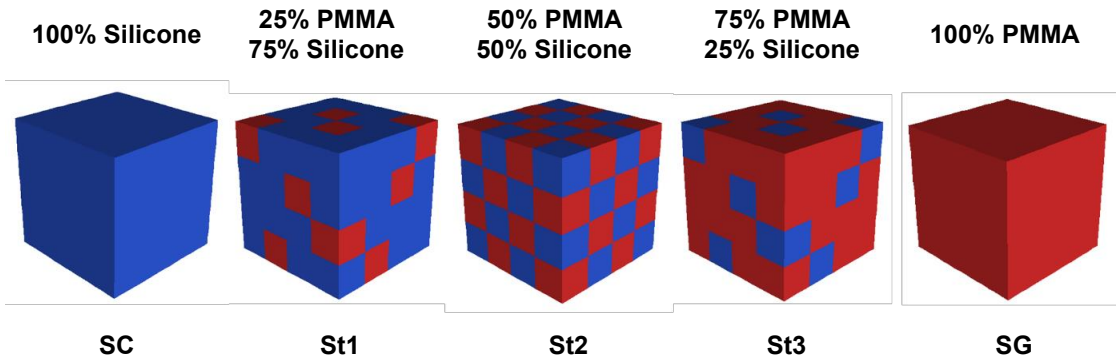

Figure 3.12: Unit cells for soft callus (SC), temporal stage 1-3 (St1, St2, St3), and solid graft (SG) models showing the distribution of PMMA (red) and silicone (blue) throughout the cell.

Starting from the 100% silicone model, PMMA elements (E = 2,795MPa, ν = 0.375) (Heraeus Medical, Germany) [261] were evenly distributed throughout the unit cell to occupy 25%, 50%, 75%, and 100% of the cell (Figure 3.12). The models were loaded with a uniform compressive pressure on the steel cap and the stress-strain curve output was used to define the material properties of the graft at discrete stiffness stages between the silicone and PMMA endpoints.

The compressive stress-strain curve outputs for each unit cell are shown below in Figure 3.13. For consistency, the two endpoints for which material properties were known were also converted to unit cells and their stress-strain curves used to model their behaviour.

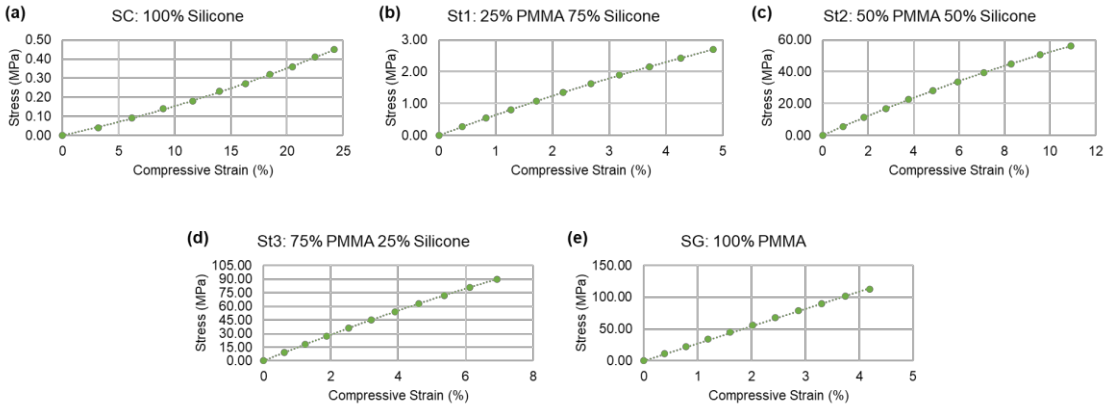

Figure 3.13: Stress-strain curves for unit cells (a) SC: 100% silicone, (b) St1: 75% silicone 25% PMMA, (c) St2: 50% silicone 50% PMMA, (d) St3: 25% silicone 75% PMMA, and (e) SG: 100% PMMA.

The gradient calculated on the stress-strain curve of the PMMA unit cell provided a Young's Modulus (E) of 2,728MPa. The value obtained from the unit cell simulation is reasonable (2.5% difference) compared to input value of 2,795MPa [261].

3.7.2 Modelling Contact Between the Endplates & Cage-Graft Construct

Modelling the temporality of fusion progression requires consideration of both material and contact changes. While material changes were modelled through the stiffness changes described, contact changes are more complex to model. Across all the FE models, the L5 superior endplate (i.e., the caudal endplate relative to the interbody cage) remained bonded to the cage and graft surface. Contact between the L4 inferior endplate

(i.e., the cephalad endplate relative to the interbody cage) and the cage-graft surface was modelled in two states: unbonded and bonded (Figure 3.14).

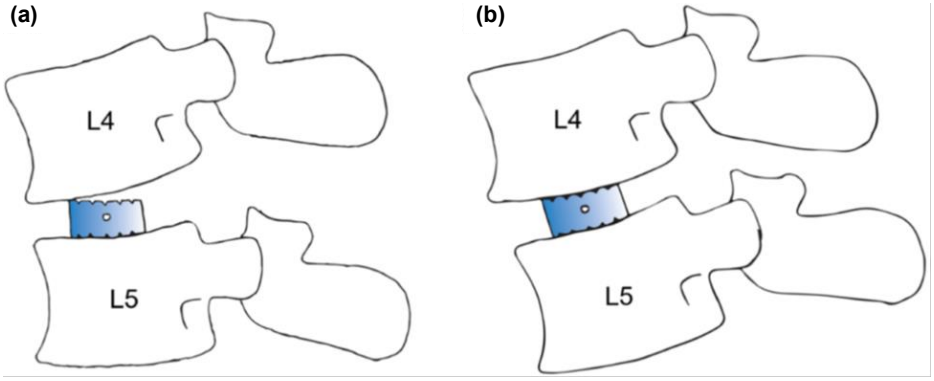

Figure 3.14: With unbonded contact (a) separation between the endplates and cage-graft construct was possible. With bonded contact (b) no separation between the construct and endplates occurred during bending.

The ideal representation of creeping substitution bone formation would include modelling partial bonding of the graft to the endplates. Due to software and modelling constraints, however, this was not achievable in a manner that would accurately represent load-transfer at this partial fusion stage. Unbonded (unfused) contact represented immature fusion progression and incomplete union where new bone has not grown into the endplates, however compressive load transfer still occurs. This contact was modelled using 300 evenly distributed *Normal Contact* elements at the interface between the cage-graft surface and the cephalad endplate. *Normal Contact* elements allowed the L4 inferior endplate to simultaneously transfer compressive loads to the construct in some regions while lifting off the cage-graft surface in other regions during bending (Figure 3.14). Five unique graft stiffnesses were modelled with unbonded contact: SC, St1, St2, St3, and SG.

Bonded (fused) contact was modelled to represent creeping substitution, whereby contact at both superior and inferior surfaces of the cage-graft construct were bonded to the respective endplates. Two unique graft stiffnesses were modelled with bonded contact: cancellous (Partial Fusion: PF) and cortical bone (Full Fusion: FF) material. PF represents progressive bone formation with attachment to the endplates, while FF simulates the final stage of bone healing, consisting of a cortical bone fusion mass with growth into each endplate.

3.8 Assigning and Calibrating Material Properties

The detailed process for material property calibration and its associated data have been published and are presented in the literature [257, 258]. Briefly, the process describes a multi-step calibration approach whereby material properties of each spinal element were adjusted until the kinematics of the L4-L5 FE spinal segment matched the kinematics of a L4-L5 segment under *in vitro* bending loads [257, 258]. Heuer et al. (2007) conducted *in vitro* biomechanical testing to calculate the range of motion on a L4-L5 spinal segment under flexion, extension, lateral bending, and torsion (10Nm) [262]. The kinematic data was firstly calculated for the intact segment. Subsequently, they excised a ligament (SSL) and re-tested the segment, capturing the kinematic data. In a stepwise manner, Heuer et al. (2007) removed a spinal element and re-tested the specimen under *in vitro* bending loads in the following stages [262]:

1. Intact segment
2. SSL removed
3. ISL removed
4. LF removed
5. Facet capsule removed
6. Vertebral arches removed
7. PLL removed
8. ALL removed
9. Nucleus pulposus removed

The final stage of Heuer et al.'s (2007) testing is matched to the first stage of calibration. The spinal segment FE model was loaded in flexion, extension, lateral bending, and torsion with the vertebral arches, ligaments, and nucleus removed to match the anatomy of the specimen from the final stage of Heuer et al.'s *in vitro* testing [262]. Material properties of the annulus were adjusted until the simulation data matched the kinematic data. Subsequently, the nucleus pulposus was added to the FE model and the process repeated in comparison to stage 8 listed above, and for all stages until the ligaments and other spinal elements had been added to the model. This calibration process ensured the material data for each calibrated spinal element matched *in vitro* kinematic data, which is superior to obtaining a global kinematic match of the entire lumbar spine model [263].

Material properties assigned to brick, beam, and nonlinear contact elements (Table 3.2 - Table 3.4) were obtained from previously published studies with identical modelling protocols in which the values were calibrated with the aforementioned process [257, 258]. Certain spinal elements could not be calibrated as they were excluded from the Heuer et al. (2007) study [262]. Due to a lack of published data on ILL and LSL, these were assigned the same material properties as the ALL.

Table 3.2: Uncalibrated material property values assigned to various elements in the FE models.

Material	**Element type**	**Material model**	**Material property values (Uncalibrated)** E: Elastic Modulus (MPa) G: Shear Modulus (MPa) v: Poisson's Ratio Ø: Diameter (millimetres) k: Stiffness (N/mm) ε: Strain %
Cancellous bone Lu et al. (1996) [260]	4-noded tetrahedral	Orthotropic	$E_{xx} = E_{yy} = 140$; $E_{zz} = 200$; $G_{xy} = G_{yz} = 48.3$; $G_{xz} = 48.3$; $v_{xx} = 0.45$; $v_{yy} = v_{zz} = 0.315$
Cortical bone Lu et al. (1996) [260]	4-noded tetrahedral	Orthotropic	$E_{xx} = E_{yy} = 11300$; $E_{zz} = 22000$; $G_{xy} = 3800$; $G_{yz} = G_{xz} = 5400$; $v_{xx} = 0.484$; $v_{yy} = v_{zz} = 0.203$
Endplates inner Polikeit et al. (2003) [264]	4-noded tetrahedral	Isotropic	E = 2000
Endplates middle Polikeit et al. (2003) [264]	4-noded tetrahedral	Isotropic	E = 6000
Endplates outer Polikeit et al. (2003) [264]	4-noded tetrahedral	Isotropic	E = 12000
PEEK Sourced from supplier (Allplastics Engineering, Australia)	4-noded tetrahedral	Isotropic	$E_t = 3900$ $E_c = 29.0$ ($\varepsilon < 1\%$), 57.0 ($1\% < \varepsilon < 5\%$), 119 ($\varepsilon > 5$).
Intertransverse ligaments Kiapour et al. (2012) [110]	Beam	Non-linear elastic	N = 16 per level Ø = 1.0 $E_t = 10.0(\varepsilon < 18\%), 58.7(\varepsilon > 18\%)$; v = 0.3
Iliolumbar ligaments No literature available	Beam	Non-linear elastic	N = 20 Ø = 1.0 $E_t = 7.8(\varepsilon < 12\%), 20.0(\varepsilon > 12\%)$; v = 0.3
Lumbosacral ligaments No literature available	Beam	Non-linear elastic	N = 22 Ø = 2.0 $E_t = 7.8(\varepsilon < 12\%), 20.0(\varepsilon > 12\%)$; v = 0.3
***Normal Contact* Elements** Strand7 (2005) [265]	Beam	Normal Contact	k = 5000

Table 3.3: Calibrated material properties assigned to various elements in the FE models [258].

Material	**Element type**	**Material model**	**Material property values (calibrated)** E: Elastic Modulus (MPa) K: Bulk Modulus (MPa) v: Poisson's Ratio k: Stiffness (N/mm) ε: Strain % C_1, C_2: Mooney-Rivlin constants T: Tension (N)
Nucleus pulposus	4-noded tetrahedral	Mooney-Rivlin 2 parameters	C_1 = 0.006; C_2 = 0.0045; K = 105
Annulus ground substance **I. Anterior** **II. Posterior** **III. Lateral** **IV. Anterolateral** **V. Posterolateral**	4-noded tetrahedral	Mooney-Rivlin 2 parameters	I. C_1 = 0.0672, C_2 = 0.0168, K = 1.68 II. C_1 = 0.0476, C_2 = 0.0119, K = 1.19 III. C_1 = 0.0364, C_2 = 0.0091, K = 0.91 IV. C_1 = 0.0476, C_2 = 0.0119, K = 1.19 V. C_1 = 0.0459, C_2 = 0.0115, K = 1.15
Annulus Fibres **I. Layer 1** **II. Layer 2** **III. Layer 3** **IV. Layer 4**	Beam	Non-linear elastic	I. E_t = 275, v = 0.3 II. E_t = 242.5, v = 0.3 III. E_t = 210, v = 0.3 IV. E_t = 180, v = 0.3
Ligaments **I. ALL** **II. PLL** **III. LF** **IV. CL** **V. ISL** **VI. SSL**	Beam	Non-linear elastic	I. N = 14 continuous, d = 4.8, E_t = 23.4(ε< 12%), 60(ε>12%), v = 0.3 II. N = 6 continuous, d = 0.7, E_t = 5(ε< 11%), 10(ε>11%), v = 0.3 III. N = 18 per level, d = 1.1, E_t = 15(ε<6.2%), 10(ε>6.2%), v = 0.3 IV. N = 48 per level, d = 0.8, E_t = 7.5(ε< 25%), 32.9(ε>25%), v = 0.3 V. N = 9 per level, d = 1.2, E_t = 10(ε< 14%), 11.6(ε>14%), v = 0.3 VI. N = 4 continuous, d = 1.5, E_t = 8(ε< 20%), 15(ε>20%), v = 0.3
***Point Contact* elements**	Beam	Non-linear Tension Contact	k = 25 T = 5

Table 3.4: Regional stiffness variation modelled in the annulus fibrosus by varying the Mooney-Rivlin constants.

Region	C_1 (MPa)	C_2 (MPa)
Annulus Anterior	0.0672	0.0168
Annulus Posterior	0.0476	0.0119
Annulus Lateral	0.0364	0.0091
Annulus Anterolateral	0.0476	0.0119
Annulus Posterolateral	0.04592	0.01148

3.9 Applying Boundary and Load Constraints

A node on the mid-sagittal plane below the anterior sacral promontory was constrained in all translational and rotational degrees of freedom. The region around the node was tessellated to form a network of rigid links, reducing artificial stresses arising from the constrained node and ensuring the surface of the sacrum remained constrained (Figure 3.15).

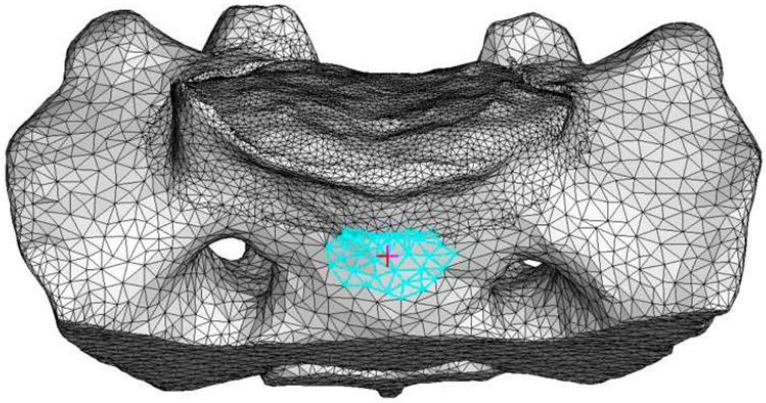

Figure 3.15: Sacrum of the FE model depicting the constrained node (pink +) and the area of tessellated rigid links (blue).

To apply flexion and extension loads, a steel crossbeam structure was constructed on the superior surface of the L1 vertebra. 2D plate elements were created on the L1 superior surface, which were extruded to create a 5mm stainless steel cap (E = 200GPa, ν = 0.25). The centrally aligned crossbeam structure was constructed out of beam elements on the cap surface with stainless steel properties (E = 200GPa, ν = 0.25). A force couple was generated by applying a force of equal magnitude (200N) in opposite directions at either

extremity of the crossbeam (l = 50mm, 200N at each node) to create a pure unconstrained 10Nm bending moment in flexion and extension individually (Figure 3.16). The loads were applied, however, in a gradual stepwise manner from 0Nm to 10Nm. The loading setup was constructed to replicate *in vitro* load testing of a lumbar spine [262, 266].

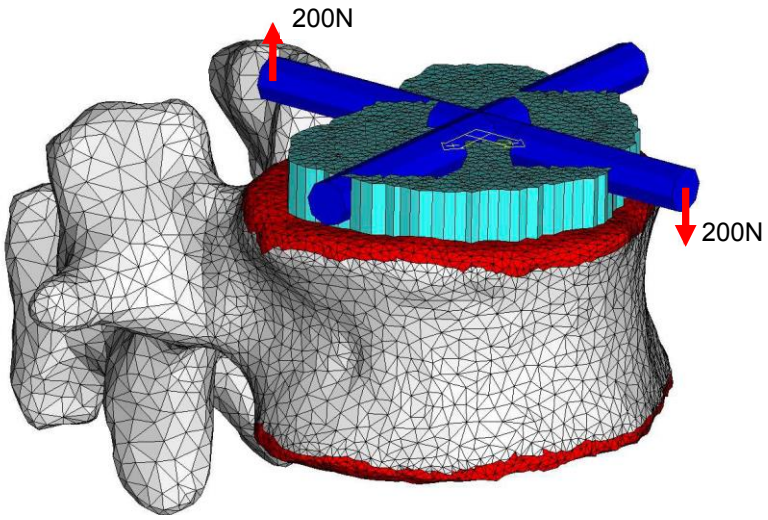

Figure 3.16: The steel crossbeam structure atop the steel cap at the L1 superior surface with a force couple applied for a flexion bending load.

The model was solved using the *Nonlinear Static Solver* in Strand7, accounting for material, geometric, and boundary nonlinearities. Additional model information is presented in Table 3.5.

Table 3.5: Additional model information outlining the number of nodes, elements, and beams modelled in each annulus layer from Layer 1 (Outermost: O) to Layer 4 (Innermost: I).

	SC	St1	St2	St3	SG	PF	FF
Nodes	192,011	192,011	192,011	192,011	192,011	187,329	187,329
4-Noded Tetrahedral Elements	1,063,748	1,063,748	1,063,748	1,063,748	1,063,748	1,063,748	1,063,748
Annulus fibres (Cylindrical Beam Elements) in each layer							
L1-L2	(O) 384-380-362-234 (I)	(O) 384-380-362-234 (I)	(O) 384-380-362-234 (I)	(O) 384-380-362-234 (I)	(O) 384-380-362-234 (I)	(O) 384-380-362-234 (I)	(O) 384-380-362-234 (I)
L2-L3	(O) 298-297-298-197 (I)	(O) 298-297-298-197 (I)	(O) 298-297-298-197 (I)	(O) 298-297-298-197 (I)	(O) 298-297-298-197 (I)	(O) 298-297-298-197 (I)	(O) 298-297-298-197 (I)
L3-L4	(O) 321-319-318-211 (I)	(O) 321-319-318-211 (I)	(O) 321-319-318-211 (I)	(O) 321-319-318-211 (I)	(O) 321-319-318-211 (I)	(O) 321-319-318-211 (I)	(O) 321-319-318-211 (I)
L4-L5	(O) 130-124-102-54 (I)	(O) 130-124-102-54 (I)	(O) 130-124-102-54 (I)	(O) 130-124-102-54 (I)	(O) 130-124-102-54 (I)	(O) 130-124-102-54 (I)	(O) 130-124-102-54 (I)
L5-S1	(O) 519-504-466-293 (I)	(O) 519-504-466-293 (I)	(O) 519-504-466-293 (I)	(O) 519-504-466-293 (I)	(O) 519-504-466-293 (I)	(O) 519-504-466-293 (I)	(O) 519-504-466-293 (I)

3.10 Results

All results were calculated under the maximum applied bending moment (10Nm).

3.10.1 Loads on the Interbody Cage

Average stress was calculated by averaging the stress (compressive or anterior) experienced by all tetrahedral elements in the cage obtained directly from Strand7.

In both flexion (Fx) and extension (Ex), compressive stress on the interbody cage reduced by 20% with increasing graft stiffness from the SC to SG stage in the unfused case (Fx: 0.86MPa (SC) to 0.69MPa (SG); Ex: 1.01MPa (SC) to 0.81MPa (SG)). Cage stress

increased, however, after complete bonding with both cancellous and cortical grafts (Fx: 1.47MPa (PF), 1.22MPa (FF); Ex: 1.53MPa (PF), 1.31MPa (FF)) (Figure 3.17).

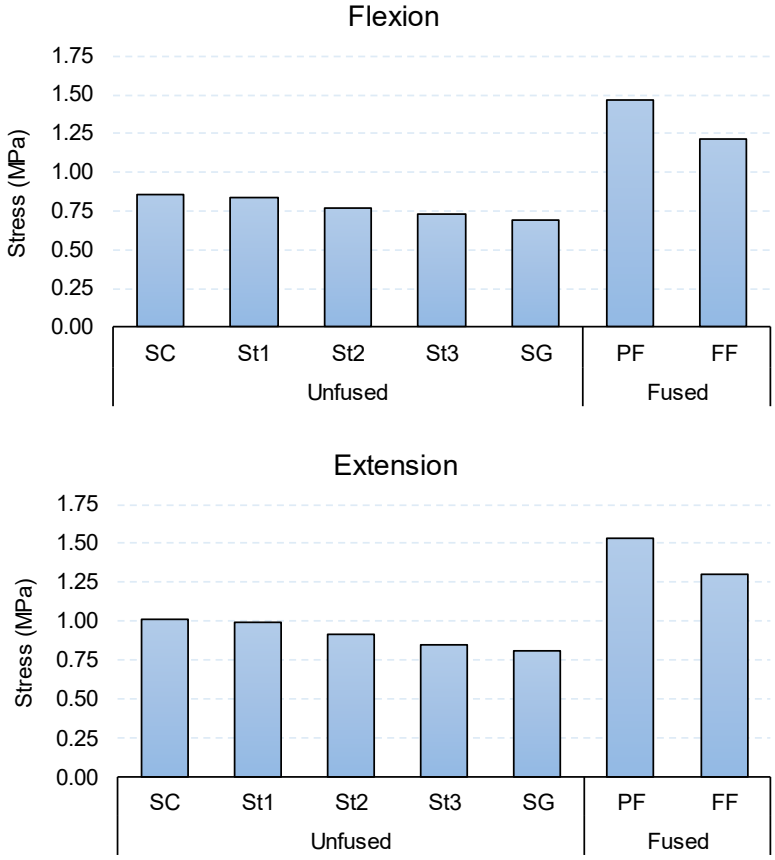

Figure 3.17: Average compressive stress (MPa) on the interbody cage in flexion and extension.

Stress accounts for change both in area and force. The relative change in compressive force (F) can be calculated by the sum of the relative change in compressive pressure (P) and the relative change in the area under compression (A):

$$\% \Delta F = \% \Delta P + \% \Delta A$$

Equation 3-1

Change in compressive force is reported normalised to the SC model. Progressive off-loading of the cage was observed with stiffening graft, simulating advancing fusion, from SC to SG in flexion only (St1: -18%, St2: -31%, St3: -39%, SG: -42%) (Figure 3.18). Change in compressive force in all unfused models was less than 10% in extension. Cephalad endplate bonding increased normalised force in both fused contact models (Fx: 55% (PF), 16% (FF); Ex: 47% (PF), 28% (FF)).

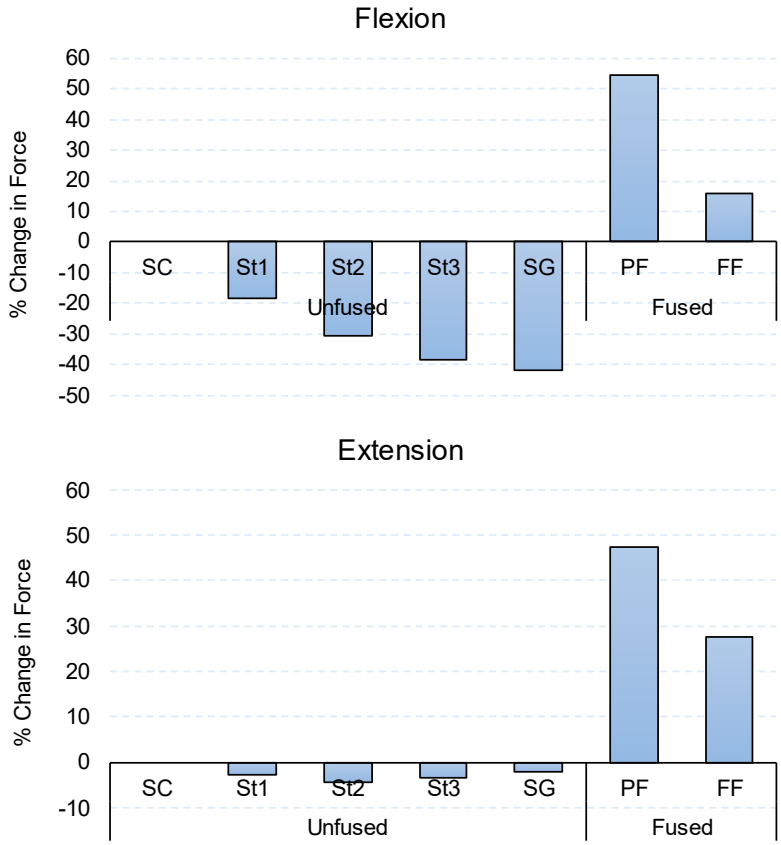

Figure 3.18: Percentage change in compressive force on the interbody cage normalised to the SC model.

With increasing graft stiffness in the unbonded models, compressive stress in the anterior and posterior regions of the cage reduced in flexion and extension respectively (Figure 3.19). In flexion, posterior regions of the cage were noticeably under compression in the SC, St1, and St2 models, but not in St3 or SG. In extension, as graft stiffness increased in the unbonded models, the centre of the cage experienced more stress. There were, however, comparatively larger stress concentrations in the fused models in both bending modes.

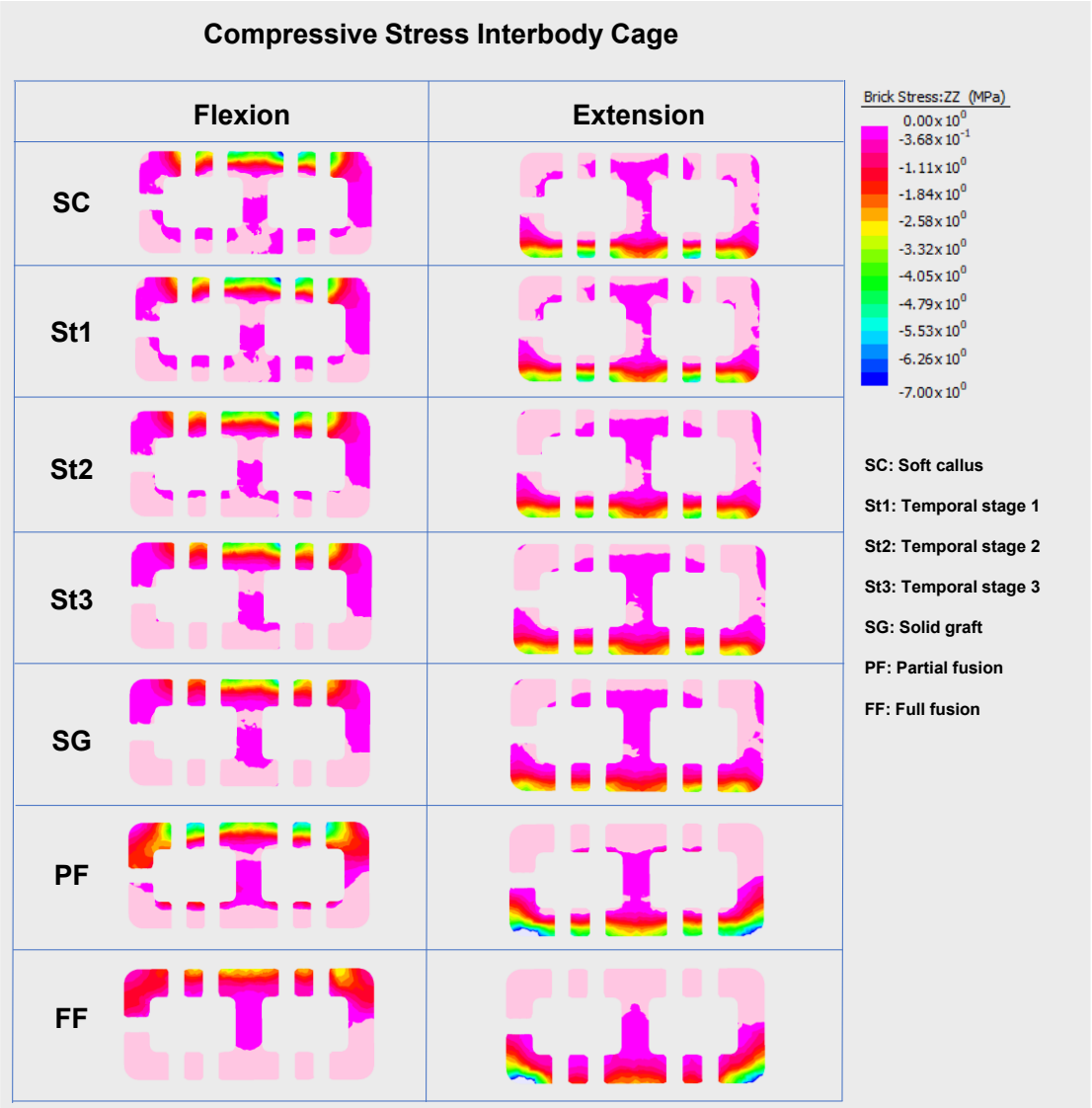

Figure 3.19: Distribution of compressive stress (MPa) on the interbody cage in flexion and extension. Anterior direction at top of image. ZZ direction into the plane of the image.

Across the unfused models, stiffening of the bone graft reduced anteriorly directed force on the cage. Anterior force decreased by 5%, 21%, 29%, and 33% respectively for St1, St2, St3, and SG in flexion compared to SC (Figure 3.20). Smaller changes were found in extension (-3% (St1), -6% (St2), -11% (St3), -17% (SG)). As with normalised compressive force, normalised anterior force accounted for both change in anterior directed stress and change in area under anterior stress. The difference in contact modelling between the fused contact and unfused contact groups prevents the comparison of anterior forces between the two groups.

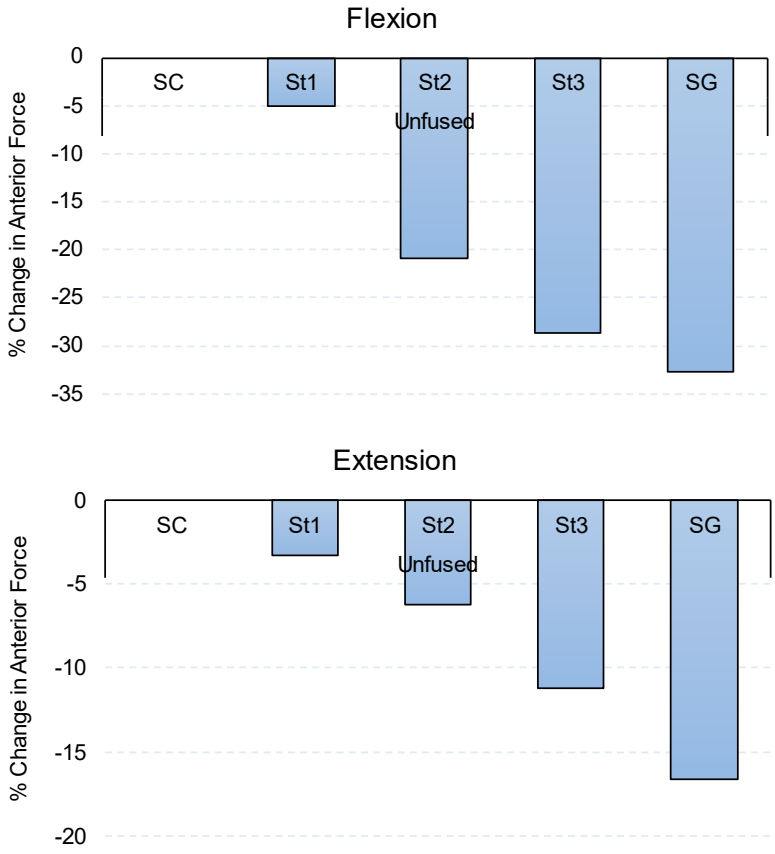

Figure 3.20: Percentage change in anterior force in the unfused models normalised to SC.

3.10.2 Loads on the Graft

Average compressive stress was calculated by averaging the compressive stress experienced by all tetrahedral elements in the graft obtained directly from Strand7.

Compressive graft stress showed an increase associated with graft stiffness in flexion (SC: 0.00MPa, St1: 0.02MPa, St2: 0.09MPa, St3: 0.15MPa, SG: 0.22MPa) and extension (SC: 0.00MPa, St1: 0.02MPa, St2: 0.08MPa, St3: 0.14MPa, SG: 0.20MPa), shown in Figure 3.21. Stress on the graft in the PF model (Fx: 0.08MPa, Ex: 0.07MPa) was comparable to the St2 unbonded model given its similar stiffness properties. Stress on the graft in the FF model was 0.81MPa in flexion and 0.63MPa in extension.

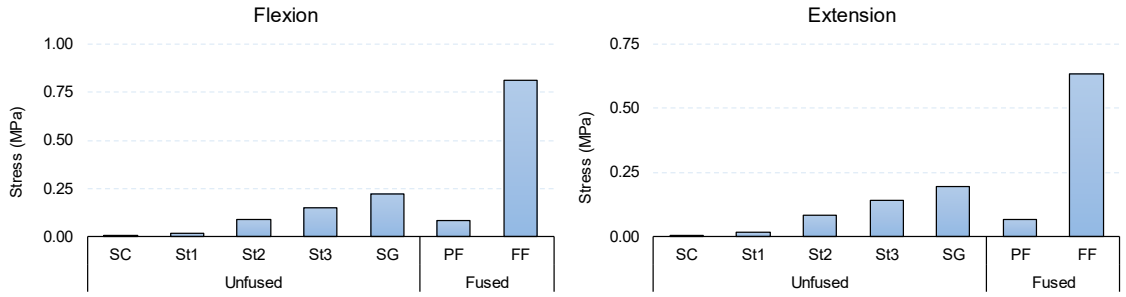

Figure 3.21: Average compressive stress (MPa) on the graft in flexion and extension.

A similar trend was observed in normalised compressive force results (Figure 3.22).

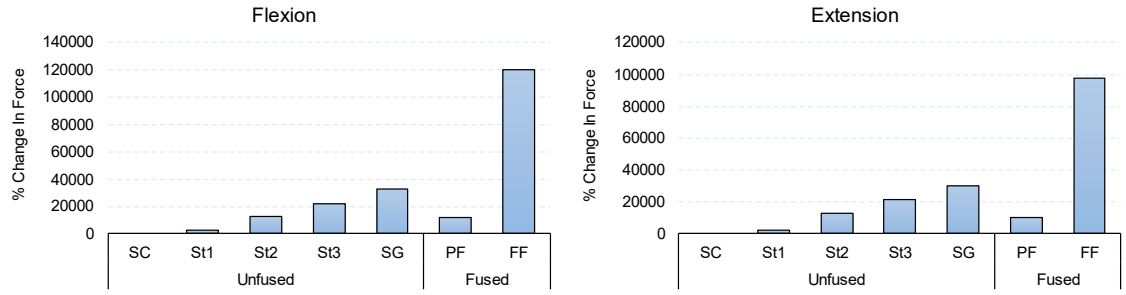

Figure 3.22: Percentage change in compressive force on the graft normalised to the SC model.

3.10.3 Cage to Graft Load-Share

Increasing graft stiffness improved the compressive load-sharing between the cage and graft, calculated as a percentage of compressive stress on the entire cage-graft construct (Figure 3.23). The SC model exhibited 99.9% stress on the cage (0.1% on graft) in forward and backward bending. The SG model showed off-loading of the cage and more stress on the graft in flexion (75.6% cage, 24.4% graft) and extension (80.4% cage, 19.6% graft). Stress-sharing between the cage and graft was associated with graft stiffness and not bonding to the endplates (Fx: 94.7% cage, 5.3% graft (PF), 60.0% cage, 40.0% graft (FF); Ex: 95.8% cage, 4.2% graft (PF), 67.3% cage, 32.7% graft (FF)).

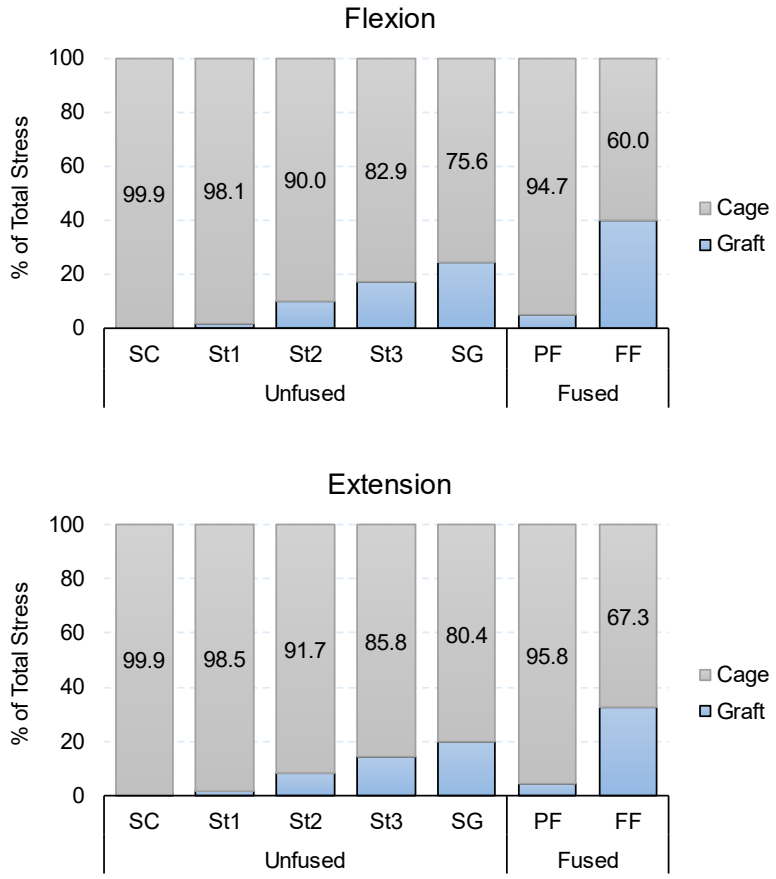

Figure 3.23: Compressive stress on the cage and graft as a percentage of total compressive stress on the construct.

3.10.4 Axial Force on the Facets

Axial force in each *Point Contact* element between the articulating facet surfaces was obtained directly from Strand7 and totalled to calculate the axial force transferred through each facet joint.

When analysing results from regions adjacent to the implant, changes were not significant within the group of unbonded models (SC, St1, St2, St3, SG) and bonded models (PF, FF). In reporting results for facets, ligaments, and the intervertebral disc, the pertinent comparison is between the fused and unfused contact states, which are discussed as averages of their respective groups.

Axial force results from the facets (Table 3.6) represent the compressive load transferred through the joint. No considerable differences were measured between models within

the fused group, however some differences were found between unfused and fused models.

In flexion, no compressive load transfer was noted in fused contact group through the L4-L5 facets. L3-L4 axial force was reduced by 11% (Fx) and no substantial change was observed at L5-S1. Compressive load through L4-L5 during extension was reduced by 87% with fused contact; no notable changes were found at adjacent facets.

Table 3.6: Total axial force through the facets in Newtons (N).

		Unfused					Fused	
		SC	**St1**	**St2**	**St3**	**SG**	**PF**	**FF**
L3-L4	**Fx**	2.7159	2.7156	2.7143	2.7133	2.7125	2.4261	2.4200
	Ex	12.1387	12.1386	12.1382	12.1379	12.1376	11.8734	11.8713
L4-L5	**Fx**	1.3372	1.3368	1.3427	1.3528	1.3650	0.0000	0.0000
	Ex	11.0250	11.0223	11.0199	11.0165	11.0125	1.4474	1.3695
L5-S1	**Fx**	1.8662	1.8657	1.8644	1.8637	1.8632	2.0048	1.9982
	Ex	4.6760	4.6765	4.6793	4.6813	4.6829	4.7204	4.7267

3.10.5 Ligament Strains

Strain in the ligaments was calculated from nodal coordinates and displacement values obtained from Strand7. The length (L) of each ligament fibre was calculated in the unloaded (0Nm) and loaded (10Nm) state from coordinate data at each end of the beam ($E1$, $E2$).

$$L = \sqrt{(x_{E1} - x_{E2})^2 + (y_{E1} - y_{E2})^2 + (z_{E1} - z_{E2})^2}$$

Equation 3-2

The axial strain was calculated as the ratio of the change in length to the original length for each fibre and averaged across all the fibres that constituted the ligament. Lax ligaments were excluded from the calculation of average axial strain.

$$Axial\ Strain = \frac{L_{10Nm} - L_{0Nm}}{L_{0Nm}}$$

Equation 3-3

Ligaments actively resist motion when they are in tension, however are inactive when they are lax and do not transfer compressive loads. The posterior ligaments showed reduced strain at the index level during flexion in the fused models (Table 3.7). They did not exhibit tensile strain in extension. In the fused contact models, the strain in the LF, ISL, and SSL was reduced at the L4-L5 level by 70%, 63%, and 66% respectively compared to unfused contact models. Changes in these ligaments were not substantive at the adjacent levels (Table 3.8, Table 3.9). PLL strain at L4-L5 reduced by 77% (Table 3.7) in the fused contact models, accompanied by a decrease of 15% at the level above the fusion (Table 3.8) and 37% at the level below (Table 3.9). In flexion, strain in the CL reduced by 70% at the index level with no accompanied change at L3-L4 or L5-S1 for the bonded contact models.

Table 3.7: Average axial strain in the posterior ligaments during flexion at L4-L5.

	Unfused					**Fused**	
	SC	**St1**	**St2**	**St3**	**SG**	**PF**	**FF**
PLL	0.0498	0.0498	0.0498	0.0498	0.0498	0.0116	0.0111
LF	0.0607	0.0607	0.0607	0.0606	0.0606	0.0186	0.0177
ISL	0.2011	0.2010	0.2008	0.2006	0.2005	0.0757	0.0722
SSL	0.0795	0.0794	0.0793	0.0792	0.0791	0.0280	0.0267
CL	0.1573	0.1573	0.1573	0.1573	0.1572	0.0489	0.0469

Table 3.8: Average axial strain in the posterior ligaments during flexion at L3-L4.

	Unfused					**Fused**	
	SC	**St1**	**St2**	**St3**	**SG**	**PF**	**FF**
PLL	0.0004	0.0004	0.0004	0.0004	0.0004	0.0003	0.0003
LF	0.0753	0.0753	0.0753	0.0753	0.0753	0.0753	0.0753
ISL	0.2242	0.2242	0.2242	0.2242	0.2242	0.2232	0.2232
SSL	0.0973	0.0973	0.0973	0.0973	0.0973	0.0968	0.0968
CL	0.2031	0.2031	0.2031	0.2031	0.2031	0.2031	0.2031

Table 3.9: Average axial strain in the posterior ligaments during flexion at L5-S1.

	Unfused					Fused	
	SC	**St1**	**St2**	**St3**	**SG**	**PF**	**FF**
PLL	0.0004	0.0004	0.0004	0.0004	0.0004	0.0002	0.0002
LF	0.1138	0.1139	0.1139	0.1139	0.1139	0.1135	0.1135
ISL	0.2307	0.2308	0.2308	0.2308	0.2308	0.2300	0.2301
SSL	0.1406	0.1406	0.1406	0.1406	0.1406	0.1397	0.1398
CL	0.1644	0.1644	0.1645	0.1645	0.1645	0.1642	0.1643

In the ALL during extension, the fused contact models demonstrated an 89% reduction in strain at L4-L5 (Table 3.10) and a 28% and 38% off-loading at the cephalad (Table 3.11) and caudal levels (Table 3.12), respectively. The ALL was lax in flexion. In extension, the CL was off-loaded at L4-L5 by 97%, however there was a 23% increase in CL strain at L3-L4. No considerable change was observed at L5-S1.

Table 3.10: Average axial strain in the ALL and CL during extension at L4-L5.

	Unfused					Fused	
	SC	**St1**	**St2**	**St3**	**SG**	**PF**	**FF**
ALL	0.0453	0.0453	0.0453	0.0453	0.0453	0.0051	0.0048
CL	0.0378	0.0378	0.0379	0.0379	0.0380	0.0012	0.0009

Table 3.11: Average axial strain in the ALL and CL during extension at L3-L4.

	Unfused					Fused	
	SC	**St1**	**St2**	**St3**	**SG**	**PF**	**FF**
ALL	0.0014	0.0014	0.0014	0.0014	0.0014	0.0010	0.0010
CL	0.0193	0.0193	0.0193	0.0193	0.0193	0.0237	0.0237

Table 3.12: Average axial strain in the ALL and CL during extension at L5-S1.

	Unfused					Fused	
	SC	**St1**	**St2**	**St3**	**SG**	**PF**	**FF**
ALL	0.0015	0.0015	0.0015	0.0015	0.0015	0.0010	0.0010
CL	0.1259	0.1259	0.1259	0.1259	0.1260	0.1274	0.1274

3.10.6 Loads on Adjacent Intervertebral Discs

Average compressive stress in the intervertebral disc was calculated by averaging the compressive stress experienced by all tetrahedral elements (obtained directly from Strand7) in the annulus fibrosus and nucleus pulposus respectively.

Changes in compressive stress at the L3-L4 (Table 3.13) and L5-S1 (Table 3.14) intervertebral discs were unsubstantial when comparing the fused and unfused contact groups.

Table 3.13: Average compressive stress (MPa) in the L3-L4 annulus fibrosus (AF) and nucleus pulposus (NP).

		Unfused					Fused	
		SC	**St1**	**St2**	**St3**	**SG**	**PF**	**FF**
AF	**Fx**	0.1070	0.1070	0.1070	0.1070	0.1070	0.1082	0.1082
	Ex	0.1045	0.1045	0.1045	0.1044	0.1044	0.1076	0.1076
NP	**Fx**	1.1414	1.1414	1.1416	1.1416	1.1416	1.1457	1.1457
	Ex	1.0658	1.0658	1.0659	1.0659	1.0659	1.0856	1.0857

Table 3.14: Average compressive stress (MPa) in the L5-S1 annulus fibrosus (AF) and nucleus pulposus (NP).

		Unfused					Fused	
		SC	**St1**	**St2**	**St3**	**SG**	**PF**	**FF**
AF	**Fx**	0.0688	0.0688	0.0688	0.0688	0.0688	0.0694	0.0694
	Ex	0.2839	0.2838	0.2838	0.2839	0.2839	0.2887	0.2887
NP	**Fx**	1.2162	1.2163	1.2165	1.2165	1.2164	1.2282	1.2278
	Ex	0.9786	0.9785	0.9786	0.9786	0.9785	0.9845	0.9848

3.11 Discussion

There are no practical techniques that surgeons can use to reliably assess the impacts of fusion progression on the instrumented region and adjacent spinal structures. Post-surgery, clinicians are typically blinded to the changes occurring in the spine unless assessed in periodic radiological follow-up or as a result of patient discomfort. While postoperative imaging may identify a complication, tissue degeneration, or other source

of pain, the mechanisms behind these outcomes are not well-understood, especially due to the lack of information on the biomechanics of fusion. In this scenario, computational modelling provides an alternate perspective.

The objective of this computational analysis was to develop a clinically-accurate FE model that quantifies the biomechanical changes resulting from a L4-L5 XLIF as it progresses from soft callus formation to solid fusion. Published studies have demonstrated the higher stresses present in stiffer bone grafts [245, 247]; however, the load-sharing ratio between cage and graft and consequent changes to load-distribution at adjacent levels has not been quantified previously. Loads on the passive elements are of particular interest in the context of XLIF, which is intentionally designed to maintain the integrity of the ligaments and facets. Furthermore, this suite of FE models accounts for the progression from unfused to fused contact in addition to temporal graft stiffening.

3.11.1 Findings on Subsidence from the Cage Footprint

Across the fused and unfused states, results showed that graft stiffness influences the strain distribution at the endplate-prosthesis interface, or cage footprint. Agarwal et al. (2013) detailed the effect that uniformly distributed stress across the endplates has on cage subsidence [89]. Stress risers on the cage surface are likely to increase the risk of subsidence [89]. Hence, cage footprints with evenly distributed stress patterns are desirable in LIF surgeries. Progressive off-loading of the cage and increased loading on the graft favourably redistributed load across the cage footprint as the graft progressed from the SC to SG stage, as shown in Figure 3.24. Similarly, FF produced a more even footprint than PF (Figure 3.24). Notably, stress risers on the extremities of the cage footprint reduced with increasing graft stiffness.

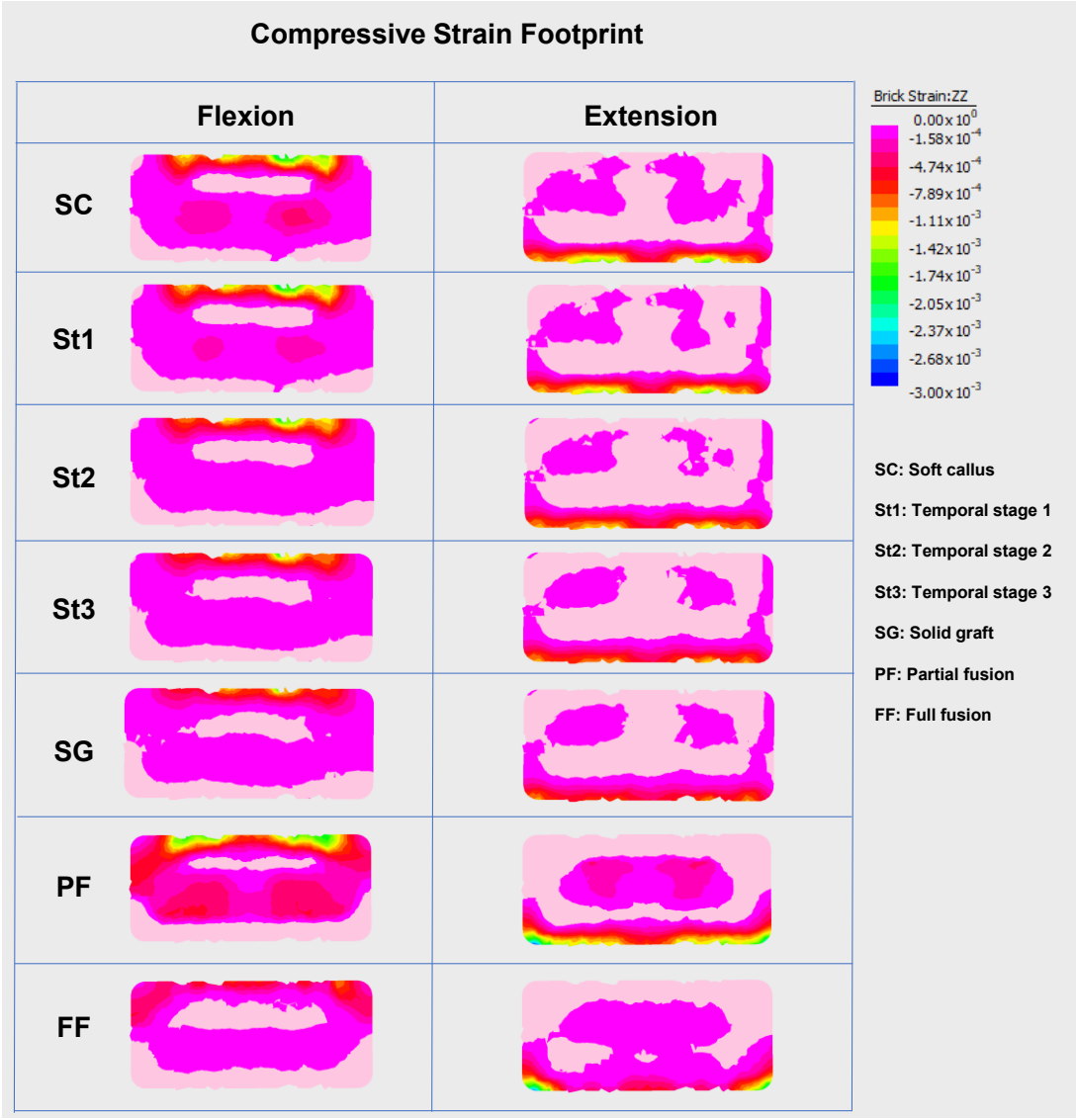

Figure 3.24: Distribution of compressive strain on the cage-graft construct in flexion and extension. Anterior direction at top of image. ZZ direction into the plane of the image.

Despite progression to complete fusion with bonding to the endplates, force through the graft remained stiffness-dependent. In the PF model, the cancellous graft bore 5% of total compressive stress in flexion and 4% in extension, comparable to the results from St1 and St2. In FF, however, cortical fusion bone absorbed 40% of compressive stress in flexion and 33% in extension. Evidently, the requisite to shift the load-sharing ratio towards the theoretically ideal value, based on the proportional cross-sectional area of the graft and cage, was a significantly stiffer fusion mass. Despite the cage occupying only 51% of the cross-sectional area, in the final stage of fusion it shared 60% of the compressive load in flexion and 67% in extension. Cortical bone modulus is 3-7 times

higher than that of PEEK and approximately 80 times higher than cancellous bone [260]. Notwithstanding the influence of bone quality on subsidence risk [267], it is clear that increasing graft stiffness impacts the cage footprint and load-distribution through the cage-graft construct in a manner that reduces the likelihood of stress risers on the cage and subsequent subsidence. Whether the fusion mass is likely to reach a stiffness as high as cortical bone remains debatable and subject to *in vivo* research.

3.11.2 Clinical Implications of Changes in Anterior Forces

The unfused models experienced a reduction in anteriorly directed forces with increasing graft stiffness in flexion (-33% from SC to SG) and extension (-17% from SC to SG). Comparison of anterior forces between the fused and unfused contact groups was not suitable given the difference in contact modelling. Moreover, after solid fusion the onset of instability-related conditions is unlikely. Regardless, the understanding of anterior forces with respect to temporal fusion progression in its early stages is relevant to the postoperative management of a standalone XLIF and decisions regarding supplemental fixation. Further, results from the SG model, with graft properties of PMMA, have implications for the use of stiff grafts such as allograft with similar material characteristics. From a biomechanical standpoint, a stiffer graft will provide more stability to the construct and improve load-sharing between the cage and graft from the early postoperative stage. Further, examining fusion as a case of fracture fixation, the reduced shear and anterior force combined with increased axial load associated with a stiffer graft will likely reduce the risk of delayed union [268].

3.11.3 The Impact of Endplate Union on Load-Distribution

Compressive force results suggest that union between the cage-graft construct and the endplate above increases the load passing through the cage. With bonded contact, less load was transferred through the LF, ISL, CL, PLL, and SSL at the level of the fusion in flexion (Figure 3.25). Further reductions were noted in the PLL at adjacent levels. In extension, the CL, which is responsible for tensile force transfer at the facets, was off-loaded at L4-L5, however strain increased at L3-L4 (Figure 3.26). The ALL was less strained at the index and adjacent levels with bonded contact. Less compressive force was measured through the facets at L4-L5 in both bending motions with respect to the unfused state, while L3-L4 facets were off-loaded in flexion only (Figure 3.27). No changes were observed to loads in the adjacent discs. Regardless of the mechanical

properties of the fusion mass, it is clear that after complete bonding is achieved, more load passes through the cage and less load is transferred through ligaments and facets.

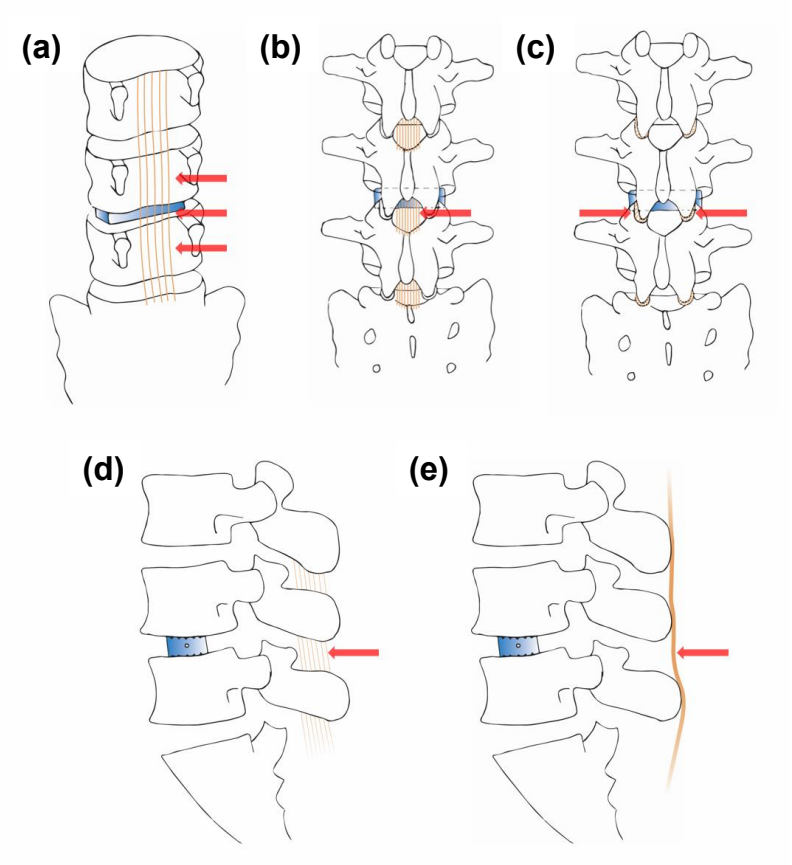

Figure 3.25: Ligaments that were off-loaded as a result of bonding the construct to the endplates during flexion: PLL (a), LF (b), CL (c), ISL (d), SSL (e).

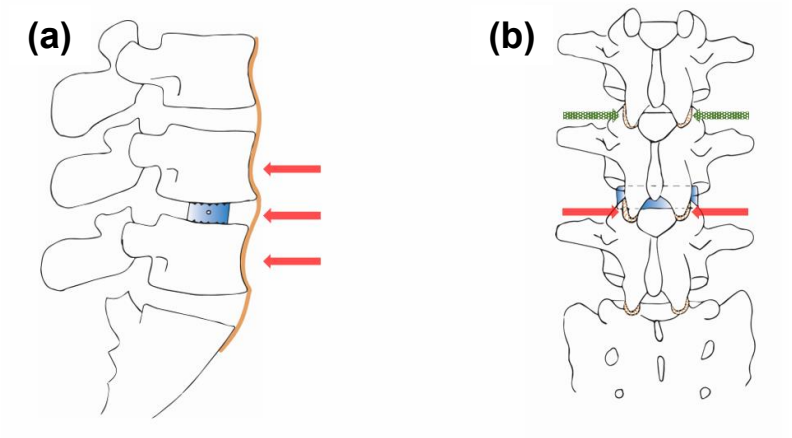

Figure 3.26: Ligaments that were off-loaded as a result of bonding the construct to the endplates during extension: ALL (a), CL (b).

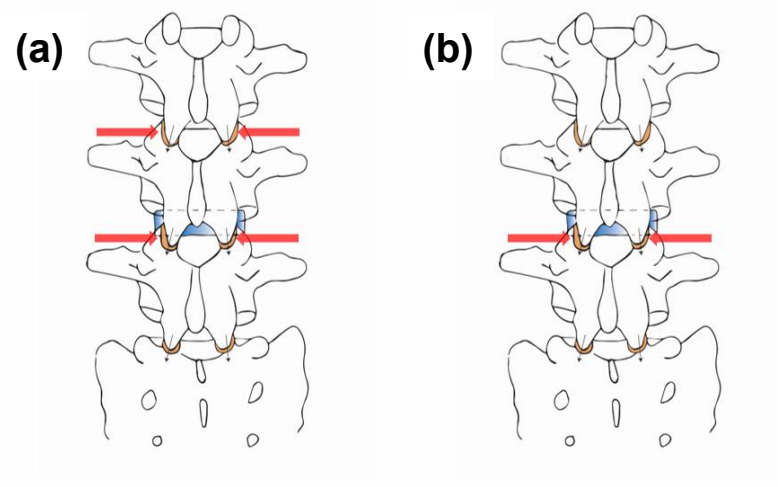

Figure 3.27: Facets that experienced less axial force in flexion (a) and extension (b) as a result of bonding the construct to the endplates.

The results suggest that fused contact between the cage-graft complex and the adjacent endplates shifts load-distribution pathways from the ligaments and facets to the implant. Where the fused bone is comparable to cancellous bone, the stiffness may not be high enough to share the load with the cage and suitably balance the load transfer despite complete union at the superior surface. While the substantially stiffer cortical bone graft improved load-share between the cage and graft, load-distribution among the other spinal structures did not change compared to PF. Stiffness of the fusing bone affects load-share in the cage and graft region, while union with the endplates affects load-distribution in the ligaments and facets. A key purpose of standalone XLIF is to avoid disruption to the natural load-transfer mechanisms of the spine [40]. These results suggest that once complete fusion is achieved, these existing load paths are seemingly diminished. Prior to that point, these structures may have an active stabilising role. Alterations in load-distribution have implications for rehabilitation advice during the early stages of bone formation after LIF surgery.

In the comparison of complete fusion and the unfused states, the results do not suggest an increased likelihood of adjacent segment degeneration stemming from increased loading. Despite the fused contact from L4 to L5, only the L3-L4 CL experienced increased load in extension where all other adjacent structures were off-loaded or exhibited no change.

3.11.4 Limitations

Some modelling limitations were noted in this study. In the modelling of partial fusion (PF), the cage and graft superior surfaces were bonded to the L4 inferior endplate. Modelling of partial bonding between the graft and endplate was met with software limitations. As such, the representation of bone healing by creeping substitution, by which ossification progresses from the graft-host interface to the centre of the graft, was somewhat limited. Contact modelling was further limited by insufficient data on friction coefficients for the interfacing materials. Modelling partial bonding would more accurately represent the clinical presentation of partial fusion, while modelling friction coefficients would particularly improve the accuracy of shear results extracted from the models. These results have implications for understanding joint stability and endplate changes with progressing ossification.

To the best of my knowledge, there is no published data examining the mechanical properties of *in vivo* fusion bone. As such, modelling the stiffness properties was challenging and relied on existing properties for cancellous and cortical bone in the fused states. Furthermore, the models were unable to account for the gradual replacement of cartilage, osteoid, or fibrous granulation tissue that occurs throughout the fusing bone at the micro-level during fusion. As such, the material models attempted to capture the macroscopic material behaviour of the graft in different healing stages. Regardless, these models represent a single anatomy and it is difficult to generalise the results across all populations.

Lastly, only four layers of collagen fibres were modelled within the annulus fibrosus with superior and inferior interlamellar bridges, but no translamellar bridges throughout the height of the annulus.

3.11.5 Future Considerations

(a) Further Clinical Applications

Future research should focus on a comparison between intact and XLIF surgery models to determine whether changes at adjacent levels are likely to cause adjacent segment degeneration before the commencement of fusion bone formation. While results from this FE analysis have shown that subsidence risk may decrease with increasing graft stiffness, further research should ascertain whether this assertion remains valid across

different states of bone quality. The impact of spinal fusion, on the index level and adjacent levels as fusion progresses, remains an evolving area of study, especially when micromotions are involved. The ideal loading patterns that promote bone formation in accordance with Wolff's law while not placing the implant at risk of mechanical failure require further investigation [269]. Such studies are important in designing personalised rehabilitation strategies for patients post-fusion. Further, given the maintained integrity of ligaments and facets after an XLIF, future computational work can investigate the extent to which these stabilising structures are active following XLIF compared to before the surgery. The current work can form part of the building blocks towards these endeavours.

Computational modelling provides the environment necessary to study the biomechanics of fusion while controlling extraneous variables. While the findings should always be validated clinically, simulation techniques uncover mechanisms that could only be speculated on with cohort-based clinical and observational studies. Furthermore, FE analysis is well-placed to study factors influencing subsidence, such as bone quality, where its parameters can be finely adjusted to represent the affected population without the need of large-scale patient recruitment.

(b) Implant Development

Results from these computational models have implications for prosthesis design and development. The PF model indicates that interbody cage designs that anchor in the endplates are unlikely to produce a desirable load-share between the cage and graft in the initial postoperative stages. Bonding the implant to the endplates increases the load on the implant, however improved load-share between the cage and graft requires ossification of the graft. As such, anchored cages may not reduce subsidence risk. Endplate-conformal cages, however, will likely reduce stress concentrations and improve the distribution of load across the endplate surface. Further research can investigate this claim.

The models provide insights for 'smart' implant development. The results clearly show the extent to which load transfers from the implant to the graft as the fusion mass ossifies. There is an approximate 20% reduction in average cage stress with increasing graft stiffness (SC to SG) in the unbonded models, and 15-17% reduction from PF to FF. These measurable changes, excluding the impact of static compressive loads, suggest

that an appropriately sensitive pressure sensor embedded within the interbody cage will be able to monitor fusion progression without the need for postoperative imaging. Optimising sensor placement in the anterior, posterior, and central regions of the cage that experience more substantial load changes with fusion progression will improve the performance of the 'smart' cage.

The findings have further highlighted the importance of the endplates in postoperative monitoring. While mechanical changes in the endplate may be indicative of osteoporosis or subsidence onset, the results also clearly demonstrate the difference in load-distribution between the fused and unfused models. Using measurements from a sensor-enabled interbody cage as a proxy for assessing the health of the endplates will be clinically advantageous.

(c) Surgical Guidance

In the preoperative planning phase, surgeons consider the type of fusion to perform, the cage dimensions, the choice of graft, and the level of fixation to instrument (if any). The results suggest that stiffer grafts will improve the load-share between the cage and fusion mass, and elicit a more even load distribution on the endplates. Where their ability to facilitate bone growth is equivalent, stiffer grafts are biomechanically advantageous. The results from this study provide insight into how a standalone L4-L5 XLIF impacts the proximate and distant spine regions over the period of fusion. Cognisant of the patient's anatomy and condition, surgeons will be better equipped to determine the suitability of a L4-L5 XLIF through consideration of its biomechanical impacts on adjacent ligaments and facets, and potential subsidence risk.

Improved modelling tools, such as automated CT segmentation and meshing, will precipitate patient-specific FE models that act as a quantitative aid to surgical decision-making regarding the appropriate fusion approach given an individual's anatomy. The current modelling approaches, however, are able to provide broad biomechanical inputs to pre-surgical planning. XLIF cages are often implanted with posterior supplemental fixation for added stability. The biomechanical consequences of posterior fixation are not well-understood and surgeons do not consider these consequences during surgical planning. FE analysis can be used to inform a surgeon's choice of fixation.

3.12 Conclusion

The FE models developed have quantified how fusion progression in a standalone XLIF affects loads on the implant, graft, and surrounding spinal structures. While graft stiffness affects load-share on the implant, growth into the endplates affects load-distribution among the ligaments and facets.

After a fusion operation, surgeons are unable to quantify the mechanical changes occurring in the instrumented region. Results from the biomechanical fusion models provide insight into such postoperative changes. With the range of fusion designs and approaches available to surgeons, the FE models provide a link between their associated biomechanical effects on the spine and potential complications that should be considered specific to each patient. The findings have clear clinical implications for addressing subsidence and pseudarthrosis, monitoring growth of the fusion mass into the endplates, and 'smart' implant design. Further, the computational techniques presented in this chapter can be adapted to provide biomechanical inputs to pre-surgical planning.

4. Biomechanically Rational Pre-Surgical Planning using CT-Based Finite Element Modelling

Preface

The finite element modelling approach of the previous chapter clearly demonstrates that interbody cage design, graft stiffness, and endplate ingrowth of the fusion mass can influence complication risk. In the pre-surgical planning phase, however, surgeons are without a clear link between surgical decisions and biomechanical outcomes that lead to complications. This chapter extends the finite element approach to simulate 3 common fixation approaches in extreme lateral interbody fusion, providing surgeons with rationales that allow them to consider the biomechanical implications of their decisions specific to each patient. The work in this chapter further highlights the need for patient-specific approaches to pre-surgical planning.

The findings in this chapter are published in the following peer-reviewed journal article:

> V.A.S. Ramakrishna, U. Chamoli, A.G. Larosa, S.C. Mukhopadhyay, B.G. Prusty and A.D. Diwan, "A biomechanical comparison of posterior fixation approaches in lumbar fusion using computed tomography based lumbosacral spine modelling," *Proc IMechE Part H: Journal of Engineering in Medicine*, Jan 2023, doi: 10.1177/09544119221149119.

4.1 Current Considerations in Surgical Planning for Fusion

Extreme lateral interbody fusion (XLIF) leverages its trans-psoas access point to achieve stability by maintaining the integrity of the surrounding ligaments and facets, and using a large footprint cage [40, 244]. The XLIF approach is unique compared to transforaminal (TLIF) and posterior (PLIF) lumbar interbody fusion (LIF) approaches that require resection of ligaments and facets [40, 244]. Consequently, PLIF and TLIF operations proceed with additional fixation by way of pedicle screws and rods for additional stability [40, 244]. The natural stability afforded by the XLIF approach allows it to be performed as a standalone procedure, that is, without the need of additional fixation [270, 271]. Not all XLIF procedures, however, are performed with a standalone implant. Many patients are instrumented with additional posterior fixation (unilateral or bilateral pedicle screws) to improve the stability of the joint [40]. It is difficult to estimate the number of XLIF procedures performed with each level of fixation due to the variability of practice between surgeons and the demographics of the patients they operate on [272]. Such variability provides impetus to closely examine the factors under consideration in pre-surgical planning during which surgeons determine the level of fixation a patient requires.

Pre-surgical planning considerations are currently dominated by clinical factors. Operating time, blood loss, cost, and time to ambulation influence the level of fixation a patient may receive [40, 50-52, 271]. Standalone XLIF requires a single point of access during the surgery and no additional fixation, resulting in less operating time, blood loss, and cost [271]. Intuitively, with additional instrumentation, the cost of materials, theatre time, and staff increases. Compared to bilateral pedicle screw fixation, unilateral fixation reduces postoperative pain, surgical muscle damage, hospital stay and, subsequently, time to ambulation [50-52, 273]. Conversely, Fukushima et al. found no difference in blood loss between the two levels of fixation [273]. Unilateral fixation is most commonly inserted through the same side accessed for cage insertion, however bilateral fixation requires repositioning the patient during surgery and introducing a new access point, increasing the invasiveness of the operation and the patient's postoperative discomfort. While clinical factors involved in an XLIF operation are pertinent, complication rates and surgical outcomes also influence preoperative decision-making.

The literature has predominantly presented comparisons between unilateral and bilateral fixation in terms of fusion rate, postoperative pain, pseudarthrosis, and subsidence. Standalone XLIF has been associated with higher rates of subsidence and restenosis [274-276]. Conversely, bilateral pedicle screw fixation provides a higher level of biomechanical stability and, therefore, is theoretically the most likely configuration to arrest facet micromotions and prevent postoperative pain and complications arising therefrom [277-280]. In lateral lumbar interbody fusion (LLIF), which is a comparable approach to XLIF, no difference in subsidence incidence or fusion rate was reported between unilateral and bilateral fixation groups [273]. While the unilateral group had better functional outcomes on clinical assessment, they also had a higher incidence of re-operation [273]. Oblique lateral interbody fusion (OLIF) is a lateral access approach anterior to the psoas muscle. Wen et al. found no difference in fusion rate between OLIF with unilateral and bilateral posterior fixation [281]. Lu et al. made similar findings in their meta-analysis of TLIF and PLIF surgeries [282]. Ren et al.'s meta-analysis, however, reported a higher rate of pseudarthrosis in unilateral compared to bilateral fixation in TLIF [283]. Further, higher rates of cage subsidence were found in the unilateral fixation groups of the PLIF and TLIF studies [282, 283], while Wen et al. reported no difference between unilateral and bilateral fixation groups in OLIF [281]. Zhang et al. and Xiao et al. found no difference between unilateral and bilateral fixation groups across the clinical outcomes and complication rates in TLIF and PLIF surgeries [51, 52].

Evidently, the literature does not reach a consensus on the outcomes achieved with either unilateral or bilateral posterior fixation across the spectrum of lumbar fusion approaches. PLIF and TLIF are distinct surgical techniques that partially resect ligaments and other bony structures that are preserved in an XLIF, limiting the extent of any comparisons. Further, each approach has a corresponding cage design that may not provide stability comparable to a large-footprint lateral access cage. Therefore, the clinical outcomes and complications findings from the OLIF and LLIF studies are most relevant to pre-surgical planning for XLIF.

4.2 The Necessity of Biomechanical Rationales

Notwithstanding the importance of clinical factors in surgical decision-making, they only represent a single aspect of preoperative planning. It is worthwhile investigating the biomechanical sources of clinical risk factors. Quantifiable biomechanical inputs are

not usually a significant consideration in surgical planning, mostly due to a lack of literature and the absence of patient-specific modelling tools. Complications such as subsidence and pseudarthrosis have biomechanical causes. Understanding the links between the complications, outcomes, and their biomechanical correlates will better equip surgeons when considering the extent of additional fixation required for a patient.

In a finite element (FE) study, Zhang et al. examined the impacts of XLIF and fixation on spinal structures, showing that XLIF reduces strain on the facets compared to TLIF, however no considerable difference between unilateral and bilateral fixation was found [284]. Unilateral fixation produced a similar level of stability to bilateral fixation, however only the L4-L5 segment was modelled and the authors did not study standalone XLIF [284]. Other FE analyses have reported a reduction in instrumentation stress [277], increased stability, and reduced cage-endplate interface stress with bilateral pedicle screws [279, 285, 286], however the studies did not model XLIF cages or assess adjacent segments. In cadaveric studies, Godzik et al. demonstrated that bilateral fixation does not provide a substantial reduction in motion compared to unilateral fixation in LLIF, while Lai et al. found a substantial increase in stability with bilateral fixation in multilevel LLIF [287, 288].

The biomechanics literature has focused on assessing posterior fixation predominantly in terms of stability. Questions remain surrounding the impact of supplemental posterior fixation on cage loads and adjacent segments, and potential complications such as pseudarthrosis and cage subsidence. In this chapter, FE analysis is used to examine whether standalone XLIF allows for more facet micromotions and cage loads while reducing biomechanical changes at adjacent levels compared to XLIF with unilateral and bilateral posterior fixation, and whether these changes are consistent in both early and late stages of fusion. The aim is to enhance biomechanical perspectives on pre-surgical planning regarding the extent of posterior fixation required for a patient in an XLIF procedure.

4.3 Finite Element Modelling of Posterior Fixation

The FE modelling protocol in this chapter largely follows the method presented in Chapter 3.

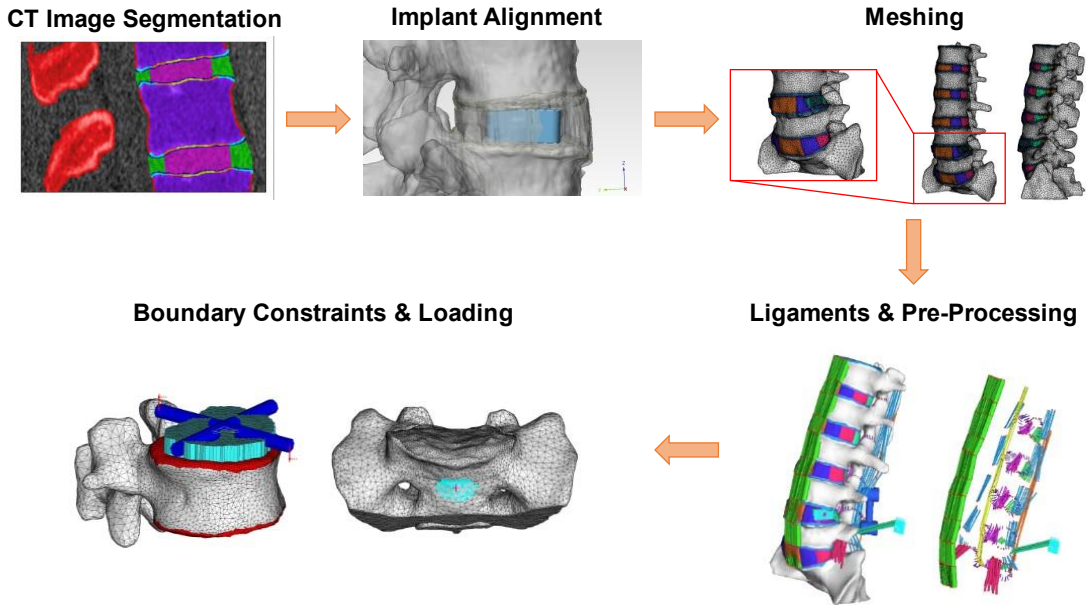

Figure 4.1: Overview of the procedure for building the FE models.

4.3.1 Modelling Pedicle Screws & Rods

Following computed tomography (CT) image segmentation into the anatomical regions of interest, the pedicle screws and rods were inserted at L4-L5 during the surface meshing stage in Materialise 3-Matic (Materialise NV 2018a, Belgium) using the same technique that was used to insert the interbody cage (Section 3.3.2).

3D model files (STL) of the pedicle screws (⌀ 6.5mm, 66mm including tulip), and rod (⌀ 6.5mm, 42mm) were imported to 3-Matic and embedded at the L4-L5 level (Figure 4.2). The dimensions of the construct were matched to commercially available NuVasive (San Diego, USA) Coroent XL implants. The creation of the *Non-Manifold Assembly* with the pedicle screws and rods as the *Intersecting Entity* allowed for the removal of the bone material from the respective intersecting spaces. Pedicle screws were inserted with traditional trajectory unilaterally and bilaterally. The unilateral pedicle screws were inserted on the left side – the same side used for cage insertion in accordance with standard clinical practice.

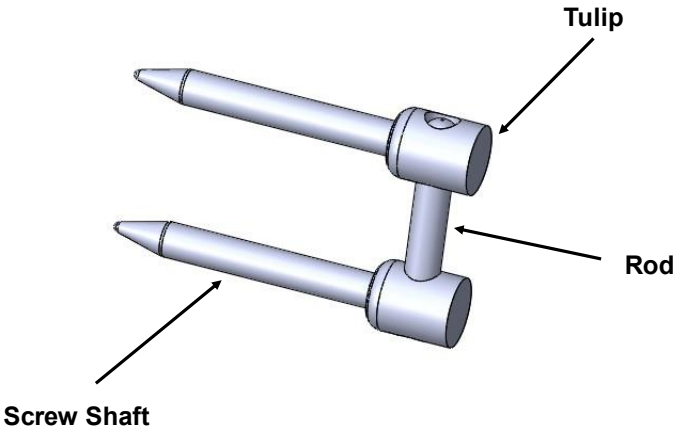

Figure 4.2: 3D model of the pedicle screw and rod construct developed in Solidworks (Dassault Systèmes SE, France) and imported into Materialise 3-Matic.

4.3.2 Meshing

Subsequent re-meshing of the geometry allowed for surface element quality improvement as described in Section 3.3.3. The screw thread was not modelled, as it introduced complexities in surface mesh refinement arising from *Non-Manifold Assembly* creation. Further, the thread feature would not produce a considerable biomechanical impact. Three 3D volumetric meshes of 4-noded tetrahedrons were generated and imported into Strand7 (vers. 2.4.6, Strand7 Pty. Ltd., Australia) FE modelling software for pre-processing (Figure 4.3):

- Standalone XLIF / No fixation (NF)
- Unilateral pedicle screw fixation (UL)
- Bilateral pedicle screw fixation (BL)

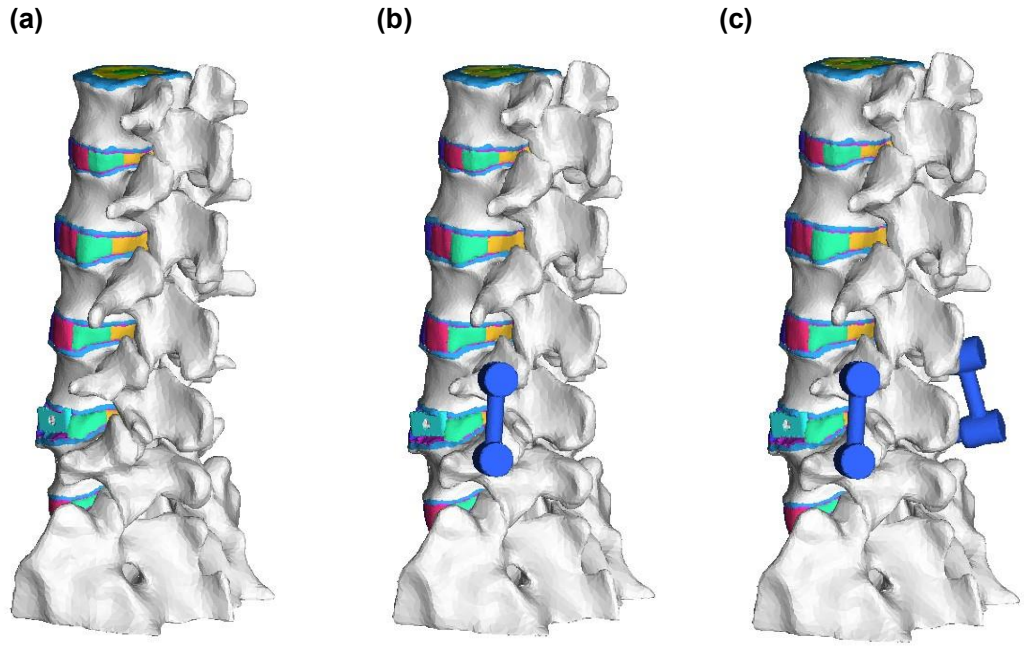

Figure 4.3: NF (a), UL (b), and BL (c) model geometries imported into Strand7.

4.3.3 Modelling Fusion State and Contact

Each geometry was modelled with partial (PF) and full (FF) fusion of the graft with bonded contact to the L4 inferior and L5 superior endplates, as described in Section 3.7.2. The bonded contact in the PF and FF states is a representation of creeping substitution, allowing two distinct states of fusion to be examined while maintaining the same contact modelling at both endpoints. Similarly, the cage surface was also bonded to the endplates.

Contact between the screws and bone was also bonded. The purpose of this study was to examine loads on the cage and adjacent spinal structures as an input to surgical decision-making rather than studying screw loosening or its mechanics. It is, therefore, reasonable to model the ideal contact scenario. Studies that have focused on the mechanics of screw behaviour have used frictional [289, 290] and frictionless [291, 292] interface elements to model screw-bone interface characteristics. Bonded contact is also common, particularly when examining changes outside the pedicle screw [293-296].

4.3.4 Additional Pre-Processing

The PF state was modelled with cancellous bone graft and the FF state was modelled with cortical bone, as previously described Section 3.7.2. The pedicle screws and rods

were assigned isotropic titanium (Ti-6Al-4V) material properties (E = 112GPa, v = 0.31) [297]. All other calibrated and uncalibrated material properties were assigned as per Section 3.8.

The modelling procedure for the ligaments, intervertebral disc fibres, and facet contact was identical to Sections 3.4, 3.5, and 3.6 respectively. Additional model information is presented in Table 4.1.

Table 4.1: Additional model information outlining the number of nodes, elements, and beams modelled in each annulus layer from Layer 1 (Outermost: O) to Layer 4 (Innermost: I).

	NF	**UL**	**BL**
Nodes	187,329	191,955	194,671
4-Noded Tetrahedral Elements	1,063,748	1,085,399	1,096,306
Annulus fibres (Cylindrical Beam Elements) in each layer			
L1-L2	(O) 384-380-362-234 (I)	(O) 385-381-367-240 (I)	(O) 385-381-367-240 (I)
L2-L3	(O) 298-297-298-197 (I)	(O) 357-360-359-237 (I)	(O) 357-360-359-237 (I)
L3-L4	(O) 321-319-318-211 (I)	(O) 352-351-345-227 (I)	(O) 352-351-345-227 (I)
L4-L5	(O) 130-124-102-54 (I)	(O) 255-222-185-102 (I)	(O) 255-222-185-102 (I)
L5-S1	(O) 519-504-466-293 (I)	(O) 485-457-437-284 (I)	(O) 485-457-437-284 (I)

4.3.5 Loading and Boundary Constraints

As per Section 3.9, the model was constrained at the sacrum and loads were applied using a steel crossbeam structure atop a steel cap on the L1 superior endplate. Force couples were applied to generate a pure unconstrained 10Nm bending moment in flexion and extension individually. The model was solved using the *Nonlinear Static Solver* in Strand7, in a stepwise manner from 0Nm to 10Nm, accounting for material, geometric, and boundary nonlinearities.

4.4 Results

All results were calculated under the maximum applied bending moment (10Nm). Percentage changes are reported normalised to the NF model in its respective PF or FF state.

4.4.1 Index Level

(a) Facet Axial Forces

The axial force in each *Point Contact* element between the articulating facet surfaces was obtained directly from Strand7 and totalled to calculate the axial force transferred through each facet joint.

Fusion state did not produce notable differences in facet forces. Compared to extension, the loads measured at the L4-L5 facets on both sides during flexion were small and the differences between the models were negligible (Figure 4.4a).

During extension, however, there was a progressive off-loading of the index facets with increasing fixation (Figure 4.4b). Compared to the standalone XLIF model, at both partial and full fusion there was a 76% reduction in axial force through the left index facet with unilateral fixation; in the right facet, total axial load reduced by 91%. There was a greater load reduction in the right facet compared to the left, despite the unilateral pedicle screws inserted on the left side. With the addition of further instrumentation, the BL model recorded no force through either L4-L5 facet during extension.

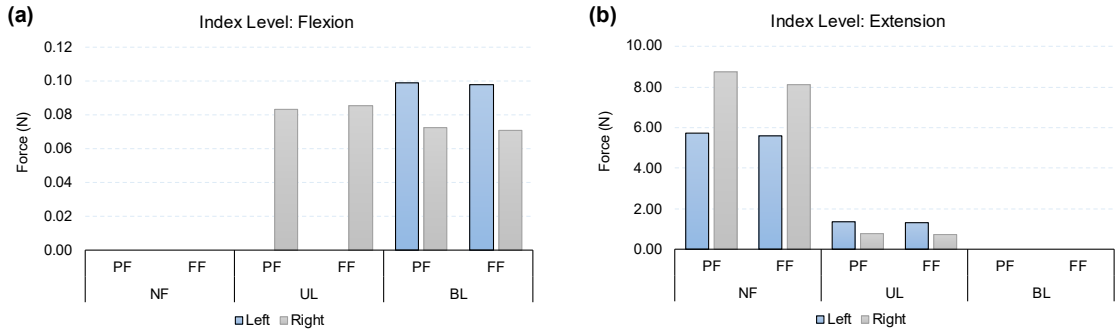

Figure 4.4: Total axial force (N) passing through the index level (L4-L5) facets during flexion (a) and extension (b).

(b) Capsular Ligament Strain

Strain in the capsular ligament (CL) was calculated from nodal coordinates and displacement values obtained from Strand7. The length (L) of each ligament fibre was calculated in the unloaded and loaded (10Nm force couple) state from coordinate data at each end of the beam ($E1$, $E2$).

$$L = \sqrt{(x_{E1} - x_{E2})^2 + (y_{E1} - y_{E2})^2 + (z_{E1} - z_{E2})^2}$$

Equation 4-1

The axial strain was calculated as the ratio of the change in length to the original length for each fibre and averaged across all the fibres that constituted the ligament. Lax ligaments were excluded from the calculation of average axial strain.

$$Axial\ Strain = \frac{L_{10Nm} - L_{0Nm}}{L_{0Nm}}$$

Equation 4-2

Fusion state did not produce notable differences in CL strain. The CL was strained in flexion, however, was lax in extension and did not transfer significant tensile loads to the facets.

In flexion, the CL was progressively off-loaded on both sides with increasing fixation at the index level (Figure 4.5). On the left side, there was a 78% (PF) to 80% (FF) reduction in CL strain for the UL models compared to the NF models, while the left CL strain in the BL models was reduced by 94% in both fusion states. A similar pattern was found at the right index facet; a 72% (PF) to 73% (FF) reduction in CL strain with UL fixation and a 95% reduction with BL fixation in both fusion states.

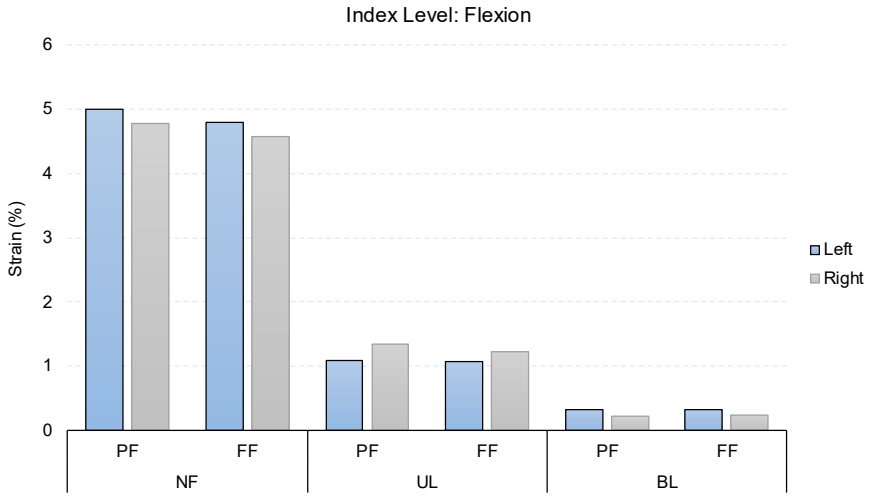

Figure 4.5: Average axial strain in the capsular ligament at the index (L4-L5) level facets.

(c) Cage and Graft Compressive Loads

Compressive stress concentrations in the anterior and posterior of the standalone cage in flexion and extension respectively were off-loaded in the UL and BL models (Figure 4.6). While both fixation types reduced compressive stress on the interbody cage, the UL models exhibited an asymmetrical stress distribution compared to both BL and NF models. As such, notable stress-risers were found in the right-posterior region of the cage in UL models during extension. The addition of the extra pedicle screws in the BL models off-loaded the stressed regions and reinstated a symmetrical stress distribution. In flexion, the area of the cage under compression increased with unilateral (PF: 14%, FF: 14%) and bilateral (PF: 33%, FF: 44%) fixation compared to standalone XLIF; in extension there was no substantial change.

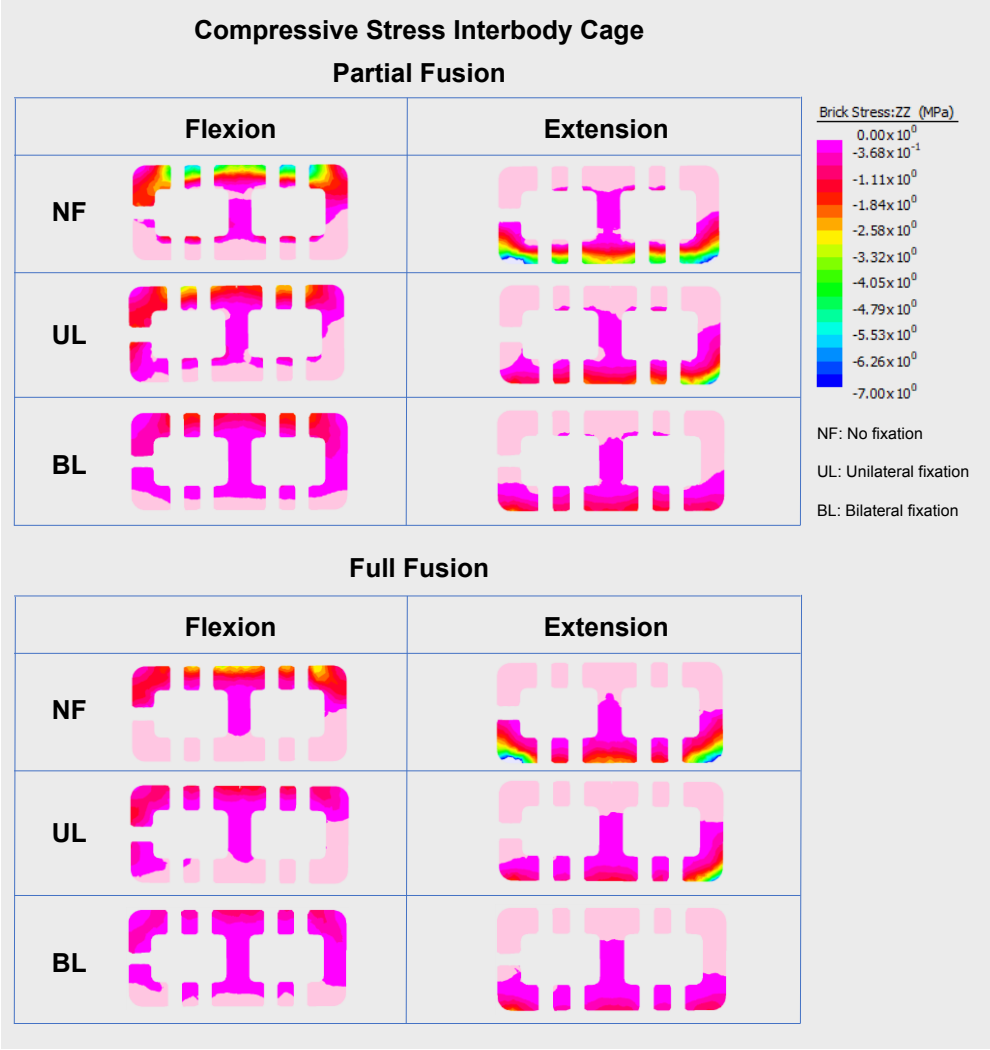

Figure 4.6: Compressive stress (MPa) distribution at the mid-axial plane of the interbody cage. Anterior direction at the top of the image; ZZ direction into the plane of the image.

Average compressive stress was calculated by averaging the compressive stress experienced by all tetrahedral elements in the cage or graft constructs obtained directly from Strand7. Graft stiffening and the addition of posterior fixation reduced the average compressive stress on the cage in flexion and extension (Table 4.2). The FF graft experienced more compressive stress than the PF graft, however stress on both grafts reduced with increasing levels of fixation (Table 4.3). The relative stress reduction from NF to UL was greater than from UL to BL.

Table 4.2: Average compressive stress (MPa) on the interbody cage during flexion and extension.

	NF		**UL**		**BL**	
	PF	**FF**	**PF**	**FF**	**PF**	**FF**
Flexion	1.561	1.320	0.721	0.586	0.439	0.336
Extension	1.631	1.405	0.693	0.590	0.410	0.350

Table 4.3: Average compressive stress (MPa) on the graft during flexion and extension.

	NF		**UL**		**BL**	
	PF	**FF**	**PF**	**FF**	**PF**	**FF**
Flexion	0.084	0.871	0.057	0.464	0.050	0.325
Extension	0.070	0.708	0.046	0.374	0.039	0.286

Change in stress is simultaneously reflective of change in compressive force and change in the area under compressive stress. Change in force normalised to the NF models, however, is a measure of compressive cage loads that considers both changes individually. The relative change in compressive force (F) can be calculated by the sum of the relative change in compressive pressure (P) and the relative change in the area under compression (A):

$$\% \Delta F = \% \Delta P + \% \Delta A$$

Equation 4-3

In the PF state, cage compressive force reduced by similar amounts in both UL (40%) and BL (39%) models during flexion (Table 4.4). In extension, the degree of off-loading corresponded to the level of fixation (UL: 56%, BL: 82%). In the FF state, a greater reduction in force was measured in the UL model (42%) compared to the BL model (31%)

during flexion (Table 4.4). In extension, however, the force reduction on the cage again corresponded to the level of fixation (UL: 61%, BL: 83%).

In flexion, UL and BL models experienced similar reductions in compressive graft force in both the partially and fully fused states (PF-UL: -30%, PF-BL: -34%, FF-UL: -35%, FF-BL: -39%) (Table 4.5). In extension, a more substantial off-loading of the graft was measured in the BL models (PF: -84%, FF: -66%) compared to the UL models (PF: -56%, FF: -43%).

Table 4.4: Percentage change in compressive force on the interbody cage in the partially and fully fused state, normalised to the NF model.

		PF		FF	
		UL	**BL**	**UL**	**BL**
% ΔF	**Flexion**	-40	-39	-42	-31
	Extension	-56	-82	-61	-83

Table 4.5: Percentage change in compressive force on the graft in the partially and fully fused state, normalised to the NF model.

		PF		FF	
		UL	**BL**	**UL**	**BL**
% ΔF	**Flexion**	-30	-34	-35	-39
	Extension	-56	-84	-43	-66

(d) Shear Strain on Interbody Cage

Average shear strain was calculated by averaging the shear strain experienced by all tetrahedral elements in the cage obtained directly from Strand7.

The highest level of shear strain was measured in the NF models (Table 4.6). In the UL models, regions of high shear strain remained in the central, anterolateral, and posterolateral regions of the interbody cage in flexion and extension (Figure 4.7). Region A, on the left side depicted in Figure 4.7, exhibited higher peak shear strain in the NF models (PF Flexion: 0.13%, PF Extension: 0.103%, FF Flexion: 0.128%, FF Extension: 0.117%) compared to UL (PF Flexion: 0.001%, PF Extension: 0.001%, FF Flexion: 0.007%, FF Extension: 0.013%). Region B, however, experienced higher peak shear strain in the UL models (PF Flexion: 0.017%, PF Extension: 0.013%,

FF Flexion: 0.012%, FF Extension: 0.009%) compared to NF models (PF Flexion: 0.004%, PF Extension: 0.001%, FF Flexion: 0.002%, FF Extension: 0.002%). Peak shear strains were comparable in Region C. Regions of high shear strain in the NF and UL models tended to persist at the point of full fusion. Average shear strain was considerably reduced in the BL models compared to UL and NF.

Table 4.6: Average shear strain (%) on the interbody cage during flexion and extension.

	NF		UL		BL	
	PF	**FF**	**PF**	**FF**	**PF**	**FF**
Flexion	0.022	0.020	0.016	0.013	0.005	0.004
Extension	0.021	0.019	0.015	0.012	0.009	0.007

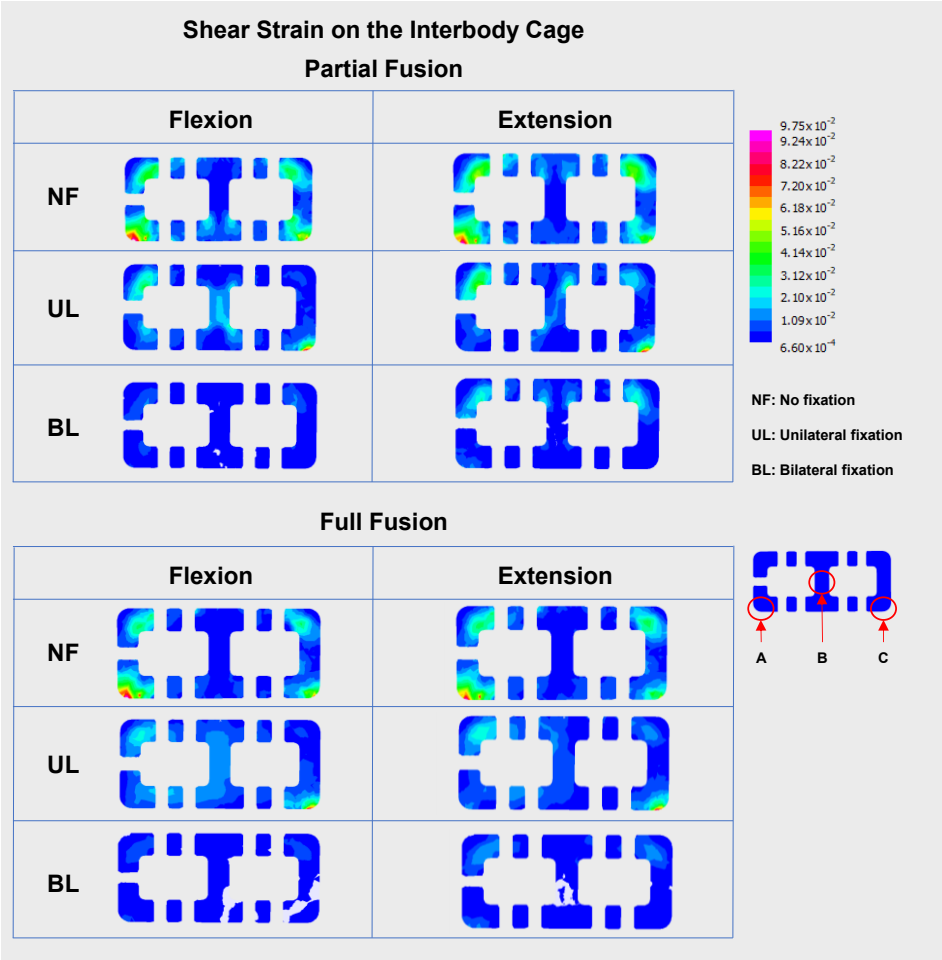

Figure 4.7: Shear strain (%) distribution at the mid-axial plan of the interbody cage. Anterior direction at top of page. Region A represents the left posterolateral region of the cage; Region B represents the central region of the cage; Region C represents the right posterolateral region of the cage.

4.4.2 Adjacent Levels

(a) Facet Axial Forces

Axial force through the left cephalad facet was reduced with the addition of unilateral (-63%) and bilateral (-66%) pedicle screws in both the PF and FF states during flexion (Figure 4.8a), however no considerable change was noted in extension compared to the NF models (Figure 4.8b). On the left side, there was a significant increase in facet axial loads at the caudal level during flexion (UL: 361%, BL: 358%) (Figure 4.8a) and extension (UL: 38%, BL: 37%) (Figure 4.8b) in both fusion states.

On the right side, no axial force was transferred through the L3-L4 facets during flexion in the NF model, however small loads (PF-UL: 1.28N, FF-UL: 1.27N, PF-BL: 1.36N, FF-BL: 1.35N) were measured in the models with supplemental fixation (Figure 4.8c). In UL and BL models, there was a 53% reduction in caudal facet force during flexion in both fusion states. No substantial changes were measured at the cephalad level during extension. Compared to NF, there was a 29% increase in L5-S1 right facet forces in the UL models, and a 32% increase in the BL models in both fusion states (Figure 4.8d).

Supplemental fixation induced load changes at the adjacent facets, however there were no considerable differences in the changes induced between the two levels of fixation. The left and right facets may show different patterns in flexion due to their orientation and the contact elements activated as a consequence.

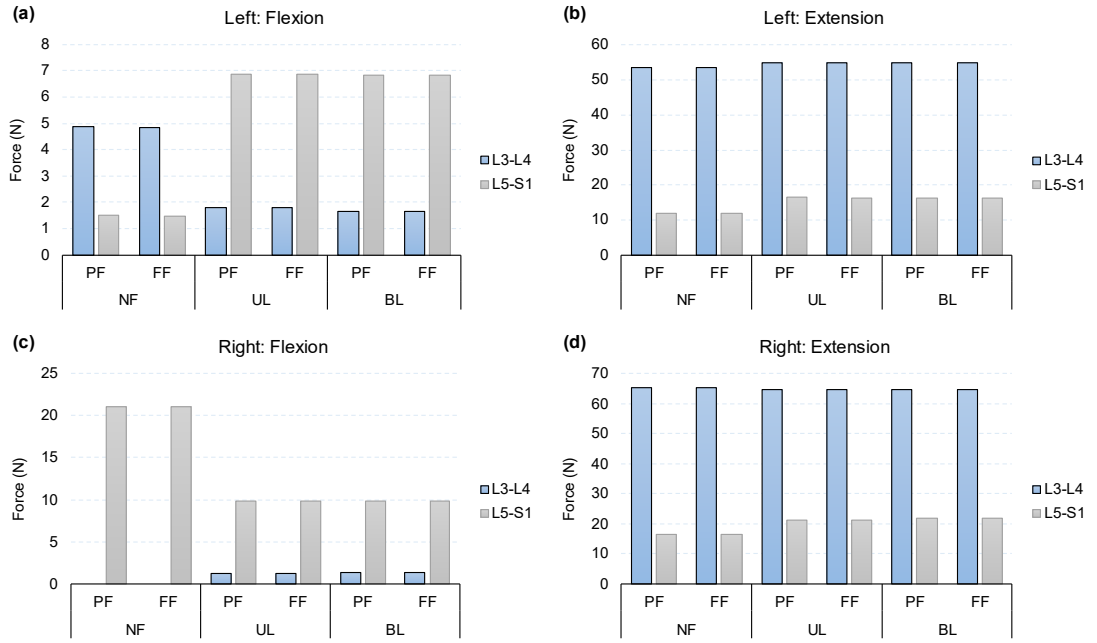

Figure 4.8: Total axial force in Newtons (N) through the left (a; b) and right (c; d) cephalad (L3-L4) and caudal (L5-S1) facets in flexion and extension.

(b) Capsular Ligament Strain

The CL was lax in extension and, as such, these results are not presented.

On the left side in flexion, there was a 21% reduction in CL strain at the cephalad level in the UL models compared to the NF models, while BL models recorded a 22% reduction in PF and FF states (Figure 4.9a). At the caudal level, strain in the CL increased with both fixation configurations compared to the NF models in flexion (PF-UL: 25%, FF-UL: 24%, PF-BL: 24%, FF-BL: 24%).

On the right side in flexion, UL and BL models recorded a 14% and 15% increase in L3-L4 CL strain respectively, compared to NF in both fusion states (Figure 4.9b). No notable difference was found at the caudal CL in flexion.

Supplemental fixation induced changes in CL axial strain at adjacent levels, however there were no considerable differences in the changes induced between the two levels of fixation. As with axial force, left and right facets may show different patterns in flexion due to their orientation.

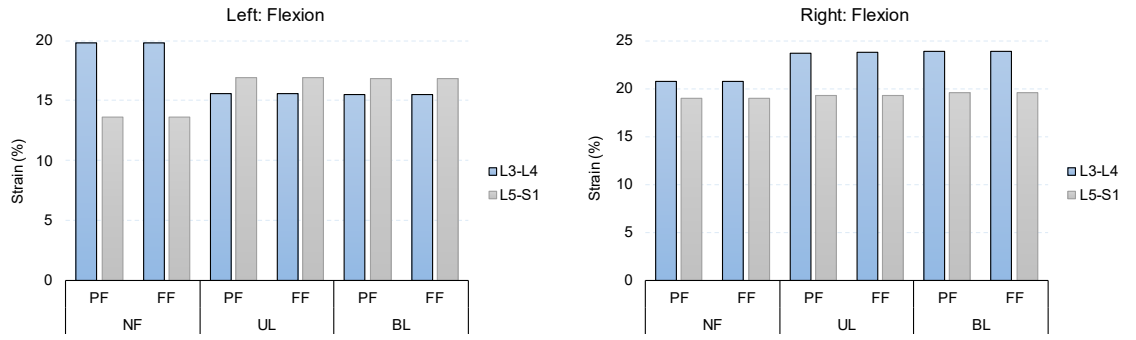

Figure 4.9: Average axial strain in the left (a) and right (b) cephalad (L3-L4) and caudal (L5-S1) facet capsular ligaments in flexion.

(c) Intervertebral Disc Compressive Stress

Average compressive stress in the intervertebral disc was calculated by averaging the compressive stress experienced by all tetrahedral elements (obtained directly from Strand7) in the annulus fibrosus and nucleus pulposus respectively (Table 4.7, Table 4.8). The only considerable change was measured in the L5-S1 annulus, which underwent a 15% decrease in compressive stress during extension after the addition of posterior fixation, while the difference between unilateral and bilateral fixation was negligible (Table 4.8). No other notable changes were measured in the adjacent discs.

Table 4.7: Average compressive stress (MPa) at the L3-L4 disc. AF: Annulus fibrosus, NP: Nucleus pulposus.

		NF		UL		BL	
		PF	**FF**	**PF**	**FF**	**PF**	**FF**
AF	**Flexion**	0.108	0.108	0.108	0.108	0.108	0.108
	Extension	0.108	0.108	0.104	0.104	0.104	0.104
NP	**Flexion**	1.146	1.146	1.116	1.116	1.115	1.115
	Extension	1.086	1.086	1.042	1.042	1.043	1.043

Table 4.8: Average compressive stress (MPa) at the L5-S1 disc. AF: Annulus fibrosus, NP: Nucleus pulposus.

		NF		UL		BL	
		PF	**FF**	**PF**	**FF**	**PF**	**FF**
AF	**Flexion**	0.069	0.069	0.071	0.071	0.071	0.071
	Extension	0.289	0.289	0.245	0.245	0.245	0.245
NP	**Flexion**	1.228	1.228	1.230	1.230	1.227	1.227
	Extension	0.985	0.985	0.919	0.919	0.920	0.921

4.5 Discussion

This FE analysis quantifies the impact of different levels of posterior fixation in XLIF on index-level loads and load-distribution in adjacent structures in both early and late stages of fusion. In doing so, the aim was to provide surgeons with biomechanical inputs to the surgical decision-making process when considering the extent of posterior fixation to instrument.

4.5.1 Findings from the Facets and Adjacent Intervertebral Discs

Facet micromotions, measured by CL strain, were considerably lower at the index level compared to adjacent levels, however there was a progressive off-loading of the facet capsule with unilateral and bilateral fixation. Similarly, axial loads measured at the index facets during extension in the standalone XLIF model were substantially diminished with the addition of unilateral fixation, followed by a further, smaller reduction with bilateral fixation.

Adjacent facets underwent load-pattern changes with the addition of unilateral and bilateral pedicle screws at L4-L5. In extension, axial force in the facets increased at the caudal level on both sides with posterior fixation, with no change at the cephalad level. Changes in capsular ligament strains and axial forces in flexion were not consistent between the left and right sides at adjacent levels. That is, the change in CL strain induced by fixation at the left facet was different to the change induced at the right facet. While the results clearly show changes in load-distribution amongst the adjacent facets after the addition of posterior fixation, that persist at the point of full fusion, the seemingly unclear nature of these biomechanical changes suggests they may be anatomically dependent [284].

Arresting facet micromotions is key to maintaining segmental stability at adjacent levels and preventing postoperative low back pain and potential pseudarthrosis complications [278, 280]. At adjacent levels, there was no biomechanical difference between unilateral and bilateral fixation. Further, at the index level, loading of the left and right facets was similar with unilateral fixation. These results suggest that single-sided fixation provides sufficient biomechanical stability to both left and right facets, confirming previous findings [284]. Surgical decisions should account for these changes in facet loads in the

context of the micromotions they may produce, and as a potential source of postoperative pain.

In both the partially and fully fused states, the only considerable biomechanical change measured in the adjacent intervertebral discs was a reduction in caudal annulus compressive stress in extension with posterior fixation. Several studies have shown links between pedicle screw fixation and adjacent segment degeneration (ASD), particularly at the suprajacent level [298-300]. These studies also cite facet joint violation as a potential influencing factor, emphasising the importance of facet stabilisation in achieving good clinical outcomes [298-300]. The models developed in this FE study simulated traditional pedicle screw trajectory. Though unable to account for potential clinical risks such as facet joint violation, the bonded screw-bone contact modelling may be similarly demonstrative of the importance of screw positioning and fixation in stabilising the segment and preventing hypermobility and subsequent degenerative changes at adjacent levels. This study supports that appropriately instrumented pedicle screws do not increase the risk of ASD.

4.5.2 Findings from the Implant Construct

In the PF and FF states, compressive stress on the cage reduced with fixation level. Lower cage stresses reduce the likelihood of cage subsidence [89]. Cage compressive force progressively reduced in extension, however in flexion the reduction in force in the UL and BL models was comparable due to the increase in contact between the endplates and the cage-graft surface induced by the bilateral pedicle screws. The risk of subsidence is likely to be highest in standalone XLIF due to the regions of high stress at the anterior and posterior extremities of the implant. There was a prominent off-loading of these regions with the addition of posterior fixation, as supported by Liu et al. [279]. The UL models, however, exhibited some compressive stress and shear strain hotspots, which may still place the cage at increased risk of subsidence instigated in those specific regions. No such regions were found with bilateral fixation. This finding should be considered in the context of Fukushima et al.'s study which showed no difference in subsidence rate between unilateral and bilateral fixation [273]. The cage load results may be seen as indicative of endplate loading, where the even distribution found in the BL models can be associated with reduced risk of endplate fractures and subsidence [89], in accordance with findings by Liang et al. [286].

In accordance with the cage results, force on the graft in flexion was similar in both unilateral and bilateral configurations. In extension, however, the graft was loaded considerably less in the BL models compared to the UL models across both PF and FF states. Examining graft loading in the partially fused state is pertinent to understanding fusion progression in accordance with Wolff's law [193]. Based on the current literature, it is not clear whether unilateral fixation leads to higher rates of pseudarthrosis compared to bilateral fixation [282, 283], though it seems unlikely based on the relevant OLIF and LLIF studies [273, 281]. Under-loading and instability are both risk factors for delayed union [193, 268]. From a biomechanical standpoint, there are no justifiable load-pattern changes that suggest unilateral fixation increases the risk of delayed union compared to bilateral fixation, in accordance with published literature [273]. On average, standalone LLIF and XLIF have a high fusion rate, although there is considerable variability in fusion rate between studies [301]. While the standalone procedure increases load on the graft promoting bone fusion, excessive micromotion in the fusion mass is also a risk factor for delayed or non-union and poor bone quality [268]. More inputs are required to select appropriate patients for standalone XLIF [301] and the quantitative results from the graft region lay the foundations for further mechanobiological research on the influence of loads on bone formation.

4.5.3 Implications for Surgical Planning

There are considerable biomechanical differences between standalone XLIF and XLIF with posterior fixation. Loads and micromotions at adjacent facets are altered, while cage and graft loads are increased in standalone XLIF in a manner that warrants consideration alongside risks of subsidence and pseudarthrosis. Given the similarity in the biomechanical changes produced by unilateral and bilateral configurations, unilateral pedicle screws may be preferrable albeit with consideration of the patient's specific stability requirements and bone quality. While the results do not suggest a link with ASD, the choice of fixation has implications for subsidence risk and fusion rate. Surgeons should be aware of clinical risk factors that may be compounded by these biomechanical correlates. Further, surgeons should consider the biomechanics associated with each fixation configuration cognisant that additional instrumentation introduces additional complication risks, risk of instrumentation failure, operating time, blood loss, costs, and

recovery time. The findings, however, only remain valid for a single-level XLIF at L4-L5 and may not be generalisable to other levels.

This FE analysis has demonstrated that computational modelling can be used to provide biomechanical insights to complement clinical factors during pre-surgical planning. While the study does not account for different anatomies, it provides an indication of biomechanical changes that occur in a controlled environment without the influence of extraneous variables. Studying different patient anatomies may elicit insights into the impact of facet orientation, lordosis, and intervertebral disc shapes on biomechanics and how they influence decisions regarding posterior fixation. The FE analysis in this chapter provides holistic biomechanical insights into the pertinent factors that should be considered alongside patient-specific information.

In doing so, the findings demonstrate the detailed outputs that can be analysed to guide surgical decision-making through advances in patient-specific FE analysis during pre-surgical planning. Results from the facets, for example, highlight the importance of considering individual anatomies. The processes required in image segmentation and meshing to develop this suite of FE models were complex and time-consuming. Automated image segmentation and meshing will expedite the time to simulation. Further, the convergence of statistical and FE modelling in the field of probabilistic modelling allows mechanical data to be understood in the context of population variance in factors such as age, sex, and anatomy. Such an approach, including modelling a variety of fusion approaches, will enable the development of biomechanical rationales for use in pre-surgical lumbar fusion planning. While the findings from this FE analysis provide broad inputs for surgeons' consideration, advances in modelling will precipitate more explicit patient-specific guidance arising from a combination of mechanical and clinical factors.

4.5.4 Limitations

Some modelling limitations should be noted in this study. The FE software did not allow modelling of partial bonding between the endplate and cage-graft surface, limiting the representation of creeping substitution in the partially fused models. Further, a lack of literature on material behaviour of the interfacing surfaces prevented modelling of friction between the endplates and implant surfaces. As such, the contact was bonded.

The *in vivo* properties of fusion bone are not well-documented and, therefore, stiffness properties were modelled as cancellous and cortical bone for PF and FF states respectively. Similarly, the contact between the pedicle screws and bone was also bonded, limiting the extent to which mechanical data from the fixation constructs can be analysed in isolation. Only four layers of collagen fibres were modelled within the annulus fibrosus without translamellar bridges throughout the height of the annulus. Lastly, the various configurations of lateral fixation with vertebral body screws were not modelled.

4.6 Conclusion

This FE analysis provides inputs to pre-surgical planning by examining the biomechanical implications of unilateral, bilateral, or no fixation in XLIF surgery, at the index (L4-L5) and adjacent levels. The findings highlight the complications that can arise with improper decision-making regarding supplemental fixation. Commensurate off-loading occurs at the index level facets with the extent of posterior fixation, while changes produced at adjacent levels may be anatomically-dependent. Further, unilateral fixation arrests motions on left and right sides equally. Unilateral and bilateral fixation produce similar biomechanical changes and, as such, unilateral pedicle screws may be preferrable, albeit with consideration of subsidence and pseudarthrosis risk. Disc compressive stress results suggest that posterior fixation is unlikely to be implicated in adjacent disc degeneration. Advances in modelling and biomechanical research will enable surgeons to evaluate the various XLIF fixation options cognisant of the biomechanical changes they produce and the stability requirements of the patient.

5. Design and Development of a 'Smart' Interbody Cage

Preface

So far, this thesis has used finite element analysis to study lumbar interbody fusion, uncovering and addressing links between biomechanics and potential postoperative complications. Some complications arising from other clinical and unpredictable factors, however, are unavoidable. Postoperative monitoring can not be addressed with computational modelling, but rather requires novel methods for direct measurement within the body. This chapter describes the development of a proof-of-concept 'smart' interbody cage for postoperative monitoring as an alternative to the currently ineffective radiological imaging. The load-sensing cage is tested under compression, aiming to distinguish between graft and endplate stiffness states. This mechanical data is a useful tool for monitoring fusion progression and assessing the risk of implant migration and non-union. While more effective preoperative planning can reduce the rate of complications, the 'smart' implant approach presents an opportunity to proactively detect, manage, and prevent complications.

The findings in this chapter are published in the following peer-reviewed journal article:

> V.A.S. Ramakrishna, U. Chamoli, S.C. Mukhopadhyay, A.D. Diwan and B.G. Prusty, "Measuring compressive loads on a 'smart' lumbar interbody fusion cage: Proof of concept," *Journal of Biomechanics*, Jan 2023, doi: 10.1016/j.jbiomech.2023.111440.

5.1 Clinical Objectives

Lumbar interbody fusion (LIF) surgery is a treatment option for low back pain that aims to immobilise and stabilise degenerate, unstable spinal segments. The intervertebral disc is removed at the affected spinal level and replaced by an interbody cage inserted between the vertebrae, which may be further secured with metallic instrumentation. Cavities in the cage are filled with osteoconductive material (such as allograft, demineralised bone matrix, bone morphogenetic proteins, and ceramics [302]) that promotes bone growth through the implant until the two vertebrae are fused. As highlighted in Sections 2.2.3 and 2.2.4, pseudarthrosis and subsidence present a multifaceted challenge in the postoperative management of the patient.

Pseudarthrosis is the incomplete bony union between the adjoining vertebrae following LIF surgery, characterised by persistent pain and associated with several other complications [61]. The time taken to reach full bone fusion may vary from 6 to 12 months, however rates of pseudarthrosis at least one year after LIF surgery range from 3-20% in patients with healthy bone, while occurring in 20-30% of patients with osteoporosis [49, 61, 78-82]; low bone density is a risk factor for subsidence [87, 93, 94]. Bone quality alone, however, is not the only factor influencing the onset of pseudarthrosis and subsidence. Hsu et al. reviewed fusion outcomes against graft biologics, demonstrating the high variation in fusion rate with different bone graft substitutes (autograft, allograft, BMP-2, bone marrow aspirate, ceramics, demineralised bone matrix, growth factors) and, as such, the influence of bone graft substitutes on bone formation after fusion surgery [20]. The relative stiffness of titanium increases subsidence risk, however its superior osteoconductive properties result in lower rates of pseudarthrosis compared to polyether ether ketone (PEEK) [61, 62]. While implant design and surgical approach influence subsidence risk [88], factors such as surgical revision, disc angle, and anterior disc height have been demonstrated to affect bone maturation after fusion surgery [303]. Fusion rate may also be influenced by several lifestyle factors, such as nutrition, smoking, and medication [303-306]. Given the number of factors influencing fusion progression and subsidence, the early diagnosis of these complications is a critical component of postoperative care following a spinal fusion operation.

Section 2.2.3 establishes that current methods of diagnosis and monitoring are inaccurate and ineffective, while exposing patients to ionising radiation. Unless detected by postoperative imaging, complications are only uncovered at the onset of painful symptoms. The failure of current technology necessitates the development of novel tools for postoperative monitoring. The evolution of instrumented sensor-enabled implants, or 'smart' implants, continues to re-shape the course of musculoskeletal care. Sensors are being designed with the specific purpose of monitoring bone healing in fracture fixation plates [307]. In spinal fusion rods, sensors have been used to monitor loads after fusion surgery [181, 182, 184, 308]. The studies quantified loads on the fixators during different movements and activities, however the data has limited clinical utility [181, 182, 184, 308]. However, in a single sheep study, Windolf et al. demonstrated a sensor-recorded reduction in loads on fusion rods as the fusion mass ossified in the facet joint gap [186]. Ledet et al. instrumented an interbody cage with sensors to record loads on the implant in two baboons over a six-week period [189, 309]. While the size of spinal implants has consistently been a limiting factor in their sensor-enablement [138, 310], research has demonstrated that embedding sensors and associated electronics in an interbody cage is feasible [189, 190, 309].

Given the growth of 'smart' implants in orthopaedics and the deficiencies in LIF postoperative monitoring, it follows that a load-sensing interbody cage is a practical alternative to imaging, using *in vivo* data to assist postoperative management. A broad range of clinical objectives are addressable with an advanced 'smart' interbody cage:

I. Real-time, continuous bone growth assessment
II. Subsidence detection
III. Identification of implant malpositioning
IV. Assessment of instability
V. Development of personalised rehabilitation programs

Multi-modality sensing will enable the collection of kinematic data from the implant, helping to identify whether an implant has been appropriately aligned in the patient. Further, measuring shear loads will establish criteria for instrumenting supplementary fixation in patients who require extra stabilisation. Real-time monitoring of loads during postoperative rehabilitation can be used to optimise the program and reduce the risk of complications arising therefrom.

This chapter, however, aims to address Clinical Objective I and II, describing the design and development of a proof-of-concept 'smart' interbody cage for quantifying load-distribution changes resulting from graft and endplate stiffness changes under compressive pressure in an *in vitro* experimental setup.

5.2 User Requirements

The concept of a 'smart' interbody cage consists of mechanical and kinematic sensors embedded within the implant, actively collecting data from within the body for direct feedback to clinicians and patients. Durability, clinical utility, and wireless actualisation are critical to achieving clinical adoption and replacing radiological follow-up. The first step is to identify an effective sensing modality. This chapter presents the design, development, and testing of an interbody cage embedded with load (pressure, force, or strain) sensors only. Preparation for wireless integration is discussed in Chapter 6.

The below criteria represent the broad user requirements for sensors within a clinically used 'smart' implant. At this early proof-of-concept and prototyping stage, each user requirement can not be addressed to its full extent. They are, however, used as the guiding principles in the design of the load-sensing aspect of the 'smart' cage. Detailed design inputs are extracted from the broad user requirements in Section 5.3. User requirements and design inputs related to the specifics of wireless integration are discussed in Section 6.7.

I. Load limits

Sensors that can withstand a high-impact, high-deformation spinal joint.

II. Spatial resolution

The ability to obtain data from multiple regions of the interbody cage through a high-resolution sensor or combination of sensors that achieves the same. Such an arrangement will enable the assessment of bending loads.

III. Accuracy, reliability, and sensitivity

Sensors must be accurate enough to be clinically useful, sensitive to the biological changes they are attempting to measure, and reliable in the period of measurement. Sensor measurements are most useful in the period prior to complete fusion, which is at least 12 months.

IV. Wireless interfacing capacity

The sensors must have the potential to interface with a wireless telemetry module.

V. Biocompatibility

All materials used in the 'smart' implant must meet the requirements of ISO 10993 for implantable devices.

VI. Usability

The implant must be surgically implantable using traditional fusion approaches and not disruptive to the natural biomechanics of the spine.

5.3 Translating User Requirements into Design Inputs

Design inputs represent more specific design choices extracted from the user requirements. Where possible, design inputs have been defined based on the literature, standards, and current best practice. For some requirements, there was no relevant information to guide the identification of design inputs. In any case, design inputs should be reviewed and refined as an outcome of testing.

5.3.1 Load Limits

Load limits are guided by the physiological pre-load specified in the guiding ASTM standards for testing interbody fusion devices (ASTM F2077-18, ASTM F2267-22) [311, 312]. The standard only defines the pre-load for testing a lumbar fusion device at 500N, however ASTM F2346-05 for testing total disc replacements requires compressive loads applied up to 1200N [313]. Based on the applicable standards, the load limit considered is 900N.

The dimensions of the load-sensing cage were defined by modifying a NuVasive (San Diego, USA) hyper-lordotic extreme lateral interbody fusion (XLIF) cage (22 x 50 x 14mm, 0° lordosis) [255, 256]. The two graft cavities measured 17.3 x 11.0mm, spanning the axial height of the implant. All dimensions were obtained from the manufacturer.

The surface area of the cage is calculated by:

$$A = (22\ \times 50) - (17.3\ \times 11 \times 2) = 719.4\ mm^2$$

Equation 5-1

The pressure limit is calculated by:

$$P = \frac{900N}{719.4mm^2} = 1.25\ MPa$$

Equation 5-2

A load factor of 1.25 is considered to ensure safety of the sensors under compressive loading.

5.3.2 Spatial Resolution

The chosen sensors must effectively combine to efficiently collect data from different regions of the cage or have a high spatial resolution to measure loads across a given area (e.g. film-based sensors). Measuring loads from multiple regions is important in a research context to detect load-distribution changes under different conditions. Further, it provides the means to identify locations prone to failure that are critical from a clinical utility perspective. Considering the findings from Section 3.11.5(b), data should be captured from anterior, posterior, and lateral regions of the cage to ensure all bending modes can be sufficiently identified. Additionally, it is important to collect data from the centre of the interbody cage, as it interfaces with the softest endplate region, which is most susceptible to subsidence [91, 250]. There is no data available to suggest an appropriate number of sensors or spatial resolution. For a conventional XLIF cage design, 7 sensors is likely to provide a detailed description of the load-distribution on the cage surface.

5.3.3 Accuracy, Reliability & Sensitivity

As a design input, it is difficult to determine the accuracy, reliability, and sensitivity of an industrial sensor. This criterion was instead assessed as an output of the experimental work conducted. Accuracy of the sensors can be informed by comparison of the measurements with simulation results. The reliability of the sensors can only reasonably be assessed over the number of trials conducted. In this *in vitro* setup, the sensors are tested for their sensitivity to changes in graft and endplate stiffness under compressive loads.

Beyond the scope of this thesis, more extensive experimental work with intermediate graft stiffnesses, irregular and clinically accurate endplate geometries, and regional

stiffness variation in the endplates would yield a more extensive understanding of sensitivity. Moreover, assessment of reliability requires studies on sensor drift and cyclical loading for the average 12 month fusion period.

5.3.4 Wireless Interfacing Capacity

Sensors must be adaptable to wireless telemetry systems such as near-field communication (NFC) or radiofrequency identification (RFID) transmission. As such, certain commercial film-based sensors and optical fibre sensors are not suitable as there are no means to feasibly integrate them with existing wireless telemetry protocols. Piezoresistive and piezoelectric sensors are suitable sensing candidates, as they can be bonded to printed circuit boards (PCBs) that facilitate raw data transfer to a connected wireless telemetry module.

5.3.5 Biocompatibility

Biocompatibility is not considered at this stage of development given the further work required to finalise a sensing approach, encapsulation, and manufacturing before reaching *in vivo* testing. Later development stages should aim to comply with ISO 10993 to evaluate the biocompatibility of the device.

5.3.6 Usability

The usability user requirement can be broken down into inputs relating to the design of the implant and the ability to insert it using established surgical approaches. While usability of the implant design in clinical scenarios is considered, it is not within the scope of this thesis to determine whether new surgical techniques are required to insert the 'smart' implant without the use of heavy impact forces that are currently used for interference fit and cage placement, which may damage the sensor components. Further, technological usability is not within scope due to the early stage of development and data acquisition prototyping work to be completed.

Size requirements are applied only to the sensors embedded within the implant and not to the external data collection setup, which will require miniaturisation. Usability of the design is maintained by modifying existing commercially available XLIF cages and maintaining their major dimensions. XLIF cages provide a larger footprint amongst the lumbar fusion approaches [40, 244], simultaneously providing the most flexibility for embedding sensors with regards to space within the implant. Generally, for XLIF cages

manufactured by NuVasive, the maximum width (W, Figure 5.1) that may be found for embedding a sensor is approximately 5.0 ± 0.5mm [255, 256]. Cage heights vary depending on the level of the spine being instrumented and anatomy of the patient, however, height does not generally exceed 16mm. The maximum allowable space for a sensor in the vertical (cephalocaudal) direction is 4mm, as bone graft cavities (Figure 5.1) would prevent integration of a sensor with larger height. The maximum sensor dimensions considered are 3.5 x 3.5mm to allow space for the PCB and account for manufacturing processes, such as CNC milling, which would not be able to reliably machine to a lower resolution. No restriction is set in the axial direction, however sensors with irregular geometries were excluded due to the expected challenges with embedding such sensors.

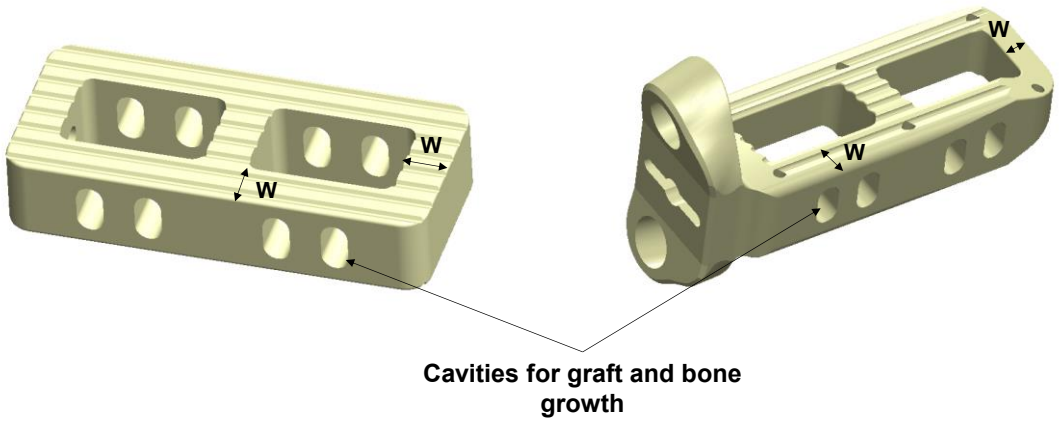

Figure 5.1: Generic PEEK XLIF cage design by NuVasive, with lateral screw wings (right) and standalone (left), depicting the regions for graft placement and bone growth.

Precision manufacturing is required to fabricate the load-sensing cage with the required fit for the sensors and PCB. The two most common materials for lumbar fusion cages are PEEK and titanium [314, 315]. PEEK is chosen due to its availability, cost, and electrically insulative properties [316]. There is a risk that titanium may interfere with sensor measurements or wireless power transmission in future iterations due to its conductivity. The small titanium pins used for gripping the endplates may interfere to a lesser extent. For industrial applications, PEEK implants are currently manufactured using injection moulding or machining processes from bulk PEEK [71], however injection moulding is not suitable for prototyping due to the significant resource

requirements. While additive manufacturing is a rapidly progressing field, the high temperatures required for printing PEEK pose challenges to precision manufacturing implants to the required resolution. CNC milling is the most viable manufacturing method. The load-sensing implant is designed with consideration of this manufacturing requirement.

5.4 Fabrication of a Load-Sensing Interbody Cage

5.4.1 Sensors and PCB Design

Following an extensive market search of the available pressure, strain, and force sensors, the Amphenol (Novasensor, USA) P122 High Silicon Pressure Sensor Die was selected for integration with the interbody cage due to its piezoresistive operating principle, embeddable size (2.5 x 2.5 x 2.0mm), regular shape, and suitable pressure limit. Many other sensor options did not simultaneously meet the criteria for size or shape, such that they may be implantable, and meet the required loading parameters (e.g., Omron 2SMPB-02E, Murata SCB10H-B012FB) (Figure 5.2). Film-based sensors (e.g., Tekscan, K-Scan) did not have suitable load limits, though their spatial resolution was high. Other load-transducers had irregular geometries (e.g., TE MS5637-30BA) that prevented their enclosure in the implant. The sensors were embedded at 7 locations in the interbody cage (Figure 5.3). Data was extracted from 5 sensors, as shown in Figure 5.3, which did not adversely impact the results or depth of the conclusions given the symmetry of the design.

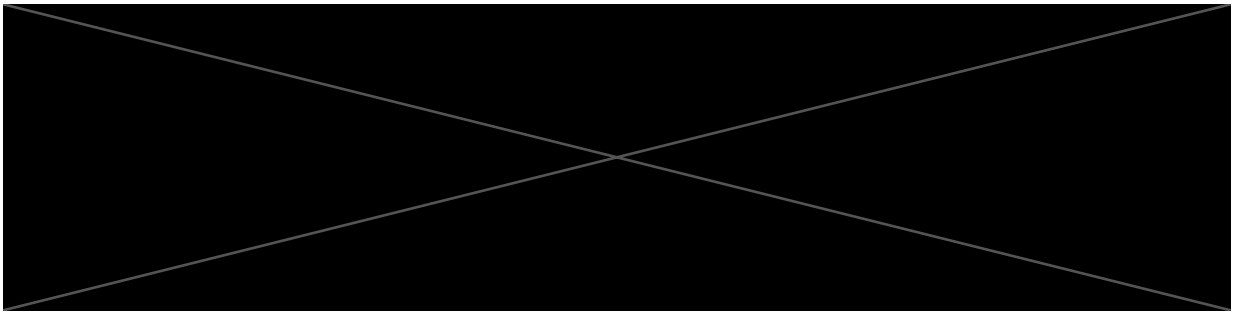

Figure 5.2: Irregular Omron (left) and Murata (right) sensor geometries.

Two PCBs were designed to control data transfer from the sensors and allow them to be embedded into the interbody cage. PCB-A was a small PCB (thickness = 0.41mm) onto which the sensors were bonded using flip-chip bonding. The addition of PCB-A allowed for sensors to be more readily removed and replaced if they were damaged or as process

development continued for the flip-chip bonding parameters. PCB-B was a large PCB (thickness = 1.16mm) that largely followed the footprint of the interbody cage with an extruded edge that held connections for data transfer and processing. PCB-A was hand-soldered to PCB-B at the 7 required locations.

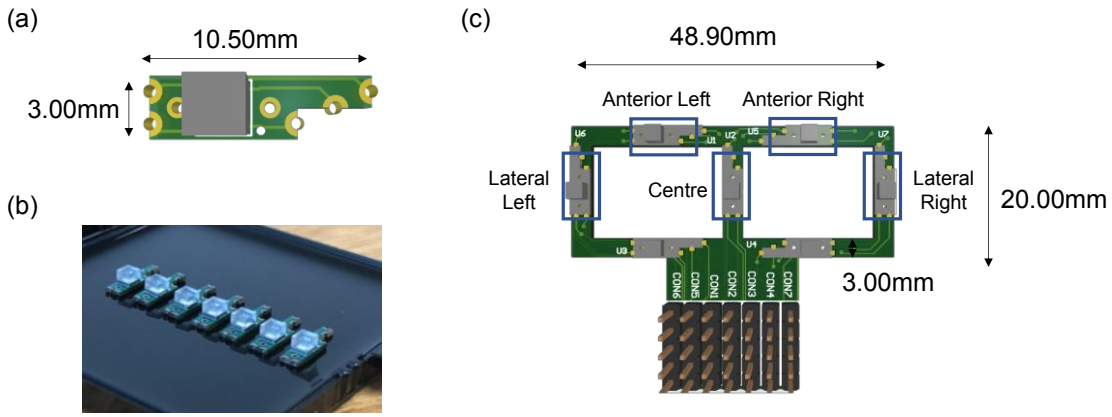

Figure 5.3: PCB-A (a, b) was designed to simplify the bonding and replacement process for damaged sensors. PCB-B was designed according to the footprint of the interbody cage. Data was extracted from the Lateral Left (Lat Left), Anterior Left (Ant Left), Centre, Anterior Right (Ant Right), and Lateral Right (Lat Right) sensors (c).

Each sensor requires 5 pins, as shown in Figure 5.4. The sensor requires a minimum 1mA excitation and a maximum 10V operating voltage. The differential voltage is the signal output for measuring pressure. As such, for each of the 7 channels (one channel per sensor), 5 pins were included in the extruded PCB connector on PCB-B shown in Figure 5.6c-d. Pins were subsequently combined to provide a shared voltage supply and ground by connecting pins with copper or solder on the underside of PCB-B, reducing the number of required wired connections (Figure 5.5).

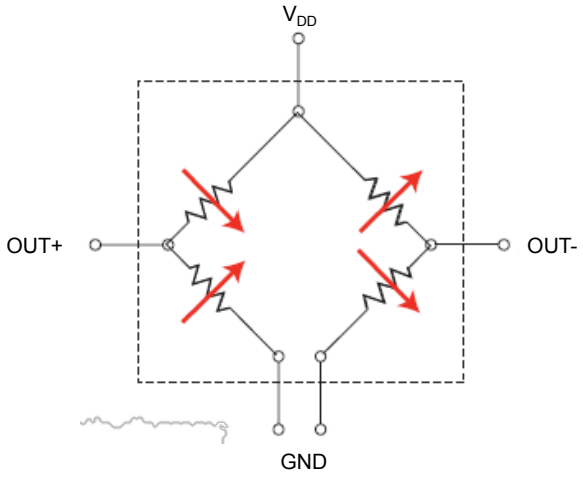

Figure 5.4: P122 sensor schematic showing the input voltage (V_{DD}), differential voltage outputs (OUT-, OUT+) and ground (GND) terminals. Nominal resistance = 5kΩ.

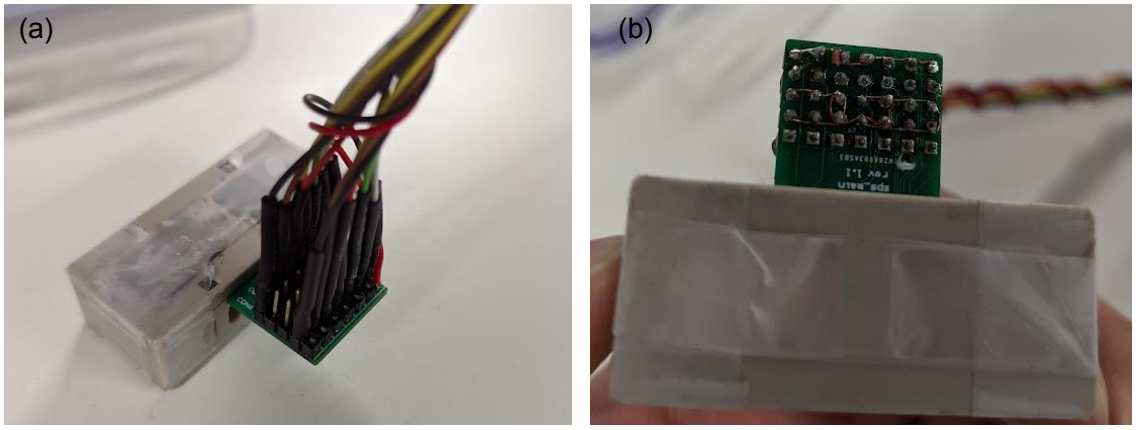

Figure 5.5: Connections for data collection (a) were wired from the PCB extrusion. Voltage supply and ground pins were connected with copper or solder (1st, 3rd, and 4th row of connections from the top) on the underside of the PCB (b).

5.4.2 Flip-Chip Bonding

The pressure sensing dies were bonded to PCB-A using a flip-chip bonding process. Gold bumps were bonded to the 5 PCB attachment pads using the TPT HB100 Wire Bonder and 25µm gold wires at 150°C (100mW, 200ms, 250mN). A Finetech Fineplacer Lambda Die Bonder was used to apply thermocompression bonding, with a force of 4N for 60 seconds at 320°C, to attach the pressure sensor die to PCB-A.

EpoTek 301-2 epoxy was applied as an underfill between the die and PCB-A. The samples were desiccated in a vacuum for 20 minutes before curing at 80°C for 3 hours.

The integrity of the bonding and underfill process was verified by applying 40N of direct compressive force (0.6mm/min) to 5 bonded sensors with the Instron 3369 Universal Testing Machine. The applied force did not induce any electrical or mechanical continuity failures in the 5 samples. As such, PCB-A was hand-soldered to PCB-B at the required locations.

Continuity was tested with static loads, which represented the final loading scenario for this proof-of-concept study. Dynamic, creep, and fatigue loading would elicit deeper insights into the durability of the bond, however this was not the aim of the present work.

5.4.3 Interbody Cage Design and Manufacturing

The load-sensing interbody cage was developed by modifying existing XLIF cage designs (Coroent XL, NuVasive). XLIF cages are currently used in clinical practice. The XLIF approach generally affords a larger footprint for XLIF cages compared to posterior LIF (PLIF) or transforaminal LIF (TLIF) approaches. This larger implant design provided the necessary space required to prototype the integration of sensors and PCBs.

XLIF cages produced by NuVasive have dimensions ranging from 18-22mm in the anterior-posterior direction, 45-60mm in width, and 8-16mm in height [255, 256]. The load-sensing XLIF cage (22.0 x 50.0 x 14.5mm, 0° lordosis) (Figure 5.6) was manufactured using CNC milling from PEEK material supplied by Dotmar Engineering Plastics (NSW, Australia). The cage was designed with 0° lordosis to simplify the loading setup, sensor integration, and results interpretation.

Cavities were designed for the for graft (17.3 x 11.0mm) in addition to cuts through the vertical faces of the cage that allow for bone growth in commercially available XLIF fusion implants. Grooves were machined in the cage to fit the sensor-bonded PCB (Figure 5.6b-d).

Room-temperature vulcanising silicone was applied with a syringe to the sensor tops (0.5mm) and levelled with the cage surface. Upon curing, the silicone acted as a protective layer on the sensor against stiff contacting surfaces and ensured load transfer to each sensor.

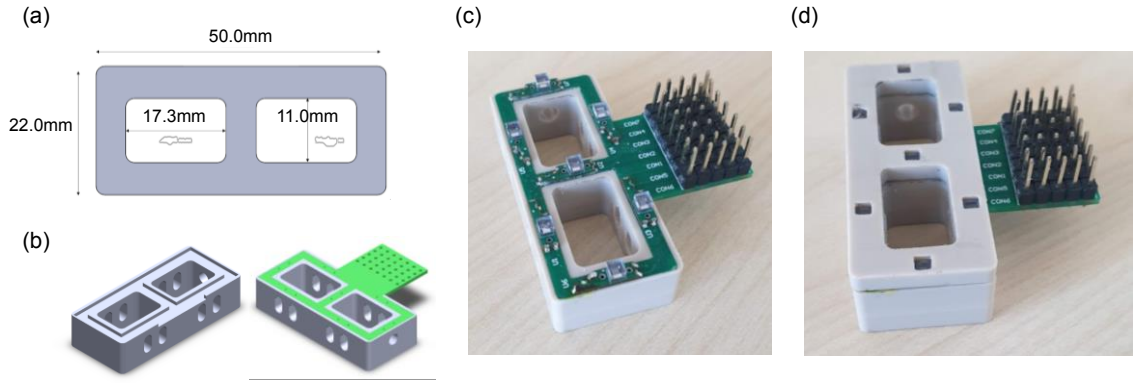

Figure 5.6: Top-view dimensions of the interbody cage (a), 14.5mm tall. The cage was manufactured to fit the designed PCB layout and sensors (b-d).

5.4.4 Data Collection Module v1.0

The first prototype designed for data collection included the following additional components:

- ADC Differential Pi
  - 8 channel, 17 bit analogue to digital converter (ADC). The ADC Pi contains two Microchip (Arizona, USA) MCP3424 ADCs, each with 4 analogue inputs. The MCP3424 is a delta-sigma ADC with low noise differential inputs.
- Raspberry Pi 4
  - 5V USB-C power supplied board with USB-A connectivity for data transfer from the Raspberry Pi (Cambridge, UK). The board contains a 40 pin GPIO header, 4GB of RAM, and a Broadcom BCM2711, Quad-core Cortex-A72 processor.
- Pre-loaded Micro-SD Card
  - The Raspberry Pi 4 comes with a pre-loaded Micro-SD card for an operating system and data storage.

The design prioritised resource-efficient data collection over miniaturisation or minimalistic design. The aims of this system were to process and store data from all the sensors embedded within the cage. In doing so, affordable hardware components were used in this module, such as the Raspberry Pi, which were simple to program and reduced the complexity in efficiently testing the load-sensing cage. Figure 5.7 demonstrates the connection between hardware (green) and software (orange)

components used to extract data from the load-sensing cage. The size and obtrusiveness of the electronics were not considered in the first prototype, but rather were improved and refined thereafter.

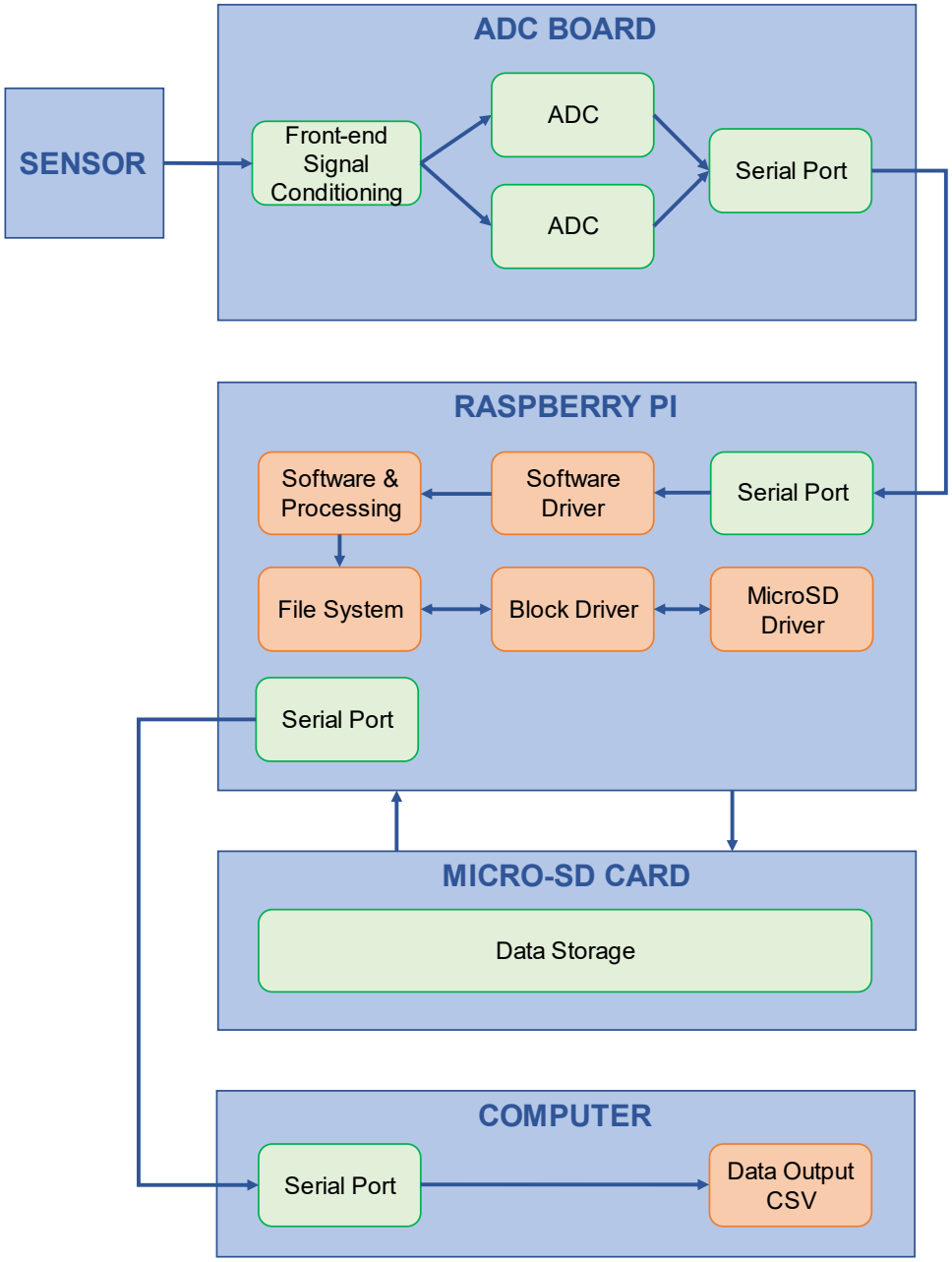

Figure 5.7: Block diagram for v1.0 data collection setup.

Sensor data is received by a front-end signal conditioning module on the ADC board. The voltage differential is received by the two ADC chip components and sent to the Raspberry Pi via Serial Peripheral Interface (SPI). The software driver allows the Python code to act on the received ADC values. Similarly, file system, block driver, and Micro-

SD driver software components represent two-way processes that facilitate communication and data transfer. The file system allows the Python code to access the local file system on the computer file navigation, while the block driver ensures access to the computer memory. The Micro-SD driver allows data to be stored on the Micro-SD card, connected via SPI to the Raspberry Pi.

The Raspberry Pi was externally powered via mains connection. Command-line prompted Python code commenced data collection from the sensors. While running, data collected from the sensors was stored on the MicroSD card and periodically transferred via USB connection to the computer. Python code handled the incoming data, storing it as a time-stamped CSV file only once the command-line process was exited.

The system for data collection from the sensor-bonded PCB presents numerous challenges to actualisation *in vivo* in addition to challenges in the *in vitro* context. The system was successfully implemented for sensor calibration (see 5.4.6 Sensor Calibration), however heavy reliance on hardware components highlighted several limitations and potential points for improvement that may progress the design towards the *in vivo* use-case.

The Raspberry Pi microcontroller has a considerable supply requirement (5V). Reducing the power consumption of the microcontroller was a key aim to improve usability, such that future designs can leverage wireless power transmission and avoid implantable batteries for safety reasons. Similarly, size reduction of the microcontroller was another key aim for the next iteration of the communication module. The first iteration (v1.0) of the data collection system consisted of 3 main hardware components: the ADC board, Raspberry Pi microcontroller, and Micro-SD card. Over-reliance on hardware increases the likelihood of failure through physical SPI links between components, reduces the efficiency of the system, and increases the size. Further, when fixing the load-sensing cage within the universal testing machine, considering only *in vitro* usage, there were difficulties associated with isolating hardware, wires, and connections to prevent damage from loading and displacement of the data collection module. Lastly, the module described in v1.0 prevents the real-time storage and presentation of the sensor measurements. Real-time data plotting would improve the clinical utility of the device.

With the presented limitations with v1.0, it was pertinent to re-design the communication module with the aim of reducing the power consumption of the microcontroller, facilitating real-time data presentation, and converting hardware processes to software processes to reduce the size of the system and improve its durability. Given the sensors only require a minimum 1mA excitation, the power consumption constraint of the microcontroller was prioritised in the context of wireless communication and power methods that may be used in the following iteration of the communication module. The component with the highest power consumption was the Raspberry Pi 4, therefore the module was re-designed to replace this microcontroller with a low-power alternative. Wireless power transfer through magnetic induction and NFC, for example, can reach up to 10mW [317]. Power consumption should be reduced within this maximum power transfer limit and to a level that is as low as practically achievable.

5.4.5 Data Collection Module v2.0

Hardware components were reduced by choosing a smaller microcontroller that consumes less power and prioritising software processes over hardware. Processes previously performed by the Raspberry Pi and Micro-SD were split between Python-coded software and a 32 pin EFM8BB52 microcontroller (Silicon Labs, Texas, USA).

The chosen microcontroller has dimensions of 5.0 x 5.0 x 0.8mm, representing a considerable size reduction compared to the Raspberry Pi and Micro-SD configuration. The microcontroller requires a minimum 1.8V supply and contains a 12-bit, 16-channel ADC, replacing the two 4-channel ADCs in v1.0. The low power consumption of the microcontroller allows it to be powered via the serial port connection to the computer.

The conversion of hardware processes (green) to software processes (orange) is evident in Figure 5.8. Sensor data is received by the microcontroller at the analogue front-end. The voltage signal is passed to the sample and hold (S/H) circuit, which samples the analogue signal and locks its value for a set interval. The ADC converts the locked analogue value to a digital ADC number from 0 to 4096. The ADC values are transmitted via serial port to the computer. The software manager collects the ADC values from the port and converts the values back to a voltage signal. The Python software processes the

data and performs the differential calculation. The data enters a temporary store from where it is plotted real-time and stored in a CSV file.

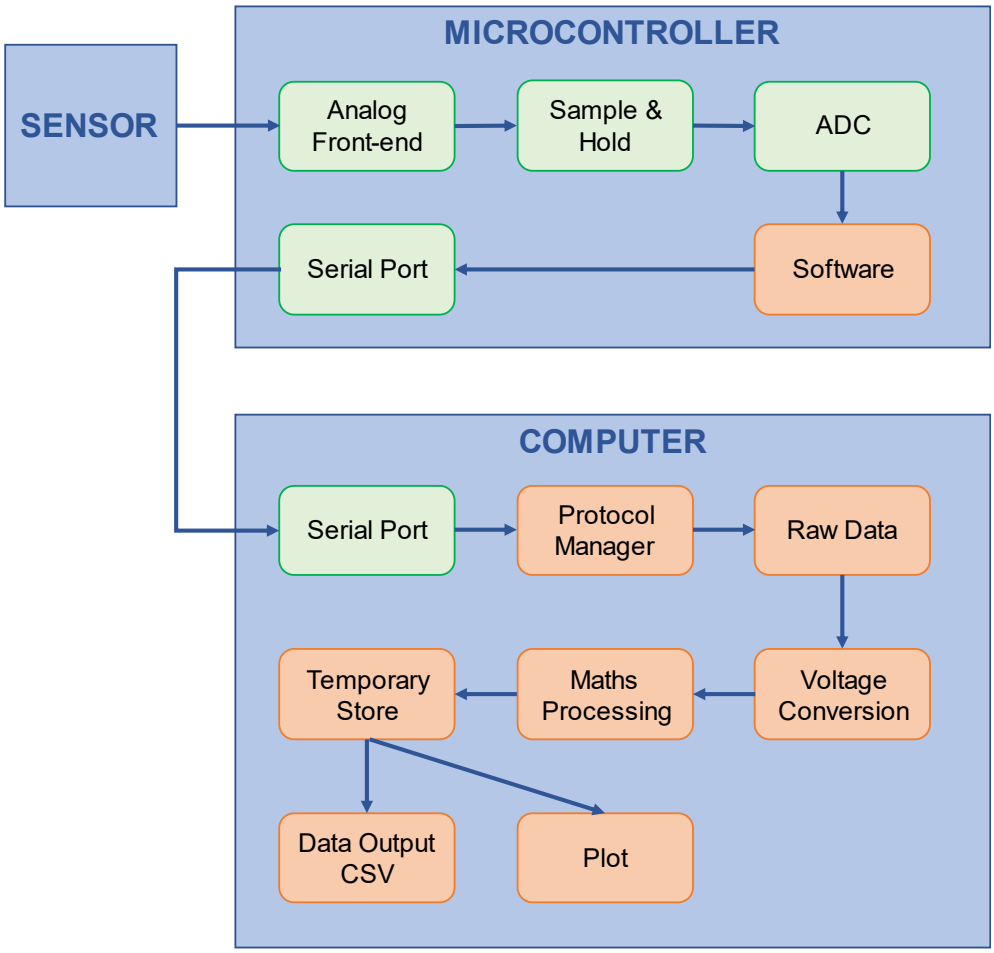

Figure 5.8: Block diagram for v2.0 data collection setup.

v2.0 reduced the size of the module, improved connectivity, and provided real-time data visualisation as shown in Figure 5.9. The v1.0 Raspberry Pi covered an area of 85.6 x 56.5mm, however the v2.0 microcontroller covers an area of 5.0 x 5.0mm. Further, the system now requires a single USB connection for power and data transfer, however the v1.0 system required external power, USB, and SPI links. Lastly, the operating requirements of the combined sensing and communication (v2.0) modules are within the capacity of wireless power transfer technologies, simplifying the development process for the wireless communication module.

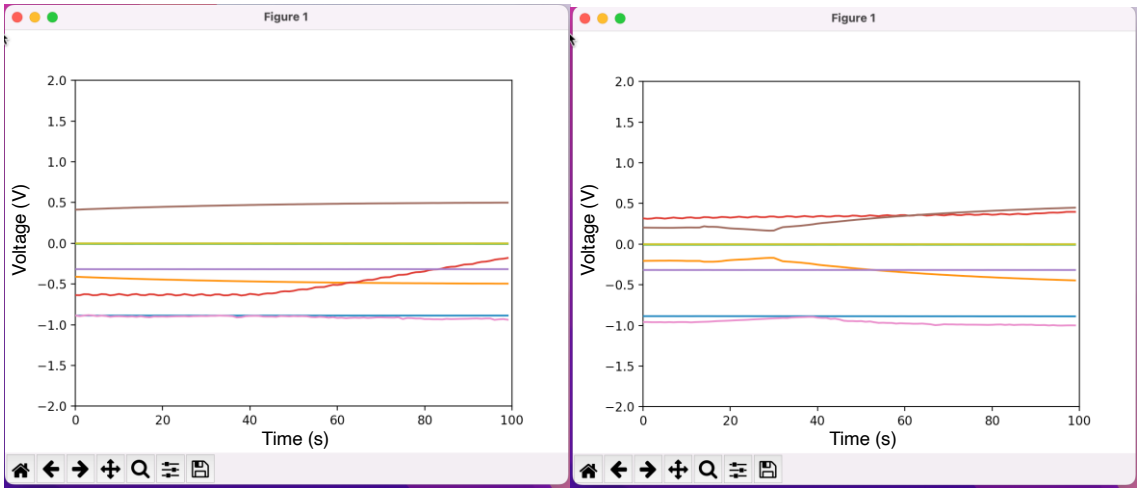

Figure 5.9: Real-time data plotting showing fluctuations in sensor measurements.

5.4.6 Sensor Calibration

Sensor calibration was performed by applying load directly to each sensor individually, using a cylindrical attachment covering the surface of only one sensor at a time, and recording the output with the v1.0 data collection module. Compressive load was applied using an ESM-Mark10 Motorised Test Stand up to 25N at 0.5mm/min. Given the sensing area of 2.5 x 2.5mm, the equivalent applied pressure on each sensor was 4MPa. The applied load was within the overpressure limit specified on the sensor datasheet. The ADC output was recorded and calibrated against the known applied pressure, such that for each change in ADC output, a change in pressure could be calculated from the calibration curve. A calibration curve was produced for each of the 5 operating sensors (Figure 5.10 - Figure 5.14). The anterior left sensor underwent higher loading than expected, likely due to manufacturing inconsistencies in the cage or PCB resulting in uneven loading. As such, this sensor was recalibrated to a higher pressure limit.

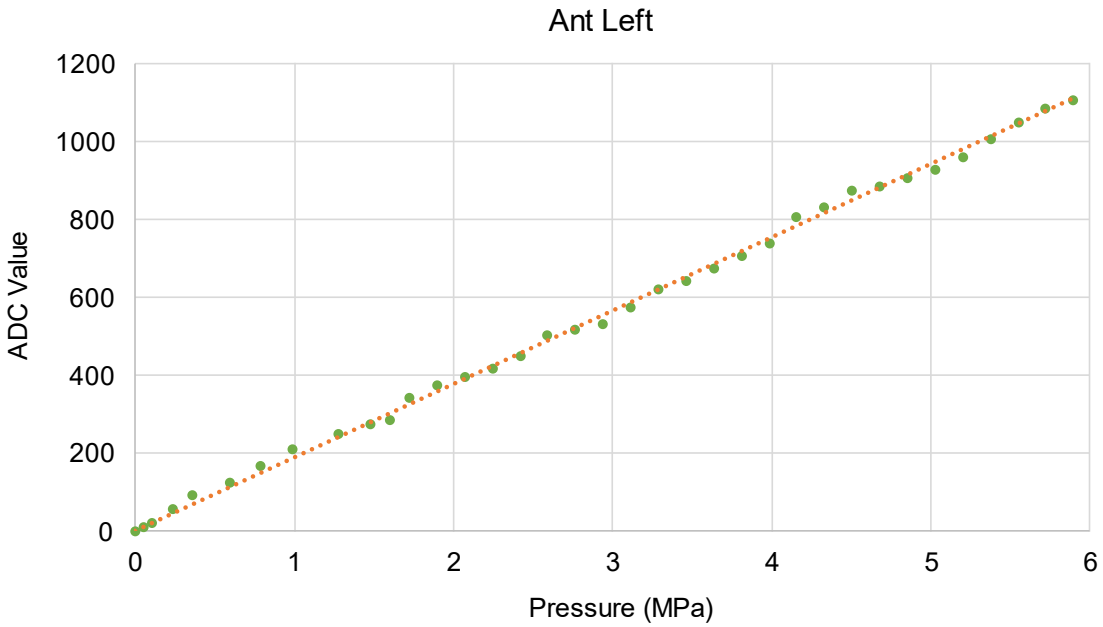

Figure 5.10: Calibration curve for anterior left sensor. This sensor was re-calibrated to a higher load, as it recorded higher pressures compared to other sensors.

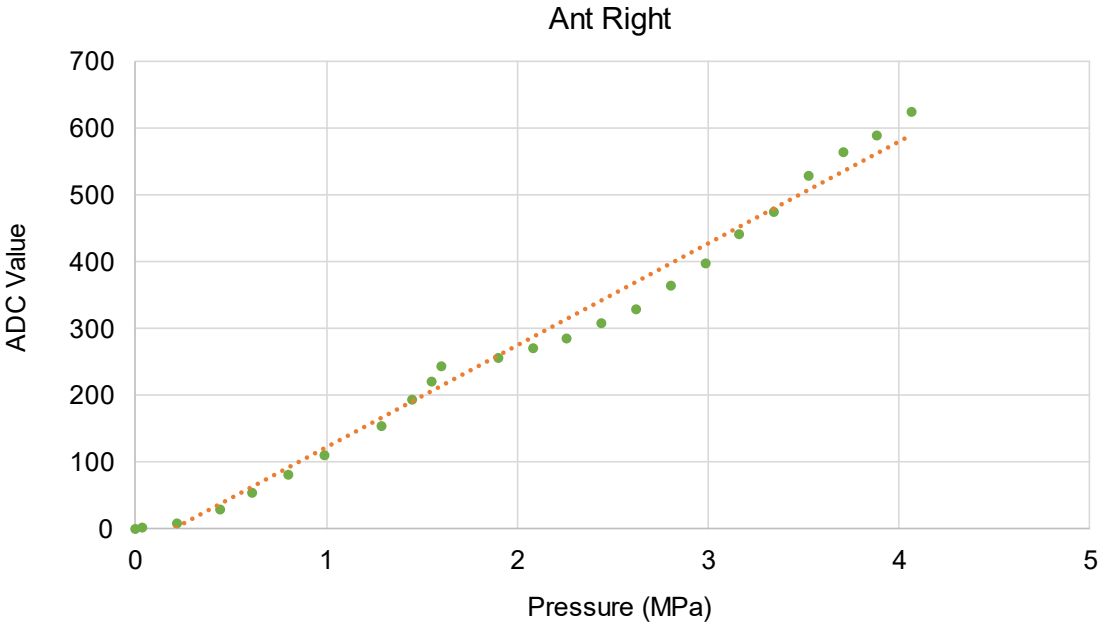

Figure 5.11: Calibration curve for the anterior right sensor.

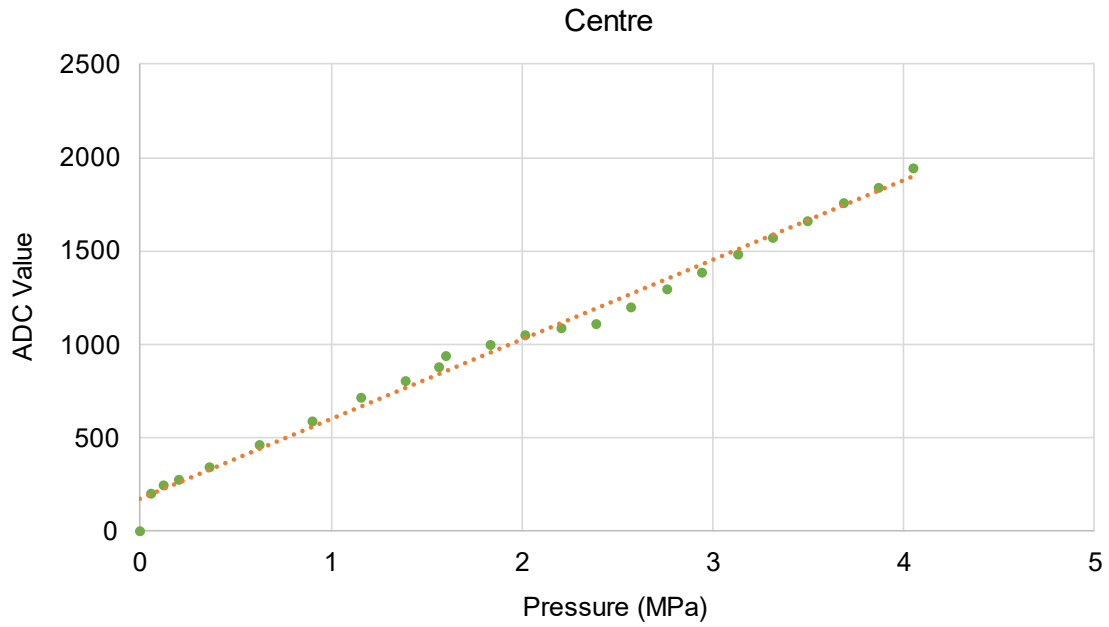

Figure 5.12: Calibration curve for the centre sensor.

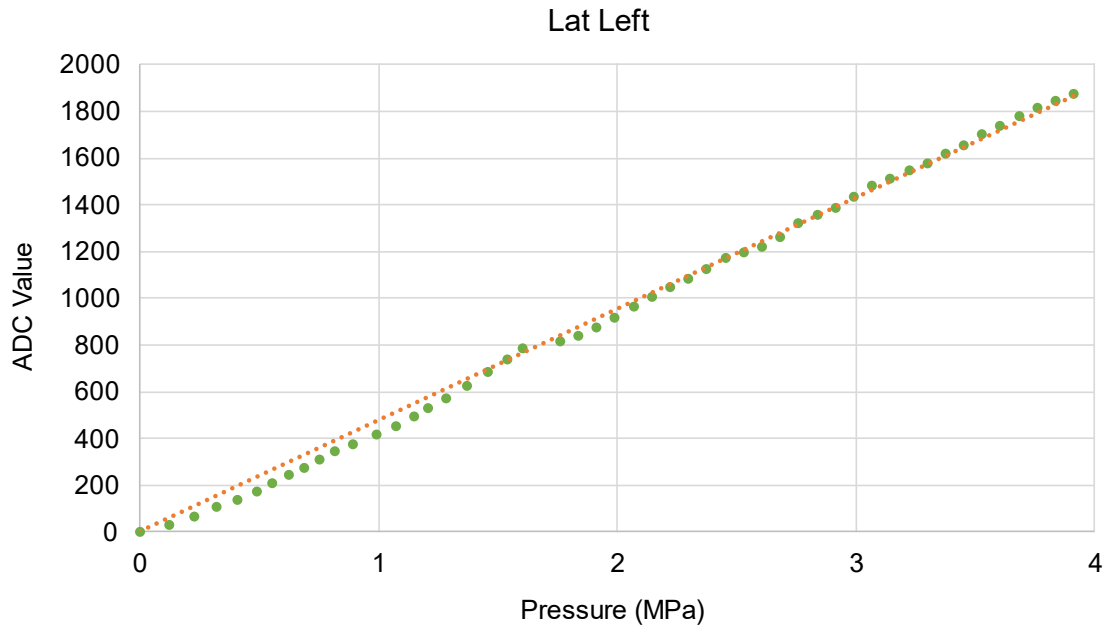

Figure 5.13: Calibration curve for the lateral left sensor.

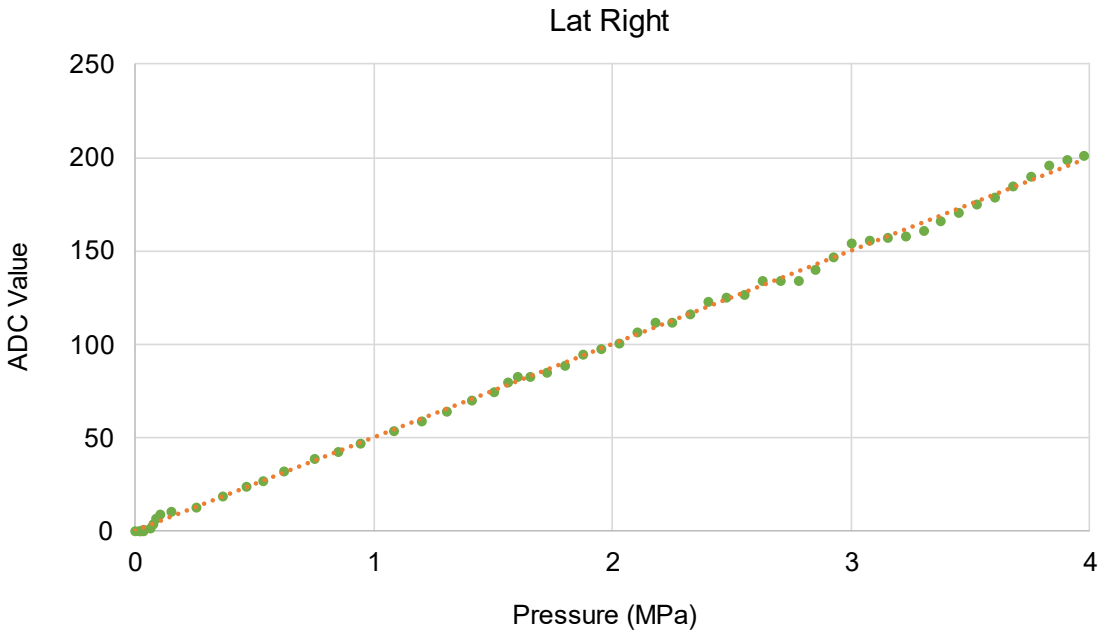

Figure 5.14: Calibration curve for the lateral right sensor.

The Anterior Left, Lateral Left, and Lateral Right sensors demonstrated a consistent linear response to the applied load. The Centre and Anterior Right sensors showed some nonlinear characteristics at low loads. Given the pressure measurement range of interest, generally above 1MPa, the nonlinearity at low loads is not likely to affect the interpretation of experimental results. Minor inconsistencies and nonlinearities can arise from nonlinear material behaviour of the PCB, bonding to the PCB or other electrical inconsistencies, or stress on the underfill between the sensor and PCB. Future studies should be performed to determine the source of the nonlinearity and potential improvements to the sensor bonding process. The findings therefrom can be used to optimise the design of the sensor-board configuration.

5.5 Graft Materials

Two points of bone fusion were simulated in the *in vitro* setup: early fusion and solid fusion. Depending on the type of graft used, the histological characterisation of the early fusion stage may be different, though inclusive of endochondral, fibro-cartilaginous, or membranous histological stages, or a combination of these stages, which are mechanically non-solid. As such, silicone rubber was inserted in the graft regions to represent early fusion. Poly(methyl methacrylate) (PMMA) was used to represent late-

stage ossification of the bony fusion mass (solid fusion), however may also represent the use of a solid bone graft.

Moulds were 3D-printed to the dimensions of the graft cavities in the interbody cage. The moulds were filled with a non-commercial room-temperature vulcanising silicone in a flowable state and cured for 30 minutes prior to de-moulding. Similarly, clinical-grade Palacos bone cement (PMMA) (Heraeus Medical, Germany) was prepared according to the manufacturer's instructions. During its application phase, the mixture was inserted into the moulds and cured for at least 7 minutes prior to de-moulding, ensuring the cement was solid and would not deform during the de-moulding process.

5.6 Experimental Setup

The load-sensing cage was placed between two pieces of synthetic bone (Sawbones, USA) that were cut to the average dimensions of lumbar vertebral bodies (50 x 35 x 30mm) (Figure 5.15) [318]. Sawbones biomechanical materials are manufactured to mimic the mechanical properties of human bone. The synthetic vertebrae consisted of a 2mm thick layer of cortical bone and 28mm of cancellous bone. All loads were applied with the Instron 3369 (1kN load cell) to 900N at 0.6mm/min for 3 trials. Sensor output was recorded during the load tests to measure pressure in response to changes in graft stiffness with different contacting bone stiffnesses and load types.

5.6.1 Distributed Load

A 3mm thick aluminium plate was placed on the superior surface of the upper synthetic vertebral body to ensure even distribution of the applied load. The distributed load was applied with the cancellous bone contacting the cage surface (cancellous contact). The load tests were completed with silicone (early fusion) and PMMA (solid fusion) graft materials.

The vertebral body was then inverted such that the cortical bone was contacting the interbody cage surface (cortical contact) and the distributed load tests were repeated with both grafts.

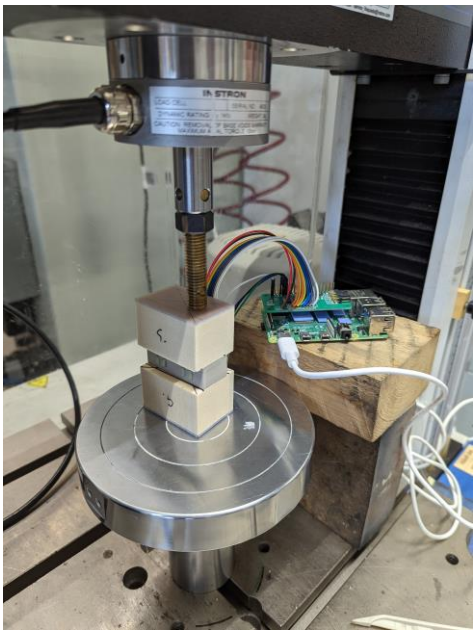

Figure 5.15: Experimental setup showing the interbody cage placed between the synthetic vertebrae (cancellous contact) under eccentric load from the Instron 3369.

5.6.2 Eccentric Loads

Eccentric loads were applied with cancellous contact only. Loads were applied at 4 locations around the cage centre (without the aluminium plate) as indicated in Figure 5.16. The loads were applied with a 5mm diameter cylindrical attachment.

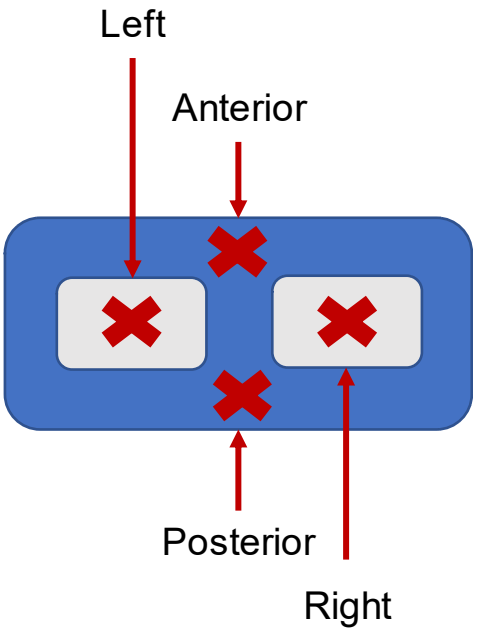

Figure 5.16: Top view of interbody cage depicting the points of eccentric load application.

5.7 Finite Element Analysis

A 3D finite element (FE) model was developed in Strand7 (vers. 2.4.6, Strand7 Pty. Ltd, Australia) commercial software as a validation tool for the sensor outputs and to determine an indicative predicted shift in expected pressure as a result of changing the graft and endplate material. The model was developed to replicate the experimental setup. A half-symmetry model geometry was built in Strand7, reducing the computational time and allowing for a finer mesh (Figure 5.17, Figure 5.18). 2D plate elements were subdivided to increase the mesh density and extruded to create the 3D geometry of the implant and graft. Graft cavities were created to replicate the manufactured interbody cage. Subsequently, the adjacent synthetic cancellous and cortical bone structures were modelled with bonded contact to the cage and graft surface. The PCBs, sensors, and graft were modelled by grouping the respective regions and assigning suitable material properties (Table 5.1). The model consisted of 501,358 bricks and 508,024 nodes, mostly consisting of 0.5 x 0.5 x 0.5mm brick elements where straight edges were achievable in the model geometry. The cross-sectional plane was constrained by a symmetric boundary, preventing out-of-plane translations and rotations. The nodes on the bottom surface were constrained in all translational and rotational degrees of freedom. The model was loaded in compression from the top surface with an evenly distributed pressure equivalent to 450N.

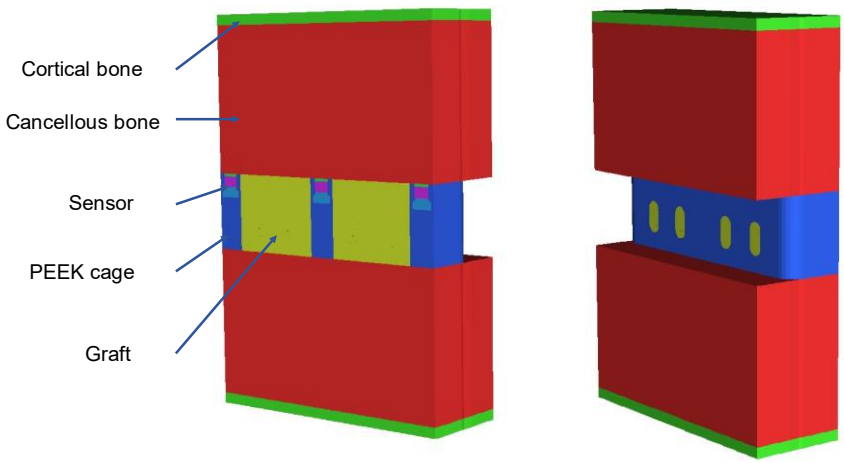

Figure 5.17: Half-symmetry FE model developed to mimic the experimental setup shown with cancellous contact. The face shown in the left image was constrained with a symmetric boundary.

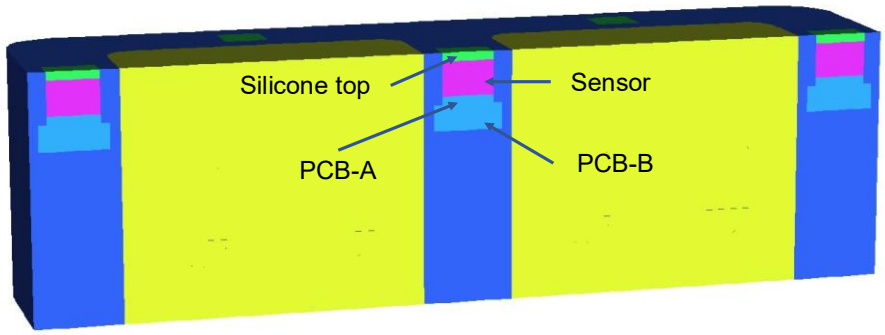

Figure 5.18: FE model showing the interbody cage and sensors embedded with both PCBs and silicone tops. The sensors were modelled as a volume of silicon (2.5 x 2.5 x 2.0mm)

Table 5.1: Material properties used in the FE model.

Material	**Material Model**	**Properties** E: Elastic Modulus (MPa) G: Shear Modulus (MPa) K: Bulk Modulus (MPa) v: Poisson's Ratio C: Neo-Hookean Constant
PEEK Manufacturer supplied (Dotmar Engineering Plastics)	Isotropic	E = 3750 v = 0.38
Sawbones Cancellous Manufacturer supplied (Sawbones)	Isotropic	$E_{Tension}$ = 284 $E_{Compression}$ = 210
Sawbones Cortical Manufacturer supplied (Sawbones)	Isotropic	$E_{Tension}$ = 16000 $E_{Compression}$ = 17000
FR4 PCB Wang et al. (2006) [319]	Orthotropic	$E_{xx} = E_{yy}$ = 22000, E_{zz} = 9800 $G_{xy} = G_{yz}$ = 3500, G_{xz} = 2500 $v_{xx} = v_{yy}$ = 0.28, v_{zz} = 0.11
Silicone Manufacturer supplied (Kunovus)	Neo-Hookean	C = 0.207 K = 20.7MPa
PMMA Dall et al. (2007) [261] Manufacturer Supplied (Heraeus Medical)	Isotropic	E = 2795 v = 0.375
Silicon Die Hopcroft et al. (2010) [320]	Isotropic	E = 130000 v = 0.28

5.8 Results

Three trials were conducted for each experimental loading scenario with averages reported in the results below.

5.8.1 Distributed Loads

Sensor-recorded measurements showed a reduction in pressure at all locations in the solid fusion state compared to early fusion with cancellous contact (Figure 5.19). Under the maximum 900N load, there was a 58% and 56% reduction in pressure in the anterior left and right sensors respectively. Pressure on the centre sensor reduced by 45%, while lateral left and right sensors reduced by 36% and 37% respectively.

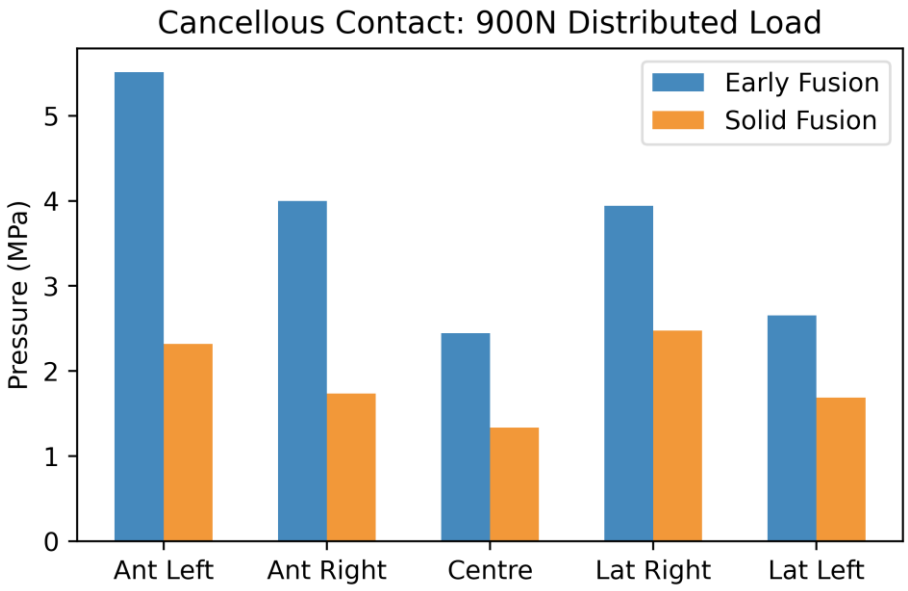

Figure 5.19: Sensor-recorded pressure (MPa) at early fusion and solid fusion under a 900N distributed load with cancellous contact.

Similarly with cortical contact, pressure measured in the interbody cage was lower with solid fusion compared to early fusion under a 900N distributed load (Figure 5.20). The anterior left and right pressures reduced by 56% and 60% respectively, however the centre sensor recorded a 71% reduction in stress with solid fusion. Pressure recorded at the lateral locations reduced by 63% (right) and 51% (left). Lateral and centre sensors demonstrated a larger reduction in stress with graft stiffness when the contacting bone was stiffer.

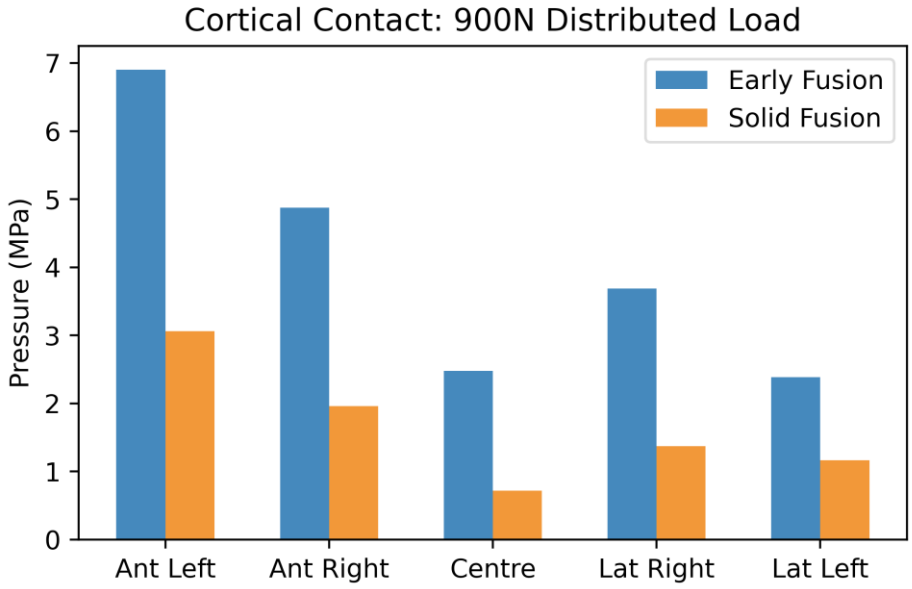

Figure 5.20: Sensor-recorded pressure (MPa) at early fusion and solid fusion under a 900N distributed load with cortical contact.

Comparing the two contact stiffnesses at the points of early fusion and solid fusion provides a clear indication of the regional pressure variation that is occurring (Figure 5.21). At early fusion, the anterior left and right locations experienced higher pressure (Ant Left = 25%, Ant Right = 21%) with the stiffer cortical bone compared to cancellous. This pattern was consistent at solid fusion (Ant Left = 32%, Ant Right = 13%). In the lateral regions, however, the opposite trend was observed, with pressure reducing under the stiffer cortical endplate (Early Fusion: Lat Left = -10%, Lat Right = -6%; Solid Fusion: Lat Left = -31%, Lat Right = -44%). Increasing stiffness of the endplate increased the stress on the anterior of the cage and reduced the stress at the lateral regions. No considerable difference was measured at the centre sensor with the soft (silicone) graft. At solid fusion, however, pressure was 46% lower at the centre location with cortical contacting bone compared to cancellous.

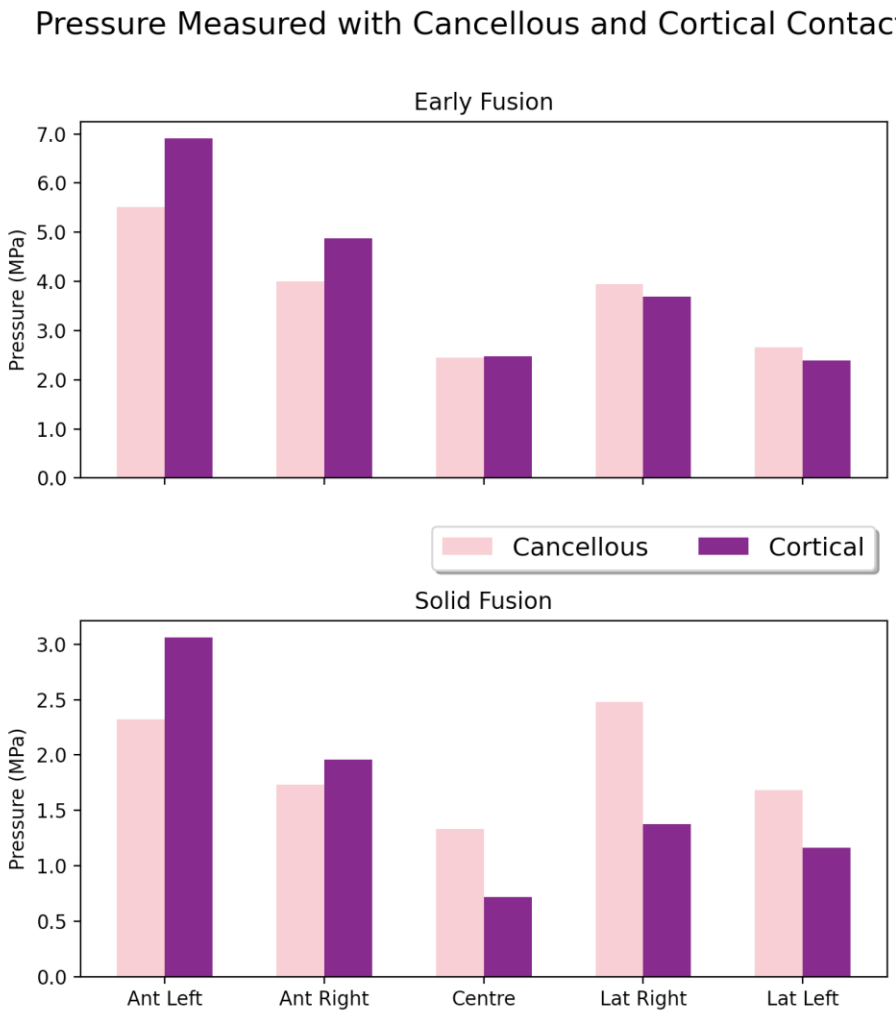

Figure 5.21: Sensor-recorded pressure (MPa) under a 900N distributed load demonstrating the influence of endplate stiffness on implant stress in different regions.

On the load path from 0N to 900N, there were no noteworthy trends in the pressure differential between the early fusion and solid fusion states (Figure 5.22, Figure 5.23). With both cancellous and cortical contact, there was a consistent difference between the pressures measured with silicone and PMMA grafts. Across the loads, the two states remain distinguishable by sensor-recorded pressure.

In the early fusion state, the highest absolute pressure was measured at the anterior left sensor (Cancellous = 5.51MPa; Cortical = 6.91MPa). With solid graft, the lateral right sensor recorded the highest pressure with cancellous contact (2.48MPa); the anterior left sensor measured the highest with cortical contact (3.06MPa). The lowest pressures were measured at the centre location in the solid fusion state (Cancellous = 1.33MPa;

Cortical = 0.72MPa). At early fusion, the centre pressure was lowest with cancellous contact (2.45MPa), while the lateral left was lowest with cortical contact (2.39MPa).

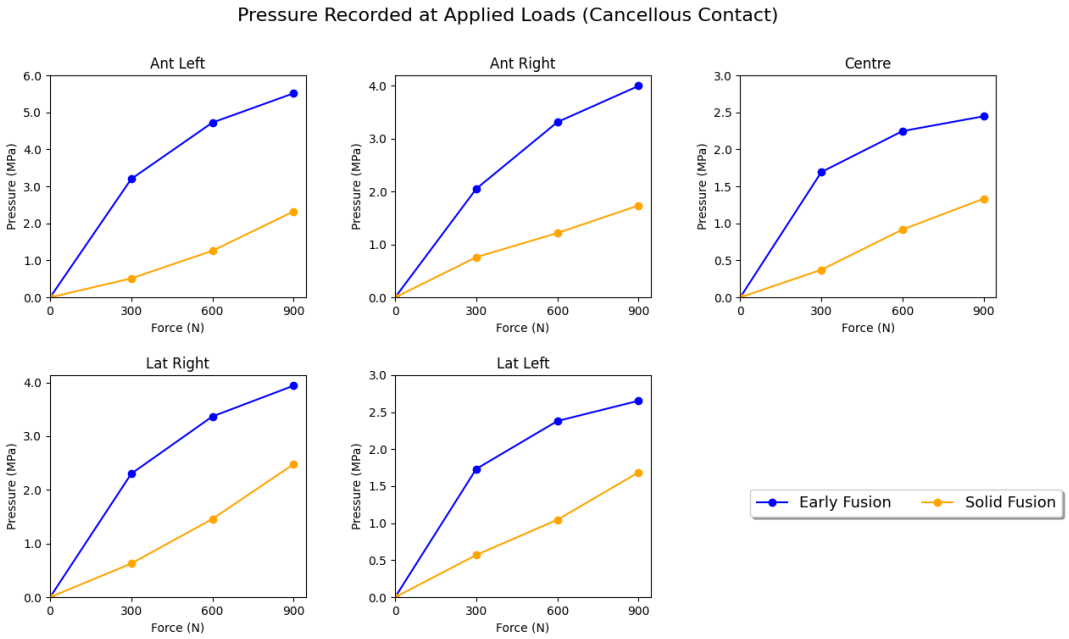

Figure 5.22: Pressures measured along the load path from 0N to 900N with cancellous contact.

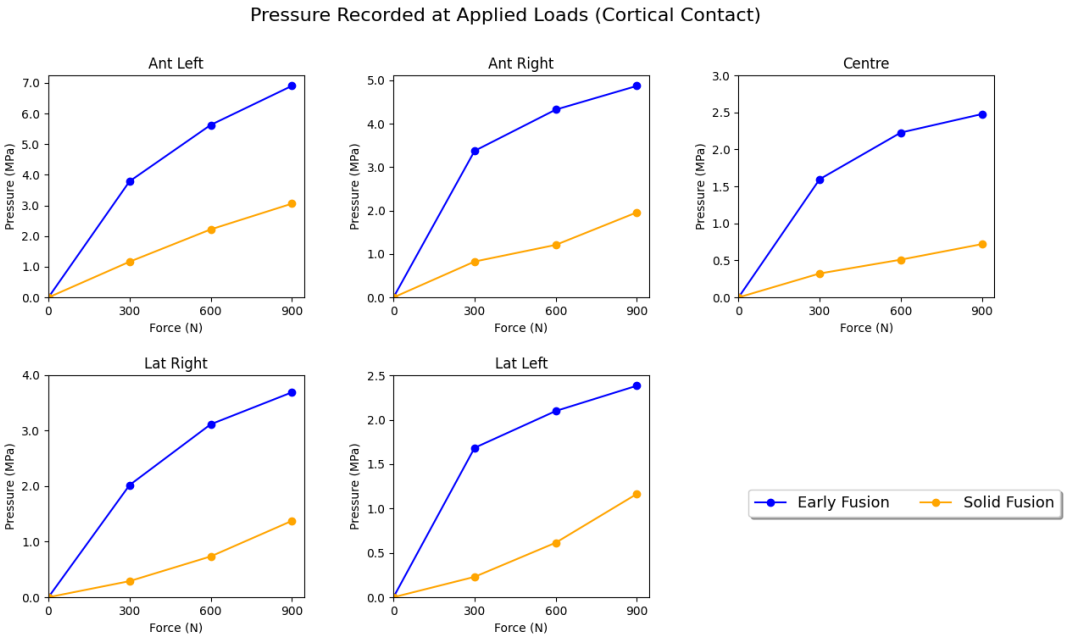

Figure 5.23: Pressures measured along the load path from 0N to 900N with cortical contact.

5.8.2 Comparison with Finite Element Analysis

Pressure measurements were extracted from the FE models as average and maximum compressive stresses in each sensor region (Figure 5.24). Experimentally obtained results were, for most measurements, within the range of the average and maximum values obtained from the FE analysis. The anterior left pressure was higher than the maximum obtained from simulation in the early fusion state (Cancellous = 4%; Cortical = 14%), while the lateral right sensor measured a 2% higher stress than the simulation maximum (cancellous contact). In the solid fusion state with cortical contact, the centre sensor measured 19% lower stress than the average obtained from simulation.

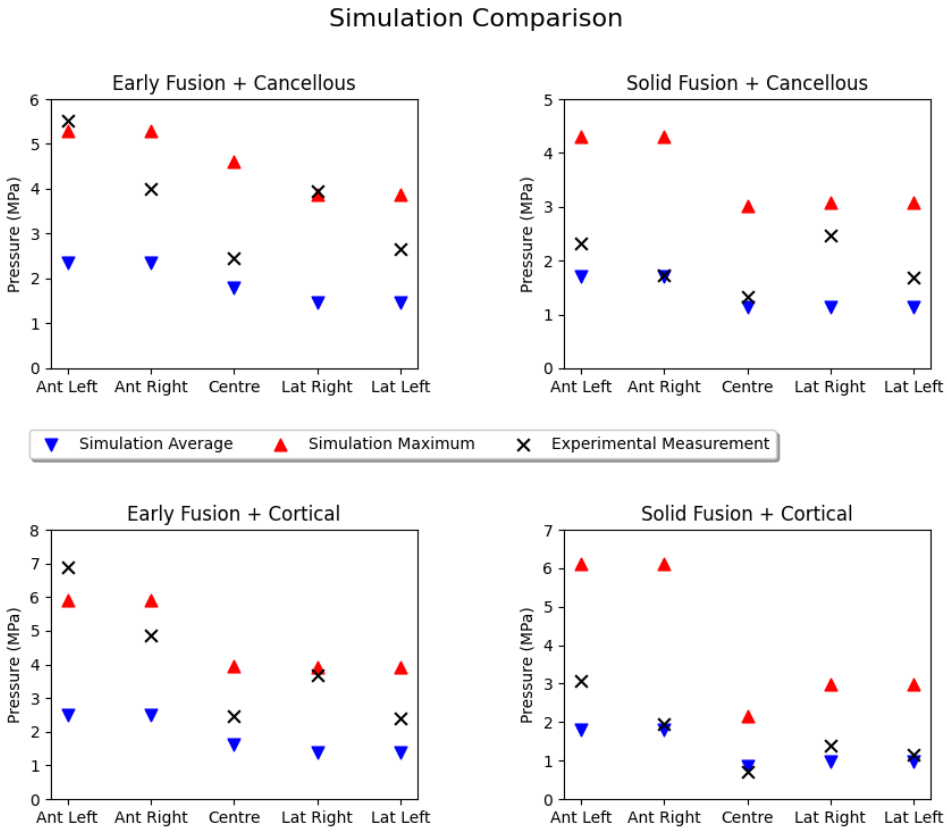

Figure 5.24: Comparison of simulation and experimental results. Average and maximum stress values were extracted from the sensor regions in the FE model.

The trends observed in the simulation were matched by experimental data in most cases (Table 5.2, Table 5.3). Some values were outside the range of the average to maximum stress values obtained from the simulation (Ant Left in early fusion; Centre in solid fusion with cortical contact; Lateral Right in early fusion with cancellous contact). The

FE analysis showed an increase in stress at the anterior sensors at early fusion with stiffer cortical contact compared to cancellous, however a decrease in pressure on the lateral and central sensors. Experimentally, the sensors measured increases in the anterior sensors, decreases in the lateral sensors, and no change at the centre. Similarly, at solid fusion with the change to cortical contact, the simulation showed increases in stress at the anterior sensor regions and decreases in all others, with experimental values aligning with this trend. There were, however, some notable discrepancies between the simulation and experimental values with regards to the magnitude of the changes.

Table 5.2: Percentage change in sensor-recorded pressure from cancellous to cortical bone contact in the early fusion state.

		Simulation Average (%)	Simulation Maximum (%)	Experimental Measurement (%)
Early Fusion	**Ant Left**	6	11	25
	Ant Right	6	11	22
	Centre	-9	-14	1
	Lat Right	-6	1	-6
	Lat Left	-6	1	-10

Table 5.3: Percentage change in sensor-recorded pressure from cancellous to cortical bone contact in the solid fusion state.

		Simulation Average (%)	Simulation Maximum (%)	Experimental Measurement (%)
Solid Fusion	**Ant Left**	5	42	32
	Ant Right	5	42	13
	Centre	-25	-29	-46
	Lat Right	-14	-3	-44
	Lat Left	-14	-3	-31

5.8.3 Eccentric Loads

The percentage change in sensor-recorded pressure between the eccentric load and distributed load is shown in Figure 5.25. Anterior loading resulted in an increase in stress in the anterior sensors and reduced stress in remaining sensors, with the exception of the lateral right sensor in the early fusion state. Similarly, posterior loading reduced stress in the anterior locations. Left eccentric loading increased stress in the lateral left

and anterior left locations while stress on all other sensors reduced. A similar pattern was found under right eccentric loading, with lateral right and anterior right stresses increasing and all others demonstrating reduced stress. The magnitude of change between each eccentric load and the distributed load was higher with solid fusion compared to early fusion. Absolute pressure values are presented in Table 5.4.

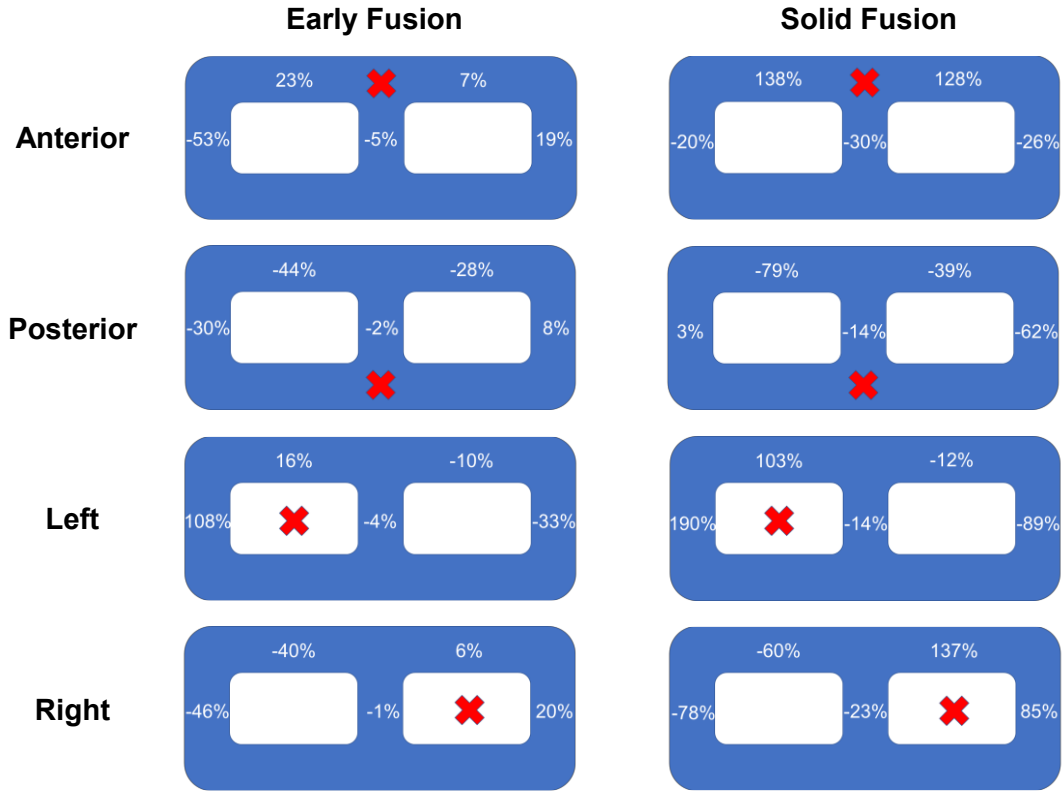

Figure 5.25: Top view of the interbody cage depicting the change in pressure at each location under each eccentric load compared to distributed load.

Table 5.4: Average sensor-recorded pressure measurements (MPa) across 3 trials under different eccentric loading conditions at early fusion (a) and solid fusion (b).

(a)		Eccentric Load Location			
		Left	**Right**	**Anterior**	**Posterior**
Early Fusion	**Ant Left**	6.38	3.31	6.79	3.08
	Ant Right	3.61	4.25	4.29	2.88
	Centre	2.35	2.43	2.33	2.40
	Lat Right	2.65	4.71	4.68	4.25
	Lat Left	5.52	1.44	1.26	1.87

(b)		Eccentric Load Location			
		Left	**Right**	**Anterior**	**Posterior**
Solid Fusion	**Ant Left**	4.70	0.94	5.53	0.49
	Ant Right	1.52	4.12	3.95	1.07
	Centre	1.15	1.03	0.94	1.15
	Lat Right	0.27	4.58	1.83	0.93
	Lat Left	4.90	0.37	1.35	1.74

5.9 Discussion

The aim of this work was to develop and test a proof-of-concept load-sensing interbody cage capable of detecting stiffness changes in the graft region evaluated with a distributed load, eccentric loads, and with different contacting bone stiffnesses.

The load-sensing cage was designed to extract data from multiple locations in the implant. As such, the PCB was designed to align with the cage footprint. Similarly, the communication module initially did not consider power and connectivity requirements. The module was re-designed to reduce the operating power of the system and the number of required connections, and display real-time data. In doing so, the future transition to wireless actualisation was simplified.

Sensor-enabled interbody cages have previously been used to assess loads *in vivo* (animal) and *in vitro* (cadaver), however the findings were not associated with fusion progression or endplate health [189, 190, 309]. The aim of these studies was to quantify the loads on the implant during different movements and activities, identifying those which increase the risk of mechanical failure [189, 190, 309].

5.9.1 Assessing Graft Stiffness Changes

Under a distributed load, the load-sensing cage described in this chapter demonstrated good differentiation between the early fusion and solid fusion states, simulated with silicone and PMMA material respectively. With cancellous contact, the reduction in sensor-recorded stress at solid fusion ranged from 36-58% depending on sensor location. The anterior regions of the cage were off-loaded more than the lateral regions of the cage with the stiffer graft material. This pattern was consistent with the simulation results. The FE analysis showed the largest off-loading of the cage in the central region, which was not supported by the experimental findings. With cortical contact, however, the largest off-loading was recorded at the central sensor (71%). In a clinical scenario,

however, it is the time-dependent change from baseline in the postoperative phase that is meaningful for clinicians.

In other orthopaedic prostheses, sensors have been used to monitor bone healing. Interbody fusion may be considered an exaggerated case of the same. Borchani et al. established the feasibility of piezo floating gate sensors for monitoring bone healing in a femoral fracture fixation plate, differentiating between different states of bone healing [307]. Similarly, the results of this load test demonstrate the measurable difference in fusion implant stress at the two endpoints of bone healing: early bone formation and solid fusion. Expanding the scope of this study may allow for the construction of bone-healing curves that account for more bone formation conditions and growth into the endplates. Alternatively, further improvements to sensor performance leading to better agreement with the simulation findings may allow FE analysis to be used as a tool to better understand the biomechanical implications of bone healing in LIF.

5.9.2 Assessing Endplate Contact Changes

Sensors in the interbody cage were able to detect regional pressure variation resulting from changes to stiffness in the contacting bone. The anterior of the cage experienced more stress with cortical contact while the lateral regions were off-loaded compared to the cancellous contact condition. These patterns were consistent at both early and solid fusion states. Stress reduction at the centre location resulting from a stiffer endplate was only measured in the solid fusion state. There is a load shift that occurs away from the lateral regions and towards the anterior of the cage with stiffer contacting bone. The experimental setup mimics a clinical XLIF procedure, with the cage spanning to the lateral extremities of the interfacing bone, but not the anterior-posterior extremities. As such, micro-deformation of the cancellous bone contacting the implant is more likely to occur at the anterior extremity of the cage. The strain distribution in Figure 5.26 shows more deformation of the contacting cancellous bone compared to cortical. With more deformation of the contacting vertebral body, less load is transferred to the interbody cage in the anterior region. With the cortical bone deforming less, a relative load-shift occurs towards the anterior of the cage and away from the lateral and central regions with cortical contact. This increase in anterior cage stress is evident in Figure 5.27. These load-pattern changes were found in the simulation results (Table 5.2, Table 5.3), demonstrating that the sensors are detecting the trend of an expected load-shift. The

magnitude of change measured by the sensors is, however, larger than expected in most regions.

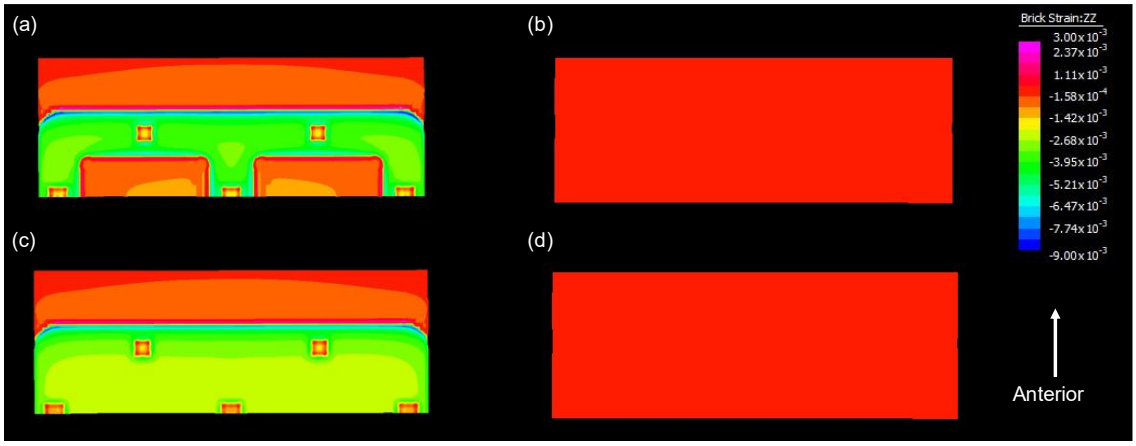

(a) Cancellous contact at early fusion. (b) Cortical contact at early fusion. (c) Cancellous contact at solid fusion. (d) Cortical contact at solid fusion.

Figure 5.26: Normal strain distribution on the interfacing bone contacting the top surface of the interbody cage under a distributed load. The strain distribution on the cortical endplate is even and, therefore, presents as a one continuous colour on the plot. ZZ direction into the plane of the image.

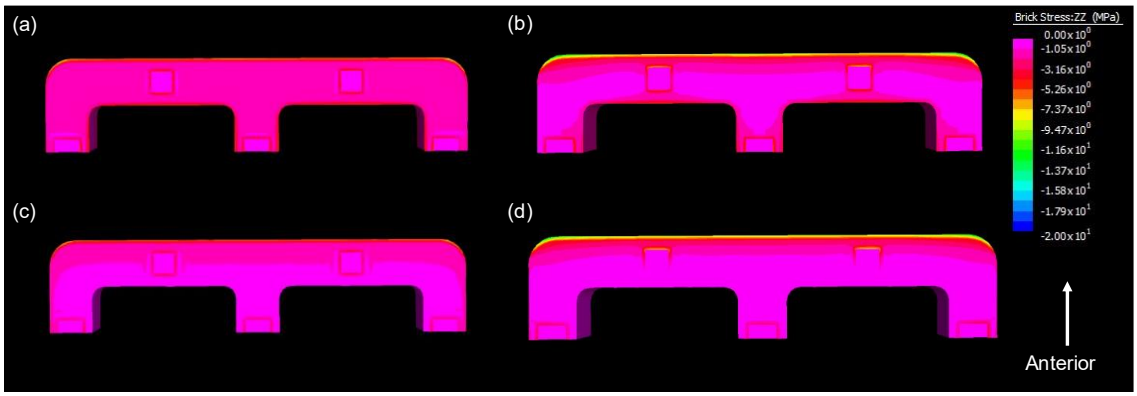

(a) Cancellous contact at early fusion. (b) Cortical contact at early fusion. (c) Cancellous contact at solid fusion. (d) Cortical contact at solid fusion.

Figure 5.27: Compressive stress (MPa) on the top surface of the cage obtained from FE analysis under a distributed load. ZZ direction into the plane of the image.

Cancellous and cortical contact have been used to emulate different endplate conditions. Given pseudarthrosis rates vary between osteoporotic and healthy patients, and the high

incidence of subsidence with lumbar fusion, measurements from the interbody cage that differentiate between endplate stiffness states are clinically relevant. Sensor-enabled fusion rods have been studied extensively, with most of the existing literature unable to use the devices to assess fusion progression [181, 182, 184, 188, 308]. Szivek et al. were not able to detect reduced loads on the fusion rod with fusion mass ossification, however successfully measured this change from sensors placed directly on the lamina [188]. A recently published animal study by Windolf et al., however, demonstrated 'smart' fusion rods can monitor fusion progression [186]. The fusion mass in the operated goat, however, ossified between the facets, nearer to the posterolateral screws and rods, as opposed to between the vertebral bodies. The current body of research on 'smart' fusion rods suggests that achieving accurate monitoring of interbody fusion progression may require sensors to be embedded proximate to the fusion mass. Further, sensor-embedded fusion rods have not been used to detect mechanical changes in the endplates.

5.9.3 Performance Under Eccentric Loading

Sensors at the anterior of the cage were loaded more with anterior eccentric loading and less with posterior loading compared to the distributed load results. However, results from the lateral sensors under anterior and posterior loads were less reliable. Left and right eccentric loads, however, resulted in the expected loading pattern, increasing stress on the proximate sensors and reducing stress on the distant sensors compared to distributed loading. The magnitude of the pressure change at each location between eccentric and distributed load cases was considerably higher with solid fusion compared to early fusion. With the softer graft, the cage bears a higher share of the load compared to the graft. Given the existing high stress on the cage at the point of early fusion under a distributed load, eccentric loads only cause a small increase in cage stress measured at the sensor locations. The solid graft, however, reduces the load on the cage. As such, the cage experiences a more substantial stress increase under eccentric loading at the point of solid fusion. At most locations, the graft states remained distinguishable by pressure measurement under eccentric loads (Table 5.5). Generally, sensors distant from the applied load point showed the greatest pressure differential between the two graft states. The results suggest that the current sensor layout is able to distinguish between the graft states and different eccentric loads, however alterations to this sensor layout may not be able to establish the same.

The eccentric loads represent a pseudo-bending load applied to the implant. Notwithstanding the simplicity of the experimental setup, the results provide confidence that with the current sensing arrangement the 'smart' cage will be able to distinguish between flexion, extension, and left and right lateral bending. Further validation, however, would be required in a multi-segment spine model under appropriate bending moments.

Table 5.5: Percentage difference in pressure at solid fusion compared to early fusion under eccentric loading.

	Eccentric Load Location			
	Left	**Right**	**Anterior**	**Posterior**
Ant Left	-26	-72	-18	-84
Ant Right	-58	-3	-8	-63
Centre	-51	-57	-60	-52
Lat Right	-90	-3	-61	-78
Lat Left	-11	-74	8	-7

5.9.4 Limitations

Some inconsistencies were noted in the experimental results. Under a distributed load, sensor measurements tended to vary between locations that were symmetrically aligned on the cage. Further, while the experimental measurements generally followed the trends obtained from FE analysis, there were discrepancies in the magnitude of those trends. The design and manufacturing of the load-sensing cage was complex, introducing several joints (sensor to PCB, PCB-A to PCB-B, cage to sensing-board) at which loading inconsistencies could be introduced due to imprecise manufacturing or bonding processes, accounting for both intra-cage pressure variation and discrepancies between experimental and simulation data. The bonding processes may have introduced electrical inconsistencies in the signals measured from the sensors.

The complex material interaction between the different components of the device presented an additional modelling challenge that may have introduced inaccuracies in the simulation. The FE analysis accurately modelled the geometry of each sensor (Figure 5.18). With each sensor occupying a volume of 12.5mm^3, it is unclear whether the stress value from the FE model for comparison to experimental measurements should be considered as: (i) the average of stress in all elements within the sensor volume, (ii) the

maximum stress of an element within the sensor volume, or (iii) stress at any other defined point(s) within the sensor region. While the simulation measures the pressure on the sensing region, it can not account for discrepancies that may be induced in the conversion of that pressure to an electrical signal as obtained experimentally. While FE analysis is a useful comparison, it is not the most suitable validation method. The designed system lacks sensing validation due to an absence of available comparable sensors. Alternate commercially available sensors did not have a comparable size and shape, which would necessitate changes to the cage geometry to properly enclose them, in turn reducing confidence in the validity of the comparison between those sensors. While the results of this study sufficiently assess the ability of the proof-of-concept design to monitor fusion and endplate changes, a suitable validation method should be sought in future works.

Variation in pressure measurements over the three trials may indicate sensor degradation or damage. Further, sensor drift is likely to occur with consistent static loading over a long period of time *in vivo*. The conducted experiments are not able to evaluate the impact of sensor drift. Future research should aim to identify durable sensing modalities and perform long-term drift studies to identify encapsulation and compensation methods to address this limitation.

Only one load-sensing cage could be developed due to the extensive prototyping conducted and associated resources. While the XLIF cage design was suitable for the study conducted, this is a notable limitation given the prevalence of smaller interbody cages and expandable cages available in clinical practice. The cage design and associated loading scenario are applicable only to the lumbar spine, although similar concepts could be adapted for the cervical spine. At this proof-of-concept stage, the loading scenarios investigated were basic, not accounting for posterior load-bearing structures of the spine such as the pedicles, lamina, and facets. As such, true bending moments could not be suitably applied with this setup. The endplates were limited to cancellous and cortical material due to the absence of better synthetic equivalents, and did not have anatomically accurate curvature.

5.9.5 Reviewing and Addressing the User Requirements

(a) Design Inputs

Design inputs derived from User Requirements I to IV were partially addressed with the outlined design and development works. User Requirement VI was considered in the design process, while User Requirement V was not addressed.

I. Load limits

The sensors were able to withstand the loads subjected on the interbody cage. A pressure difference was recorded between the graft states at lower loads (300N) and the highest load (900N) applied. A 900N load is equivalent to 92kg of body weight above the waist. Assuming 60% of body weight is above the waist, the static loading scenario represents a 153kg individual. The sensors were able to function and discern the graft states at the loads subjected in each trial. Some motion preserving implants are tested to 1200N according to ASTM F2346-05 [313], however fusion implants inherently restrict motion.

User Requirement I may be better addressed by:

- Improving sensor encapsulation.
- Embedding sensors in locations that are not subject to direct contact loads.

Future design inputs include:

- Sensors withstanding creep loads according to ASTM D2990-01 [321].
- Sensors withstanding fatigue loads according to ASTM F2077-18 [311].

II. Spatial Resolution

Data was extracted from five sensors embedded within the interbody cage. The design of the cage was symmetric and, therefore, the layout of the sensors was sufficient for the experiments conducted. The current layout was capable of detecting regional pressure variations in response to endplate stiffness changes in accordance with simulation data. Further, the sensors distinguished between different points of eccentric loading, suggesting they would be similarly capable of discerning flexion, extension, and lateral bending motions in the spine. Conversely, the layout is not necessarily applicable where the cage design is not symmetric. Further loading with different sensing configurations would uncover

a more optimal sensing layout that would achieve the same objectives with fewer sensors.

User Requirement II may be better addressed by:

- Relocating sensors to the posterior of the cage.

Future design inputs include:

- Sensor configuration functioning in asymmetrical implant designs, such as bullet, or kidney shaped interbody cages.
- Sensor configuration functioning in cages with lordosis.

III. Accuracy, reliability, and sensitivity

The sensors demonstrated they are sensitive to changes in graft and endplate stiffness, which is clinically useful. The variation in sensor measurement between trials likely indicates degradation under the applied loads over time, however they were able to distinguish between the graft and endplate states in all three trials individually. This reliability issue may arise from damage to the sensor or to the bonds between the sensor and PCB (see 5.9.4). Accuracy of the sensors is difficult to assess, however the comparison to FE analysis provided a generally positive appraisal of accuracy. The sensors detected the expected pressure variation trends based on the simulation. While there were discrepancies in the magnitude of the changes observed, sources for these discrepancies were identifiable (see 5.9.4).

User Requirement III may be better addressed by:

- Improving sensor encapsulation.
- Reducing fabrication failure points.
- Embedding sensors in locations that are not subject to direct contact loads.

Future design inputs include:

- Measurements comparable to a suitable gold-standard sensor.
- Sensors distinguish between intermediate graft and endplate stiffnesses.

IV. Wireless interfacing capacity

The sensor-bonded PCB approach to data collection facilitates wireless integration by connecting the raw data output pins from the sensors to the required pins on the wireless communication module. With the reduction in power consumption, hardware components, and size achieved in v2.0, the

system has the capacity to interface with a wireless telemetry module, such as RFID, NFC or similar. The sensors operate on 1mA of excitation and represent a small proportion of the total power consumption of the system. Initially, v1.0 included a Raspberry Pi 4 that operated on 5V; however this was reduced to 1.8V with the EFM8BB52 microcontroller. The system remained within an operating limit that is reasonably deliverable with inductive coupling, avoiding the need for battery power with future refinement. The system currently operates on more power than can be generated with *in vivo* energy harvesting.

User Requirement IV may be better addressed by:

- Reducing the number of sensing components.
- Reducing overall power consumption.

V. Biocompatibility

Biocompatibility was not considered or tested in this set of experiments, however is necessary to address prior to any animal or human testing.

VI. Usability

The load-sensing cage was designed based on a clinically used and commercially available XLIF cage. During the design process, the aim was to make as few changes to the cage design as practically achievable by choosing small sensors with regular geometries. In doing so, the results remain clinically relevant and the device remains as implantable as possible. The load-sensing cage, however, was not wireless. In the pursuit of wireless actualisation, more telemetric electronics will need to be embedded within the implant.

Discounting the external electronics, the current design did not interfere with the natural biomechanics of the joint tested in this study. Conversely, the two-piece cage design for housing the sensors and PCBs in addition to the loading setup prevented testing the load-sensing cage under bending loads.

User Requirement VI may be better addressed by:

- Investigating advanced manufacturing methods such that sensors are wholly enclosed within the implant.
- Reducing the number of sensing components.

Future design inputs include:

- Complete encapsulation of required electronics within the implant.

(b) Clinical Objectives

I. Real-time, continuous bone growth assessment

The load-sensing cage demonstrated it was able to detect the difference between the two end points of fusion, however further studies should be conducted to determine the sensitivity of the device to changes throughout the fusion process. Bending loads and implanting the device within a lumbar spine model will provide further confidence in this respect. Further, while data storage was achieved in v1.0, real-time logging and presentation of the data was achieved in v2.0.

II. Subsidence detection

The ability of the load-sensing cage to distinguish between endplate stiffness is relevant to the detection of subsidence. Firstly, bone quality is directly related to subsidence risk [82, 322, 323]. Quantifying bone stiffness changes can enable early identification of subsidence risk. Secondly, the bone tissue within the vertebral body is softer than the endplates. There will, therefore, be a change in the contacting bone stiffness if an implant subsides.

III. Identification of implant malpositioning

&

IV. Assessment of instability

Identification of implant malpositioning, poor alignment, and instability after a fusion operation would likely require the addition of accelerometric and/or gyrometric sensors. Kinematic data would provide a clearer indication of abnormal motion patterns compared to stress and load data.

V. Development of personalised rehabilitation programs

The results from this set of experiments show that eccentric and distributed loads can be measured in a load-sensing cage. Assuming the implant will perform similarly under bending loads, it is feasible that a load-sensing cage would provide useful data when performing postoperative rehabilitation. Monitoring data can be used to ensure that exercises that place excessive loads on the implant are avoided, particularly where patients are at a high risk of subsidence. With further research, there is potential to identify the optimal loads that promote bone growth without placing the implant at risk of mechanical failure.

5.10 Conclusion

Through a proof-of-concept design, the findings demonstrate the load-sensing interbody cage is a feasible technology for assessing bony union, bone stiffness, and different loading conditions. The research conducted has prioritised obtaining experimental data from the 'smart' implant, laying the foundation for further development, optimisation, and sensor reduction for improved implantability *in vivo*. The literature has established the wide-ranging utility of 'smart' interbody cages and fusion rods [138, 181, 182, 184, 186, 188, 189, 308], while the research presented in this thesis specifically shows the response of the 'smart' cage to different graft stiffnesses, endplate stiffnesses, and loading conditions using a spatial sensing distribution. These measures further the clinical utility of a 'smart' fusion cage, with applications in monitoring fusion progression, endplate health, and subsidence risk. Equipped with this information, surgeons can proactively assess complication risk and take appropriate actions to avoid the occurrence thereof, without relying on the onset of symptoms to prompt an investigation. With further development, load-sensing interbody cages can replace ineffective, periodic radiological follow-up and reduce complication rates.

Future research should aim to improve the implantability of the device, by reducing the number of sensors, investigating sensor modality alternatives, improving durability, and optimising the sensing configuration. Further work should be undertaken to prepare the load-sensing cage for wireless integration.

6. Sensor Optimisation and Wireless Telemetry

Preface

The previous chapter outlined the design and testing of a 'smart' interbody cage, detailing its utility and feasibility in clinical practice. In order to advance the device towards clinical adoption, sensor optimisation and wireless telemetry are required. In preparation for wireless integration, this chapter describes the investigation of multidirectional strain as an alternate measurand to determine whether (i) it is more effective than unidirectional pressure and (ii) an optimum sensing configuration can be designed with less components. A reduction in embedded components will enable better encapsulation within the implant and improve its mechanical integrity. Subsequently, a proof-of-concept wireless telemetry module is designed and validated. The feasibility of near-field communication is assessed for handling wireless power and data transfer in an implanted 'smart' cage.

6.1 Introduction

'Smart' implants, to be clinically useful and operate safely, must be wireless and entirely contained within the body. It follows that the load-sensing cage presented in Chapter 5 must be prepared for wireless integration. Wireless data acquisition provides real-time feedback to patients and clinicians while simplifying the process of data collection without the need for periodic imaging. As established in the review of design inputs in Section 5.9.5, a reduction in sensing components and size will better address multiple user requirements.

The works in this chapter aim to prepare the load-sensing cage for wireless integration. An alternate sensing modality is studied as an approach to optimise the sensing configuration and reduce the number of required embedded sensors. Subsequently, one approach to wireless telemetry is explored by designing and validating its wireless power and data transfer performance in a simulated benchtop environment.

While the sensing configuration is but one of several design aspects that can be improved to better meet the user requirements, it traverses several limitations of the current device. Similarly, only one telemetry protocol is developed and tested to assess its feasibility, necessitating further refinement to reach clinical adoption.

6.2 Investigating Optimisation of the Sensing Configuration

The load-sensing interbody cage developed in Chapter 5 is capable of quantifying compressive pressure only. The designed sensing configuration distinguished between graft and endplate stiffnesses, however comprised of 5 functioning sensors, which required a printed circuit board (PCB) and complex bonding process to acquire the data, while the sensors are prone to damage. These limitations of the existing design are considerations for optimisation of the sensing configuration. The previously defined user requirements from Section 5.2 can be better addressed by investigating an alternate sensing modality (Table 6.1).

Table 6.1: Potential improvements in meeting user requirements by investigating an alternate measurand.

User Requirement	Description	Improvement
I	Load limits	More durable sensors
II	Spatial resolution	Improved spatial efficiency
III	Accuracy, reliability, sensitivity	More accurate, reliable, and sensitive sensors
IV	Wireless interfacing capacity	Reduced number of sensors for data collection
V	Biocompatibility	-
VI	Usability	Improved clinical utility; Smaller implant dimensions

Consolidating the sensing system simplifies the process of designing a wireless data collection module. Reducing the number of embedded sensors addresses User Requirement II, IV, and VI, whereby less space within the implant is occupied by sensors and PCBs, improving its mechanical integrity and enabling integration with smaller interbody cages. When investigating sensing optimisation, it is worthwhile considering the accuracy, reliability, sensitivity, and durability of alternate sensing modalities and measurands (User Requirement I & III). Accordingly, it is important to determine whether multidirectional load patterns provide added clinical utility or mechanical inputs that could not be obtained from unidirectional pressure (User Requirement VI). Studying multidirectional strain measures may present opportunities to extract more mechanical information from less sensors, ultimately reducing the number of required sensing components and lowering barriers to wireless integration (User Requirement IV). Strain gauges are used to investigate potential avenues for optimisation of the sensing configuration.

Strain gauges are the gold standard sensor for measuring loads, often used to validate the performance of other sensing modalities and commonly embedded in 'smart' orthopaedic implants [140, 143, 171, 175-178, 181-185]. Biaxial strain gauges measure parallel and perpendicular strains in the plane of the applied load. Strain gauges may not necessarily be adopted for an implantable 'smart' interbody cage, however studying their performance provides an indication of whether multidirectional strain is more sensitive, reliable, and clinically useful than compressive pressure. For example, regions of tension can be measured on the implant face opposite to the applied eccentric load;

strains perpendicular to the applied load may be more sensitive to graft stiffness changes than those parallel. It is not the aim of this work to assess the utility of the strain gauge as a sensor, but rather the utility of multidirectional strain as a measurand. As such, some performance metrics, such as drift and durability, will be a function of the strain gauge design and material. Novel methods are available to embed or etch strain gauge patterns directly into a flexible PCB (bypassing the sensor bonding processes), which can be investigated as an alternate sensing configuration with improved spatial resolution, encapsulation, and size if multidirectional strain is identified as a more useful measure than unidirectional pressure. For this reason, the performance of the metric is more important than the performance of the sensor.

The aim of this study was to determine whether multidirectional strain provides more biomechanical and clinical utility than the previously designed unidirectional pressure sensing system under compressive loads.

6.3 Multidirectional Load Mapping using Strain Gauge Rosettes

Biaxial strain gauge rosettes (0° and 90°; Gauge Length = 2mm; Gauge Resistance = 120Ω; Tokyo Measuring Instruments, Japan) were fixed in the anterior (Ant.) and lateral right (Lat. Right) positions on the interbody cage (Figure 6.1) using a thin layer of Loctite (Henkel Group, USA) super glue, allowed to cure for 1 hour at room temperature. The centre of the strain gauge was aligned to the mid-axial plane of the implant. The anterior strain gauge rosette was positioned to measure ZZ and YY strains, while the lateral right strain gauge was aligned to ZZ and XX axes. Loads were applied in the negative-Z direction.

The interbody cage was designed in accordance with commercially-available Coroent XL NuVasive extreme lateral interbody fusion (XLIF) cages (22.0 x 50.0 x 14.5mm, 0° lordosis) of the same dimensions as Section 5.4.3, manufactured by CNC milling from polyether ether ketone (PEEK) material supplied by Dotmar Engineering Plastics (NSW, Australia). Apart from the cavities machined to accommodate the sensors and PCBs, the interbody cage in this study matched the dimensions of the load-sensing cage described in Section 5.4.3. Distributed loads were applied with cancellous and cortical endplate contact as per Section 5.6.1. Eccentric loads were applied with cancellous contact only as

per Section 5.6.2. Silicone material was inserted in the graft region to simulate early fusion; poly(methyl methacrylate) (PMMA) was used to simulate solid fusion as per Section 5.5. The loading setup with the affixed strain gauges is shown in Figure 6.2.

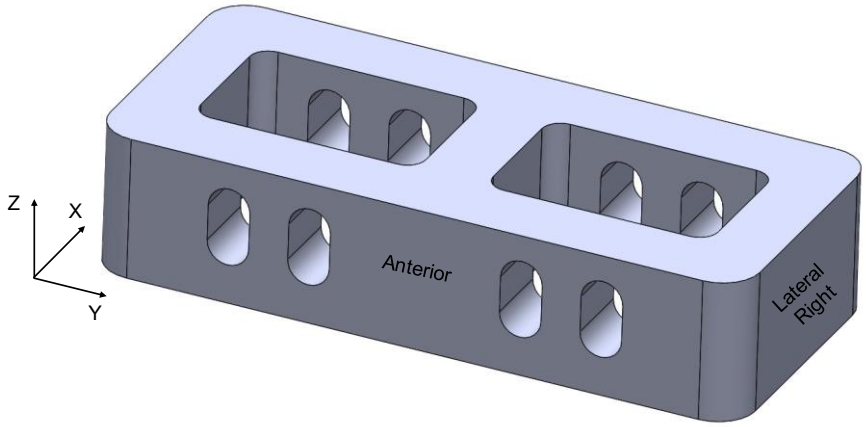

Figure 6.1: Axes and strain gauge locations on the interbody cage. The load was applied in the negative-Z direction.

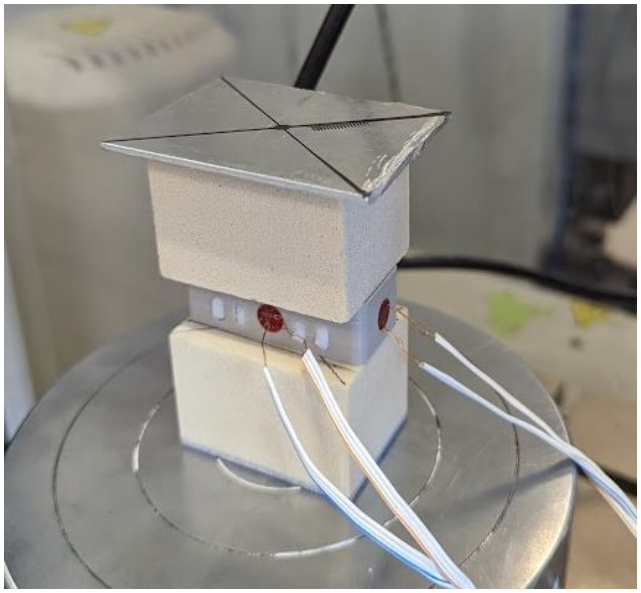

Figure 6.2: Loading setup of the interbody cage affixed with two biaxial strain gauges in the anterior and lateral right locations. The setup is shown with cancellous contact.

6.4 Finite Element Analysis

A 3D finite element (FE) model was developed in Strand7 (vers. 2.4.6, Strand7 Pty. Ltd, Australia) commercial software, using the same method described in Section 5.7, as a comparison for the strain gauge data and to provide broader links between strain patterns at the anterior and lateral regions of the cage. The model was developed to replicate the experimental setup. A half-symmetry model geometry was built in Strand7 to reduce the computational time (Figure 6.3). Material properties were assigned according to Table 6.2. The model consisted of 499,136 bricks and 523,199 nodes, mostly comprising of 0.5 x 0.5 x 0.5mm brick elements where straight edges were achievable in the model geometry. The cross-sectional plane was constrained by a symmetric boundary, preventing out-of-plane translations and rotations. The nodes on the bottom surface were constrained in all translational and rotational degrees of freedom. The model was loaded in compression from the top surface with an evenly distributed pressure equivalent to 450N.

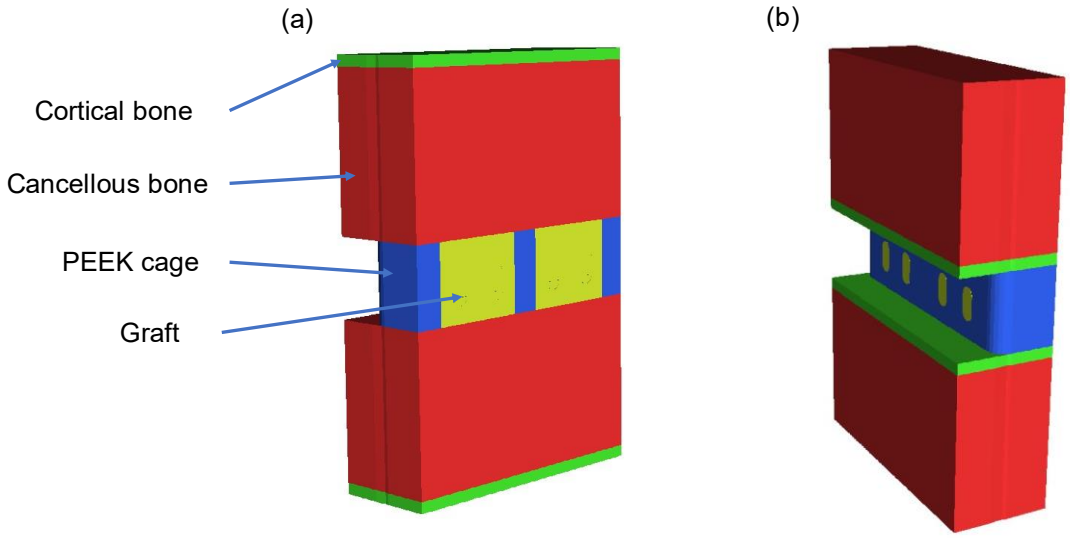

Figure 6.3: Half-symmetry FE model simulating the experimental setup with (a) cancellous contact and (b) cortical contact.

Table 6.2: Material properties used in the FE model.

Material	Material Model	Properties E: Elastic Modulus (MPa) K: Bulk Modulus (MPa) v: Poisson's Ratio C: Neo-Hookean Constant
PEEK Manufacturer supplied (Dotmar Engineering Plastics)	Isotropic	E = 3750 v = 0.38
Sawbones Cancellous Manufacturer supplied (Sawbones, 20PCF)	Isotropic	$E_{Tension}$ = 284 $E_{Compression}$ = 210
Sawbones Cortical Manufacturer supplied (Sawbones, 20PCF)	Isotropic	$E_{Tension}$ = 16000 $E_{Compression}$ = 17000
Silicone Manufacturer supplied (Kunovus)	Neo-Hookean	C = 0.207 K = 20.7MPa
PMMA Dall et al. (2007) [261] Manufacturer Supplied (Heraeus Medical)	Isotropic	E = 2795 v = 0.375

6.5 Strain Gauge Results

6.5.1 Distributed Loads

Under a 900N distributed load with cancellous contact, both strain gauges aligned along the ZZ direction recorded a reduction in strain (Lat. Right = -23%; Ant. = -9%) in the solid fusion state compared to early fusion (Figure 6.4). Strain in the YY direction was tensile with both grafts, however the strain was 21% higher at solid fusion compared to early fusion. Strain in the XX direction was tensile at early fusion and compressive at solid fusion, with a difference of 114% with respect to early fusion.

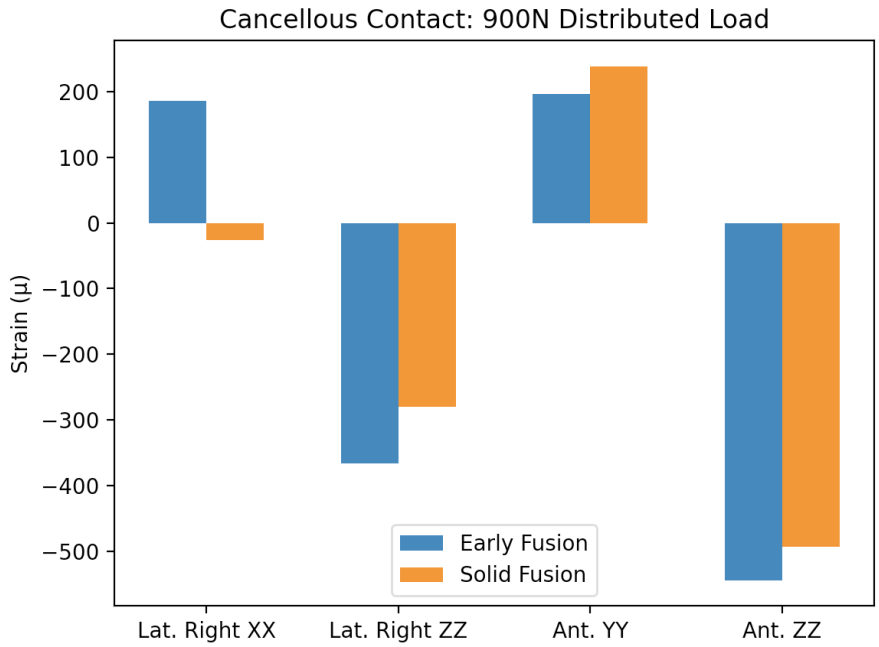

Figure 6.4: Strains (με) measured in each direction under a 900N distributed load with cancellous contact.

A lack of structural support from the softer silicone graft in the anterior region at early fusion likely caused micro-scale buckling of that region, as shown in Figure 6.5. The buckling counteracted the tensile YY strains in the anterior region of the cage, resulting in lower YY strain in early fusion compared to solid fusion. Further, these strain patterns at the anterior are likely to have induced the tensile strains measured in the XX direction at early fusion. Support provided in the anterior region by the stiffer graft at solid fusion improved the load distribution at the top surface of the interbody cage (Figure 6.6), inducing compressive strain in the XX direction. Regions of high compressive strain are evident above the anterior graft cavities at early fusion (Figure 6.6).

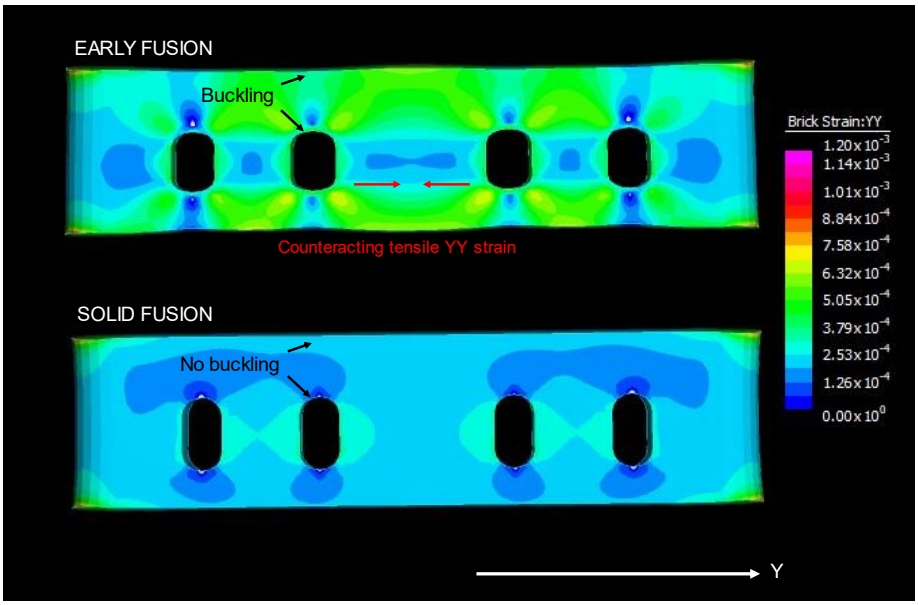

Figure 6.5: Strain in the YY direction obtained from FE analysis under an equivalent 900N distributed load with cancellous contact. Deformations have been exaggerated by 100x to illustrate the micro-scale deformations.

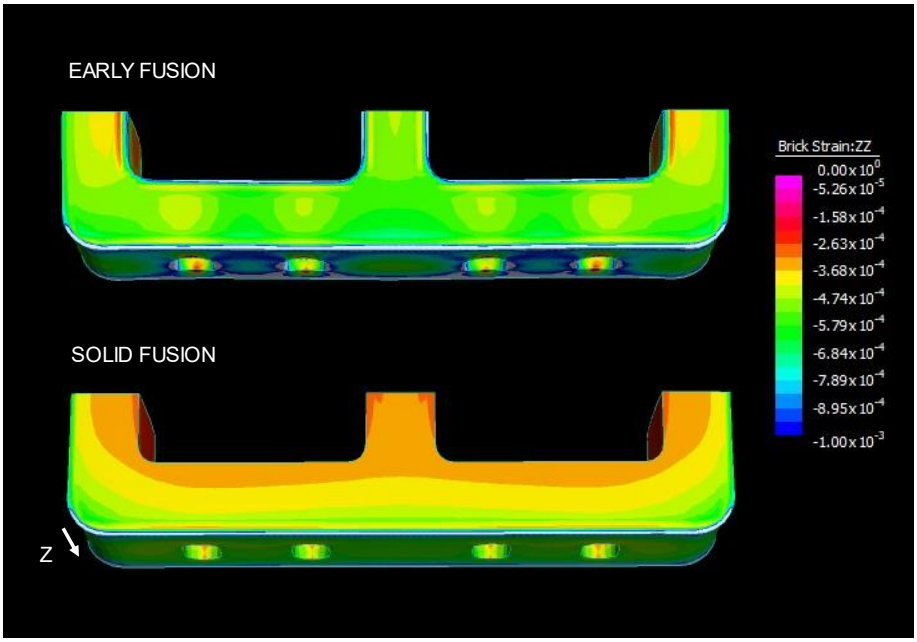

Figure 6.6: ZZ strain distribution at the top surface of the cage, obtained from FE analysis under an equivalent 900N distributed load with cancellous contact.

With cortical contact under a 900N distributed load, solid fusion caused a 16% reduction in compressive strain at the anterior gauge in the ZZ direction, while a 37% reduction was measured in the YY direction with respect to the early fusion state (Figure 6.7).

Conversely, at the lateral strain gauge, increases were measured in both XX (72%) and ZZ (182%) directions with solid fusion compared to early fusion.

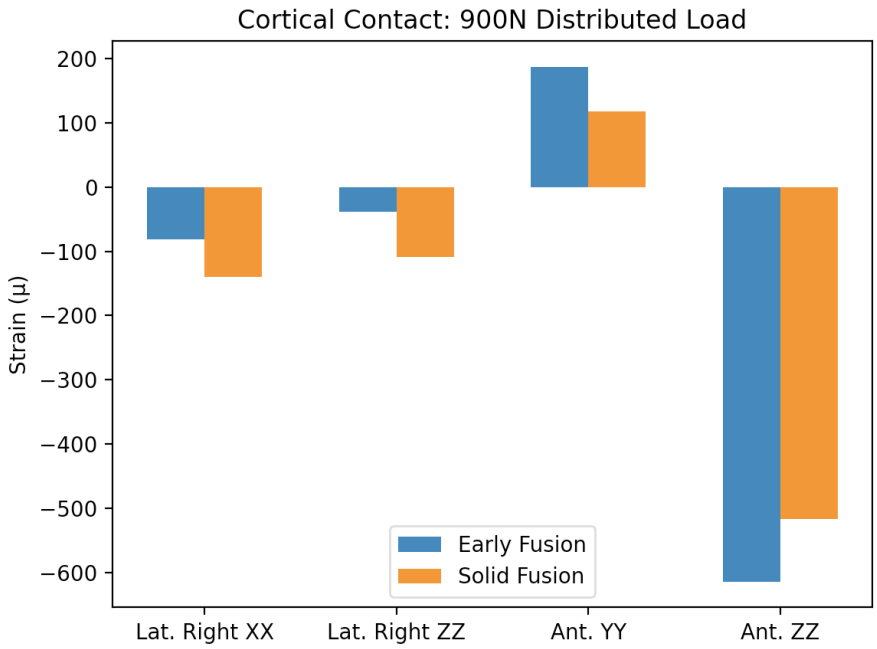

Figure 6.7: Strains (με) measured in each direction under a 900N distributed load with cortical contact.

Cortical contact caused an increase in ZZ compressive strain at the anterior of the cage. The lack of structural support from the silicone graft in the anterior region at early fusion caused more compressive strain in the ZZ direction (Figure 6.8) and tensile strain in the YY direction. Larger deformations in the anterior cage likely resulted in less compressive strain in the lateral region in both ZZ and XX directions. The support provided by the solid graft, however, improved load distribution at the superior cage surface towards the lateral regions, resulting in larger compressive strains at the lateral right strain gauge in XX and ZZ directions. Regions of high compressive strain are more evident at early fusion above the anterior graft cavities (Figure 6.9).

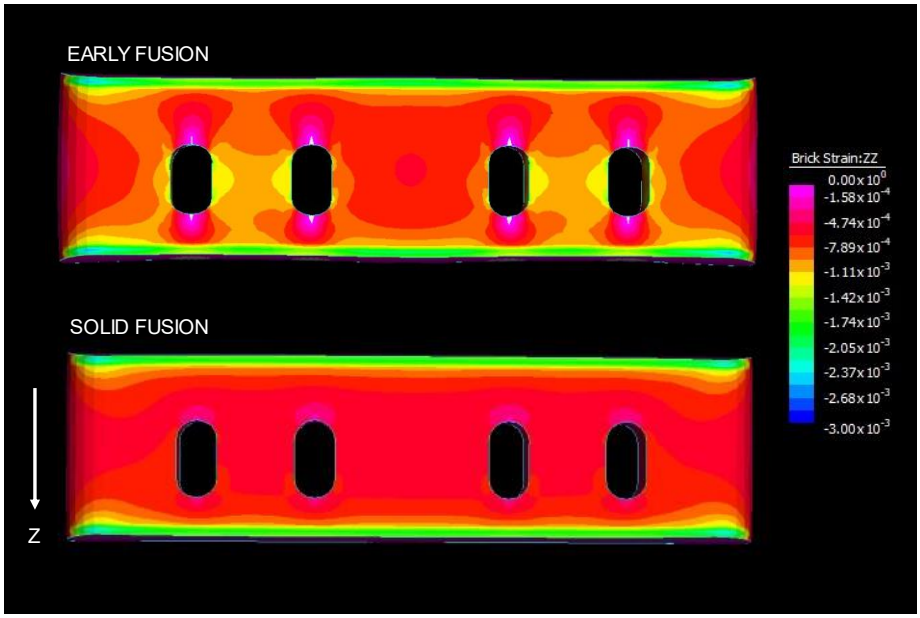

Figure 6.8: Strain in the ZZ direction obtained from FE analysis under an equivalent 900N distributed load with cortical contact. Deformations have been exaggerated by 100x to illustrate the micro-scale deformations.

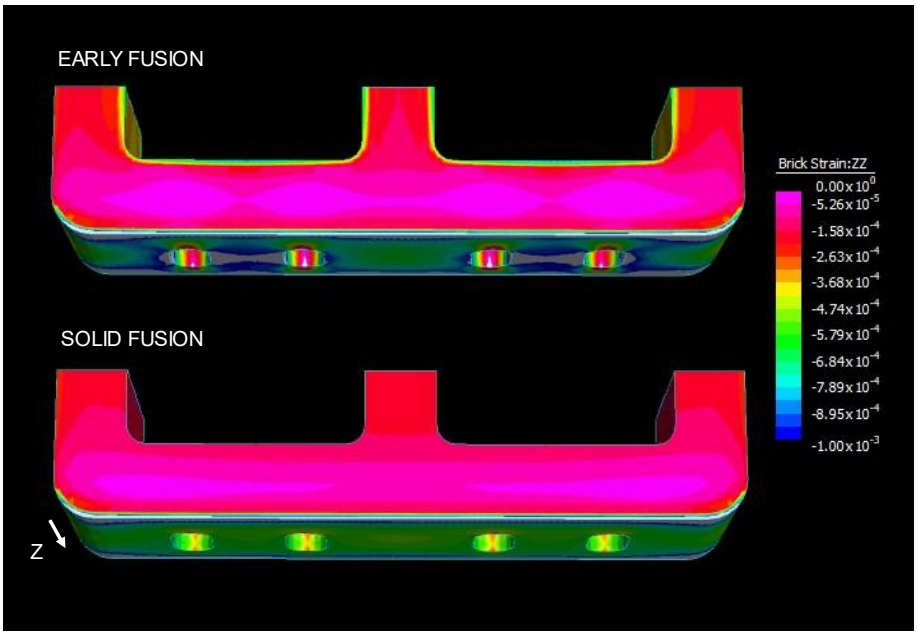

Figure 6.9: ZZ strain distribution at the top surface of the cage, obtained from FE analysis under an equivalent 900N distributed load with cortical contact.

The cortical bone endplate caused a modest increase in compressive strain experienced at the anterior of the cage in the ZZ direction compared to the cancellous bone endplate (Early Fusion = 13%; Solid Fusion = 5%) (Figure 6.10). Cortical contact substantially

reduced ZZ strain in the lateral region of the cage (Early Fusion = -90%; Solid Fusion = -61%). Strain patterns in the XX and YY directions, however, were more complex. Anterior YY strain was similar with both endplate contacts at early fusion, however recorded a 50% lower strain with cortical contact at solid fusion. The lateral strain gauge recorded tensile strain at early fusion and compressive strain at solid fusion in the XX direction with cancellous contact, while XX compressive strain was 72% higher with cortical contact compared to cancellous contact at solid fusion. In the solid graft state, the stiffer cortical endplate increased compressive load transfer to the anterior region of the interbody cage.

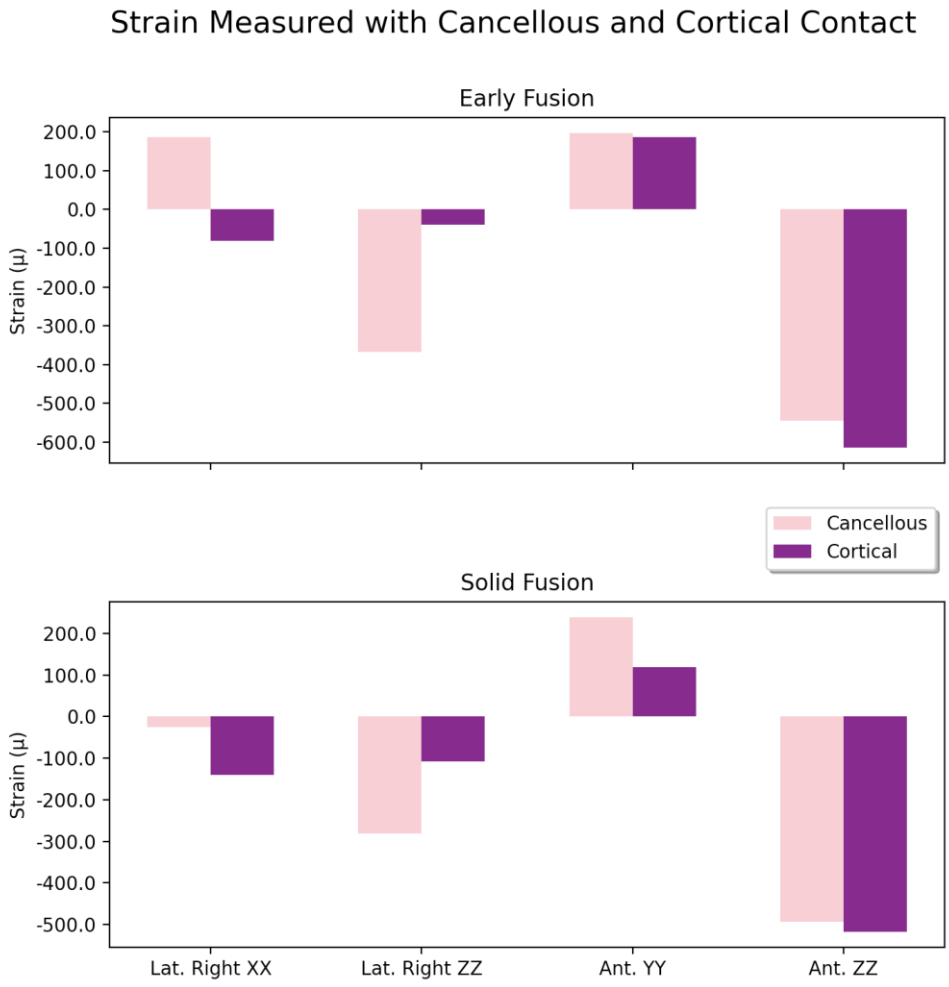

Figure 6.10: Comparison of strain (με) measured with cancellous and cortical contact under a 900N distributed load.

Strain measurements in the early fusion and solid fusion states generally became more discernible at the lateral location with increasing load under cancellous contact (Figure

6.11). Compressive ZZ strain at the anterior location was similar between the two graft states regardless of the load applied. At 300N, anterior YY strain was higher at early fusion, however at 900N, a higher strain was measured at solid fusion.

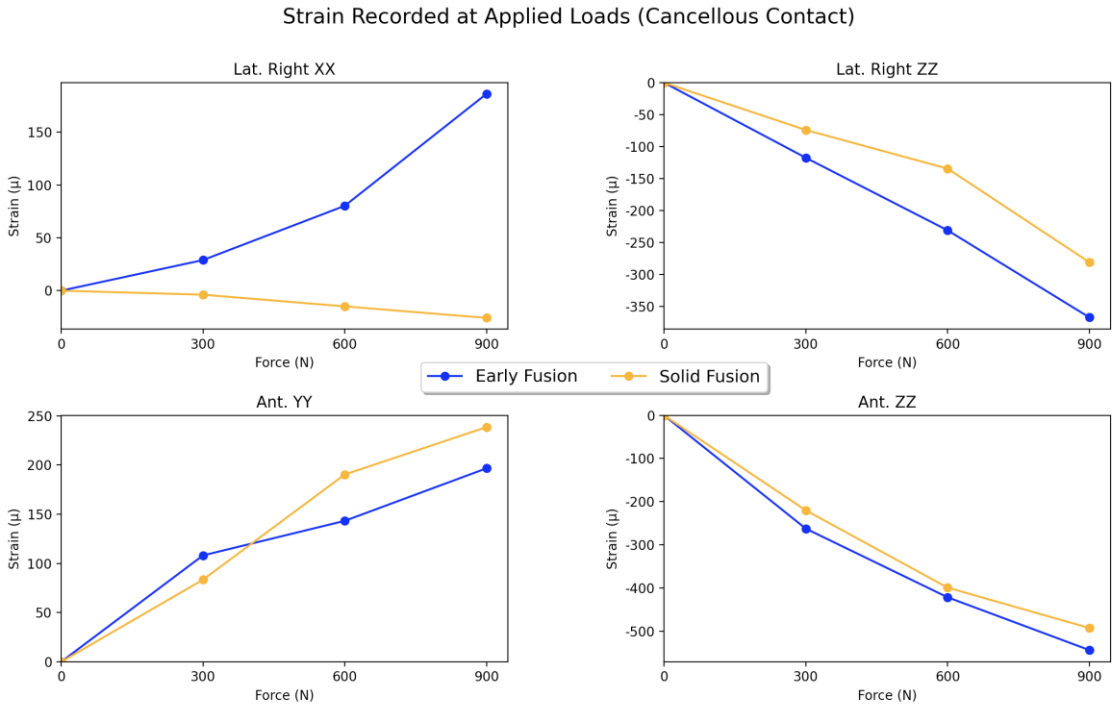

Figure 6.11: Strains (με) recorded at each location with cancellous contact as the applied load increased up to 900N.

Under cortical contact (Figure 6.12), there were some notable similarities to cancellous contact in the observed strain patterns. The graft states were well-distinguished by strain measurements at the lateral location. While early and solid fusion anterior ZZ strain curves exhibited a greater separation with cortical contact compared to cancellous contact, this measure was the least effective at discerning the graft states. Anterior YY strain was comparable between the graft states at 300N, however at 900N a higher strain was recorded at early fusion compared to solid fusion.

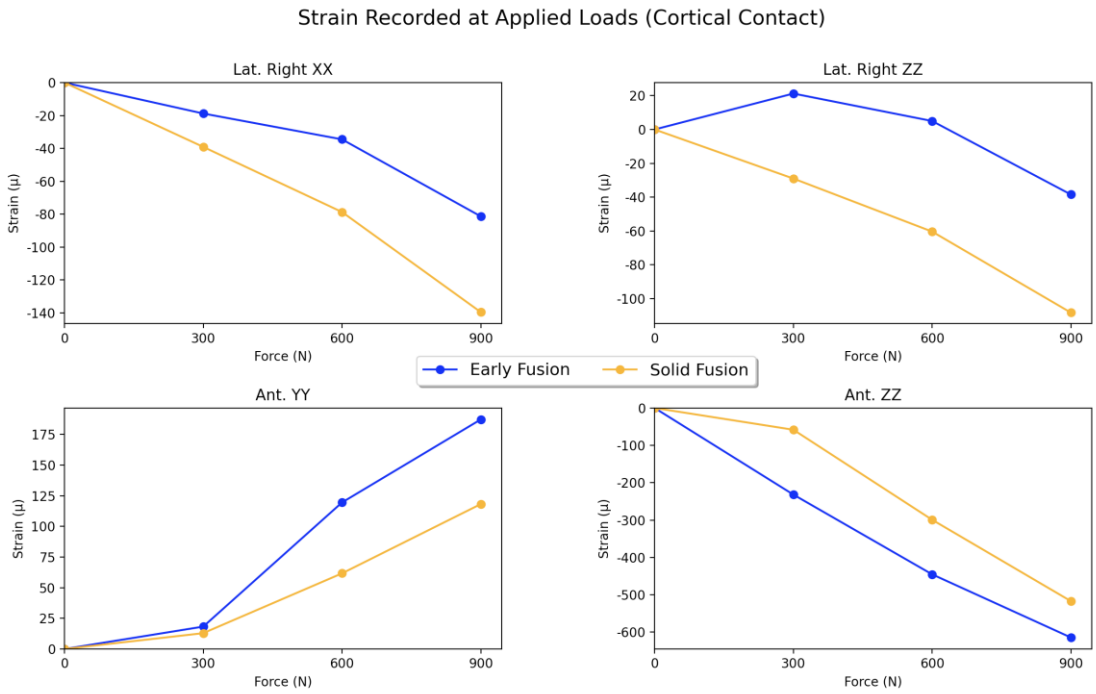

Figure 6.12: Strains (με) recorded at each location with cortical contact as the applied load increased up to 900N.

6.5.2 Eccentric Loads

Percentage change in strain under each eccentric load is reported with respect to the strain measured under the 900N distributed load with cancellous contact.

At early fusion, anterior eccentric loading caused a substantial increase in tensile YY strain and compressive ZZ strain in the anterior region, however a 45% increase was also measured in compressive ZZ strain in the lateral right region (Figure 6.13). Further, compressive ZZ strain increased by 9% at the lateral right location under posterior eccentric load, with decreases recorded in the remaining gauges. Left eccentric loading caused a decrease in tensile XX strain and compressive ZZ strain measured at the lateral right location; however, increases were measured in tensile YY strain and compressive ZZ strain at the anterior location. Under right eccentric load, tensile strain increased in the YY and XX directions, while compressive strain increased in the ZZ direction at lateral right and anterior locations; increases were more pronounced at the lateral strain gauge.

At early fusion, strains that were compressive under a distributed load remained compressive under eccentric loads; strains that were tensile under a distributed load remained tensile under eccentric loads.

	Early Fusion			
	Lat. Right XX	Lat. Right ZZ	Anterior YY	Anterior ZZ
Anterior 	108.26 -42%	-531.60 45%	378.99 93%	-1088.57 100%
Posterior 	104.44 -44%	-398.96 9%	98.99 -50%	-366.23 -33%
Left 	62.35 -67%	-107.53 -71%	217.71 11%	-677.44 24%
Right 	290.95 56%	-949.83 159%	226.51 15%	-736.27 35%

Figure 6.13: Strain measured at each strain gauge (με) at early fusion under each eccentric load point and reported as a percentage change compared to the 900N distributed load with cancellous contact.

At solid fusion under anterior eccentric loading, the interbody cage experienced a similar strain pattern in the anterior region with a lower magnitude of change compared to early fusion (Figure 6.14). Conversely, the lateral location recorded a decrease in compressive strain in the ZZ direction and an increase in compressive strain in the XX direction. Compressive XX and ZZ strains (Lat. Right), and tensile YY strain (Ant.) reduced under both posterior and left eccentric loading. Under posterior loading, a low tensile strain was measured in the ZZ direction at the anterior location, while YY strain was compressive; under left eccentric loading YY strain was tensile and ZZ strain was compressive. Right eccentric loading caused a substantial increase in compressive XX and ZZ strain at the lateral location accompanied by a decrease in tensile YY strain and compressive ZZ strain at the anterior location.

Anterior YY strain was tensile under distributed loading, however recorded compressive strains under posterior and right eccentric loads. Similarly, the Anterior ZZ strain gauge recorded tensile strain under posterior and right eccentric loads despite measuring compressive strains under a distributed load. A substantial shift from compressive XX strain under a distributed load to tensile XX strain under right eccentric loading was observed at the right lateral gauge.

	Solid Fusion			
	Lat. Right XX	Lat. Right ZZ	Anterior YY	Anterior ZZ
Anterior 	-29.30 14%	-26.84 -90%	277.09 16%	-620.14 26%
Posterior 	-25.64 -1%	-56.98 -80%	-39.25 -116%	19.53 -104%
Left 	-10.02 -61%	6.00 -102%	24.80 -90%	-16.43 -97%
Right 	138.66 638%	-588.62 110%	-8.23 -103%	19.51 -104%

Figure 6.14: Strain measured at each strain gauge (με) at solid fusion under each eccentric load point and reported as a percentage change compared to the 900N distributed load with cancellous contact. Strains which changed from tensile to compressive, or vice versa, with the shift from distributed to eccentric loading are underlined.

6.5.3 Simulation Comparison

The results from the strain gauges were comparable to the values obtained from the FE analysis. The simulation strains presented in Table 6.3 were obtained from the element at the centre point of the strain gauge location. The margin between the simulation and experimental results was within an acceptable range (maximum difference = 14%) with the exception of the lateral right ZZ strain measurement at early fusion with cortical contact. Discrepancies between FE analysis and experimental data did not show

consistent patterns to suggest they arose from issues with sensor bonding or uneven load application.

Table 6.3: Comparison of strains (με) obtained from FE analysis (simulation) and experimentally.

		Cancellous Contact		Cortical Contact	
		Simulation	**Experimental**	**Simulation**	**Experimental**
Early Fusion	Lat. Right XX	212.74	186.27	-85.70	-81.35
	Lat. Right ZZ	-381.06	-366.76	-5.99	-38.43
	Ant. YY	187.43	196.62	196.18	187.18
	Ant. ZZ	-534.08	-544.18	-626.85	-614.24
Solid Fusion	Lat. Right XX	-30.03	-25.79	-154.04	-139.61
	Lat. Right ZZ	-312.70	-280.59	-109.23	-108.23
	Ant. YY	230.21	238.50	131.91	118.16
	Ant. ZZ	-533.87	-492.92	-526.49	-516.98

6.6 Performance and Utility of Multidirectional Strain Measurement

6.6.1 Performance of Strain Gauges Under Distributed Loads

Despite recording different measurands, the strain gauges and pressure sensors demonstrated some similarities. With both sensing modalities, higher compressive loads were measured at the anterior of the cage regardless of the endplate contact. Further, both sensing systems measured a shift in compressive load from the lateral to the anterior regions of the cage with the stiffer cortical endplate. Both modalities recorded a greater difference in load between the graft states with cortical contact compared to cancellous contact.

Detailed comparisons of the measurements between the two systems, however, are limited, as their embedded locations in the cage differ. Rather, it is more relevant to examine the performance of the sensing modalities in terms of their objectives. The strain gauges distinguished between the fusion endpoints with cancellous contact, however the difference in ZZ strain between the states in the range of 9-23% does not suggest that the sensors would reliably distinguish intermediate graft stiffnesses. Under cortical contact, the strain difference between early and solid fusion states was more pronounced. In contrast, the pressure sensors recorded a consistent and appreciable

difference with both endplate contacts. While the distinction between the graft states was evident from XX and YY strains, overall the strain gauges were more effective at 900N, whereas the performance of the pressure sensors was consistent from 300N to 900N. Strain in the XX direction yielded sizeable differences with graft and endplate stiffness, however given the strain traverses both tensile and compressive zones under simple distributed loads, using XX strain alone to discern graft stiffness states would be complex.

A substantial difference in strain was measured between the two endplates at the lateral right gauge, which was consistent at early and solid fusion. The anterior ZZ gauge recorded a small increase with cortical contact compared to cancellous, while a notable change in YY strain was only produced at solid fusion. In comparison, the pressure dies sensed small differences in load between the endplates, which were evident at early and solid fusion.

6.6.2 Performance of Strain Gauges Under Eccentric Loads

Changes in strain under eccentric loads were evaluated in comparison to strains measured under a distributed load. At solid fusion, the anterior ZZ gauge recorded an increase in compressive strain under anterior loading; under posterior loading anterior ZZ strain was tensile. Similarly, anterior YY strain was tensile and increased under anterior loading, however was compressive under posterior loading. In contrast, at early fusion anterior ZZ strain remained compressive and YY strain was tensile under posterior eccentric loading. In both graft states, strain in the XX direction was appropriately similar under anterior and posterior loading given the symmetry of the implant and loading profile. Conversely, notable inconsistency was observed in lateral ZZ strain between anterior and posterior loads. There is considerable ambiguity in how eccentric loads were captured by multidirectional strain. Loading distribution inconsistency was controlled by performing experiments on 3 unique samples, however minor variations in the load application point may still introduce irregularities in the results.

Under left eccentric loading, strains at the lateral right location decreased in both graft stiffness states. At early fusion, however, strains at the anterior gauge increased, while at solid fusion anterior strains decreased. At solid fusion, ZZ strain at the right lateral

location was in tension under left eccentric loading. Similarly, under right eccentric loading, anterior strains increased at early fusion and decreased at solid fusion. The right lateral gauge recorded an increase in strain at both early and solid fusion.

Each eccentric load produced a unique strain pattern. Given their ability to sense compressive and tensile strain, the strain gauges should theoretically outperform pressure sensors at detecting eccentric loads. At solid fusion specifically, left and posterior eccentric loads were detectable due to the tensile ZZ strains measured in the location opposite to the applied load. In contrast, the same expected tensile strains were not measured at early fusion, which would have improved the ability of the strain gauges to distinguish between the eccentric load points. Further, the magnitudes of change from distributed to eccentric loads were not consistent between early fusion and solid fusion, further complicating interpretation of the data. Certain strain patterns did not have clear mechanical correlates, for example the right lateral ZZ gauge measured an increase in strain under anterior and posterior eccentric loading at early fusion and a decrease at solid fusion. While the unidirectional pressure sensors were sufficient to detect eccentric load points, the results suggest ZZ strain alone would not be sufficient to determine the location of the applied load. The application of true bending loads may provide a more effective method to characterise different loading profiles.

6.6.3 Inputs from Finite Element Analysis

While the pressure sensors followed the same trends as those observed in the FE analysis, the strain gauge data showed superior alignment with the simulation results. As previously mentioned, there are difficulties in comparing the pressure measurements with the FE model, however the comparison with strain gauge outputs is straightforward. The similarity of the strain gauge and simulation results substantiates the accuracy of the data obtained. With the strain gauges fixed to the vertical faces of the interbody cage under indirect load, they are less prone to degradation and damage. In contrast, the pressure sensors were embedded directly under axial compressive load, potentially influencing their accuracy and reliability, and increasing the risk of damage. Consequently, the strain gauges showed less variation over the 6 trials and did not show signs of degradation.

Sensitivity of the sensors to changes in graft and endplate stiffness may vary by sensing modality, location, or both. The anterior pressure sensors were more sensitive than anterior ZZ strain gauges. Considering the alignment between strain gauge and simulation data, it is not likely that the low sensitivity to graft and endplate changes of certain strain measurements is a consequence of the sensor itself, but rather of the measurand and gauge location. Lateral ZZ strain remained compressive under distributed loading and was more sensitive to graft and endplate stiffness changes than anterior ZZ strain, however opposite trends were measured under cancellous and cortical contact with regards to graft stiffness. Despite being mechanically informative and supported by FE analysis, complex trends and responses to biomechanical changes are not clinically useful.

6.6.4 Biomechanical and Clinical Utility

The utility of multidirectional strain data must be examined for its ability to produce clinically and mechanically useful information. The results establish that pressure measurements were more effective than strain at distinguishing graft and endplate stiffnesses. Despite the presence of inconsistencies in both pressure and strain data under eccentric loads, the simplicity of unidirectional pressure is advantageous. However, multidirectional strain data clearly provided more biomechanical information than unidirectional pressure data. The combination of axial and transverse strains comprehensively described the mechanical changes experienced by the interbody cage. Buckling at the anterior of the implant at early fusion, load redistribution at solid fusion, and load transfer to the anterior region with cortical contact are clearly illustrated by the strain data. The clinical utility of such data, however, is questionable. Despite being more accurate, multidirectional strains did not yield a meaningful improvement in clinical utility compared to the pressure-sensing cage.

The intricate data obtained from strain gauges may be more useful than pressure sensors when subjected to more complex and realistic loading scenarios. Notwithstanding the complexity of the data, the lateral gauge was sensitive to changes in the graft and endplates. As such, further experimentation is required to understand the fluctuating compressive-tensile response of XX strain and investigate the inconsistencies in lateral ZZ strain under complex loading scenarios with intermediate graft stiffnesses. Based on

the data obtained under compressive loading, however, multidirectional strain provides limited additional utility compared to the pressure-sensing cage.

Complex data necessitates complex testing to confidently identify clinical correlates, the outcome of which may result in a combination of multidirectional strain and pressure sensors, each optimised for assessing changes in the graft, endplates, or loading conditions specifically. As previously summarised in Section 2.4, 'smart' orthopaedic implants have successfully employed strain gauges to characterise different movements and activities. Pressure sensors have not been thoroughly investigated, particularly in spine implants. While identifying movement patterns is important, as the primary goal of a 'smart' implant it provides little clinical utility. Rather, 'smart' implants should be designed and optimised to provide clinical benefit in the areas of diagnosis, monitoring, and treatment.

It was not the aim of this work to assess the utility of the strain gauge as a sensor, but rather the utility of multidirectional strain as a measurand. As such, sensor performance metrics, such as durability, were not studied. Sensor performance is a function of the strain sensor design and material, and assessment of clinical utility is incomplete without thorough characterisation.

6.6.5 Optimisation of the Sensing Configuration for Wireless Integration

Notwithstanding the effect of the sensor design, the results of this study suggest that measuring indirect loads (not under direct contact) may lower the risk of sensor damage, and improve the accuracy and reliability of the data obtained. In the context of the results of this study, integrating strain gauge patterns directly within the PCB would enhance performance in these areas, while also reducing the number of mechanical and electrical failure points, improving encapsulation, reducing the size of the embedded electronics, and consequently lowering barriers to wireless integration. Nevertheless, it is also clear that strain gauges did not match the clinical utility of pressure sensors and, as such, an optimised sensing configuration would include:

I. A combination of PCB-embedded strain gauge patterns and pressure sensors

II. Improved durability and reliability of the pressure sensors

The central pressure sensor can be eliminated to reduce the number of components in the load-sensing cage and prevent unnecessary power consumption, as it is the least sensitive to positional load changes while performing similarly to the remaining sensors in all other metrics. Anterior pressure sensors are more sensitive than anterior strain gauges, while the performance of the lateral strain gauge warrants further study.

Holistically, considering the primary objective of monitoring fusion progression while remaining cognisant of detecting endplate changes and eccentric or bending loads, an optimised sensing configuration for further biomechanical validation would include:

- Pressure Sensor: Anterior Left
- Pressure Sensor: Posterior Right
- Biaxial Strain Gauge Pattern: Lateral Left or Right

The optimised configuration reduces the number of embedded components and size of the PCBs, however it does not reduce the number of failure points or address reliability and durability issues associated with rigid pressure sensors. While optimisation of sensor performance and optimisation of the sensing configuration for peak biomechanical and clinical utility can be considered unique objectives, both of which are subject to further work, a holistic approach that considers manufacturing, encapsulation, and sensing together will yield greater outcomes.

Multimodality sensing presents challenges with regards to handling distinct power requirements, degradation patterns, reliability, and drift characteristics of the respective sensors. While these challenges complicate the development of a wireless telemetry system, the biomechanical and clinical utility of the design should not be compromised in the pursuit thereof. A wireless telemetry module for a load-sensing cage is adaptable and ideally supports multiple sensing modalities.

6.7 User Requirements for a Wireless Telemetry Module

The aim of a wireless data collection module is to gather the sensor measurements without any necessary physical connection between the sensing board and the computer used for data logging and presentation. The aim, therefore, is two-fold, inclusive of both wireless telemetry and wireless power delivery to supply the microcontroller and sensing array. Near-field communication (NFC) is a telemetric technology and protocol

capable of addressing both power and data aspects of wireless transmission (see Section 6.7.1). The following broad user requirements are translated into design inputs in Section 6.8.

I. Wireless power delivery

Supply of sufficient power for operation of the sensing components without implantable batteries or physical percutaneous connection.

II. Wireless data transfer

Retrieval and storage of data from the implanted device to a host computer at an appropriate sampling rate without physical percutaneous connection.

III. Sufficient transmission distance

Capacity to transmit power to the required depth at the location of the receiver coil and accurately record data from the sensor-embedded implant.

IV. Implantable size

The wireless telemetry system should be enclosable within the implant.

V. Biocompatibility

All materials used in the wireless module must meet the requirements of ISO 10993 for implantable devices.

VI. Adaptability

The wireless module should be agnostic to the sensing modality to the greatest extent that is practically achievable. The system should avoid fixed parameters that restrict data extraction.

6.7.1 Overview of Near-Field Communication (NFC)

NFC is a high-frequency subset of the radiofrequency identification (RFID) system, operating around 13.56MHz, that handles wireless data and power transfer [324]. NFC facilitates contactless wireless data transfer between NFC-enabled devices generally within 5-10cm [325]. The RFID protocol can transfer data over a distance up to 6 metres unidirectionally from the tag to the receiver [326]. Bluetooth, WiFi, and to a limited extent Zigbee, are other comparable wireless data transfer methods that consist of hardware components that have previously been embedded in implantable medical devices [327, 328]. While reliable, they require battery power in addition to a complex

pairing process and Transmission Control Protocol (TCP) infrastructure for data transfer [329, 330]. Bluetooth, WiFi, and Zigbee are active communication technologies that do not have an in-built passive mode. Conversely, NFC is inexpensive, seamlessly operates whenever activated in the near-field, and does not require a battery on the receiver end. Operating in passive mode, the NFC tag will activate and send data via load modulation only when initiated by the transmitter [326]. Further, NFC has been demonstrated as an effective telemetric method in recent literature on biomedical devices [324]. Its simple design, operating principles, affordability, and low power consumption (2V) are also favourable in its selection for implementation in the wireless telemetry module.

While there are inherent limitations in the transfer distance achieved by NFC, the size increase of radiative mid-field telemetric systems is well-established [331]. Despite novel advancements in capacitive coupling that have produced flexible, efficient systems that are robust to misalignment, challenges remain in achieving greater range and smaller receiver footprints [331]. Conversely, advancements in NFC have resulted in read ranges up to 50cm, however this distance must be considered in the context of implantable devices and the likelihood of interference from tissue and proximate metallic instruments [332]. Recent studies into NFC design and tag fabrication have established methods to optimise for metallic interference and transmission distance [333, 334]. Nonetheless, it is not within scope to optimise the NFC system, but rather test its feasibility for a 'smart' interbody cage.

A tag, antenna, and reader are the three basic components of a NFC system, whereby a reader transmits a radiofrequency signal at 13.56MHz to the tag antenna, which processes and interrogates the signal before responding with the requested information [326]. The NFC tag can be a microchip that contains memory. NFC operates on the principles of magnetic coupling in the near-field between a transmitting and receiving coil. When an alternating magnetic field is generated in the transmitter coil, a current will be generated in the proximate passive receiver coil used to power the accessories at the receiving end (Figure 6.15) [326]. In this case, the active transmitter coil is externally powered and hosted on the reader, while the receiver coil is hosted on the NFC tag. A matched impedance network on the transmitter and receiver sides improves the efficiency of power transfer [326].

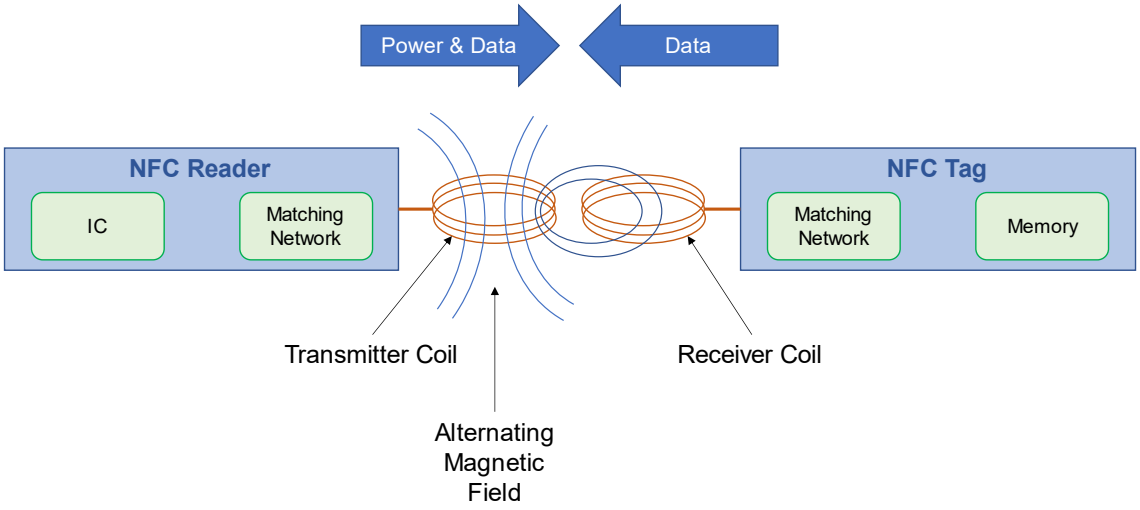

Figure 6.15: Overview of NFC data transfer and coupling mechanism [326].

NFC can operate three different communication modes:

- Peer-to-peer
- Card emulation
- Reader/writer

The peer-to-peer mode operates between two active NFC tags, both with the ability to initiate the radiofrequency field. With both ends active, the mode permits bidirectional data exchange between the two devices [325, 326].

Card emulation mode allows the NFC device to act as an NFC tag for an external reader, such as a contactless card [325, 326]. In this mode, the NFC device can behave like a regular passive NFC tag.

In reader/writer mode, an active NFC device is able to read a passive NFC tag. The active side is considered the reader/writer side. Reader/writer mode allows the NFC reader to collect data stored in an NFC tag [326]. The wireless data collection module developed for the 'smart' interbody cage is designed with NFC operating in reader/writer mode such that data can be written to the NFC tag from the sensor array and collected by the external NFC reader. The requirement for data transfer is unidirectional (from sensor to computer), making it the most suitable communication mode.

NFC is not typically designed for continuous operation. In this context, continuous operation can be considered as real-time data transfer from within the body to an external host without cessation, which requires ongoing inductive coupling. Rather, NFC is designed to operate in a transactional manner, transferring data when placed proximate to the reader and terminating upon removal of the reader from the near-field [335]. Despite the inherent safety of this approach (requiring physical proximity to acquire data), this feature has potentially resulted in a paucity of NFC-based implantable medical devices [317].

A 'smart' interbody cage does not require continuous operation, but rather seamless measurement on demand. The implanted NFC tag, therefore, remains passive until activated by the reader in the near-field which triggers data collection and transfer. There are safety and durability benefits of such an approach, whereby surrounding tissues are not exposed to continuous high-frequency electromagnetic energy and embedded hardware components are not powered for longer than necessary. Using NFC to achieve this requires adapting the transactional approach such that real-time *in vivo* data can be collected over a clinically relevant measurement period.

6.8 Translating User Requirements into Design Inputs

6.8.1 Wireless Power Delivery

The system must be entirely wireless such that external readers can collect the data recorded from the implanted sensor-embedded cage. As such, all power must be delivered wirelessly due to the safety concerns associated with *in vivo* battery-powered devices [218].

The previously studied Amphenol (Novasensor, USA) P122 sensors operate at 1mA with a maximum voltage of 10V, while the EFM8BB52 microcontroller (Silicon Labs, Texas, USA) operates at 1.8V. Strain gauge patterns are comparatively low resistive loads (120Ω) compared to the piezoresistive pressure sensors (5kΩ). As such, the strain sensors are unlikely to increase the required supply voltage. The embedded NFC module, therefore, should not substantially increase the power consumption of the system and should be capable of delivering at least 1.8V.

6.8.2 Wireless Data Transfer

The system must be capable of wirelessly collecting data from the sensors and transmitting it to a proximate computer for logging and presentation. The implanted electronics should not require network or cloud access capabilities. The system may require devices that are external to the patient to amplify or project the signal from the *in vivo* implant to the host computer.

The frequency of data collection should be no less than 2Hz based on the assumption that the most pertinent monitoring scenario will be in clinic. In such settings, exercises and activities performed would be monitored by a clinician and performed in a controlled manner that ensures the quality of the data captured. For example, bending slowly and holding a position over a number of seconds allows for the collection of a sufficient number of data points at a rate of 2Hz. A data collection rate of less than 2Hz may require patients to perform movements and hold positions for an uncomfortably long period of time. Higher data sampling rates will increase the scope of activities that will generate clinically meaningful data, for example, walking or running, which produce more rapid load changes on the implant.

6.8.3 Sufficient Transmission Distance

The NFC tag must be capable of transmitting the data to a reader wirelessly through a distance of at least 100mm, based on measurement of a magnetic resonance imaging (MRI) scan (Figure 6.16), if the receiver coil is to be embedded on or within the implant. Similarly, power transfer from the transmitter coil to the receiver coil must be achievable across the same distance. Data and power transmission must be functional through a medium consisting of bone, muscle, ligament, and fat tissues at a minimum. The receiver may not necessarily be the host computer, but rather an amplifier or any other device that projects or sends the data to the proximate host computer for logging and presentation.

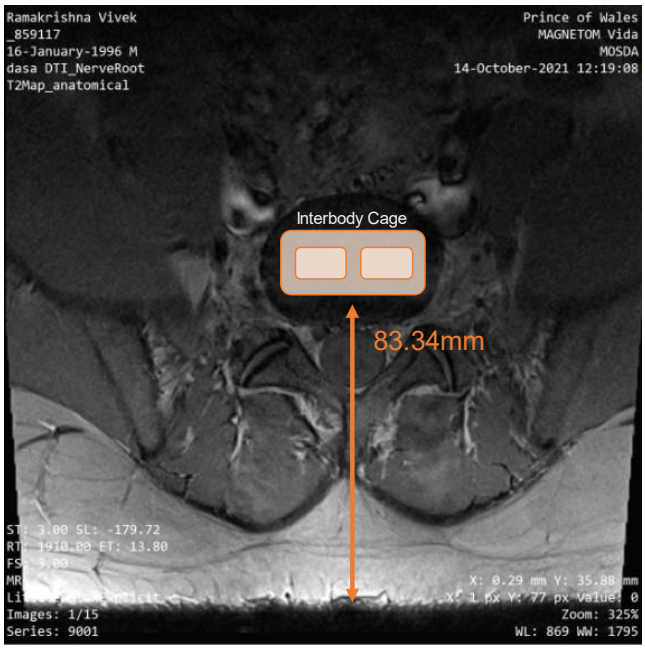

Figure 6.16: MRI scan showing the distance between the dorsal aspect of the vertebral body and the outer surface of the skin is 83.34mm in this example.

6.8.4 Implantable Size

The wireless module must be small enough to fit within the implant. Subcutaneous housing of electronics within the body physically connected to the implant presents additional risks to data collection and patient safety.

Reducing the number of embedded sensors affords space for the telemetry module within the implant. Considering the same XLIF cage dimensions as Section 5.4.3, the maximum length for an embedded telemetry module is 3.5mm in its minor axis, however it may occupy a length up to 45mm in the current XLIF cage. The maximum height for the module in the vertical (cephalocaudal) direction is 4mm, due to the presence of the bone graft cavities (Figure 5.1).

6.8.5 Biocompatibility

Biocompatibility is not considered at this stage of development given the further work required to finalise encapsulation and manufacturing before reaching *in vivo* testing. Later development stages should aim to comply with ISO 10993 to evaluate the biocompatibility of the device.

6.8.6 Adaptability

Given the findings of the sensor optimisation analysis and potential developments towards kinematic data collection, the wireless telemetry module should support various sensing modalities, for example pressure and strain. Within the power constraints, the module should accommodate increasing and expanding the sensor components without changes to the system architecture. The telemetric hardware should not restrict data collection and processing activities to the greatest extent possible. Further, as mentioned in Section 6.8.2, an adaptable data sampling frequency will enable logging of clinically meaningful data in different measurement contexts.

6.9 Wireless Module System Overview

An overview of the designed wireless data collection module is shown in Figure 6.17.

Figure 6.17 describes how data is collected wirelessly from the sensor target embedded in the interbody cage. The microcontroller (EFM8BB52) processes the signal from the sensors, as previously described, including signal conditioning and analogue to digital conversion (ADC). The microcontroller, operating at 1.8V, is supplied by the NFC chip (NT3H2211; NXP Semiconductors, Netherlands), which is in-turn wirelessly powered by the magnetic coupling between the receiver and transmitter coils.

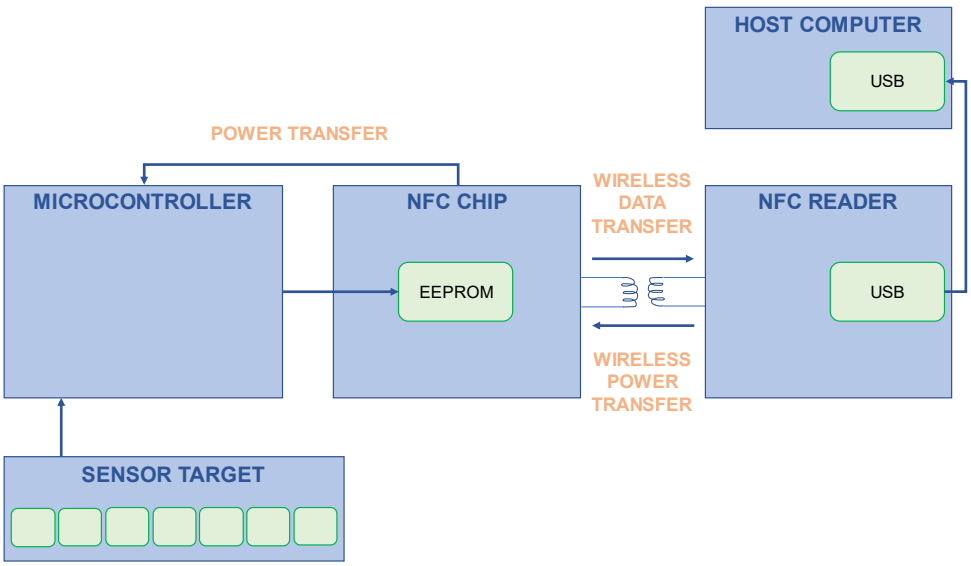

Figure 6.17: Overview of the wireless data collection module. The details within the microcontroller and host computer are unchanged from v2.0 of the previously described data collection module in Section 5.4.5.

The schematic of this system is shown in Figure 6.18. The NT3H2211 NFC chip was selected due to its affordability, suitable size, and low power consumption (2V, 2mA). The two coils are enamel copper wires (0.4mm thick, 4 turns) of 30mm in diameter (Figure 6.19). Processed data from the microcontroller is written to the NFC chip memory (EEPROM: Electrically Erasable Programmable Read Only Memory). The data is received by the NFC reader and transferred to the host computer via USB connection. The USB connection simultaneously facilitates data and power transfer between the computer and NFC reader. Power supply to the NFC reader allows it to generate the alternating magnetic field. The NFC system is designed to be agnostic to the sensor target; the 7-sensor system is presented as an example.

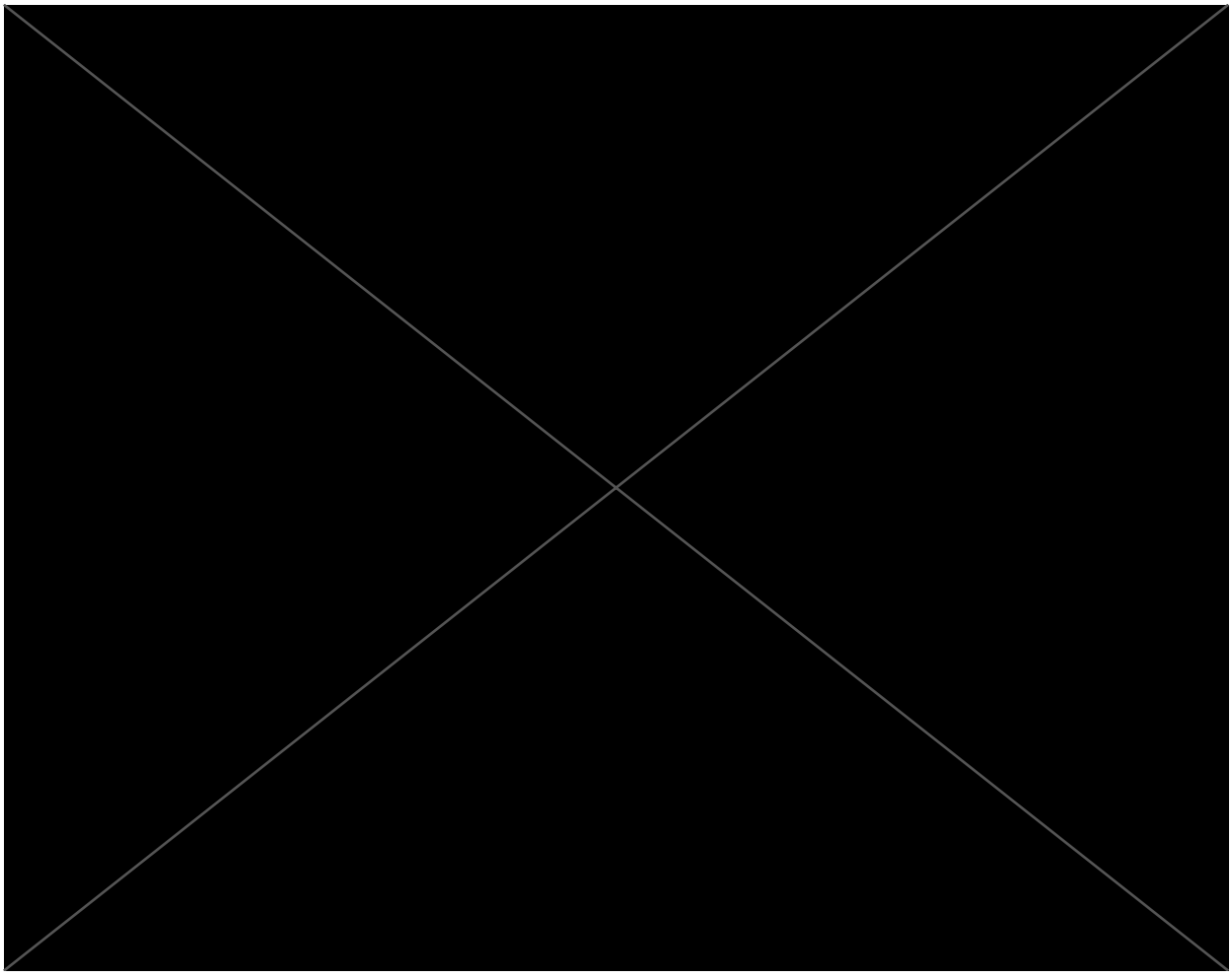

Figure 6.18: Schematic of the NFC tag and microcontroller.

The fabricated NFC tag and reader are shown in Figure 6.19. Dimensions of the inductive coils were not studied or optimised.

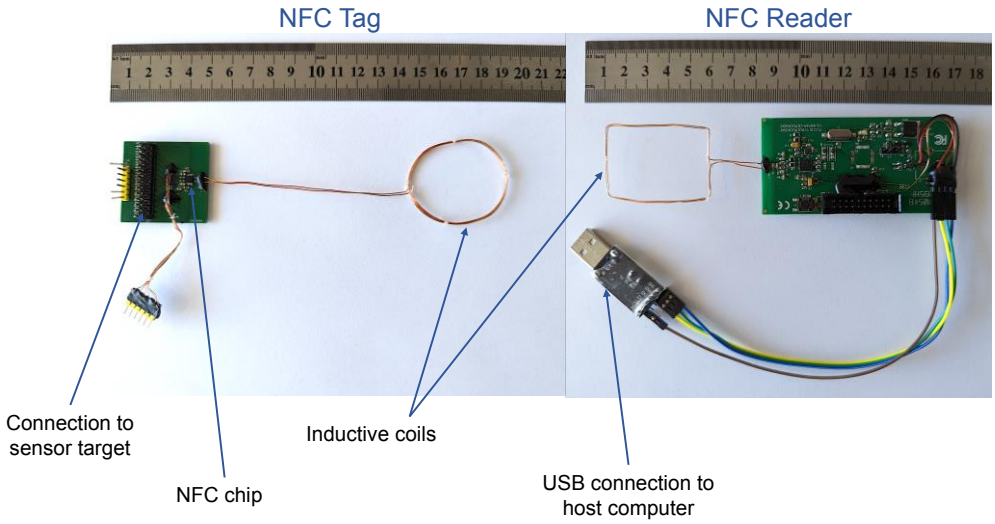

Figure 6.19: Fabricated NFC tag and NFC reader as per the schematic and overview.

6.9.1 Read/Write Protocol

The NFC reader operates the protocol outlined in Figure 6.20.

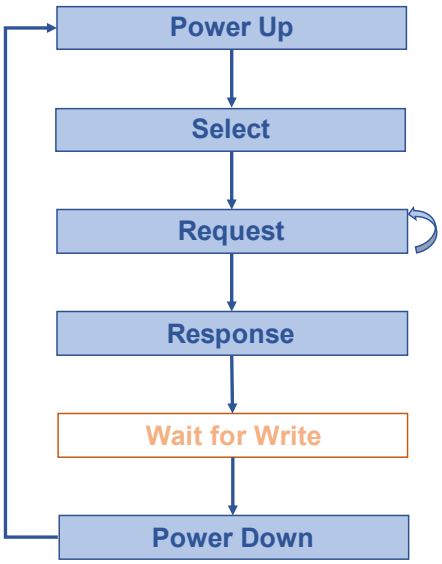

Figure 6.20: Protocol for the NFC reader to collect data from the NFC tag.

After powering up, the NFC reader selects the target within the radiofrequency field. The reader sends a request to the NFC chip, which contains the stored data. The request may be declined by the NFC chip, for example, if it occurs during the initialisation period when the NFC chip is in the immediate phase following power-up. When the reader obtains an affirmative response from the NFC chip, it collects the data that was stored in the EEPROM and sends it to the computer via USB connection (Figure 6.17). Following

a response, the NFC reader will not make any requests to the NFC chip, allocating a fixed time to have data written from the microcontroller to the memory. The NFC reader then powers down.

Figure 6.21 shows at the time point t_0, the power up has been triggered, however the NFC chip does not begin to function until the power delivered to the NFC tag crosses the threshold operational voltage V_{th}, which is 2V for the NT3H2211 NFC chip (time point t_1). Power delivered continues to increase until the maximum deliverable power from magnetic induction between the coils is achieved. V_D is 3.16V for the designed module without separation between the coils, however power delivery is studied further in Section 6.11. Between time points t_1 and t_2, the NFC chip conducts its initialisation processes. During this period, no read or write processes are performed. From t_2 to t_3, the NFC EEPROM allows data to be read by the NFC reader, and from t_3 to t_4, data from the microcontroller is written to the NFC EEPROM. The NFC powers down at t_4 and completely switches off after the voltage drops below V_{th}.

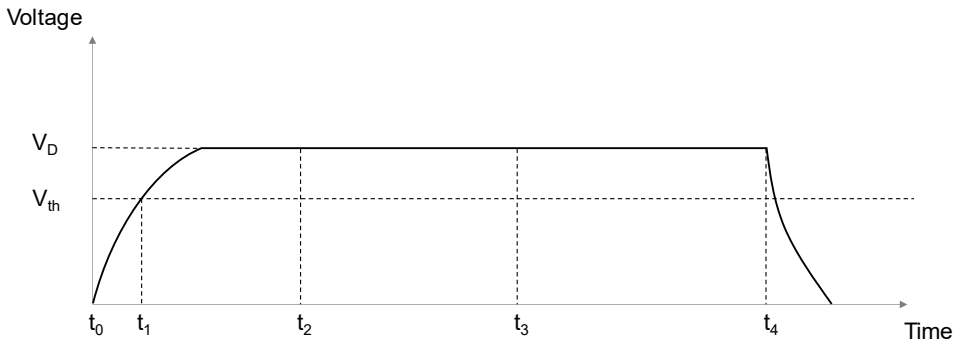

Figure 6.21: Read and write protocol as an analogue function of time and voltage.

6.9.2 Sampling Rate

Figure 6.22 illustrates how the process of powering on and off triggers the read and write process. In the first period t_r after powering up, the NFC is locked into a read mode where the data stored in the NFC EEPROM is being read by the NFC reader and passed on for logging and visualisation. Simultaneously, data is being gathered from the sensors and held by the microcontroller, however can not be written to the EEPROM during the read process. In the immediate period after the read process, during t_m, the new measurements collected from the sensors are written to the NFC EEPROM. During this

write process, data can not be read from memory by the NFC reader. Following the write process, the NFC reader powers down (t_{off}).

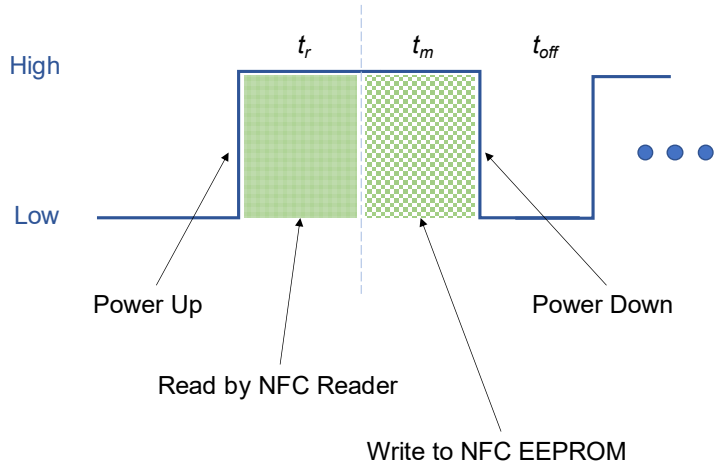

Figure 6.22: Read and write protocol for NFC module presented digitally.

The read (t_r) and minimum turn-off (t_{off}) durations are negligible compared to the measurement time (t_m). The measurement period, t_m, is the duration of time for which data from the sensors is being collected and stored. In a clinical setting, this measurement period is of interest depending on the activity or movement being monitored.

The NFC EEPROM can store a maximum of 1024 readings. If the NFC module is, for example, connected to a PCB with 7 dual-channel sensors as per Section 5.4.1, with additional temperature and input voltage channels (16 channels total), then a total of 64 measurements per sensor can be stored in the EEPROM. The sampling frequency can be adjusted up to a maximum of 100Hz, however the EEPROM memory limit can not be exceeded. In this chapter, the sampling frequency is set to 1Hz for a measurement period of 10 seconds.

6.10 Demonstration of NFC Data Transactions with the Wireless Interface

The transactions between the microcontroller and NFC tag demonstrate that the power delivered to the NFC tag, in addition to the software protocols, were sufficient to allow data to be written from the microcontroller to the NFC EEPROM. The connection between the sensors and the microcontroller did not change between the v2.0 module and the wireless NFC module. NFC transactions were interrogated using the Saleae

Logic Pro 8 and associated Logic2 software package (Saleae, San Francisco, USA). If wireless power delivery through the NFC and magnetic induction were insufficient, the sensor data would not be written to the NFC memory. The aim of verifying the NFC transactions is to ensure that data is being accurately written to the NFC memory with the power being delivered wirelessly.

Figure 6.23 shows rising edges on the clock and data acquisition channels. Simultaneous rising edges on both channels indicates that the NFC chip is powering up through the wireless interface. In any other circumstance, the data and clock channels should not have simultaneous rising edges. The immediate delay thereafter is the period in which the NFC chip is performing its internal initialisation processes.

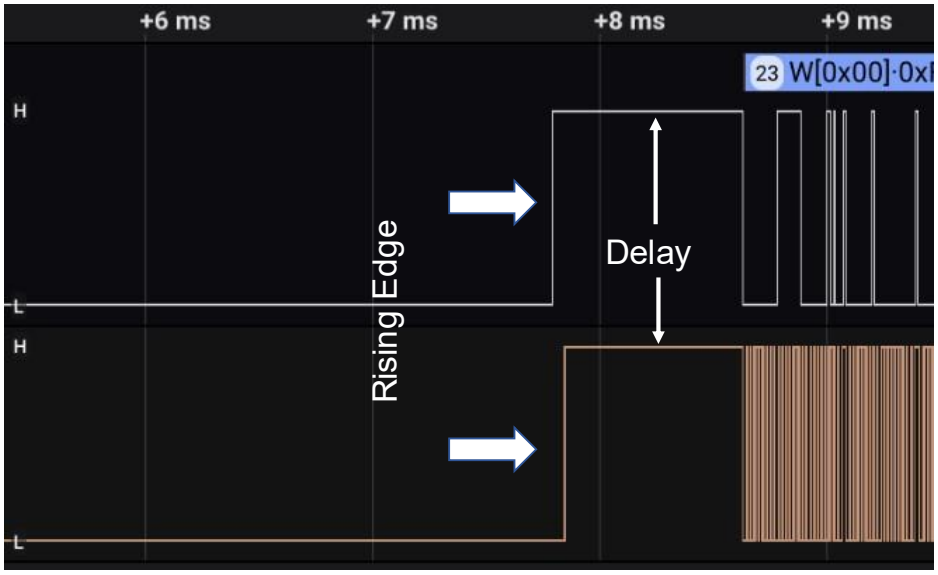

Figure 6.23: NFC transaction showing rising edges upon powering up. Data acquisition is shown on the top (white) and the clock is shown on the bottom (orange).

Figure 6.24 depicts two data transactions between the microcontroller and NFC chip where data is being written to the EEPROM. The hexadecimal sensor values are shown at the top of the figure. The data transactions demonstrate that the NFC chip and microcontroller are sufficiently powered through the wireless interface such that data is being collected from the sensors and written to NFC memory.

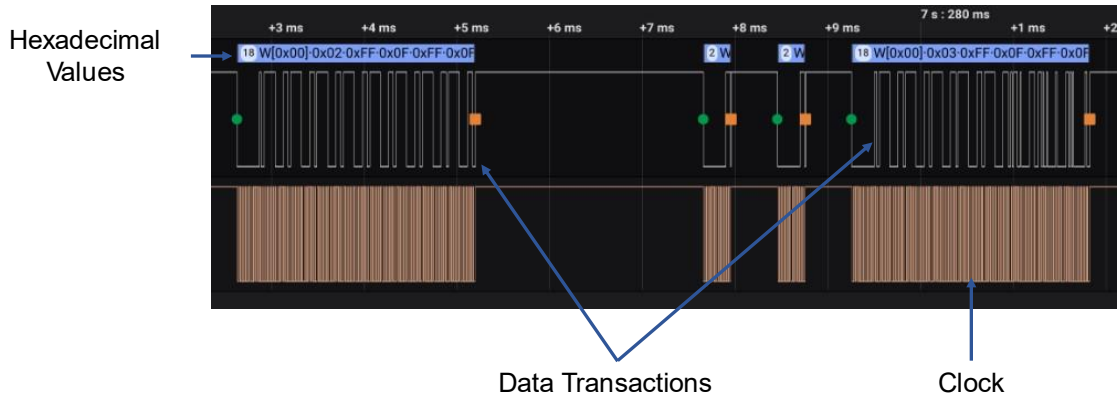

Figure 6.24: Data transactions between the microcontroller and NFC chip.

The NFC module is capable of operating two modes. In the first mode shown in Figure 6.25, the NFC chip powers up and immediately waits for the NFC reader to collect the data that has been stored in the NFC EEPROM. Once the read process is completed, new data is written to the memory.

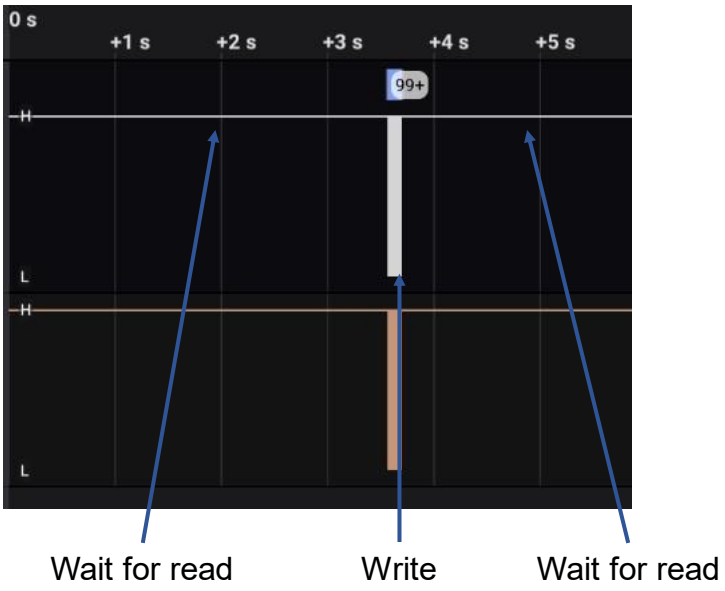

Figure 6.25: NFC transaction in read-first mode. The NFC operating in a mode where it reads what is collected in the NFC memory upon powering up before writing any new data to the NFC EEPROM.

In the second mode, immediately after initialisation of the NFC chip, data is written to the EEPROM from the microcontroller prior to the NFC chip waiting for the read process to occur. This mode is depicted in the transactions in Figure 6.26.

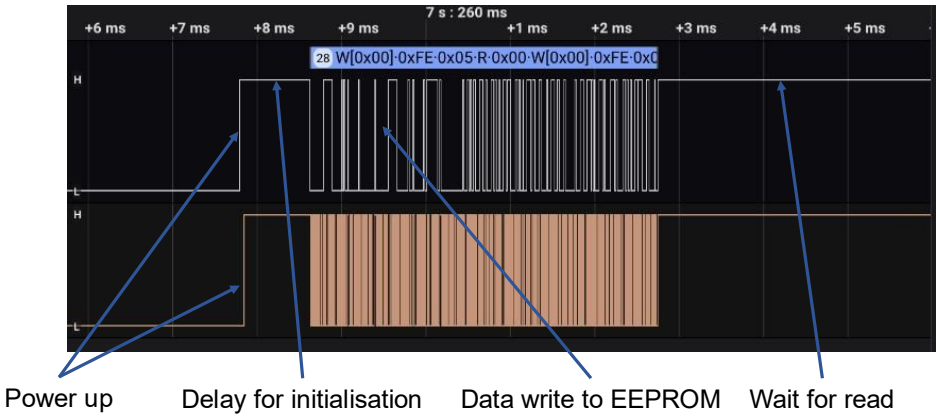

Figure 6.26: NFC transaction in write-first mode. The NFC operating in a mode where data is immediately written to the EEPROM before it waits for the read process.

The two-mode operation is a consequence of the system architecture, however it allows control over the timing of the delay and flexibility to determine when data is transmitted and stored based on the user's needs. The 'read-first' mode was adopted in the current work.

6.11 Testing the Effectiveness of Wireless Power Transmission

Wireless power delivery to the NFC tag was assessed through 4 media; air, tissue, bone, and gel. The media were placed between the NFC reader and NFC tag, entirely covering the surface area of the receiver coil (Figure 6.27). Turkey breast meat (1.5mm slices) was used to simulate the muscle tissue medium, representative of skin and muscle through which power transmission is required. Sawbones (USA) synthetic cancellous bone represented the bone medium. It is necessary to examine the extent to which the signal could be attenuated by proximate bony structures, in addition to potential attenuation by the fusion mass which may ossify outside the graft cavities. Lastly, gelatine was used to simulate fluids such as cerebrospinal fluid (CSF). The gel material may be seen as similarly demonstrative of the mechanical properties of fat, notwithstanding its high water content. While a fluid solution is more suitable to represent CSF, the gel provided greater control of the medium thickness. The gel medium consisted of 1 part salt, 2 parts gelatine powder, and 5 parts water by weight. Blue dye was added to improve visualisation. Given the different properties of the media, not every medium could be cut to the same thickness. For example, the turkey slices were 1.5mm thick, however the

gel could not be produced in the same thickness due to its softer texture and tendency to break.

Voltage was measured by a SainSmart (USA) DDS-140 USB Oscilloscope at the V_{DD} line of the NFC tag (Figure 6.18). The aim of the presented testing was not to extensively investigate power transmission distance, but rather to determine the feasibility of the chosen NFC design in the context of a 'smart' interbody cage. Thereafter, further optimisation and integration testing will lead to refinement and more rigorous experimentation.

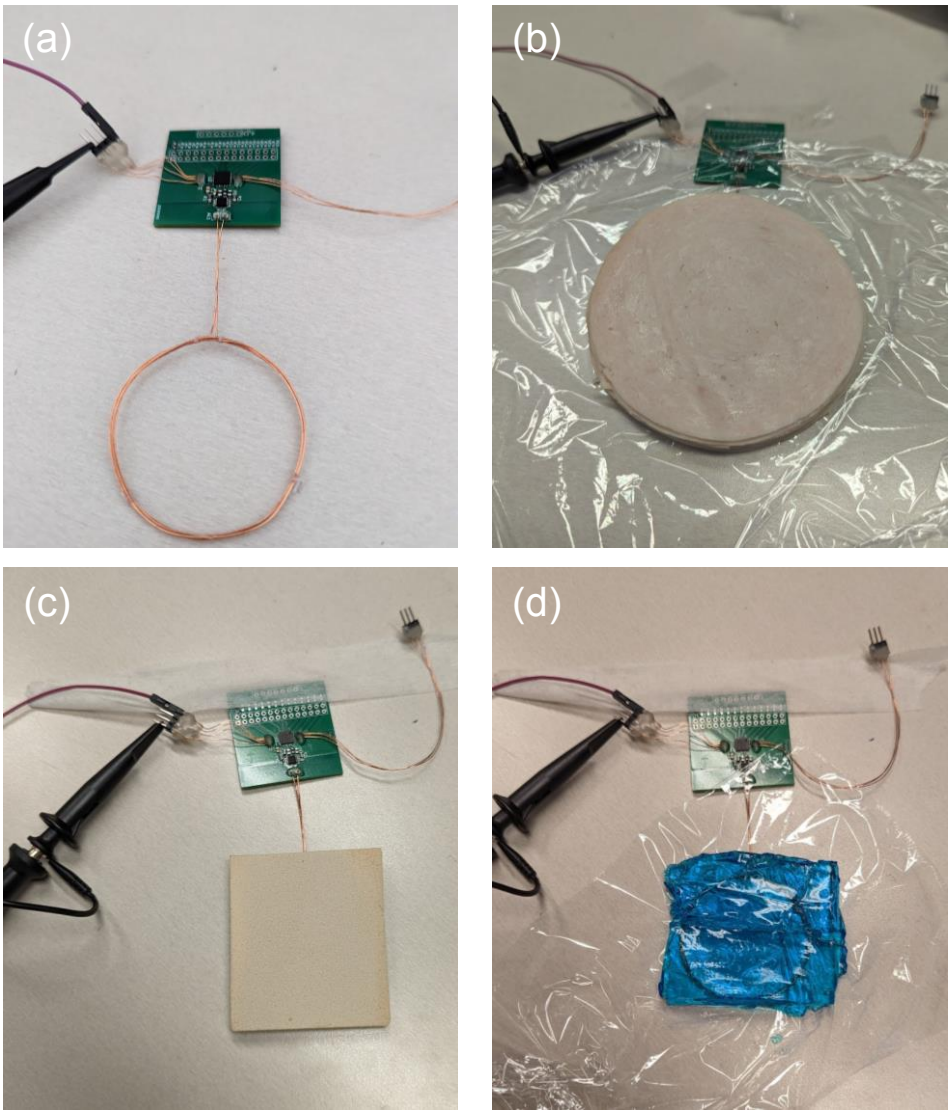

Figure 6.27: Receiver coil and NFC tag with (a) air, (b) tissue, (c) bone, and (d) gel media. The surface of the receiver coil was entirely covered by each medium.

Figure 6.28 illustrates the effectiveness of wireless power transfer through the 4 media at different distances. The minimum required voltage for the NFC chip to operate is 2V. Through the air medium, 2V was delivered at a maximum distance of 42mm. No attenuation was observed between 0mm and 5mm. The measured voltage dropped between 5 and 15mm, however 2.63V was consistently received between 15mm and 30mm. Through the remaining 3 media, the distance through which 2V was delivered was comparable (Bone = 24mm; Gel = 25mm, Tissue = 28mm). Consistent and reliable power transfer was observed up to 25mm for gel and 26mm for tissue, but only 15mm for bone. Thereafter, sharp attenuation occurred. The acute attenuative characteristics of bone are worth noting in the context of fusion mass ossification. Further studies may elucidate the impact of adjacent bony structures on signal attenuation more explicitly. It is pertinent to study the behaviour of tissue and gel media more thoroughly in the region of 15mm to 30mm, where there is a moderate voltage drop per unit distance prior to falling below the 2V minimum requirement, to confirm whether power delivery remains consistent and reliable in that transmission range. Voltage fluctuations were observed through the gel material from 30mm to 35mm and in the tissue medium from 31mm to 33mm.

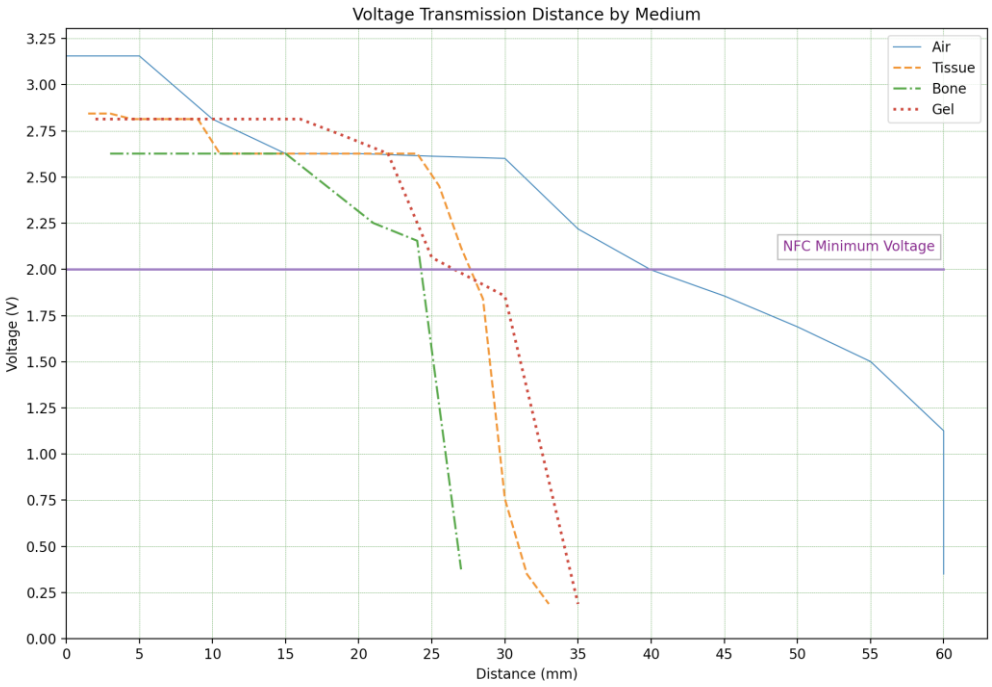

Figure 6.28: Voltage measured at the NFC tag for different distances of power transmission through the 4 media.

There are some notable limitations with the media used to test power transmission. Firstly, it was not possible to completely surround the receiver coil in the material in all directions, due to the limited number of samples and risk of damage. Further, it presented additional challenges in controlling the thickness of the medium. Secondly, while the media attempted to represent the physical characteristics of the bone, tissue, and CSF, they are not able to replicate the same chemical and biological characteristics. Hydration in muscle tissue, calcium in bone, and electrolytes in CSF may attenuate the power signal differently to the media tested. Lastly, it was not practical to simulate the variety of tissues present in the body, such as tendon and fat.

6.12 Validating the Accuracy of Wireless Data Telemetry

6.12.1 Simulation Board Design

Section 6.10 demonstrated that data from the sensors is stored in the NFC EEPROM using wireless power only, while Section 6.11 assessed the extent of power delivery. The accuracy of wireless data transfer between the NFC tag and the host computer requires validation. To evaluate the accuracy of data transferred wirelessly using NFC, a board was assembled containing 14 potentiometers (3006p 503 Suntan, Hong Kong; 15 turn; 50kΩ), simulating the channels of 7 piezoresistive sensors (Figure 6.29). The potentiometer board is used as an example to validate data accuracy only, with the number of sensor components likely to change with ongoing experimentation.

The simulation board was connected to the NFC tag as the sensor target according to Figure 6.18. Potentiometers were used rather than sensors, as the values can be controlled and outputs can be verified by oscilloscope measurement. Conversely, the sensors are less reliable, and its outputs are not controlled or verifiable. Further, the wireless telemetry module is agnostic to the sensing modality where it produces changes in resistance or potential. The potentiometers represent this versatility. While the sensors used in Chapter 5 were 5kΩ resistive loads, assembling 7 such potentiometers would push the 2mA limit of the microcontroller internal regulator. As such, 50kΩ potentiometers were used on the simulation board.

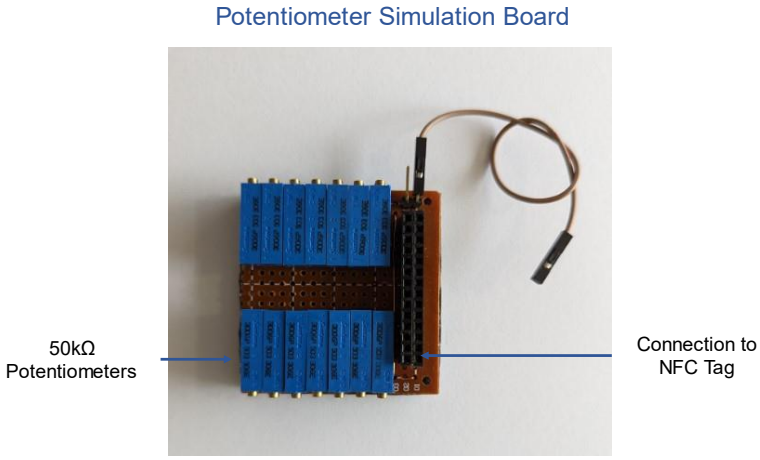

Figure 6.29: Fabricated potentiometer simulation board used as a sensor target for the NFC tag.

6.12.2 Data Validation

An example of a wireless data capture is shown in Figure 6.30, with channels 0 to 13 recording voltages at the potentiometers, channel 14 displaying the supply voltage (V_{DD}), and channel 15 representing temperature. The capture shows the data collected over a 10 second measurement period at 1Hz.

ADC Readings
2023-01-30 10:02:51

Channel	Volts ADC 1	Volts ADC 2	Volts ADC 3	Volts ADC 4	Volts ADC 5	Volts ADC 6	Volts ADC 7	Volts ADC 8	Volts ADC 9	Volts ADC 10
0	0.6451	0.6451	0.6451	0.6451	0.6460	0.6451	0.6451	0.6451	0.6451	0.6451
1	0.8420	0.8648	0.8420	0.8402	0.8648	0.8402	0.8402	0.8420	0.8420	0.8402
2	0.8420	0.8420	0.8420	0.8420	0.8420	0.8420	0.8420	0.8420	0.8420	0.8420
3	0.6961	0.6961	0.6961	0.6961	0.6961	0.6961	0.6961	0.6961	0.6961	0.6961
4	0.8016	0.8016	0.8016	0.8016	0.8016	0.8016	0.8016	0.8016	0.8016	0.8016
5	0.6715	0.6750	0.6750	0.6715	0.6680	0.6715	0.6750	0.6680	0.6715	0.6715
6	0.7014	0.7014	0.7014	0.7014	0.6996	0.7014	0.7014	0.6996	0.7014	0.7014
7	0.6750	0.6750	0.6750	0.6820	0.6750	0.6891	0.6750	0.6750	0.6750	0.6891
8	0.6996	0.7014	0.6996	0.6996	0.6996	0.6996	0.7014	0.6996	0.7014	0.6996
9	0.9272	0.9272	0.9272	0.9277	0.9272	0.9277	0.9272	0.9277	0.9272	0.9277
10	0.9211	0.9211	0.9211	0.9211	0.9211	0.9211	0.9211	0.9211	0.9211	0.9211
11	0.7014	0.7014	0.7014	0.7014	0.7014	0.7014	0.7014	0.7014	0.7014	0.7014
12	0.8701	0.8701	0.8701	0.8701	0.8701	0.8701	0.8701	0.8701	0.8701	0.8701
13	0.6961	0.6961	0.6961	0.6961	0.6961	0.6961	0.6961	0.6961	0.6961	0.6961
14	1.1461	1.1461	1.1461	1.1461	1.1461	1.1461	1.1461	1.1461	1.1461	1.1461
15	0.3516	0.3516	0.3516	0.3516	0.3516	0.3516	0.3516	0.3516	0.3516	0.3516

Figure 6.30: Example of voltage measurements from the simulation board over a 10 second measurement period at 1Hz. Channels 0 to 13 represent the sensor measurements. The data was printed to the terminal.

Data obtained wirelessly (coil separation = 20mm) was compared to oscilloscope measurements at the potentiometer baselines, 5 turns, 10 turns, and 15 turns (Table 6.4). The voltage output at each potentiometer was measured using a SainSmart DDS-140 USB Oscilloscope. Measurements from the oscilloscope were adjusted to compensate for -0.022V of noise measured in the grounded state.

The comparison between NFC-obtained and oscilloscope-measured data validates that the wireless telemetry module is accurately transferring data from the sensor target to the computer terminal across the required range of voltages. The errors were within an acceptable range as discussed further in Section 6.13.2.

Data transmission was also tested through Bone, Gel, and Tissue media at the 2V cut-off distance for each material (Bone = 24mm; Gel = 25mm, Tissue = 28mm). No variation or corruption of data was observed over the 10 time points. At greater distances, communication between the tag and reader failed, however there was no logging of partial or corrupt data.

Table 6.4: Simulation board voltage measurements (V) from the oscilloscope and wirelessly transmitted by NFC.

	Baseline		**5 Turns**		**10 Turns**		**15 Turns**	
Channel	**Oscilloscope**	**NFC**	**Oscilloscope**	**NFC**	**Oscilloscope**	**NFC**	**Oscilloscope**	**NFC**
0	0.000	0.000	0.539	0.539	1.357	1.339	1.766	1.746
1	0.000	0.000	0.711	0.703	1.529	1.504	1.766	1.746
2	0.000	0.000	0.711	0.704	1.529	1.504	1.766	1.746
3	0.000	0.000	0.582	0.582	1.400	1.386	1.766	1.746
4	0.000	0.000	0.668	0.670	1.465	1.457	1.766	1.746
5	0.000	0.000	0.560	0.562	1.378	1.340	1.766	1.746
6	0.000	0.000	0.603	0.587	1.400	1.387	1.766	1.746
7	0.000	0.000	0.560	0.576	1.378	1.363	1.766	1.746
8	0.000	0.000	0.582	0.585	1.400	1.386	1.766	1.746
9	0.000	0.000	0.797	0.776	1.615	1.505	1.766	1.746
10	0.000	0.000	0.754	0.770	1.594	1.505	1.766	1.746
11	0.000	0.000	0.603	0.587	1.400	1.386	1.766	1.746
12	0.000	0.000	0.732	0.728	1.551	1.505	1.766	1.746
13	0.000	0.000	0.582	0.582	1.400	1.363	1.766	1.746

The percentage error in NFC-obtained data with respect to the oscilloscope measurements is presented in Table 6.5.

Table 6.5: Percentage error in NFC-obtained data with respect to the oscilloscope measurements.

Channel	Baseline	5 Turns	10 Turns	15 Turns
0	0.0	0.1	-1.3	-1.2
1	0.0	-1.2	-1.6	-1.2
2	0.0	-1.0	-1.7	-1.2
3	0.0	0.0	-1.0	-1.2
4	0.0	0.3	-0.6	-1.2
5	0.0	0.3	-2.8	-1.2
6	0.0	-2.7	-0.9	-1.2
7	0.0	2.9	-1.1	-1.2
8	0.0	0.5	-1.0	-1.2
9	0.0	-2.7	-6.8	-1.2
10	0.0	2.2	-5.6	-1.2
11	0.0	-2.7	-1.0	-1.2
12	0.0	-0.6	-3.0	-1.2
13	0.0	0.0	-2.6	-1.2

6.13 Addressing the Requirements for Wireless Telemetry

6.13.1 Wireless Power Delivery

The wireless power transfer results, NFC data transactions, and simulation board results establish the sufficiency of power supplied through inductive coupling. With sufficient power transfer, implanted batteries are not required, and the associated risks are avoided. Above the 2V minimum, the designed system is robust to fluctuations in power delivery that may arise from bioelectrical interference or minor movements of the coils. The voltage regulator ensures a maximum supply of 1.8V to the microcontroller and sensor target.

In practice, 7 sensors with nominal loads of 5kΩ would not be supported by this NFC module in a 'smart' interbody cage due to the 2mA limit of the microcontroller internal regulator. This example, however, was used to prove the concept and feasibility of NFC for this application. A reduction in sensing components, in accordance with the findings of Section 6.6.5, is necessary to ensure reliable power supply through NFC. Nevertheless, the wireless power delivered to the simulation board was stable across the 10 second measurement period.

Multimodality sensing will likely require a more thorough investigation of power consumption, however the presented results demonstrate that NFC is a feasible method for wireless power delivery. In future iterations of the telemetry module that integrate with a multimodality sensing board, power supply to each unique sensing modality can be tailored to meet its specifications using additional software features and bias resistors.

6.13.2 Wireless Data Transfer

The NFC system was capable of wireless data transfer between the sensor target and host computer. The maximum sampling frequency of the designed module is 100Hz, however, of more relevance is the maximum number of readings that can be stored in the NFC EEPROM. As previously stated, the EEPROM can store a maximum of 1024 readings, equating to 64 measurements per sensor for a 7-sensor board. The sampling frequency of the system can be adjusted to collect the 64 measurements per sensor at a rate appropriate to the activity being monitored. For example, the full set of data can be collected over a measurement period (t_m) of 64 seconds at a rate of 1Hz, 32 seconds at a rate of 2Hz, or 128 seconds at a rate of 0.5Hz. In this chapter, the sampling frequency was set to 1Hz for a measurement period of 10 seconds, however the utility of this setting was not assessed, as the sensor target was not subjected to time-dependent change. Reducing the number of sensors will enable a higher sampling frequency to be used over a longer measurement period. Further research is required to determine suitable data sampling frequencies for monitoring postoperative activities of clinical interest. Nevertheless, the alterable sampling frequency provides versatility in its clinical use.

Using live data transfer, the system is capable of reliably transferring 128 readings per second, equating to 8 measurements per sensor per second using the above example. While this is within the capability of the module, implementation would require software modifications that are beyond the scope of works in this thesis.

The accuracy of the wirelessly transmitted data was validated by the results from the simulation board. The bone, gel, and tissue media did not corrupt the data. Excluding the voltages recorded at 10 turns from channel 9 (6.8%) and channel 10 (5.6%), the discrepancy between the wireless data and oscilloscope measurements was less than 5%. The discrepancies are reasonable considering the potential sources of error. The maximum measured voltage from the oscilloscope was 1.766V; 2% lower than the typical

output from the (EFM8BB52) microcontroller voltage regulator, but within the bounds of its specified range (1.75-1.85V). This error can be addressed by using a more stable external reference voltage. Further, the EFM8BB52 microcontroller datasheet specifies a maximum 1% nonlinearity error arising from the ADC, and a maximum 5% error arising from noise and other factors. The discrepancies observed between the wireless data and oscilloscope measurements fall within the bounds of expected errors specified by the datasheet. Noise and nonlinearity errors can be compensated using software post-processing techniques and oversampling to reduce the error rate and increase the number of effective bits.

6.13.3 Sufficient Transmission Distance

The wireless power transfer results through different media suggest that the telemetry system, in its current state, is not capable of delivering power through ~100mm of tissue to the location of the interbody cage. While housing the receiver coil on the implant is advantageous for encapsulation purposes, there are several challenges associated with this approach, assuming the coil and circuitry can be optimised to achieve such wireless transfer distances. Firstly, wirelessly transmitting high-frequency electromagnetic energy towards the implant will require tissue safety studies, particularly considering the neural tissues proximate to the implant site. Wireless energy transfer over larger distances increases the field of adjacent tissues that absorb the signal. This approach may risk damage to nerve roots and the spinal cord, however further research is required to confirm such effects. Secondly, interbody cages are commonly implanted with metallic supplemental fixation constructs, such as screws, rods, and plates. Further, small metallic pins are common features of interbody cages to improve endplate traction. The presence of these metallic components in the vicinity of the receiver coil will likely cause interference with wireless power and data transfer. Potential absorption and refocusing of radiofrequency waves by metals presents an additional challenge to maintaining the safety of surrounding tissue.

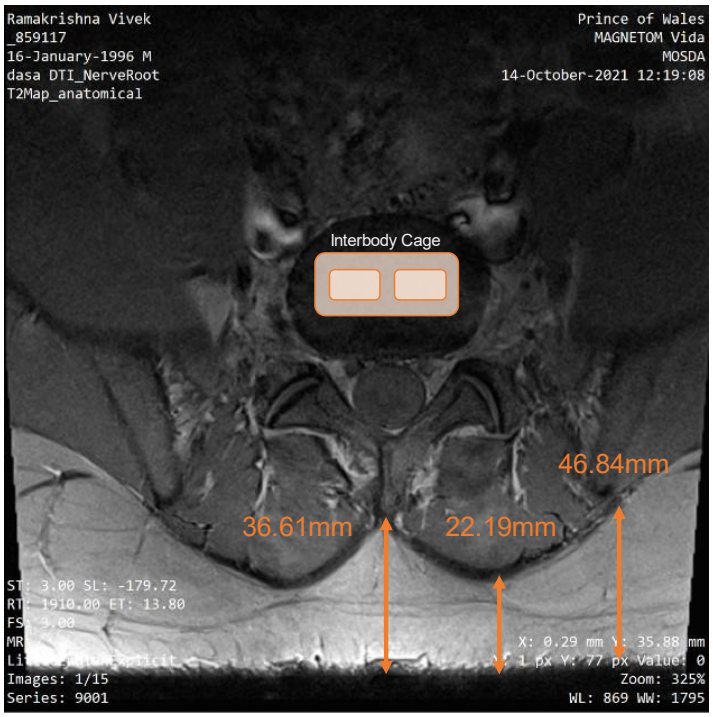

Figure 6.31: Approximate distances between the epidermis and dermis in different locations near the lumbar spine.

The results suggest that consistent wireless power transfer can be achieved over a distance of 25-28mm. As Figure 6.31 suggests, wireless transfer can be achieved between a transmitter coil on the external surface of the skin and an extra-fascial sub-dermal receiver coil, depending on their locations. This arrangement, however, would require physical connection between the receiver coil and the interbody cage, which houses the sensors and microcontroller, similar to pacemakers which use hybrid silicone wiring over longer distances between the device and the heart [336]. There is an associated risk of wire dislodgement using this approach, however metallic interference will be avoided.

While the wireless power transfer results through tissue and gel media suggest that sub-dermal energy transfer is feasible, further testing should be performed with more realistic material models, accounting for bioelectrical interference and resistive losses in transmission between the receiver coil and the interbody cage. Circuit and coil optimisation were not performed in this work, however such investigations may yield increases in wireless transmission distances.

6.13.4 Implantable Size

The presented NFC tag was not designed for implantation, but rather as a proof-of-concept, with dimensions of 41 x 38 x 3mm. The attached coil had a diameter of 30mm, however coil size was not studied or optimised in this thesis. Notwithstanding the further work required to optimise the sensing configuration and finalise the design of the sensor target board, Figure 6.32 demonstrates that the PCB design can be optimised to reduce the size of the implanted NFC tag. On a flexible PCB, the dimensions of the board can be reduced to 45 x 18 x 0.8mm for further prototyping while experimenting further with sensor integration, and 40 x 10 x 0.8mm for an implantable 'smart' cage.

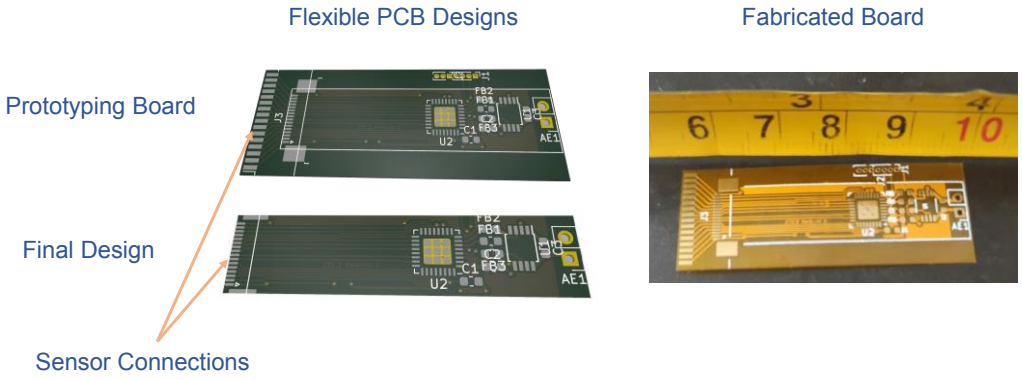

Figure 6.32: PCB layouts and fabricated board showing miniaturisation of the implanted NFC tag and microcontroller board.

With a reduction in the embedded sensing components, the final NFC tag design is within the bounds of commercially available XLIF cage dimensions. The NFC tag supports 7 sensors, however embedding less sensors will enable further miniaturisation of the PCB. Advanced manufacturing techniques should be investigated to optimise enclosure of the NFC tag within the implant.

6.13.5 Biocompatibility

Biocompatibility was not addressed in this thesis. The position of the implanted receiver coil will have a substantive bearing on the biocompatibility of the 'smart' implant. If the coil is positioned sub-dermal, exposed enamel copper wires are not suitable for *in vivo* use, however silicone wires are a biocompatible alternative.

6.13.6 Adaptability

The presented telemetry module is sufficiently adaptable to different sensing modalities, measurement applications, and post-processing pipelines. The NFC system was designed to use software-driven processes with broad-scope, generic hardware components. As such, the performance of the system is not limited by the choice of sensors, but rather remains versatile with modifications to the operating software. At a high-level, the system was designed to wirelessly gather raw voltages from the sensor outputs, performing all other necessary processing using software. Post-processing, such as linearisation, temperature compensation, and drift compensation can be readily incorporated in the software.

As previously discussed, the sampling frequency can be practically adjusted in the software up to 100Hz, with an associated trade-off in the duration of the measurement period. The sampling frequency and measurement period can be modified in the software to suit the activity or motion of clinical interest, as the rate of mechanical change produced will vary by the type of movement being performed. In this case, the versatility of the design sustains its clinical utility. Nevertheless, NFC and inductive powering are designed to be discontinuous, that is, the system does not record or transmit data continuously over time periods in the order of minutes (or longer) regardless of any software adjustments. Discontinuity ensures the body is not unnecessarily exposed to electromagnetic energy and circuitry is not powered for longer than required, improving the lifetime of the implanted hardware components.

Within the scope of the electrical loads tested in the current work, the NFC system is adaptable to other sensing modalities. By focusing on raw data collection, the telemetry unit permits the connection of alternate sensors to this module with software features handling power delivery to the sensors. Taking the example of the integrated sensing approach using piezoresistive pressure dies (5kΩ) and strain gauge patterns (~120Ω), the two sensors have substantially different electrical loads that necessitate different voltage supplies. Using bias resistors, the supply voltage can remain at 1.8V, while the software cyclically adjusts the reference voltage (V_{ref}) for each sensor type, such that V_{ref} for the pressure die is 1.8V, but lower for the strain sensor. Cycling between the respective reference voltages in a time-dependent manner will enable data collection from each sensor during the measurement period, however it will likely reduce the maximum

achievable sampling frequency. Lowering the maximum sampling frequency below 100Hz is unlikely to affect the clinical utility of the system in this postoperative monitoring application. Allowing the user to select a static reference voltage for one of the sensors prior to a measurement period would enable pressure and strain data to be recorded separately depending on the movement being monitored. The adaptability of the NFC module further advances the clinical utility of the 'smart' interbody cage.

6.14 Summary on the Feasibility of NFC

The purpose of the presented work was to determine whether NFC is a feasible protocol for wireless actualisation of a 'smart' interbody cage. It was not within the scope of this thesis to characterise and optimise the design and power transfer performance of the module in detail.

The NFC module developed is a feasible approach for data collection from the embedded sensors. Battery power and its associated safety risks are avoided with wireless telemetry. NFC facilitates sufficient power transfer and accurate data transmission across short distances. The system is discontinuous, whereby the embedded NFC tag is passive unless triggered in the near-field by the external NFC reader, which activates the operation of the sensors. There are inherent safety advantages with this approach; surrounding tissue is not exposed to continuous electromagnetic energy and any potential malfunctions will not occur outside of a clinical setting in which the system would be activated for measurement. Further, the NFC module delivers a maximum power (4mW) within safe limits for an implantable medical device [218, 337], and the internal regulator is robust to fluctuations in power delivery, maintaining a consistent 1.8V supply. The telemetry module is driven by software and uses generic hardware to maintain flexibility in sampling frequency, post-processing, and sensing modalities; the combination of which establishes its clinical utility.

Albeit a feasible approach, further work is required to prepare a NFC module for clinical adoption. Options to mitigate the low transmission distances must be considered apart from sub-dermal coil positioning. Sub-dermal medical devices are not inherently novel and their risks have been well-classified [338, 339]. With physical connection between the sub-dermal coil and the implant, however, there is a risk of dislodgement at either

site. Optimisation of coil parameters, centre frequency, and the quality factor (Q-factor) may present safer alternative approaches. Biocompatibility and bioelectrical interference also require further study prior to adoption. Lastly, while the discontinuous approach is suitable for this application from the perspective of monitoring for the onset of complications, measurement periods are limited and data collection during other daily activities would be challenging.

6.15 Conclusion

In preparation for wireless integration, the works presented in this chapter aimed to identify a more efficient sensing configuration and assess the feasibility of the NFC protocol. The investigation into multidirectional strain suggested that the clinical utility of the 'smart' cage can be maintained with a reduced number of sensors and a combination of pressure and strain modalities. Further research is required to validate the performance of such a configuration under dynamic bending and fatigue loads. Sensor characterisation should be performed with concurrent consideration of its durability and enclosed position within the implant.

The wireless telemetry module evaluated in this chapter demonstrates that NFC is a feasible approach for powering and data transfer in a 'smart' interbody cage. The NFC module provided sufficient power across a limited distance for accurate data retrieval from the sensor target. The NFC tag dimensions can be reduced to an embeddable size, however further work is required to optimise power transfer prior to clinical adoption. The completed studies set clear development directions for finalising the design of a NFC-enabled 'smart' interbody cage capable of monitoring fusion progression and assessing subsidence risk in the postoperative phase.

7. Conclusions and Future Work

7.1 Research Aims and Contributions

The overall aim of this thesis was to provide biomechanical insights into lumbar interbody fusion (LIF) surgery by addressing its complications using computational modelling and 'smart' implant approaches. This thesis primarily examined pseudarthrosis and subsidence. Both are common complications that cause pain and may require surgical revision, but can be avoided by improving the quality of preoperative planning and postoperative monitoring.

The collection of works in this thesis contributed towards this aim in 3 distinct ways:

- Finite element (FE) analysis was used to uncover clinically relevant biomechanical insights into *in vivo* processes during LIF, eliciting a better understanding of how the surgery impacts load-distribution in surrounding spinal structures as fusion progresses.
- FE modelling was used to simulate a pre-surgical planning scenario, highlighting the pertinent biomechanical considerations for surgeons to prevent the occurrence of complications.
- Lastly, a 'smart' interbody cage was designed as a proof-of-concept alternative to postoperative imaging for early detection of subsidence and ongoing fusion monitoring. Design advancements were made by investigating optimisation of the sensing configuration and developing a wireless telemetry module.

In the context of clinical translation, the work in this thesis has progressed the 'smart' interbody cage towards clinical adoption by:

- Demonstrating its effectiveness at distinguishing the endpoints of fusion mass ossification.
- Demonstrating its effectiveness at distinguishing endplate contact stiffnesses.
- Highlighting a path forward for multimodality sensing.
- Assessing the feasibility of NFC for wireless telemetry in this application.

7.2 Thesis Summary

7.2.1 Assessing the Biomechanics of Fusion

Chapter 3 enhanced biomechanical perspectives on extreme lateral interbody fusion (XLIF) by quantifying its impact on adjacent spinal structures and describing its influence on subsidence and pseudarthrosis risk from the early to late stages of ossification. Of immediate interest to clinicians, the FE models detailed how endplate in-growth of the fusion mass does not reduce subsidence risk alone, but rather requires stiffer mechanical properties to off-load the cage. Regardless of the graft stiffness, however, endplate bonding affects load-distribution through adjacent facets and ligaments in a manner that warrants consideration by surgeons alongside the patient's clinical condition. Further, the use of solid grafts, such as allografts, will produce a more favourable load-share between the cage and graft, reducing the risk of concentrated stress-induced subsidence and non-union arising from excessive shear. The results from this chapter have implications for implant design, indicating that endplate-anchoring cages are unlikely to produce a desirable load-share between the cage and graft in the initial postoperative stages.

The findings from this chapter demonstrate that FE analysis is an effective tool for analysing mechanical changes that occur *in vivo* following XLIF surgery. Detailed biomechanical insights into operations and implant designs will improve postoperative outcomes and engender targeted treatment plans, subject to clinical validation.

7.2.2 Biomechanical Modelling in Pre-Surgical Planning

In Chapter 4, FE analysis was used to simulate a common pre-surgical planning scenario regarding posterior fixation. The extent of posterior fixation used in a patient often relies on clinical and operational factors without consideration of biomechanical consequences. The findings of this chapter, however, can be used as broad inputs to pre-surgical planning and the methods can be adapted for patient-specific biomechanical modelling.

Unilateral fixation did not increase the risk of shear-induced pseudarthrosis. While retaining some stress concentrations on the cage, unilateral fixation was sufficient to stabilise both left and right facets. In flexion, unilateral and bilateral fixation off-loaded the cage similarly, whereas in extension bilateral fixation off-loaded the cage to a greater

extent. Predictably, no fixation resulted in substantially higher cage and graft loads. Posterior fixation did not increase loads on adjacent discs.

Given the similar biomechanical changes produced by unilateral and bilateral fixation, unilateral pedicle screws may be preferrable considering its benefits to patient recovery, operating time, and cost, albeit with consideration of subsidence risk. The loading changes at adjacent facets are likely anatomically-dependent and require further study, with such findings emphasising the importance of patient-specific biomechanical modelling.

7.2.3 Design & Development of a 'Smart' Interbody Cage

While computational models yield detailed descriptions of biomechanical behaviour, it is not a suitable approach to address the deficiencies of postoperative imaging as a monitoring tool. Chapter 5 described the development of a proof-of-concept 'smart' interbody cage designed to take direct mechanical measurements from the implant.

Under compression, the sensor-embedded interbody cage effectively discerned graft stiffness states and measured the expected load-shift that occurs with a stiffer endplate. The results were in accordance with trends observed in simulation. Further, the sensing configuration fairly reliably distinguished between different eccentric load points. These findings suggest that the 'smart' implant is a feasible alternative to radiological imaging, pending further investigation into sensor enclosure, durability, and biocompatibility.

The adoption of a 'smart' interbody cage into clinical practice would substantially contribute towards the management of postoperative complications. Equipped with *in vivo* mechanical data, surgeons can proactively assess subsidence risk and take appropriate actions to avoid the occurrence thereof or instigate early intervention, without relying on the onset of symptoms to prompt a clinical investigation. Similarly, direct measurement from the interbody cage provides an objective indication of graft ossification for safe and effective monitoring of fusion. Additionally, integrating sensors in the diverse range of commercially available cages overcomes challenges associated with the varied biomechanical and clinical responses to fusion cage designs, materials, and configurations.

7.2.4 Preparation of the 'Smart' Interbody Cage for Wireless Integration

Chapter 6 described the investigation of multidirectional strain as an alternate measurand to pressure, providing inputs for optimising the sensing configuration, simplifying wireless integration, and identifying sensor enclosure methods. Thereafter, a proof-of-concept near-field communication (NFC) telemetry module was designed and tested to assess its feasibility for wireless power and data transfer.

Multidirectional strain results exhibited superior alignment with the simulation data compared to the pressure sensors and uncovered detailed insights into mechanical changes in the cage, however the data was less effective at meeting clinical objectives under the applied compressive loads. The lateral biaxial strain gauge was sensitive to graft and endplate stiffness changes. Conversely, the strain gauge configuration was less effective at distinguishing between eccentric load points. Notably, sensing indirect loads by measuring deformations in the cage may reduce the risk of sensor damage. Based on the results, an optimum configuration includes an anterior left and posterior right pressure sensor, and a lateral biaxial strain sensor.

Testing of the NFC module demonstrated it is a feasible and novel approach for wireless power and data transfer in orthopaedic implants. The NFC device was generally adaptable to various sensor modalities and prioritised software processes to allow customisation to clinical needs in terms of measurement periods, sampling frequency, and post-processing. Power transmission was consistent through the 3 media up to a distance of approximately 25mm, suggesting the receiver coil should be located extra-fascial to sub-dermal to enable consistent power transfer. The accuracy of wireless data transmission using NFC was also validated. The findings from this chapter prepare the 'smart' cage for wireless integration and clinical adoption with further development.

7.3 Limitations

Each chapter has specifically noted the limitations of the results obtained, however, more generally, there are notable limitations with the methods employed in this thesis which, in part, resulted from resource limitations and material availability constraints. With regards to the FE analysis approach, the simulation only accounted for a single patient anatomy and XLIF cage design inserted at L4-L5. It is not practical, without the use of

automated image segmentation and meshing, to model distinct anatomies. Further, while using a single XLIF cage controlled variables associated with the design parameters and materials, it limits the generalisability of the findings across other LIF surgeries or those performed at different levels, and does not elicit insights into the impact of these features on spine biomechanics. As such, the findings on pre-surgical planning and the biomechanics of fusion can not directly influence surgical decision-making, but rather must be used as broad considerations pending clinical validation. This thesis prioritised results from flexion-extension bending, however lateral bending and axial rotation may produce additional relevant findings.

In developing the 'smart' interbody cage, this thesis used a single polyether ether ketone (PEEK) XLIF cage design due to its large footprint and the space afforded for embedding sensors. The findings may not be applicable to other, smaller cage designs for cervical fusion. Further, only one pressure-sensing cage was fabricated due to resource and practicality constraints. The fabrication methods enabled design prototyping and sensor redundancy, however induced loading inconsistencies. Only compressive loads were applied to prevent separation of the modular components of the cage. Additionally, this thesis leveraged the symmetry of the cage design, however commercially available cages do not contain the same level of symmetry and further investigation is required to optimise and test the sensor placement in these implants. By focusing entirely on PEEK cages in this thesis, issues with signal interference and attenuation that arise with using titanium cages were not addressed. While the graft and endplate materials provide clear endpoints for discernment by sensor-recorded loads, a lack of suitable materials prevented the assessment of sensor performance at intermediate stiffnesses. Lastly, the enclosure of the sensors in the design presented in Chapter 5 is not suitable for *in vivo* use. Investigating more suitable encapsulation methods necessitates re-evaluation of sensor performance in such designs.

7.4 Future Work

7.4.1 Advancements in Biomechanical Modelling for Clinical Utility

The greatest limitation to biomechanical modelling is its clinical utility. Image segmentation and meshing are time-consuming procedures that can not be performed on a patient-specific basis in a timely manner for pre-surgical planning. Artificial

intelligence and statistical modelling are being used to improve automatic image segmentation [340-342]. Integrating the approaches presented in this thesis with further developed automated segmentation and meshing will expedite the simulation process. Patient-specific biomechanical models with multiple cage designs, materials, and configurations could be used during pre-surgical planning to identify the optimum surgical solution for each patient. Nevertheless, further biomechanical research is required to clarify the links between biomechanics and complications prior to reaching adoption in pre-surgical planning.

One method to efficiently uncover such links is to capitalise on the convergence of biomechanical and statistical modelling, known as probabilistic modelling [105]. For example, sources of statistical uncertainty, such as material and geometric properties, can be used as inputs to the system to model the effects of such variations as they pertain to age- and sex-based population characteristics and implant designs [343]. These methods have been applied in orthopaedics [344, 345], but are yet to be thoroughly examined in spine modelling. Probabilistic FE analysis can be used to account for anatomical and material variations across populations, or different implant parameters, broadening the applicability of the findings for the purposes of pre-surgical planning and uncovering links with complications.

7.4.2 Sensor Characterisation and Encapsulation

Clinical adoption of the 'smart' interbody cage requires substantive work on characterising sensor performance, subjecting the implant to complex loading, and investigating advanced manufacturing methods for integrating the electronics. Further work should be initially directed towards identifying more durable pressure sensors. In the absence of a better option, encapsulation should be considered in light of the protection required to improve sensor durability.

The results from this thesis suggest that sensors embedded under indirect load may be less prone to damage than sensors under direct load. Flexible capacitive sensors and strain sensing patterns can be used to measure load-induced deformations in the cage, with further research into their long-term performance. Material characterisation of flexible capacitive sensor substrates will elicit insights into their long-term durability. The lateral biaxial strain gauge performed favourably. If further optimisation can be

achieved, there are numerous advantages to flexible sensors with regards to size and encapsulation. Strain gauge and capacitive interdigital sensor patterns can be directly etched onto the same thin flexible printed circuit board (PCB) that accommodates the NFC chip and microcontroller, overcoming concerns regarding sensor bonding. Further testing should be performed to determine whether sensor performance and clinical utility can be maintained using a flexible PCB substrate as opposed to traditional polymeric substrates. Nonetheless, the findings from Chapter 6 suggest that a combination of pressure and strain sensors should be tested. The presented approach enables multimodality sensing in different locations on a single PCB. Employing an integrated PCB approach simplifies its enclosure within the interbody cage.

Improvements to encapsulation require further research into alternate manufacturing methods. Additive manufacturing approaches for PEEK, such as selective laser sintering (SLS), can be adapted to encase the sensors within the implant during the printing process. Traditionally, this would require the embedded electronics to withstand temperatures of 300°C [346], however advancements in low-temperature polymer SLS enable printing at 180°C with similar resultant mechanical properties [347]. Techniques to sheath and protect the circuitry at this temperature during printing should be explored. Failing identification of such protective mechanisms, current machining and injection moulding approaches can be further pursued in a modular design, with improvements to sealing of the modular components. Packaging the integrated PCB in silicone or a similar material prior to positioning it within the cage will facilitate load transfer to the sensors and prevent the rigid PEEK interface from damaging the fragile components on the board. Additionally, packaging sensors in a rigid fluid-filled container will better protect the sensor surface and allow it to record load changes from deflections in the fluid. Further research should be conducted to determine an appropriate position in the cage where the sensors are not over-loaded and still record clinically useful measurements.

The chosen sensing modality must be subjected to long-term drift studies to determine the impact of constant compressive loads, representative of standing body weight, on the resting state value of the sensor. Drift studies should account for physiological loading during the relevant measurement period of at least 12 months, up to the point of full fusion. Subsequently, techniques can be explored to compensate for any baseline

drift. Machine learning models are an emerging approach for drift compensation, which can be incorporated into the post-processing pipeline without complicating the implanted hardware [348].

Extensive biomechanical testing is required to validate the performance of the sensor-enabled cage under physiological loads. Dynamic bending and torsion with compressive pre-loads, creep, and fatigue testing should be performed to determine the mechanical integrity of the 'smart' cage, validate the manufacturing processes, and confirm its clinical utility. While the endpoints of graft and endplate stiffnesses were studied, intermediate material properties should be tested to establish the sensitivity of the device across a broader range of clinical scenarios and time points.

7.4.3 Improvements to Wireless Telemetry

In this thesis, no work was performed to tune and improve the performance of the NFC-based wireless telemetry system. Future work should be directed towards improving the transfer distance and the usability of the implanted device.

Optimisation of the sampling frequency should be performed with consideration of clinically relevant measurement periods. It may be important to collect data during rehabilitation exercises, general range of motion bending, walking, running, and other daily activities in the postoperative phase. For example, running may require a higher sampling frequency than a sit-to-stand exercise. As such, the optimum data acquisition frequency should be identified for each activity or motion deemed to be clinically relevant in the postoperative phase.

The quality factor (Q-factor) of a coil determines its energy efficiency; a high Q-factor represents a low rate of energy loss whereas a low Q-factor indicates the reverse. In this application, the Q-factor represents the effect of coil resistance on power transmission. Optimising power transfer requires adjusting the centre frequency and coil parameters to achieve the highest possible Q-factor.

The first step in tuning the Q-factor is to determine the size limitations of the implanted receiver coil, as increasing the thickness of the coil will reduce its electrical resistance. The size of the target coil may vary depending on whether it is embedded in the implant or sub-dermal. Locating the coil with the interbody cage requires consideration of transmission distance and interference from metallic instrumentation (pedicle screws,

rods, cage pins) proximate to the implant. Further, there will be stricter constraints on the coil dimensions. Conversely, locating the coil sub-dermal enables larger coils to be implanted, while increasing the risk of dislodgement, bioelectrical interference, and transmission losses between the coil and the circuitry embedded in the cage. Simulation studies and *in vitro* testing should be performed to determine the most suitable location for the coil and, subsequently, its maximum dimensions.

Other methods to improve the Q-factor warrant further investigation, including modifying the coil material to reduce resistance and skin effect, tuning the centre frequency, designing a parallel coil system [349], and employing a dual-band approach [350]. The centre frequency can be tuned by adjusting the resonant circuitry after defining the coil properties.

It is worth considering that investigating improvements to wireless telemetry provides an opportunity to explore alternatives to NFC. Given the findings of Chapter 6 conclude that a subdermal wired connection between the receiver coil and interbody cage may be required to transmit data, capacitive coupling approaches, which operate in a similar manner should be investigated owing to their superior flexibility, efficiency, and robustness to misalignment [331]. Given the reliability of Bluetooth communication, it should also be investigated as an alternative notwithstanding data security concerns.

7.4.4 Studies on Implant Design and Ossification

Little is known about the *in vivo* mechanical properties of the fusion mass. Assessing its maturity is subjective and it is not clear whether different grafts generate bone of different stiffnesses. Once prepared for *in vivo* study, load-sensing interbody cages can be used to determine the optimum loading conditions for bone growth. A broad clinical study could be performed to determine how implant design, bone graft, and morphological characteristics influence fusion rate. The data can be used as feedback for pre-surgical planning and implant design optimisation with regards to stress-shielding of the graft region.

References

[1] M. Juniper, T. K. Le, and D. Mladsi, "The epidemiology, economic burden, and pharmacological treatment of chronic low back pain in France, Germany, Italy, Spain and the UK: a literature-based review," *Expert Opin Pharmacother,* vol. 10, no. 16, pp. 2581-92, Nov 2009, doi: 10.1517/14656560903304063.

[2] C. C. Lin *et al.*, "The economic burden of guideline-recommended first line care for acute low back pain," *Eur Spine J,* vol. 27, no. 1, pp. 109-116, Jan 2018, doi: 10.1007/s00586-016-4781-0.

[3] A. Parthan, C. J. Evans, and K. Le, "Chronic low back pain: epidemiology, economic burden and patient-reported outcomes in the USA," *Expert Rev Pharmacoecon Outcomes Res,* vol. 6, no. 3, pp. 359-69, Jun 2006, doi: 10.1586/14737167.6.3.359.

[4] S. M. Salerno, R. Browning, and J. L. Jackson, "The effect of antidepressant treatment on chronic back pain: a meta-analysis," *Arch Intern Med,* vol. 162, no. 1, pp. 19-24, Jan 14 2002. [Online]. Available: https://www.ncbi.nlm.nih.gov/pubmed/11784215.

[5] B. F. Walker, R. Muller, and W. D. Grant, "Low back pain in Australian adults: the economic burden," *Asia Pac J Public Health,* vol. 15, no. 2, pp. 79-87, 2003, doi: 10.1177/101053950301500202.

[6] S. Chen *et al.*, "Global, regional and national burden of low back pain 1990-2019: A systematic analysis of the Global Burden of Disease study 2019," *J Orthop Translat,* vol. 32, pp. 49-58, Jan 2022, doi: 10.1016/j.jot.2021.07.005.

[7] Global Burden of Disease Injury Incidence Prevalence Collaborators, "Global burden of 369 diseases and injuries in 204 countries and territories, 1990-2019: a systematic analysis for the Global Burden of Disease Study 2019," *Lancet,* vol. 396, no. 10258, pp. 1204-1222, Oct 17 2020, doi: 10.1016/S0140-6736(20)30925-9.

[8] Global Burden of Disease Injury Incidence Prevalence Collaborators, "Global, regional, and national incidence, prevalence, and years lived with disability for 354 diseases and injuries for 195 countries and territories, 1990-2017: a systematic

analysis for the Global Burden of Disease Study 2017," *Lancet,* vol. 392, no. 10159, pp. 1789-1858, Nov 10 2018, doi: 10.1016/S0140-6736(18)32279-7.

[9] J. Matthew, S. B. Singh, S. Garis, and A. D. Diwan, "Backing up the stories: The psychological and social costs of chronic low-back pain," *The International Journal of Spine Surgery,* vol. 7, pp. e29-e38, 2013.

[10] D. J. Schofield, E. J. Callander, R. N. Shrestha, R. Percival, S. J. Kelly, and M. E. Passey, "Labor force participation and the influence of having back problems on income poverty in Australia," (in eng), *Spine (Phila Pa 1976),* vol. 37, no. 13, pp. 1156-63, Jun 1 2012, doi: 10.1097/BRS.0b013e31824481ee.

[11] Arthritis and Osteoporosis Victoria, "The rising cost of musculoskeletal conditions in Australia," Arthritis Victoria and Osteoporosis Victoria, Elsternwick, Victoria, 2013.

[12] A. I. o. Health and Welfare, "Chronic musculoskeletal conditions," AIHW, Canberra, 2023. [Online]. Available: https://www.aihw.gov.au/reports/chronic-musculoskeletal-conditions/musculoskeletal-conditions

[13] S. Virk, S. Qureshi, and H. Sandhu, "History of Spinal Fusion: Where We Came from and Where We Are Going," *HSS J,* vol. 16, no. 2, pp. 137-142, Jul 2020, doi: 10.1007/s11420-020-09747-7.

[14] R. A. Deyo, A. Nachemson, and S. K. Mirza, "Spinal-fusion surgery - the case for restraint," *N Engl J Med,* vol. 350, no. 7, pp. 722-6, Feb 12 2004, doi: 10.1056/NEJMsb031771.

[15] S. S. Rajaee, H. W. Bae, L. E. Kanim, and R. B. Delamarter, "Spinal fusion in the United States: analysis of trends from 1998 to 2008," *Spine (Phila Pa 1976),* vol. 37, no. 1, pp. 67-76, Jan 1 2012, doi: 10.1097/BRS.0b013e31820cccfb.

[16] M. J. Reisener, M. Pumberger, J. Shue, F. P. Girardi, and A. P. Hughes, "Trends in lumbar spinal fusion-a literature review," *J Spine Surg,* vol. 6, no. 4, pp. 752-761, Dec 2020, doi: 10.21037/jss-20-492.

[17] S. R. Sheikh *et al.*, "Can We Justify It? Trends in the Utilization of Spinal Fusions and Associated Reimbursement," *Neurosurgery,* vol. 86, no. 2, pp. E193-E202, Feb 1 2020, doi: 10.1093/neuros/nyz400.

[18] M. Song *et al.*, "Stress distribution of different lumbar posterior pedicle screw insertion techniques: a combination study of finite element analysis and biomechanical test," in *Sci Rep* vol. 11, 20210621 ed, 2021, p. 12968.

[19] S. D. Kuslich, C. L. Ulstrom, S. L. Griffith, J. W. Ahern, and J. D. Dowdle, "The Bagby and Kuslich method of lumbar interbody fusion. History, techniques, and 2-year follow-up results of a United States prospective, multicenter trial," *Spine (Phila Pa 1976),* vol. 23, no. 11, pp. 1267-78; discussion 1279, Jun 1 1998, doi: 10.1097/00007632-199806010-00019.

[20] W. K. Hsu *et al.*, "Improving the clinical evidence of bone graft substitute technology in lumbar spine surgery," *Global Spine J,* vol. 2, no. 4, pp. 239-48, Dec 2012, doi: 10.1055/s-0032-1315454.

[21] S. S. Rajaee, L. E. Kanim, and H. W. Bae, "National trends in revision spinal fusion in the USA: patient characteristics and complications," *Bone Joint J,* vol. 96-B, no. 6, pp. 807-16, Jun 2014, doi: 10.1302/0301-620X.96B6.31149.

[22] I. A. Harris, A. Traeger, R. Stanford, C. G. Maher, and R. Buchbinder, "Lumbar spine fusion: what is the evidence?," *Intern Med J,* vol. 48, no. 12, pp. 1430-1434, Dec 2018, doi: 10.1111/imj.14120.

[23] B. I. Martin, S. K. Mirza, N. Spina, W. R. Spiker, B. Lawrence, and D. S. Brodke, "Trends in Lumbar Fusion Procedure Rates and Associated Hospital Costs for Degenerative Spinal Diseases in the United States, 2004 to 2015," *Spine (Phila Pa 1976),* vol. 44, no. 5, pp. 369-376, Mar 1 2019, doi: 10.1097/BRS.0000000000002822.

[24] G. Barbanti-Brodano *et al.*, "Spinal surgery complications: an unsolved problem-Is the World Health Organization Safety Surgical Checklist an useful tool to reduce them?," *Eur Spine J,* vol. 29, no. 5, pp. 927-936, May 2020, doi: 10.1007/s00586-019-06203-x.

[25] T. M. Irmola, A. Hakkinen, S. Jarvenpaa, I. Marttinen, K. Vihtonen, and M. Neva, "Reoperation Rates Following Instrumented Lumbar Spine Fusion," *Spine (Phila Pa 1976),* vol. 43, no. 4, pp. 295-301, Feb 15 2018, doi: 10.1097/BRS.0000000000002291.

[26] S. D. Glassman *et al.*, "Lumbar fusion outcomes stratified by specific diagnostic indication," *Spine J,* vol. 9, no. 1, pp. 13-21, Jan-Feb 2009, doi: 10.1016/j.spinee.2008.08.011.

[27] E. J. Carragee and I. Cheng, "Minimum acceptable outcomes after lumbar spinal fusion," *Spine J,* vol. 10, no. 4, pp. 313-20, Apr 2010, doi: 10.1016/j.spinee.2010.02.001.

[28] L. Y. Carreon, S. D. Glassman, and M. Djurasovic, "Reliability and agreement between fine-cut CT scans and plain radiography in the evaluation of posterolateral fusions," *Spine J,* vol. 7, no. 1, pp. 39-43, Jan-Feb 2007, doi: 10.1016/j.spinee.2006.04.005.

[29] L. Y. Carreon, S. D. Glassman, J. D. Schwender, B. R. Subach, M. F. Gornet, and S. Ohno, "Reliability and accuracy of fine-cut computed tomography scans to determine the status of anterior interbody fusions with metallic cages," *Spine J,* vol. 8, no. 6, pp. 998-1002, Nov-Dec 2008, doi: 10.1016/j.spinee.2007.12.004.

[30] J. Umali, A. Ghahreman, and A. Diwan, "Spinal Fusion Evaluation in Various Settings: A Summary of Human-Only Studies," in *Handbook of Spine Technology*, B. Cheng Ed. Cham: Springer International Publishing, 2019, pp. 1-17.

[31] W. F. Lestini, J. S. Fulghum, and L. A. Whitehurst, "Lumbar spinal fusion: advantages of posterior lumbar interbody fusion," *Surg Technol Int,* vol. 3, pp. 577-90, 1994. [Online]. Available: https://www.ncbi.nlm.nih.gov/pubmed/21319127.

[32] R. J. Mobbs, K. Phan, G. Malham, K. Seex, and P. J. Rao, "Lumbar interbody fusion: techniques, indications and comparison of interbody fusion options including PLIF, TLIF, MI-TLIF, OLIF/ATP, LLIF and ALIF," *J Spine Surg,* vol. 1, no. 1, pp. 2-18, Dec 2015, doi: 10.3978/j.issn.2414-469X.2015.10.05.

[33] C. D. Cole, T. D. McCall, M. H. Schmidt, and A. T. Dailey, "Comparison of low back fusion techniques: transforaminal lumbar interbody fusion (TLIF) or posterior lumbar interbody fusion (PLIF) approaches," *Curr Rev Musculoskelet Med,* vol. 2, no. 2, pp. 118-26, Jun 2009, doi: 10.1007/s12178-009-9053-8.

[34] S. W. Fan, Z. J. Hu, X. Q. Fang, F. D. Zhao, Y. Huang, and H. J. Yu, "Comparison of paraspinal muscle injury in one-level lumbar posterior inter-body fusion: modified minimally invasive and traditional open approaches," *Orthop Surg,* vol. 2, no. 3, pp. 194-200, Aug 2010, doi: 10.1111/j.1757-7861.2010.00086.x.

[35] G. M. Malham, R. M. Parker, N. J. Ellis, C. M. Blecher, F. Y. Chow, and M. H. Claydon, "Anterior lumbar interbody fusion using recombinant human bone

morphogenetic protein-2: a prospective study of complications," *J Neurosurg Spine,* vol. 21, no. 6, pp. 851-60, Dec 2014, doi: 10.3171/2014.8.SPINE13524.

[36] K. Phan and R. J. Mobbs, "Evolution of Design of Interbody Cages for Anterior Lumbar Interbody Fusion," *Orthop Surg,* vol. 8, no. 3, pp. 270-7, Aug 2016, doi: 10.1111/os.12259.

[37] S. C. Humphreys, S. D. Hodges, A. G. Patwardhan, J. C. Eck, R. B. Murphy, and L. A. Covington, "Comparison of posterior and transforaminal approaches to lumbar interbody fusion," *Spine (Phila Pa 1976),* vol. 26, no. 5, pp. 567-71, Mar 1 2001, doi: 10.1097/00007632-200103010-00023.

[38] K. Phan, G. K. Thayaparan, and R. J. Mobbs, "Anterior lumbar interbody fusion versus transforaminal lumbar interbody fusion--systematic review and meta-analysis," *Br J Neurosurg,* vol. 29, no. 5, pp. 705-11, 2015, doi: 10.3109/02688697.2015.1036838.

[39] N. Sakeb and K. Ahsan, "Comparison of the early results of transforaminal lumbar interbody fusion and posterior lumbar interbody fusion in symptomatic lumbar instability," *Indian J Orthop,* vol. 47, no. 3, pp. 255-63, May 2013, doi: 10.4103/0019-5413.111484.

[40] G. M. Malham *et al.*, "Maintenance of Segmental Lordosis and Disk Height in Stand-alone and Instrumented Extreme Lateral Interbody Fusion (XLIF)," *Clin Spine Surg,* vol. 30, no. 2, pp. E90-E98, Mar 2017, doi: 10.1097/BSD.0b013e3182aa4c94.

[41] J. H. Peck, K. D. Kavlock, B. L. Showalter, B. M. Ferrell, D. G. Peck, and A. E. Dmitriev, "Mechanical performance of lumbar intervertebral body fusion devices: An analysis of data submitted to the Food and Drug Administration," (in English), *Journal of Biomechanics,* vol. 78, pp. 87-93, Sep 10 2018, doi: 10.1016/j.jbiomech.2018.07.022.

[42] N. Ghodasara, P. H. Yi, K. Clark, E. K. Fishman, M. Farshad, and J. Fritz, "Postoperative Spinal CT: What the Radiologist Needs to Know," (in English), *Radiographics,* vol. 39, no. 6, pp. 1840-1861, Oct 2019, doi: 10.1148/rg.2019190050.

[43] Y. Assem, M. H. Pelletier, R. J. Mobbs, K. Phan, and W. R. Walsh, "Anterior Lumbar Interbody Fusion Integrated Screw Cages: Intrinsic Load Generation, Subsidence, and Torsional Stability," *Orthop Surg,* vol. 9, no. 2, pp. 191-197, May 2017, doi: 10.1111/os.12283.

[44] M. Wang, S. J. Tang, L. M. McGrady, and R. D. Rao, "Biomechanical comparison of supplemental posterior fixations for two-level anterior lumbar interbody fusion," *Proc Inst Mech Eng H,* vol. 227, no. 3, pp. 245-50, Mar 2013, doi: 10.1177/0954411912465057.

[45] J. Allain and T. Dufour, "Anterior lumbar fusion techniques: ALIF, OLIF, DLIF, LLIF, IXLIF," *Orthop Traumatol Surg Res,* vol. 106, no. 1S, pp. S149-S157, Feb 2020, doi: 10.1016/j.otsr.2019.05.024.

[46] R. DenHaese, A. Gandhi, C. Ferry, S. Farmer, and R. Porter, "An In Vitro Biomechanical Evaluation of a Lateral Lumbar Interbody Fusion Device With Integrated Lateral Modular Plate Fixation," *Global Spine J,* vol. 11, no. 3, pp. 351-358, Apr 2021, doi: 10.1177/2192568220905611.

[47] F. Galbusera, D. Volkheimer, S. Reitmaier, N. Berger-Roscher, A. Kienle, and H. J. Wilke, "Pedicle screw loosening: a clinically relevant complication?," *Eur Spine J,* vol. 24, no. 5, pp. 1005-16, May 2015, doi: 10.1007/s00586-015-3768-6.

[48] C. Herren *et al.*, "Posterior Lumbar Interbody Fusion versus Dynamic Hybrid Instrumentation: A Prospective Randomized Clinical Trial," *World Neurosurg,* vol. 117, pp. e228-e237, Sep 2018, doi: 10.1016/j.wneu.2018.06.005.

[49] Z. X. Wu *et al.*, "A comparative study on screw loosening in osteoporotic lumbar spine fusion between expandable and conventional pedicle screws," *Arch Orthop Trauma Surg,* vol. 132, no. 4, pp. 471-6, Apr 2012, doi: 10.1007/s00402-011-1439-6.

[50] K. T. Foley, L. T. Holly, and J. D. Schwender, "Minimally invasive lumbar fusion," *Spine (Phila Pa 1976),* vol. 28, no. 15 Suppl, pp. S26-35, Aug 1 2003, doi: 10.1097/01.BRS.0000076895.52418.5E.

[51] S. W. Xiao, H. Jiang, L. J. Yang, and Z. M. Xiao, "Comparison of unilateral versus bilateral pedicle screw fixation with cage fusion in degenerative lumbar diseases: a meta-analysis," *Eur Spine J,* vol. 24, no. 4, pp. 764-74, Apr 2015, doi: 10.1007/s00586-014-3717-9.

[52] K. Zhang *et al.*, "Unilateral versus bilateral instrumented transforaminal lumbar interbody fusion in two-level degenerative lumbar disorders: a prospective randomised study," *Int Orthop,* vol. 38, no. 1, pp. 111-6, Jan 2014, doi: 10.1007/s00264-013-2026-y.

[53] S. Jain, A. E. Eltorai, R. Ruttiman, and A. H. Daniels, "Advances in Spinal Interbody Cages," *Orthop Surg,* vol. 8, no. 3, pp. 278-84, Aug 2016, doi: 10.1111/os.12264.

[54] E. Chong, M. H. Pelletier, R. J. Mobbs, and W. R. Walsh, "The design evolution of interbody cages in anterior cervical discectomy and fusion: a systematic review," *BMC Musculoskelet Disord,* vol. 16, p. 99, Apr 25 2015, doi: 10.1186/s12891-015-0546-x.

[55] D. V. Patel, J. S. Yoo, S. S. Karmarkar, E. H. Lamoutte, and K. Singh, "Interbody options in lumbar fusion," *J Spine Surg,* vol. 5, no. Suppl 1, pp. S19-S24, Jun 2019, doi: 10.21037/jss.2019.04.04.

[56] G. C. Comer, A. Behn, S. Ravi, and I. Cheng, "A Biomechanical Comparison of Shape Design and Positioning of Transforaminal Lumbar Interbody Fusion Cages," *Global Spine J,* vol. 6, no. 5, pp. 432-8, Aug 2016, doi: 10.1055/s-0035-1564568.

[57] S. M. Falowski, S. F. Koga, T. Northcutt, L. Garamszegi, J. Leasure, and J. E. Block, "Improving the Management of Patients with Osteoporosis Undergoing Spinal Fusion: The Need for a Bone Mineral Density-Matched Interbody Cage," (in English), *Orthop Res Rev,* vol. 13, pp. 281-288, 2021, doi: 10.2147/Orr.S339222.

[58] Y. Chen *et al.*, "Comparison of titanium and polyetheretherketone (PEEK) cages in the surgical treatment of multilevel cervical spondylotic myelopathy: a prospective, randomized, control study with over 7-year follow-up," *Eur Spine J,* vol. 22, no. 7, pp. 1539-46, Jul 2013, doi: 10.1007/s00586-013-2772-y.

[59] P. J. Rao, M. H. Pelletier, W. R. Walsh, and R. J. Mobbs, "Spine interbody implants: material selection and modification, functionalization and bioactivation of surfaces to improve osseointegration," *Orthop Surg,* vol. 6, no. 2, pp. 81-9, May 2014, doi: 10.1111/os.12098.

[60] K. Lingutla, S. Gudipati, R. Pollock, P. Davies, I. Chopra, and S. Ahuja, "Radiological outcomes of Peek vs Titanium transforaminal lumbar interbody cages.," *Spine J,* vol. 15, S53, 2015.

[61] B. Meng, J. Bunch, D. Burton, and J. Wang, "Lumbar interbody fusion: recent advances in surgical techniques and bone healing strategies," *Eur Spine J,* vol. 30, no. 1, pp. 22-33, Jan 2021, doi: 10.1007/s00586-020-06596-0.

[62] G. Fogel *et al.*, "Choice of Spinal Interbody Fusion Cage Material and Design Influences Subsidence and Osseointegration Performance," *World Neurosurg,* vol. 162, pp. e626-e634, Jun 2022, doi: 10.1016/j.wneu.2022.03.087.

[63] S. Seaman, P. Kerezoudis, M. Bydon, J. C. Torner, and P. W. Hitchon, "Titanium vs. polyetheretherketone (PEEK) interbody fusion: Meta-analysis and review of the literature," *J Clin Neurosci,* vol. 44, pp. 23-29, Oct 2017, doi: 10.1016/j.jocn.2017.06.062.

[64] P. G. Campbell *et al.*, "PEEK versus titanium cages in lateral lumbar interbody fusion: a comparative analysis of subsidence," *Neurosurg Focus,* vol. 49, no. 3, p. E10, Sep 2020, doi: 10.3171/2020.6.FOCUS20367.

[65] F. Galbusera, H. Schmidt, and H. J. Wilke, "Lumbar interbody fusion: a parametric investigation of a novel cage design with and without posterior instrumentation," (in eng), *Eur Spine J,* vol. 21, no. 3, pp. 455-62, Mar 2012, doi: 10.1007/s00586-011-2014-0.

[66] J. J. Schimmel, M. S. Poeschmann, P. P. Horsting, D. H. Schönfeld, J. van Limbeek, and P. W. Pavlov, "PEEK Cages in Lumbar Fusion: Mid-term Clinical Outcome and Radiologic Fusion," (in eng), *Clin Spine Surg,* vol. 29, no. 5, pp. E252-8, Jun 2016, doi: 10.1097/BSD.0b013e31826eaf74.

[67] J. Ngo, M. Mousselli, and Y.-P. Lee, "Cage and graft options in lateral lumbar interbody fusion," *Seminars in Spine Surgery,* vol. 34, no. 2, p. 100943, 2022/06/01/ 2022, doi: https://doi.org/10.1016/j.semss.2022.100943.

[68] K. C. McGilvray *et al.*, "Evaluation of a polyetheretherketone (PEEK) titanium composite interbody spacer in an ovine lumbar interbody fusion model: biomechanical, microcomputed tomographic, and histologic analyses," *Spine J,* vol. 17, no. 12, pp. 1907-1916, Dec 2017, doi: 10.1016/j.spinee.2017.06.034.

[69] M. Hanc, S. K. Fokter, M. Vogrin, A. Molicnik, and G. Recnik, "Porous tantalum in spinal surgery: an overview," *Eur J Orthop Surg Traumatol,* vol. 26, no. 1, pp. 1-7, Jan 2016, doi: 10.1007/s00590-015-1654-x.

[70] F. B. Torstrick *et al.*, "Porous PEEK improves the bone-implant interface compared to plasma-sprayed titanium coating on PEEK," *Biomaterials,* vol. 185, pp. 106-116, Dec 2018, doi: 10.1016/j.biomaterials.2018.09.009.

[71] C. Basgul, T. Yu, D. W. MacDonald, R. Siskey, M. Marcolongo, and S. M. Kurtz, "Structure-Property Relationships for 3D printed PEEK Intervertebral Lumbar

Cages Produced using Fused Filament Fabrication," *J Mater Res,* vol. 33, no. 14, pp. 2040-2051, Jul 27 2018, doi: 10.1557/jmr.2018.178.

[72] C. T. Pan *et al.*, "Design of Customize Interbody Fusion Cages of Ti64ELI with Gradient Porosity by Selective Laser Melting Process," *Micromachines (Basel),* vol. 12, no. 3, Mar 15 2021, doi: 10.3390/mi12030307.

[73] P. I. Tsai *et al.*, "Additive-manufactured Ti-6Al-4 V/Polyetheretherketone composite porous cage for Interbody fusion: bone growth and biocompatibility evaluation in a porcine model," *BMC Musculoskelet Disord,* vol. 22, no. 1, p. 171, Feb 11 2021, doi: 10.1186/s12891-021-04022-0.

[74] K. C. McGilvray *et al.*, "Bony ingrowth potential of 3D-printed porous titanium alloy: a direct comparison of interbody cage materials in an in vivo ovine lumbar fusion model," *Spine J,* vol. 18, no. 7, pp. 1250-1260, Jul 2018, doi: 10.1016/j.spinee.2018.02.018.

[75] D. Adl Amini *et al.*, "Evaluation of cage subsidence in standalone lateral lumbar interbody fusion: novel 3D-printed titanium versus polyetheretherketone (PEEK) cage," *Eur Spine J,* vol. 30, no. 8, pp. 2377-2384, Aug 2021, doi: 10.1007/s00586-021-06912-2.

[76] N. Alan *et al.*, "Subsidence after lateral lumbar interbody fusion using a 3D-printed porous titanium interbody cage: single-institution case series," *J Neurosurg Spine,* pp. 1-7, May 20 2022, doi: 10.3171/2022.4.SPINE2245.

[77] C. Basgul, D. W. MacDonald, R. Siskey, and S. M. Kurtz, "Thermal Localization Improves the Interlayer Adhesion and Structural Integrity of 3D printed PEEK Lumbar Spinal Cages," *Materialia (Oxf),* vol. 10, May 2020, doi: 10.1016/j.mtla.2020.100650.

[78] G. R. Fogel, J. S. Toohey, A. Neidre, and J. W. Brantigan, "Fusion assessment of posterior lumbar interbody fusion using radiolucent cages: X-ray films and helical computed tomography scans compared with surgical exploration of fusion," *Spine J,* vol. 8, no. 4, pp. 570-7, Jul-Aug 2008, doi: 10.1016/j.spinee.2007.03.013.

[79] M. Manzur *et al.*, "The rate of fusion for stand-alone anterior lumbar interbody fusion: a systematic review," *Spine J,* vol. 19, no. 7, pp. 1294-1301, Jul 2019, doi: 10.1016/j.spinee.2019.03.001.

[80] H. Nakashima *et al.*, "Extension CT scan: its suitability for assessing fusion after posterior lumbar interbody fusion," *Eur Spine J,* vol. 20, no. 9, pp. 1496-502, Sep 2011, doi: 10.1007/s00586-011-1739-0.

[81] D. S. Chun, K. C. Baker, and W. K. Hsu, "Lumbar pseudarthrosis: a review of current diagnosis and treatment," *Neurosurg Focus,* vol. 39, no. 4, p. E10, Oct 2015, doi: 10.3171/2015.7.FOCUS15292.

[82] R. Vaidya, A. Sethi, S. Bartol, M. Jacobson, C. Coe, and J. G. Craig, "Complications in the use of rhBMP-2 in PEEK cages for interbody spinal fusions," *J Spinal Disord Tech,* vol. 21, no. 8, pp. 557-62, Dec 2008, doi: 10.1097/BSD.0b013e31815ea897.

[83] M. R. Hayeri and J. Tehranzadeh, "Diagnostic imaging of spinal fusion and complications," *Appl. Radiol.,* pp. 14-28, 2009.

[84] M. Oshina, Y. Oshima, S. Tanaka, and K. D. Riew, "Radiological Fusion Criteria of Postoperative Anterior Cervical Discectomy and Fusion: A Systematic Review," *Global Spine J,* vol. 8, no. 7, pp. 739-750, Oct 2018, doi: 10.1177/2192568218755141.

[85] E. Klineberg, M. Gupta, I. McCarthy, and R. Hostin, "Detection of Pseudarthrosis in Adult Spinal Deformity: The Use of Health-related Quality-of-life Outcomes to Predict Pseudarthrosis," *Clin Spine Surg,* vol. 29, no. 8, pp. 318-22, Oct 2016, doi: 10.1097/BSD.0000000000000062.

[86] Y. Chen *et al.*, "Subsidence of titanium mesh cage: a study based on 300 cases," *J Spinal Disord Tech,* vol. 21, no. 7, pp. 489-92, Oct 2008, doi: 10.1097/BSD.0b013e318158de22.

[87] M. A. R. Soliman *et al.*, "Vertebral bone quality score independently predicts cage subsidence following transforaminal lumbar interbody fusion," *Spine J,* vol. 22, no. 12, pp. 2017-2023, Dec 2022, doi: 10.1016/j.spinee.2022.08.002.

[88] A. Parisien, E. K. Wai, M. S. A. ElSayed, and H. Frei, "Subsidence of Spinal Fusion Cages: A Systematic Review," *Int J Spine Surg,* vol. 16, no. 6, pp. 1103-1118, Dec 2022, doi: 10.14444/8363.

[89] A. Agarwal, V. Palepu, A. K. Agarwal, V. K. Goel, and E. D. Yildirim, "Biomechanical evaluation of an endplate-conformed polycaprolactone-hydroxyapatite intervertebral fusion graft and its comparison with a typical nonconformed cortical graft," *J Biomech Eng,* vol. 135, no. 6, pp. 61005-9, Jun 2013, doi: 10.1115/1.4023988.

[90] N. de Beer and C. Scheffer, "Reducing subsidence risk by using rapid manufactured patient-specific intervertebral disc implants," *Spine J,* vol. 12, no. 11, pp. 1060-6, Nov 2012, doi: 10.1016/j.spinee.2012.10.003.

[91] L. Marchi, N. Abdala, L. Oliveira, R. Amaral, E. Coutinho, and L. Pimenta, "Radiographic and clinical evaluation of cage subsidence after stand-alone lateral interbody fusion," *J Neurosurg Spine,* vol. 19, no. 1, pp. 110-8, Jul 2013, doi: 10.3171/2013.4.SPINE12319.

[92] R. N. Alkalay, R. Adamson, and M. W. Groff, "The effect of interbody fusion cage design on the stability of the instrumented spine in response to cyclic loading: an experimental study," *Spine J,* vol. 18, no. 10, pp. 1867-1876, Oct 2018, doi: 10.1016/j.spinee.2018.03.003.

[93] A. J. Pisano, D. R. Fredericks, T. Steelman, C. Riccio, M. D. Helgeson, and S. C. Wagner, "Lumbar disc height and vertebral Hounsfield units: association with interbody cage subsidence," *Neurosurg Focus,* vol. 49, no. 2, p. E9, Aug 2020, doi: 10.3171/2020.4.FOCUS20286.

[94] Y. C. Yao, P. H. Chou, H. H. Lin, S. T. Wang, C. L. Liu, and M. C. Chang, "Risk Factors of Cage Subsidence in Patients Received Minimally Invasive Transforaminal Lumbar Interbody Fusion," *Spine (Phila Pa 1976),* vol. 45, no. 19, pp. E1279-E1285, Oct 1 2020, doi: 10.1097/BRS.0000000000003557.

[95] M. Macki, S. K. Anand, A. Surapaneni, P. Park, and V. Chang, "Subsidence Rates After Lateral Lumbar Interbody Fusion: A Systematic Review," *World Neurosurg,* vol. 122, pp. 599-606, Feb 2019, doi: 10.1016/j.wneu.2018.11.121.

[96] S. Mehta, A. Tyler, and M. Hast, "Understanding the Basics of Computational Models in Orthopaedics: A Nonnumeric Review for Surgeons," *J Am Acad Orthop Surg,* vol. 25, pp. 684-692, 2017, doi: 10.5435/JAAOS-D-16-00320.

[97] F. Harrold, A. Malhas, and C. Wigderowitz, "A novel osteotomy in shoulder joint replacement based on analysis of the cartilage/metaphyseal interface," *Clin Biomech (Bristol, Avon),* vol. 29, no. 9, pp. 1032-8, Nov 2014, doi: 10.1016/j.clinbiomech.2014.08.008.

[98] A. Ladermann *et al.*, "Effect of humeral stem design on humeral position and range of motion in reverse shoulder arthroplasty," *Int Orthop,* vol. 39, no. 11, pp. 2205-13, Nov 2015, doi: 10.1007/s00264-015-2984-3.

[99] D. D. Robertson, J. Yuan, L. U. Bigliani, E. L. Flatow, and K. Yamaguchi, "Three-dimensional analysis of the proximal part of the humerus: relevance to arthroplasty," *J Bone Joint Surg Am,* vol. 82, no. 11, pp. 1594-602, Nov 2000, doi: 10.2106/00004623-200011000-00013.

[100] K. R. Saul, S. Hayon, T. L. Smith, C. J. Tuohy, and S. Mannava, "Postural dependence of passive tension in the supraspinatus following rotator cuff repair: a simulation analysis," *Clin Biomech (Bristol, Avon),* vol. 26, no. 8, pp. 804-10, Oct 2011, doi: 10.1016/j.clinbiomech.2011.04.005.

[101] H. Hatze, "A mathematical model for the computational determination of parameter values of anthropomorphic segments," *J Biomech,* vol. 13, no. 10, pp. 833-43, 1980, doi: 10.1016/0021-9290(80)90171-2.

[102] P. de Leva, "Adjustments to Zatsiorsky-Seluyanov's segment inertia parameters," *J Biomech,* vol. 29, no. 9, pp. 1223-30, Sep 1996, doi: 10.1016/0021-9290(95)00178-6.

[103] K. Ohta, M. M. Svinin, Z. Luo, S. Hosoe, and R. Laboissiere, "Optimal trajectory formation of constrained human arm reaching movements," *Biol Cybern,* vol. 91, no. 1, pp. 23-36, Jul 2004, doi: 10.1007/s00422-004-0491-5.

[104] A. C. Schouten, E. de Vlugt, F. C. van der Helm, and G. G. Brouwn, "Optimal posture control of a musculo-skeletal arm model," *Biol Cybern,* vol. 84, no. 2, pp. 143-52, Feb 2001, doi: 10.1007/s004220000202.

[105] P. J. Laz and M. Browne, "A review of probabilistic analysis in orthopaedic biomechanics," *Proc Inst Mech Eng H,* vol. 224, no. 8, pp. 927-43, 2010, doi: 10.1243/09544119JEIM739.

[106] W. M. Park, K. Kim, and Y. H. Kim, "Effects of degenerated intervertebral discs on intersegmental rotations, intradiscal pressures, and facet joint forces of the whole lumbar spine," *Comput Biol Med,* vol. 43, no. 9, pp. 1234-40, Sep 2013, doi: 10.1016/j.compbiomed.2013.06.011.

[107] J. P. Little, H. de Visser, M. J. Pearcy, and C. J. Adam, "Are coupled rotations in the lumbar spine largely due to the osseo-ligamentous anatomy?--a modeling study," *Comput Methods Biomech Biomed Engin,* vol. 11, no. 1, pp. 95-103, Feb 2008, doi: 10.1080/10255840701552143.

[108] F. Ghezelbash, H. Schmidt, A. Shirazi-Adl, and M. El-Rich, "Internal load-sharing in the human passive lumbar spine: Review of in vitro and finite element model

studies," *J Biomech,* vol. 102, p. 109441, Mar 26 2020, doi: 10.1016/j.jbiomech.2019.109441.

[109] P. Jain, M. Rana, J. K. Biswas, and M. R. Khan, "Biomechanics of spinal implants-a review," *Biomed Phys Eng Express,* vol. 6, no. 4, p. 042002, Jul 7 2020, doi: 10.1088/2057-1976/ab9dd2.

[110] A. Kiapour, D. Ambati, R. W. Hoy, and V. K. Goel, "Effect of graded facetectomy on biomechanics of Dynesys dynamic stabilization system," *Spine (Phila Pa 1976),* vol. 37, no. 10, pp. E581-9, May 1 2012, doi: 10.1097/BRS.0b013e3182463775.

[111] H. Schmidt, F. Galbusera, A. Rohlmann, T. Zander, and H. J. Wilke, "Effect of multilevel lumbar disc arthroplasty on spine kinematics and facet joint loads in flexion and extension: a finite element analysis," *Eur Spine J,* vol. 21 Suppl 5, pp. S663-74, Jun 2012, doi: 10.1007/s00586-010-1382-1.

[112] T. Zander, A. Rohlmann, and G. Bergmann, "Influence of different artificial disc kinematics on spine biomechanics," *Clin Biomech (Bristol, Avon),* vol. 24, no. 2, pp. 135-42, Feb 2009, doi: 10.1016/j.clinbiomech.2008.11.008.

[113] C. L. Liu *et al.*, "Effect of the cord pretension of the Dynesys dynamic stabilisation system on the biomechanics of the lumbar spine: a finite element analysis," *Eur Spine J,* vol. 20, no. 11, pp. 1850-8, Nov 2011, doi: 10.1007/s00586-011-1817-3.

[114] M. Dreischarf *et al.*, "Comparison of eight published static finite element models of the intact lumbar spine: predictive power of models improves when combined together," *J Biomech,* vol. 47, no. 8, pp. 1757-66, Jun 3 2014, doi: 10.1016/j.jbiomech.2014.04.002.

[115] A. Shirazi-Adl, "Biomechanics of the lumbar spine in sagittal/lateral moments," *Spine (Phila Pa 1976),* vol. 19, no. 21, pp. 2407-14, Nov 1 1994, doi: 10.1097/00007632-199411000-00007.

[116] U. M. Ayturk and C. M. Puttlitz, "Parametric convergence sensitivity and validation of a finite element model of the human lumbar spine," *Comput Methods Biomech Biomed Engin,* vol. 14, no. 8, pp. 695-705, Aug 2011, doi: 10.1080/10255842.2010.493517.

[117] D. S. Fidalgo *et al.*, "Minimally invasive transforaminal and anterior lumbar interbody fusion surgery at level L5-S1," *Comput Methods Biomech Biomed Engin,* vol. 23, no. 8, pp. 384-395, Jun 2020, doi: 10.1080/10255842.2020.1731482.

[118] R. Oikawa *et al.*, "Comparison of the Susceptibility to Implant Failure in the Lateral, Posterior, and Transforaminal Lumbar Interbody Fusion: A Finite Element Analysis," *World Neurosurg,* vol. 164, pp. e835-e843, Aug 2022, doi: 10.1016/j.wneu.2022.05.056.

[119] H. Xu *et al.*, "Biomechanical comparison of posterior lumbar interbody fusion and transforaminal lumbar interbody fusion by finite element analysis," *Neurosurgery,* vol. 72, no. 1 Suppl Operative, pp. 21-6, Mar 2013, doi: 10.1227/NEU.0b013e3182742a69.

[120] G. Fang *et al.*, "Biomechanical Comparison of Stand-Alone and Bilateral Pedicle Screw Fixation for Oblique Lumbar Interbody Fusion Surgery-A Finite Element Analysis," (in eng), *World Neurosurg,* vol. 141, pp. e204-e212, Sep 2020, doi: 10.1016/j.wneu.2020.05.245.

[121] Q. Ling, H. Zhang, and E. He, "Screws Fixation for Oblique Lateral Lumbar Interbody Fusion (OL-LIF): A Finite Element Study," (in eng), *Biomed Res Int,* vol. 2021, p. 5542595, 2021, doi: 10.1155/2021/5542595.

[122] H. Shen, Y. Chen, Z. Liao, and W. Liu, "Biomechanical evaluation of anterior lumbar interbody fusion with various fixation options: Finite element analysis of static and vibration conditions," (in eng), *Clin Biomech (Bristol, Avon),* vol. 84, p. 105339, Apr 2021, doi: 10.1016/j.clinbiomech.2021.105339.

[123] D. A. Sin and D. H. Heo, "Comparative Finite Element Analysis of Lumbar Cortical Screws and Pedicle Screws in Transforaminal and Posterior Lumbar Interbody Fusion," (in eng), *Neurospine,* vol. 16, no. 2, pp. 298-304, Jun 2019, doi: 10.14245/ns.1836030.015.

[124] C. Song, H. Chang, D. Zhang, Y. Zhang, M. Shi, and X. Meng, "Biomechanical Evaluation of Oblique Lumbar Interbody Fusion with Various Fixation Options: A Finite Element Analysis," (in eng), *Orthop Surg,* vol. 13, no. 2, pp. 517-529, Apr 2021, doi: 10.1111/os.12877.

[125] C. E. Wong, H. T. Hu, L. H. Kao, C. J. Liu, K. C. Chen, and K. Y. Huang, "Biomechanical feasibility of semi-rigid stabilization and semi-rigid lumbar interbody fusion: a finite element study," (in eng), *BMC Musculoskelet Disord,* vol. 23, no. 1, p. 10, Jan 3 2022, doi: 10.1186/s12891-021-04958-3.

[126] J. Zhu, H. Shen, Y. Cui, G. R. Fogel, Z. Liao, and W. Liu, "Biomechanical Evaluation of Transforaminal Lumbar Interbody Fusion with Coflex-F and

Pedicle Screw Fixation: Finite Element Analysis of Static and Vibration Conditions," (in eng), *Orthop Surg,* vol. 14, no. 9, pp. 2339-2349, Sep 2022, doi: 10.1111/os.13425.

[127] C. Zhang *et al.*, "Does Osteoporosis Affect the Adjacent Segments Following Anterior Lumbar Interbody Fusion? A Finite Element Study," *World Neurosurg,* vol. 146, pp. e739-e746, Feb 2021, doi: 10.1016/j.wneu.2020.11.005.

[128] Z. Zhang, G. R. Fogel, Z. Liao, Y. Sun, and W. Liu, "Biomechanical analysis of lumbar interbody fusion cages with various lordotic angles: a finite element study," *Comput Methods Biomech Biomed Engin,* vol. 21, no. 3, pp. 247-254, Feb 2018, doi: 10.1080/10255842.2018.1442443.

[129] C. Nan, Z. Ma, Y. Liu, L. Ma, J. Li, and W. Zhang, "Impact of cage position on biomechanical performance of stand-alone lateral lumbar interbody fusion: a finite element analysis," *BMC Musculoskelet Disord,* vol. 23, no. 1, p. 920, Oct 18 2022, doi: 10.1186/s12891-022-05873-x.

[130] L. S. Chatham, V. V. Patel, C. M. Yakacki, and R. Dana Carpenter, "Interbody Spacer Material Properties and Design Conformity for Reducing Subsidence During Lumbar Interbody Fusion," (in eng), *J Biomech Eng,* vol. 139, no. 5, pp. 0510051-8, May 1 2017, doi: 10.1115/1.4036312.

[131] H. Kang, S. J. Hollister, F. La Marca, P. Park, and C. Y. Lin, "Porous biodegradable lumbar interbody fusion cage design and fabrication using integrated global-local topology optimization with laser sintering," (in eng), *J Biomech Eng,* vol. 135, no. 10, pp. 101013-8, Oct 1 2013, doi: 10.1115/1.4025102.

[132] T. Lu *et al.*, "Relationship between the elastic modulus of the cage material and the biomechanical properties of transforaminal lumbar interbody fusion: A logarithmic regression analysis based on parametric finite element simulations," (in eng), *Comput Methods Programs Biomed,* vol. 214, p. 106570, Feb 2022, doi: 10.1016/j.cmpb.2021.106570.

[133] S. Vadapalli *et al.*, "Biomechanical rationale for using polyetheretherketone (PEEK) spacers for lumbar interbody fusion-A finite element study," (in eng), *Spine (Phila Pa 1976),* vol. 31, no. 26, pp. E992-8, Dec 15 2006, doi: 10.1097/01.brs.0000250177.84168.ba.

[134] H. Wang, Y. Wan, X. Liu, B. Ren, Y. Xia, and Z. Liu, "The biomechanical effects of Ti versus PEEK used in the PLIF surgery on lumbar spine: a finite element

analysis," (in eng), *Comput Methods Biomech Biomed Engin,* vol. 24, no. 10, pp. 1115-1124, Aug 2021, doi: 10.1080/10255842.2020.1869219.

[135] Z. Zhang, H. Li, G. R. Fogel, D. Xiang, Z. Liao, and W. Liu, "Finite element model predicts the biomechanical performance of transforaminal lumbar interbody fusion with various porous additive manufactured cages," (in eng), *Comput Biol Med,* vol. 95, pp. 167-174, Apr 1 2018, doi: 10.1016/j.compbiomed.2018.02.016.

[136] M. P. Soares dos Santos *et al.*, "Instrumented hip joint replacements, femoral replacements and femoral fracture stabilizers," *Expert Rev Med Devices,* vol. 11, no. 6, pp. 617-35, Nov 2014, doi: 10.1586/17434440.2014.946695.

[137] J. N. Torrao, M. P. Dos Santos, and J. A. Ferreira, "Instrumented knee joint implants: innovations and promising concepts," *Expert Rev Med Devices,* vol. 12, no. 5, pp. 571-84, 2015, doi: 10.1586/17434440.2015.1068114.

[138] E. H. Ledet, D. D'Lima, P. Westerhoff, J. A. Szivek, R. A. Wachs, and G. Bergmann, "Implantable sensor technology: from research to clinical practice," *J Am Acad Orthop Surg,* vol. 20, no. 6, pp. 383-92, Jun 2012, doi: 10.5435/JAAOS-20-06-383.

[139] S. S. Karipott, B. D. Nelson, R. E. Guldberg, and K. G. Ong, "Clinical potential of implantable wireless sensors for orthopedic treatments," *Expert Rev Med Devices,* vol. 15, no. 4, pp. 255-264, Apr 2018, doi: 10.1080/17434440.2018.1454310.

[140] G. Bergmann, F. Graichen, A. Bender, M. Kaab, A. Rohlmann, and P. Westerhoff, "In vivo glenohumeral contact forces--measurements in the first patient 7 months postoperatively," *J Biomech,* vol. 40, no. 10, pp. 2139-49, 2007, doi: 10.1016/j.jbiomech.2006.10.037.

[141] F. Graichen, R. Arnold, A. Rohlmann, and G. Bergmann, "Implantable 9-Channel Telemetry System for In Vivo Load Measurements With Orthopedic Implants," *IEEE Transactions on Biomedical Engineering,* vol. 54, no. 2, pp. 253-251, 2007.

[142] P. Westerhoff *et al.*, "In vivo measurement of shoulder joint loads during activities of daily living," *J Biomech,* vol. 42, no. 12, pp. 1840-9, Aug 25 2009, doi: 10.1016/j.jbiomech.2009.05.035.

[143] G. Bergmann *et al.*, "In vivo gleno-humeral joint loads during forward flexion and abduction," *J Biomech,* vol. 44, no. 8, pp. 1543-52, May 17 2011, doi: 10.1016/j.jbiomech.2011.02.142.

[144] C. E. Carlson, R. W. Mann, and W. H. Harris, "A radio telemetry device for monitoring cartilage surface pressures in the human hip," *IEEE Trans Biomed Eng,* vol. 21, no. 4, pp. 257-64, Jul 1974, doi: 10.1109/TBME.1974.324311.

[145] C. E. Carlson, R. W. Mann, and W. H. Harris, "A look at the prosthesis-cartilage interface: design of a hip prosthesis containing pressure transducers," *J Biomed Mater Res,* vol. 8, no. 4 Pt 2, pp. 261-9, 1974, doi: 10.1002/jbm.820080405.

[146] W. A. Hodge *et al.*, "Contact pressures from an instrumented hip endoprosthesis," *J Bone Joint Surg Am,* vol. 71, no. 9, pp. 1378-86, Oct 1989. [Online]. Available: https://www.ncbi.nlm.nih.gov/pubmed/2793891.

[147] W. A. Hodge, R. S. Fijan, K. L. Carlson, R. G. Burgess, W. H. Harris, and R. W. Mann, "Contact pressures in the human hip joint measured in vivo," *Proc Natl Acad Sci U S A,* vol. 83, no. 9, pp. 2879-83, May 1986, doi: 10.1073/pnas.83.9.2879.

[148] D. E. Krebs, L. Elbaum, P. O. Riley, W. A. Hodge, and R. W. Mann, "Exercise and gait effects on in vivo hip contact pressures," *Phys Ther,* vol. 71, no. 4, pp. 301-9, Apr 1991, doi: 10.1093/ptj/71.4.301.

[149] C. A. McGibbon, D. E. Krebs, and R. W. Mann, "In vivo hip pressures during cane and load-carrying gait," *Arthritis Care Res,* vol. 10, no. 5, pp. 300-7, Oct 1997, doi: 10.1002/art.1790100504.

[150] C. A. McGibbon, D. E. Krebs, C. A. Trahan, S. B. Trippel, and R. W. Mann, "Cartilage degeneration in relation to repetitive pressure: case study of a unilateral hip hemiarthroplasty patient," *J Arthroplasty,* vol. 14, no. 1, pp. 52-8, Jan 1999, doi: 10.1016/s0883-5403(99)90202-4.

[151] P. D. Rushfeld, R. W. Mann, and W. H. Harris, "Influence of cartilage geometry on the pressure distribution in the human hip joint," *Science,* vol. 204, no. 4391, pp. 413-5, Apr 27 1979, doi: 10.1126/science.441729.

[152] D. L. Givens-Heiss *et al.*, "In vivo acetabular contact pressures during rehabilitation, Part II: Postacute phase," *Phys Ther,* vol. 72, no. 10, pp. 700-5; discussion 706-10, Oct 1992, doi: 10.1093/ptj/72.10.700.

[153] G. Bergmann *et al.*, "Hip contact forces and gait patterns from routine activities," *J Biomech,* vol. 34, no. 7, pp. 859-71, Jul 2001, doi: 10.1016/s0021-9290(01)00040-9.

[154] G. Bergmann, F. Graichen, and A. Rohlmann, "Is staircase walking a risk for the fixation of hip implants?," *J Biomech,* vol. 28, no. 5, pp. 535-53, May 1995, doi: 10.1016/0021-9290(94)00105-d.

[155] G. Bergmann, F. Graichen, and A. Rohlmann, "Hip joint contact forces during stumbling," *Langenbecks Arch Surg,* vol. 389, no. 1, pp. 53-9, Feb 2004, doi: 10.1007/s00423-003-0434-y.

[156] G. Bergmann, F. Graichen, A. Rohlmann, and H. Linke, "Hip joint forces during load carrying," *Clin Orthop Relat Res,* no. 335, pp. 190-201, Feb 1997. [Online]. Available: https://www.ncbi.nlm.nih.gov/pubmed/9020218.

[157] G. Bergmann, H. Kniggendorf, F. Graichen, and A. Rohlmann, "Influence of shoes and heel strike on the loading of the hip joint," *J Biomech,* vol. 28, no. 7, pp. 817-27, Jul 1995, doi: 10.1016/0021-9290(94)00129-r.

[158] P. Damm, F. Graichen, A. Rohlmann, A. Bender, and G. Bergmann, "Total hip joint prosthesis for in vivo measurement of forces and moments," *Med Eng Phys,* vol. 32, no. 1, pp. 95-100, Jan 2010, doi: 10.1016/j.medengphy.2009.10.003.

[159] F. Graichen, G. Bergmann, and A. Rohlmann, "Hip endoprosthesis for in vivo measurement of joint force and temperature," *J Biomech,* vol. 32, no. 10, pp. 1113-7, Oct 1999, doi: 10.1016/s0021-9290(99)00110-4.

[160] M. O. Heller *et al.*, "Musculo-skeletal loading conditions at the hip during walking and stair climbing," *J Biomech,* vol. 34, no. 7, pp. 883-93, Jul 2001, doi: 10.1016/s0021-9290(01)00039-2.

[161] G. M. Kotzar *et al.*, "Telemeterized in vivo hip joint force data: a report on two patients after total hip surgery," *J Orthop Res,* vol. 9, no. 5, pp. 621-33, Sep 1991, doi: 10.1002/jor.1100090502.

[162] P. Damm *et al.*, "Friction in total hip joint prosthesis measured in vivo during walking," *PLoS One,* vol. 8, no. 11, p. e78373, 2013, doi: 10.1371/journal.pone.0078373.

[163] G. Bergmann, F. Graichen, A. Rohlmann, N. Verdonschot, and G. H. van Lenthe, "Frictional heating of total hip implants. Part 1: measurements in patients," *J Biomech,* vol. 34, no. 4, pp. 421-8, Apr 2001, doi: 10.1016/s0021-9290(00)00188-3.

[164] R. Puers *et al.*, "A telemetry system for the detection of hip prosthesis loosening by vibration analysis," *Sensors and Actuators A,* vol. 85, pp. 42-47, 2000.

[165] C. O'Connor and A. Kiourti, "Wireless Sensors for Smart Orthopaedic Implants," *J Bio Tribo Corros,* vol. 3, no. 20, 2017.

[166] D. D. D'Lima, C. P. Townsend, S. W. Arms, B. A. Morris, and C. W. Colwell, Jr., "An implantable telemetry device to measure intra-articular tibial forces," *J Biomech,* vol. 38, no. 2, pp. 299-304, Feb 2005, doi: 10.1016/j.jbiomech.2004.02.011.

[167] D. D. D'Lima, S. Patil, N. Steklov, J. E. Slamin, and C. W. Colwell, Jr., "The Chitranjan Ranawat Award: in vivo knee forces after total knee arthroplasty," *Clin Orthop Relat Res,* vol. 440, pp. 45-9, Nov 2005, doi: 10.1097/01.blo.0000186559.62942.8c.

[168] D. D. D'Lima, S. Patil, N. Steklov, S. Chien, and C. W. Colwell, Jr., "In vivo knee moments and shear after total knee arthroplasty," *J Biomech,* vol. 40 Suppl 1, pp. S11-7, 2007, doi: 10.1016/j.jbiomech.2007.03.004.

[169] D. D. D'Lima, S. Patil, N. Steklov, and C. W. Colwell, Jr., "The 2011 ABJS Nicolas Andry Award: 'Lab'-in-a-knee: in vivo knee forces, kinematics, and contact analysis," *Clin Orthop Relat Res,* vol. 469, no. 10, pp. 2953-70, Oct 2011, doi: 10.1007/s11999-011-1916-9.

[170] D. D. D'Lima, N. Steklov, S. Patil, and C. W. Colwell, Jr., "The Mark Coventry Award: in vivo knee forces during recreation and exercise after knee arthroplasty," *Clin Orthop Relat Res,* vol. 466, no. 11, pp. 2605-11, Nov 2008, doi: 10.1007/s11999-008-0345-x.

[171] I. Kutzner *et al.*, "Loading of the knee joint during activities of daily living measured in vivo in five subjects," *J Biomech,* vol. 43, no. 11, pp. 2164-73, Aug 10 2010, doi: 10.1016/j.jbiomech.2010.03.046.

[172] D. D. D'Lima, B. J. Fregly, S. Patil, N. Steklov, and C. W. Colwell, Jr., "Knee joint forces: prediction, measurement, and significance," *Proc Inst Mech Eng H,* vol. 226, no. 2, pp. 95-102, Feb 2012, doi: 10.1177/0954411911433372.

[173] B. J. Fregly, D. D. D'Lima, and C. W. Colwell, Jr., "Effective gait patterns for offloading the medial compartment of the knee," *J Orthop Res,* vol. 27, no. 8, pp. 1016-21, Aug 2009, doi: 10.1002/jor.20843.

[174] A. Park. "Zimmer Biomet, Canary Medical land FDA de novo clearance for sensor-equipped 'smart' knee implant." Fierce Biotech. https://www.fiercebiotech.com/medtech/zimmer-biomet-canary-medical-land-fda-de-novo-clearance-for-sensor-equipped-smart-knee (accessed 15/09/2021, 2021).

[175] A. Rohlmann, U. Gabel, F. Graichen, A. Bender, and G. Bergmann, "An instrumented implant for vertebral body replacement that measures loads in the anterior spinal column," *Med Eng Phys,* vol. 29, no. 5, pp. 580-5, Jun 2007, doi: 10.1016/j.medengphy.2006.06.012.

[176] A. Rohlmann, F. Graichen, R. Kayser, A. Bender, and G. Bergmann, "Loads on a telemeterized vertebral body replacement measured in two patients," *Spine (Phila Pa 1976),* vol. 33, no. 11, pp. 1170-9, May 15 2008, doi: 10.1097/BRS.0b013e3181722d52.

[177] A. Rohlmann *et al.*, "Activities of everyday life with high spinal loads," *PLoS One,* vol. 9, no. 5, p. e98510, 2014, doi: 10.1371/journal.pone.0098510.

[178] A. Rohlmann, V. Schwachmeyer, F. Graichen, and G. Bergmann, "Spinal loads during post-operative physiotherapeutic exercises," *PLoS One,* vol. 9, no. 7, p. e102005, 2014, doi: 10.1371/journal.pone.0102005.

[179] M. Dreischarf *et al.*, "In vivo implant forces acting on a vertebral body replacement during upper body flexion," *J Biomech,* vol. 48, no. 4, pp. 560-565, Feb 26 2015, doi: 10.1016/j.jbiomech.2015.01.007.

[180] M. Dreischarf, A. Rohlmann, F. Graichen, G. Bergmann, and H. Schmidt, "In vivo loads on a vertebral body replacement during different lifting techniques," *J Biomech,* vol. 49, no. 6, pp. 890-895, Apr 11 2016, doi: 10.1016/j.jbiomech.2015.09.034.

[181] A. Rohlmann, G. Bergmann, and F. Graichen, "A spinal fixation device for in vivo load measurement," *J Biomech,* vol. 27, no. 7, pp. 961-7, Jul 1994, doi: 10.1016/0021-9290(94)90268-2.

[182] A. Rohlmann, G. Bergmann, F. Graichen, and H. M. Mayer, "Telemeterized load measurement using instrumented spinal internal fixators in a patient with degenerative instability," *Spine (Phila Pa 1976),* vol. 20, no. 24, pp. 2683-9, Dec 15 1995, doi: 10.1097/00007632-199512150-00009.

[183] A. Rohlmann, G. Bergmann, and F. Graichen, "Loads on an internal spinal fixation device during walking," *J Biomech,* vol. 30, no. 1, pp. 41-7, Jan 1997, doi: 10.1016/s0021-9290(96)00103-0.

[184] A. Rohlmann, G. Bergmann, and F. Graichen, "Loads on internal spinal fixators measured in different body positions," *Eur Spine J,* vol. 8, no. 5, pp. 354-9, 1999, doi: 10.1007/s005860050187.

[185] A. Rohlmann, G. Bergmann, F. Graichen, and H. M. Mayer, "Influence of muscle forces on loads in internal spinal fixation devices," *Spine (Phila Pa 1976),* vol. 23, no. 5, pp. 537-42, Mar 1 1998, doi: 10.1097/00007632-199803010-00005.

[186] M. Windolf *et al.*, "Continuous Rod Load Monitoring to Assess Spinal Fusion Status-Pilot In Vivo Data in Sheep," *Medicina (Kaunas),* vol. 58, no. 7, Jul 6 2022, doi: 10.3390/medicina58070899.

[187] M. Windolf *et al.*, "Continuous Implant Load Monitoring to Assess Bone Healing Status-Evidence from Animal Testing," *Medicina (Kaunas),* vol. 58, no. 7, Jun 27 2022, doi: 10.3390/medicina58070858.

[188] J. A. Szivek, R. F. Roberto, and D. S. Margolis, "In vivo strain measurements from hardware and lamina during spine fusion," *J Biomed Mater Res B Appl Biomater,* vol. 75, no. 2, pp. 243-50, Nov 2005, doi: 10.1002/jbm.b.30262.

[189] E. H. Ledet, M. P. Tymeson, D. J. DiRisio, B. Cohen, and R. L. Uhl, "Direct real-time measurement of in vivo forces in the lumbar spine," *Spine J,* vol. 5, no. 1, pp. 85-94, Jan-Feb 2005, doi: 10.1016/j.spinee.2004.06.017.

[190] C. K. Demetropoulos, C. R. Morgan, D. K. Sengupta, and H. N. Herkowitz, "Development of a 4-axis load cell used for lumbar interbody load measurements," *Med Eng Phys,* vol. 31, no. 7, pp. 846-51, Sep 2009, doi: 10.1016/j.medengphy.2009.04.002.

[191] E. H. Ledet, B. Liddle, K. Kradinova, and S. Harper, "Smart implants in orthopedic surgery, improving patient outcomes: a review," *Innov Entrep Health,* vol. 5, pp. 41-51, 2018, doi: 10.2147/IEH.S133518.

[192] D. Bizzoca *et al.*, "Assessment of fracture healing in orthopaedic trauma," *Injury,* Nov 7 2020, doi: 10.1016/j.injury.2020.11.014.

[193] H. M. Frost, "Wolff's Law and bone's structural adaptations to mechanical usage: an overview for clinicians," *Angle Orthod,* vol. 64, no. 3, pp. 175-88, 1994, doi: 10.1043/0003-3219(1994)064<0175:WLABSA>2.0.CO;2.

[194] F. Burny, M. Donkerwolcke, R. Bourgois, M. Domb, and O. Saric, "Twenty years experience in fracture healing measurement with strain gauges," *Orthopedics,* vol. 7, no. 12, pp. 1823-6, Dec 1 1984, doi: 10.3928/0147-7447-19841201-08.

[195] E. Schneider, M. C. Michel, M. Genge, K. Zuber, R. Ganz, and S. M. Perren, "Loads acting in an intramedullary nail during fracture healing in the human

femur," *J Biomech,* vol. 34, no. 7, pp. 849-57, Jul 2001, doi: 10.1016/s0021-9290(01)00037-9.

[196] R. H. Brown, A. H. Burstein, and V. H. Frankel, "Telemetering in vivo loads from nail plate implants," *J Biomech,* vol. 15, no. 11, pp. 815-23, 1982, doi: 10.1016/0021-9290(82)90046-x.

[197] K. Seide *et al.*, "Telemetric assessment of bone healing with an instrumented internal fixator: a preliminary study," *J Bone Joint Surg Br,* vol. 94, no. 3, pp. 398-404, Mar 2012, doi: 10.1302/0301-620X.94B3.27550.

[198] P. Augat *et al.*, "Biomechanical methods for the assessment of fracture repair," *Injury,* vol. 45 Suppl 2, pp. S32-8, Jun 2014, doi: 10.1016/j.injury.2014.04.006.

[199] B. Kienast *et al.*, "An electronically instrumented internal fixator for the assessment of bone healing," *Bone Joint Res,* vol. 5, no. 5, pp. 191-7, May 2016, doi: 10.1302/2046-3758.55.2000611.

[200] M. P. Soares Dos Santos *et al.*, "Capacitive technologies for highly controlled and personalized electrical stimulation by implantable biomedical systems," *Sci Rep,* vol. 9, no. 1, p. 5001, Mar 21 2019, doi: 10.1038/s41598-019-41540-3.

[201] M. P. Soares Dos Santos *et al.*, "New cosurface capacitive stimulators for the development of active osseointegrative implantable devices," *Sci Rep,* vol. 6, p. 30231, Jul 26 2016, doi: 10.1038/srep30231.

[202] S. C. Mukhopadhyay and I. Ihara, "Sensors and Technologies for Structural Health Monitoring: A Review," in *New Developments in Sensing Technology for Structural Health Monitoring.*, (Lecture Notes in Electrical Engineering, no. 96). Berlin, Heidelberg: Springer, 2011, pp. 1-14.

[203] P. Kudela, M. Radzienski, W. Ostachowicz, and Z. Yang, "Structural Health Monitoring system based on a concept of Lamb wave focusing by the piezoelectric array," *Mechanical Systems and Signal Processing,* vol. 108, pp. 21-32, 2018.

[204] G. T. Webb, P. J. Vardanega, N. A. Hoult, P. R. A. Fidler, P. J. Bennett, and C. R. Middleton, "Analysis of Fiber-Optic Strain-Monitoring Data from a Prestressed Concrete Bridge," *Journal of Bridge Engineering,* vol. 22, no. 5, p. 05017002, 2017/05/01 2017, doi: 10.1061/(ASCE)BE.1943-5592.0000996.

[205] A. Nair and C. S. Cai, "Acoustic emission monitoring of bridges: Review and case studies," *Engineering Structures,* vol. 32, no. 6, pp. 1704-1714, 2010/06/01/ 2010, doi: https://doi.org/10.1016/j.engstruct.2010.02.020.

[206] V. Shahsavari, M. Mashayekhi, M. Mehrkash, and E. Santini-Bell, "Diagnostic Testing of a Vertical Lift Truss Bridge for Model Verification and Decision-Making Support," *Frontiers in Built Environment,* Original Research vol. 5, 2019. [Online]. Available: https://www.frontiersin.org/articles/10.3389/fbuil.2019.00092.

[207] E. Al-Fakih, N. A. Abu Osman, and F. R. Mahamd Adikan, "The use of fiber Bragg grating sensors in biomechanics and rehabilitation applications: the state-of-the-art and ongoing research topics," *Sensors (Basel),* vol. 12, no. 10, pp. 12890-926, Sep 25 2012, doi: 10.3390/s121012890.

[208] K. A. Gustke, G. J. Golladay, M. W. Roche, L. C. Elson, and C. R. Anderson, "A Targeted Approach to Ligament Balancing Using Kinetic Sensors," *J Arthroplasty,* vol. 32, no. 7, pp. 2127-2132, Jul 2017, doi: 10.1016/j.arth.2017.02.021.

[209] A. Nag, N. Afasrimanesh, S. Feng, and S. C. Mukhopadhyay, "Strain induced graphite/PDMS sensors for biomedical applications," *Sensors and Actuators A: Physical,* vol. 271, pp. 257-269, 2018.

[210] A. Nag, A. Mitra, and S. C. Mukhopadhyay, "Graphene and its sensor-based applications: A review," *Sensors and Actuators A: Physical,* vol. 270, pp. 177-194, 2018.

[211] A. Nag, S. C. Mukhopadhyay, and J. Kosel, "Flexible carbon nanotube nanocomposite sensor for multiple physiological parameter monitoring," *Sensors and Actuators A: Physical,* vol. 251, pp. 148-155, 2016.

[212] A. Nag, S. C. Mukhopadhyay, and J. Kosel, "Sensing system for salinity testing using laser-induced graphene sensors," *Sensors and Actuators A: Physical,* vol. 264, pp. 107-116, 2017.

[213] A. E. Anderson, B. J. Ellis, S. A. Maas, C. L. Peters, and J. A. Weiss, "Validation of finite element predictions of cartilage contact pressure in the human hip joint," *J Biomech Eng,* vol. 130, no. 5, p. 051008, Oct 2008, doi: 10.1115/1.2953472.

[214] R. K. Kdolsky, B. Al Arabid, M. Fuchs, R. Schabus, and V. Vecsei, "Measuring the pressure pattern of the joint surface in the uninjured knee," *Wien Klin Wochenschr,*

vol. 116, no. 5-6, pp. 196-200, Mar 31 2004. [Online]. Available: https://www.ncbi.nlm.nih.gov/pubmed/15088995.

[215] E. I. Drewniak, J. J. Crisco, D. B. Spenciner, and B. C. Fleming, "Accuracy of circular contact area measurements with thin-film pressure sensors," *J Biomech,* vol. 40, no. 11, pp. 2569-72, 2007, doi: 10.1016/j.jbiomech.2006.12.002.

[216] M. L. Harris, P. Morberg, W. J. Bruce, and W. R. Walsh, "An improved method for measuring tibiofemoral contact areas in total knee arthroplasty: a comparison of K-scan sensor and Fuji film," *J Biomech,* vol. 32, no. 9, pp. 951-8, Sep 1999. [Online]. Available: https://www.ncbi.nlm.nih.gov/pubmed/10460132.

[217] Kenry, J. C. Yeo, and C. T. Lim, "Emerging flexible and wearable physical sensing platforms for healthcare and biomedical applications," *Microsyst Nanoeng,* vol. 2, p. 16043, 2016, doi: 10.1038/micronano.2016.43.

[218] S. R. Khan, S. K. Pavuluri, G. Cummins, and M. P. Y. Desmulliez, "Wireless Power Transfer Techniques for Implantable Medical Devices: A Review," *Sensors,* vol. 20, no. 3487, 2020, doi: doi:10.3390/s20123487.

[219] A. Ibrahim, M. Jain, E. Salman, R. Willing, and S. Towfighian, "A Smart Knee Implant Using Triboelectric Energy Harvesters," *Smart Mater Struct,* vol. 28, no. 2, Feb 2019, doi: 10.1088/1361-665X/aaf3f1.

[220] M. P. Soares dos Santos *et al.*, "Instrumented hip implants: electric supply systems," *J Biomech,* vol. 46, no. 15, pp. 2561-71, Oct 18 2013, doi: 10.1016/j.jbiomech.2013.08.002.

[221] H.-J. Kim, H. Hirayama, S. Kim, K. J. Han, R. Zhang, and J.-W. Choi, "Review of Near-Field Wireless Power and Communication for Biomedical Applications," *IEEE Access,* vol. 5, pp. 21264–21285, 2017.

[222] S. O'Driscoll, A. Poon, and T. H. Meng, "A mm-sized implantable power receiver with adaptive link compensation.," in *IEEE International Solid-State Circuits Conference-Digest of Technical Papers*, California, USA, 8–12 Febuary 2009 2009: IEEE.

[223] B. J. Varghese, P. B. Bobba, and M. Kavitha, "Effects of coil misalignment in a four coil implantable wireless power transfer system," in *IEEE 7th Power India International Conference (PIICON)*, Bikaner, India, 25-27 November, 2016 2016.

[224] M. Manoufali, K. Bialkowski, B. J. Mohammed, P. C. Mills, and A. Abbosh, "Near-Field Inductive-Coupling Link to Power a Three-Dimensional Millimeter-Size

Antenna for Brain Implantable Medical Devices," (in English), *Ieee Transactions on Biomedical Engineering,* vol. 65, no. 1, pp. 4-14, Jan 2018, doi: 10.1109/Tbme.2017.2778729.

[225] R. Jegadeesan, S. Nag, K. Agarwal, N. V. Thakor, and Y. X. Guo, "Enabling Wireless Powering and Telemetry for Peripheral Nerve Implants," (in English), *Ieee J Biomed Health,* vol. 19, no. 3, pp. 958-970, May 2015, doi: 10.1109/Jbhi.2015.2424985.

[226] C. Gong, D. Liu, Z. D. Miao, and M. Li, "A Magnetic-Balanced Inductive Link for the Simultaneous Uplink Data and Power Telemetry," (in English), *Sensors,* vol. 17, no. 8, Aug 2017, doi: ARTN 1768

10.3390/s17081768.

[227] Y. J. Kim, J. M. Maeng, and P. P. Irazoqui, "Eyeglasses-powered, contact lens-like platform with high power transfer efficiency," (in English), *Biomed Microdevices,* vol. 17, no. 4, Aug 2015, doi: ARTN 75

10.1007/s10544-015-9979-0.

[228] H. C. Stronks and G. Dagnelie, "The functional performance of the Argus II retinal prosthesis," (in English), *Expert Rev Med Devic,* vol. 11, no. 1, pp. 23-30, Jan 2014, doi: 10.1586/17434440.2014.862494.

[229] T. J. Sun, X. Xie, G. L. Li, Y. K. Gu, Y. D. Deng, and Z. H. Wang, "A Two-Hop Wireless Power Transfer System With an Efficiency-Enhanced Power Receiver for Motion-Free Capsule Endoscopy Inspection," (in English), *Ieee Transactions on Biomedical Engineering,* vol. 59, no. 11, pp. 3247-3254, Nov 2012, doi: 10.1109/Tbme.2012.2206809.

[230] G. X. Wang, W. T. Liu, M. Sivaprakasam, and G. A. Kendir, "Design and analysis of an adaptive transcutaneous power telemetry for biomedical implants," (in English), *Ieee T Circuits-I,* vol. 52, no. 10, pp. 2109-2117, Oct 2005, doi: 10.1109/Tcsi.2005.852923.

[231] R. Das and H. Yoo, "A Multiband Antenna Associating Wireless Monitoring and Nonleaky Wireless Power

Transfer System for Biomedical Implants," *IEEE Trans. Microw. Theory Tech.*, vol. 65, pp. 2485–2495, 2017.

[232] Y. Tanabe *et al.*, "High-performance wireless powering for peripheral nerve neuromodulation systems.," *PLoS ONE,* vol. 12, 2017.

[233] J. S. Ho *et al.*, "Wireless power transfer to deep-tissue microimplants.," *Proc. Natl. Acad. Sci. USA,* vol. 111, pp. 7974–7979, 2014.

[234] A. Kim, C. Powell, and B. Ziaie, "An Implantable Pressure Sensing System with Electromechanical Interrogation Scheme.," *IEEE Trans. Biomed. Eng.,* vol. 61, pp. 2209–2217, 2014.

[235] J. Charthad *et al.*, "A mm-Sized Wireless Implantable Device for Electrical Stimulation of Peripheral Nerves.," *IEEE Trans. Biomed. Circuits Syst,* vol. 12, pp. 257-270, 2018.

[236] T. Maleki, N. Cao, S. H. Song, C. Kao, S.-C. Ko, and B. Ziaie, "An Ultrasonically Powered Implantable Micro-Oxygen Generator (IMOG)." *IEEE Trans. Biomed. Eng.,* vol. 58, pp. 3104-3111, 2011.

[237] F. Duck, "Ultrasound in Medicine," *Ultrasonics,* vol. 24, p. 294, 1986.

[238] P. Hoskins, K. Martin, and A. Thrush, *Diagnostic Ultrasound: Physics and Equipment*. Cambridge, UK: Cambridge University Press, 2010.

[239] B. Lee and M. Ghovanloo, "An Overview of Data Telemetry in Inductively Powered Implantable Biomedical Devices," (in English), *Ieee Commun Mag,* vol. 57, no. 2, pp. 74-80, Feb 2019, doi: 10.1109/Mcom.2018.1800052.

[240] M. L. Navaii, M. Jalali, and H. Sadjedi, "A 34-pJ/bit Area-Efficient ASK Demodulator Based on Switching-Mode Signal Shaping," (in English), *Ieee T Circuits-Ii,* vol. 64, no. 6, pp. 640-644, Jun 2017, doi: 10.1109/Tcsii.2016.2599262.

[241] M. Ghovanloo and K. Najafi, "A wideband frequency-shift keying wireless link for inductively powered biomedical implants," (in English), *Ieee T Circuits-I,* vol. 51, no. 12, pp. 2374-2383, Dec 2004, doi: 10.1109/Tcsi.2004.838144.

[242] M. J. Karimi, A. Schmid, and C. Dehollain, "Wireless Power and Data Transmission for Implanted Devices via Inductive Links: A Systematic Review," (in English), *Ieee Sens J,* vol. 21, no. 6, pp. 7145-7161, Mar 15 2021, doi: 10.1109/Jsen.2021.3049918.

[243] A. Cappuccino *et al.*, "Biomechanical analysis and review of lateral lumbar fusion constructs," *Spine (Phila Pa 1976),* vol. 35, no. 26 Suppl, pp. S361-7, Dec 15 2010, doi: 10.1097/BRS.0b013e318202308b.

[244] B. M. Ozgur, H. E. Aryan, L. Pimenta, and W. R. Taylor, "Extreme Lateral Interbody Fusion (XLIF): a novel surgical technique for anterior lumbar interbody fusion," *Spine J,* vol. 6, no. 4, pp. 435-43, Jul-Aug 2006, doi: 10.1016/j.spinee.2005.08.012.

[245] A. Rohlmann, T. Zander, and G. Bergmann, "Effects of fusion-bone stiffness on the mechanical behavior of the lumbar spine after vertebral body replacement," *Clin Biomech (Bristol, Avon),* vol. 21, no. 3, pp. 221-7, Mar 2006, doi: 10.1016/j.clinbiomech.2005.10.012.

[246] S. N. Khan, F. P. Cammisa, Jr., H. S. Sandhu, A. D. Diwan, F. P. Girardi, and J. M. Lane, "The biology of bone grafting," *J Am Acad Orthop Surg,* vol. 13, no. 1, pp. 77-86, Jan-Feb 2005. [Online]. Available: https://www.ncbi.nlm.nih.gov/pubmed/15712985.

[247] T. Zander, A. Rohlmann, C. Klockner, and G. Bergmann, "Effect of bone graft characteristics on the mechanical behavior of the lumbar spine," *J Biomech,* vol. 35, no. 4, pp. 491-7, Apr 2002, doi: 10.1016/s0021-9290(01)00235-4.

[248] T. Steffen, A. Tsantrizos, I. Fruth, and M. Aebi, "Cages: designs and concepts," *Eur Spine J,* vol. 9 Suppl 1, pp. S89-94, Feb 2000, doi: 10.1007/pl00010027.

[249] M. J. Silva, C. Wang, T. M. Keaveny, and W. C. Hayes, "Direct and computed tomography thickness measurements of the human, lumbar vertebral shell and endplate," *Bone,* vol. 15, no. 4, pp. 409-14, Jul-Aug 1994, doi: 10.1016/8756-3282(94)90817-6.

[250] J. C. Lotz, A. J. Fields, and E. C. Liebenberg, "The role of the vertebral end plate in low back pain," *Global Spine J,* vol. 3, no. 3, pp. 153-64, Jun 2013, doi: 10.1055/s-0033-1347298.

[251] G. Denoziere and D. N. Ku, "Biomechanical comparison between fusion of two vertebrae and implantation of an artificial intervertebral disc," *J Biomech,* vol. 39, no. 4, pp. 766-75, 2006, doi: 10.1016/j.jbiomech.2004.07.039.

[252] S. Roberts, J. Menage, and J. P. Urban, "Biochemical and structural properties of the cartilage end-plate and its relation to the intervertebral disc," *Spine (Phila Pa 1976),* vol. 14, no. 2, pp. 166-74, Feb 1989, doi: 10.1097/00007632-198902000-00005.

[253] A. A. White and M. M. Panjabi, *Clinical biomechanics of the spine*. Philadelphia: Lippincott, 1978.

[254] H. Schmidt *et al.*, "Application of a new calibration method for a three-dimensional finite element model of a human lumbar annulus fibrosus," *Clin Biomech (Bristol, Avon),* vol. 21, no. 4, pp. 337-44, May 2006, doi: 10.1016/j.clinbiomech.2005.12.001.

[255] NuVasive, "CoRoent XL - W - Implant Specs," V. Ramakrishna, Ed., Implant specifications brochure ed, 2022.

[256] NuVasive, "CoRoent XL - Implant Specs," V. Ramakrishna, Ed., Implant specifications brochure ed, 2022.

[257] U. Chamoli, "Studies on lumbar spinal instability due to structural alterations and novel perspectives on spinal motion metrics," Doctor of Philosophy PhD, St. George & Sutherland Clinical School, University of New South Wales, Sydney, 2016.

[258] V. A. S. Ramakrishna, U. Chamoli, L. L. Viglione, N. Tsafnat, and A. D. Diwan, "The Role of Sacral Slope in the Progression of a Bilateral Spondylolytic Defect at L5 to Spondylolisthesis: A Biomechanical Investigation Using Finite Element Analysis," *Global Spine J,* vol. 8, no. 5, pp. 460-470, Aug 2018, doi: 10.1177/2192568217735802.

[259] M. Mengoni, B. J. Luxmoore, V. N. Wijayathunga, A. C. Jones, N. D. Broom, and R. K. Wilcox, "Derivation of inter-lamellar behaviour of the intervertebral disc annulus," *J Mech Behav Biomed Mater,* vol. 48, pp. 164-172, Aug 2015, doi: 10.1016/j.jmbbm.2015.03.028.

[260] Y. M. Lu, W. C. Hutton, and V. M. Gharpuray, "Do bending, twisting, and diurnal fluid changes in the disc affect the propensity to prolapse? A viscoelastic finite element model," *Spine (Phila Pa 1976),* vol. 21, no. 22, pp. 2570-9, Nov 15 1996, doi: 10.1097/00007632-199611150-00006.

[261] G. F. Dall, P. M. Simpson, and S. J. Breusch, "In vitro comparison of Refobacin-Palacos R with Refobacin Bone Cement and Palacos R + G," *Acta Orthop,* vol. 78, no. 3, pp. 404-11, Jun 2007, doi: 10.1080/17453670710013997.

[262] F. Heuer, H. Schmidt, Z. Klezl, L. Claes, and H. J. Wilke, "Stepwise reduction of functional spinal structures increase range of motion and change lordosis angle," *J Biomech,* vol. 40, no. 2, pp. 271-80, 2007, doi: 10.1016/j.jbiomech.2006.01.007.

[263] H. Schmidt, F. Heuer, J. Drumm, Z. Klezl, L. Claes, and H. J. Wilke, "Application of a calibration method provides more realistic results for a finite element model

of a lumbar spinal segment," *Clin Biomech (Bristol, Avon),* vol. 22, no. 4, pp. 377-84, May 2007, doi: 10.1016/j.clinbiomech.2006.11.008.

[264] A. Polikeit, S. J. Ferguson, L. P. Nolte, and T. E. Orr, "The importance of the endplate for interbody cages in the lumbar spine," *European Spine Journal,* vol. 12, no. 6, pp. 556-561, 2003/12/01 2003, doi: 10.1007/s00586-003-0556-5.

[265] *Theoretical background to the Strand7 finite element analysis system*. (2005). Strand7 Pty Ltd.

[266] U. Chamoli, M. H. Korkusuz, A. B. Sabnis, A. R. Manolescu, N. Tsafnat, and A. D. Diwan, "Global and segmental kinematic changes following sequential resection of posterior osteoligamentous structures in the lumbar spine: An in vitro biomechanical investigation using pure moment testing protocols," *Proc Inst Mech Eng H,* vol. 229, no. 11, pp. 812-21, Nov 2015, doi: 10.1177/0954411915612503.

[267] A. Polikeit, S. J. Ferguson, L. P. Nolte, and T. E. Orr, "The importance of the endplate for interbody cages in the lumbar spine," *Eur Spine J,* vol. 12, no. 6, pp. 556-61, Dec 2003, doi: 10.1007/s00586-003-0556-5.

[268] L. Claes, "Improvement of clinical fracture healing - What can be learned from mechano-biological research?," *J Biomech,* vol. 115, p. 110148, Jan 22 2021, doi: 10.1016/j.jbiomech.2020.110148.

[269] J. H. Wolf, "[Julis Wolff and his "law of bone remodeling"]," *Orthopade,* vol. 24, no. 5, pp. 378-86, Sep 1995. [Online]. Available: https://www.ncbi.nlm.nih.gov/pubmed/7478499. Julius Wolff und sein "Gesetz der Transformation der Knochen".

[270] E. Chen *et al.*, "Cage Subsidence and Fusion Rate in Extreme Lateral Interbody Fusion with and without Fixation," *World Neurosurg,* vol. 122, pp. e969-e977, Feb 2019, doi: 10.1016/j.wneu.2018.10.182.

[271] I. Dominguez, R. Luque, M. Noriega, J. Rey, J. Alia, and F. Marco-Martinez, "Extreme lateral lumbar interbody fusion. Surgical technique, outcomes and complications after a minimum of one year follow-up," *Rev Esp Cir Ortop Traumatol,* vol. 61, no. 1, pp. 8-18, Jan - Feb 2017, doi: 10.1016/j.recot.2016.09.001. Artrodesis intersomatica lumbar extralateral. Tecnica quirurgica, resultados y complicaciones con un seguimiento minimo de un ano.

[272] A. Rushton, L. White, A. Heap, and N. Heneghan, "Evaluation of current surgeon practice for patients undergoing lumbar spinal fusion surgery in the United Kingdom," *World J Orthop,* vol. 6, no. 6, pp. 483-90, Jul 18 2015, doi: 10.5312/wjo.v6.i6.483.

[273] M. Fukushima, Y. Oshima, Y. Yuzawa, S. Tanaka, and H. Inanami, "Clinical and radiographic analysis of unilateral versus bilateral instrumented one-level lateral lumbar interbody fusion," *Sci Rep,* vol. 10, no. 1, p. 3105, Feb 20 2020, doi: 10.1038/s41598-020-59706-9.

[274] E. H. Elowitz, D. S. Yanni, M. Chwajol, R. M. Starke, and N. I. Perin, "Evaluation of indirect decompression of the lumbar spinal canal following minimally invasive lateral transpsoas interbody fusion: radiographic and outcome analysis," *Minim Invasive Neurosurg,* vol. 54, no. 5-6, pp. 201-6, Oct 2011, doi: 10.1055/s-0031-1286334.

[275] L. Marchi, N. Abdala, L. Oliveira, R. Amaral, E. Coutinho, and L. Pimenta, "Stand-alone lateral interbody fusion for the treatment of low-grade degenerative spondylolisthesis," *ScientificWorldJournal,* vol. 2012, p. 456346, 2012, doi: 10.1100/2012/456346.

[276] L. Marchi *et al.*, "Lateral interbody fusion for treatment of discogenic low back pain: minimally invasive surgical techniques," *Adv Orthop,* vol. 2012, p. 282068, 2012, doi: 10.1155/2012/282068.

[277] D. V. Ambati, E. K. Wright, Jr., R. A. Lehman, Jr., D. G. Kang, S. C. Wagner, and A. E. Dmitriev, "Bilateral pedicle screw fixation provides superior biomechanical stability in transforaminal lumbar interbody fusion: a finite element study," *Spine J,* vol. 15, no. 8, pp. 1812-22, Aug 1 2015, doi: 10.1016/j.spinee.2014.06.015.

[278] K. R. Chin, F. J. Pencle, S. D. Francis, C. A. Francis, J. A. Seale, and E. A. Hothem, "Misaligned Versus Straight Placement of Anterior Cervical Plates: A Clinical and Radiologic Outcomes Study," *J Am Acad Orthop Surg,* vol. 25, no. 5, pp. 389-395, May 2017, doi: 10.5435/JAAOS-D-16-00332.

[279] X. Liu, J. Ma, P. Park, X. Huang, N. Xie, and X. Ye, "Biomechanical comparison of multilevel lateral interbody fusion with and without supplementary instrumentation: a three-dimensional finite element study," *BMC Musculoskelet Disord,* vol. 18, no. 1, p. 63, Feb 2 2017, doi: 10.1186/s12891-017-1387-6.

[280] A. J. Patel, S. Vadivelu, S. K. Desai, and A. Jea, "Congenital hypoplasia or aplasia of the lumbosacral pedicle as an unusual cause of spondylolisthesis in the pediatric age group," *J Neurosurg Pediatr,* vol. 11, no. 6, pp. 717-21, Jun 2013, doi: 10.3171/2013.3.PEDS12579.

[281] J. Wen, C. Shi, L. Yu, S. Wang, Y. Xi, and X. Ye, "Unilateral Versus Bilateral Percutaneous Pedicle Screw Fixation in Oblique Lumbar Interbody Fusion," *World Neurosurg,* vol. 134, pp. e920-e927, Feb 2020, doi: 10.1016/j.wneu.2019.11.035.

[282] P. Lu, T. Pan, T. Dai, G. Chen, and K. Q. Shi, "Is unilateral pedicle screw fixation superior than bilateral pedicle screw fixation for lumbar degenerative diseases: a meta-analysis," *J Orthop Surg Res,* vol. 13, no. 1, p. 296, Nov 22 2018, doi: 10.1186/s13018-018-1004-x.

[283] C. Ren, R. Qin, P. Sun, and P. Wang, "Effectiveness and safety of unilateral pedicle screw fixation in transforaminal lumbar interbody fusion (TLIF): a systematic review and meta-analysis," *Arch Orthop Trauma Surg,* vol. 137, no. 4, pp. 441-450, Apr 2017, doi: 10.1007/s00402-017-2641-y.

[284] T. Zhang, S. Bai, S. Dokos, J. P. Cheung, and A. D. Diwan, "XLIF interbody cage reduces stress and strain of fixation in spinal reconstructive surgery in comparison with TLIF cage with bilateral or unilateral fixation: a computational analysis," *Annu Int Conf IEEE Eng Med Biol Soc,* vol. 2019, pp. 1887-1890, Jul 2019, doi: 10.1109/EMBC.2019.8856592.

[285] H. Z. Guo *et al.*, "Stability Evaluation of Oblique Lumbar Interbody Fusion Constructs with Various Fixation Options: A Finite Element Analysis Based on Three-Dimensional Scanning Models," *World Neurosurg,* vol. 138, pp. e530-e538, Jun 2020, doi: 10.1016/j.wneu.2020.02.180.

[286] Z. Liang *et al.*, "Biomechanical evaluation of strategies for adjacent segment disease after lateral lumbar interbody fusion: is the extension of pedicle screws necessary?," *BMC Musculoskelet Disord,* vol. 21, no. 1, p. 117, Feb 21 2020, doi: 10.1186/s12891-020-3103-1.

[287] J. Godzik *et al.*, "Biomechanical Stability Afforded by Unilateral Versus Bilateral Pedicle Screw Fixation with and without Interbody Support Using Lateral Lumbar Interbody Fusion," *World Neurosurg,* vol. 113, pp. e439-e445, May 2018, doi: 10.1016/j.wneu.2018.02.053.

[288] O. Lai, Y. Chen, Q. Chen, Y. Hu, and W. Ma, "Cadaveric biomechanical analysis of multilevel lateral lumbar interbody fusion with and without supplemental instrumentation," *BMC Musculoskelet Disord,* vol. 22, no. 1, p. 280, Mar 15 2021, doi: 10.1186/s12891-021-04151-6.

[289] J. K. Biswas *et al.*, "Design factors of lumbar pedicle screws under bending load: A finite element analysis," *Biocybernetics and Biomedical Engineering,* vol. 39, no. 1, pp. 52-62, 2019/01/01/ 2019, doi: https://doi.org/10.1016/j.bbe.2018.10.003.

[290] J. Widmer, M.-R. Fasser, E. Croci, J. Spirig, J. G. Snedeker, and M. Farshad, "Individualized prediction of pedicle screw fixation strength with a finite element model," *Computer Methods in Biomechanics and Biomedical Engineering,* vol. 23, no. 4, pp. 155-167, 2020/03/11 2020, doi: 10.1080/10255842.2019.1709173.

[291] S. I. Chen, R. M. Lin, and C. H. Chang, "Biomechanical investigation of pedicle screw–vertebrae complex: a finite element approach using bonded and contact interface conditions," *Medical Engineering & Physics,* vol. 25, no. 4, pp. 275-282, 2003/05/01/ 2003, doi: https://doi.org/10.1016/S1350-4533(02)00219-9.

[292] K. Matsukawa, Y. Yato, and H. Imabayashi, "Impact of Screw Diameter and Length on Pedicle Screw Fixation Strength in Osteoporotic Vertebrae: A Finite Element Analysis," *Asian Spine J,* vol. 15, no. 5, pp. 566-574, 10 2021, doi: 10.31616/asj.2020.0353.

[293] C.-S. Chen, C.-H. Huang, and S.-L. Shih, "Biomechanical evaluation of a new pedicle screw-based posterior dynamic stabilization device (Awesome Rod System) - a finite element analysis," *BMC Musculoskeletal Disorders,* vol. 16, no. 1, p. 81, 2015/04/09 2015, doi: 10.1186/s12891-015-0538-x.

[294] S.-H. Chen, S.-C. Lin, W.-C. Tsai, C.-W. Wang, and S.-H. Chao, "Biomechanical comparison of unilateral and bilateral pedicle screws fixation for transforaminal lumbar interbody fusion after decompressive surgery -- a finite element analysis," *BMC Musculoskeletal Disorders,* vol. 13, no. 1, p. 72, 2012/05/16 2012, doi: 10.1186/1471-2474-13-72.

[295] E. Sengul, R. Ozmen, M. E. Yaman, and T. Demir, "Influence of posterior pedicle screw fixation at L4–L5 level on biomechanics of the lumbar spine with and without fusion: a finite element method," *BioMedical Engineering OnLine,* vol. 20, no. 1, p. 98, 2021/10/07 2021, doi: 10.1186/s12938-021-00940-1.

[296] M. Sensale, T. Vendeuvre, C. Schilling, T. Grupp, M. Rochette, and E. Dall'Ara, "Patient-Specific Finite Element Models of Posterior Pedicle Screw Fixation: Effect of Screw's Size and Geometry," (in English), *Frontiers in Bioengineering and Biotechnology,* Original Research vol. 9, 2021-March-10 2021, doi: 10.3389/fbioe.2021.643154.

[297] Strand7, *Theoretical background to the Strand7 finite element analysis system*, Strand7 Release 2.3 ed. Strand7 Pty Ltd, 2005.

[298] H. S. Oh and H. Y. Seo, "The Relationship between Adjacent Segment Pathology and Facet Joint Violation by Pedicle Screw after Posterior Lumbar Instrumentation Surgery," *J Clin Med,* vol. 10, no. 13, Jun 29 2021, doi: 10.3390/jcm10132911.

[299] H. Sakaura *et al.*, "Early cephalad adjacent segment degeneration after posterior lumbar interbody fusion: a comparative study between cortical bone trajectory screw fixation and traditional trajectory screw fixation," *J Neurosurg Spine,* vol. 32, no. 2, pp. 155-159, Oct 18 2019, doi: 10.3171/2019.8.SPINE19631.

[300] P. Wangsawatwong *et al.*, "Adjacent-segment effects of lumbar cortical screw-rod fixation versus pedicle screw-rod fixation with and without interbody support," *J Neurosurg Spine,* pp. 1-7, Jun 18 2021, doi: 10.3171/2020.11.SPINE20977.

[301] M. K. Manzur *et al.*, "Fusion rate for stand-alone lateral lumbar interbody fusion: a systematic review," *Spine J,* vol. 20, no. 11, pp. 1816-1825, Nov 2020, doi: 10.1016/j.spinee.2020.06.006.

[302] A. Gupta, N. Kukkar, K. Sharif, B. J. Main, C. E. Albers, and S. F. El-Amin Iii, "Bone graft substitutes for spine fusion: A brief review," *World J Orthop,* vol. 6, no. 6, pp. 449-56, Jul 18 2015, doi: 10.5312/wjo.v6.i6.449.

[303] A. Emami *et al.*, "Risk Factors for Pseudarthrosis in Minimally-Invasive Transforaminal Lumbar Interbody Fusion," *Asian Spine J,* vol. 12, no. 5, pp. 830-838, Oct 2018, doi: 10.31616/asj.2018.12.5.830.

[304] C. T. Carpenter, J. W. Dietz, K. Y. Leung, D. A. Hanscom, and T. A. Wagner, "Repair of a pseudarthrosis of the lumbar spine. A functional outcome study," *J Bone Joint Surg Am,* vol. 78, no. 5, pp. 712-20, May 1996, doi: 10.2106/00004623-199605000-00011.

[305] M. N. Hadley and S. V. Reddy, "Smoking and the human vertebral column: a review of the impact of cigarette use on vertebral bone metabolism and spinal

fusion," *Neurosurgery,* vol. 41, no. 1, pp. 116-24, Jul 1997, doi: 10.1097/00006123-199707000-00025.

[306] P. D. Sawin, C. A. Dickman, N. R. Crawford, M. S. Melton, W. D. Bichard, and V. K. Sonntag, "The effects of dexamethasone on bone fusion in an experimental model of posterolateral lumbar spinal arthrodesis," *J Neurosurg,* vol. 94, no. 1 Suppl, pp. 76-81, Jan 2001, doi: 10.3171/spi.2001.94.1.0076.

[307] W. Borchani, K. Aono, N. Lajnef, and S. Chakrabartty, "Monitoring of Postoperative Bone Healing Using Smart Trauma-Fixation Device With Integrated Self-Powered Piezo-Floating-Gate Sensors," *IEEE Transactions on Biomedical Engineering,* vol. 63, no. 7, pp. 1463-1472, 2016.

[308] J. Lin *et al.*, "Davelopment of capacitive pure bending strain sensor for wireless spinal fusion monitoring," *Sensors and Actuators A,* vol. 138, pp. 276-287, 2007.

[309] E. H. Ledet, B. L. Sachs, J. B. Brunski, C. E. Gatto, and P. S. Donzelli, "Real-time in vivo loading in the lumbar spine: part 1. Interbody implant: load cell design and preliminary results," *Spine (Phila Pa 1976),* vol. 25, no. 20, pp. 2595-600, Oct 15 2000, doi: 10.1097/00007632-200010150-00009.

[310] S. J. Kim, T. Wang, M. H. Pelletier, and W. R. Walsh, "'SMART' implantable devices for spinal implants: a systematic review on current and future trends," *J Spine Surg,* vol. 8, no. 1, pp. 117-131, Mar 2022, doi: 10.21037/jss-21-100.

[311] *Test Methods For Intervertebral Body Fusion Devices*, ASTM, 2018.

[312] *Standard Test Method for Measuring Load-Induced Subsidence of Intervertebral Body Fusion Device Under Static Axial Compression*, ASTM F2267-22, ASTM, 2022.

[313] *Standard Test Methods for Static and Dynamic Characterization of Spinal Artificial Discs*, ASTM, 2011.

[314] E. Massaad, N. Fatima, A. Kiapour, M. Hadzipasic, G. M. Shankar, and J. H. Shin, "Polyetheretherketone Versus Titanium Cages for Posterior Lumbar Interbody Fusion: Meta-Analysis and Review of the Literature," *Neurospine,* vol. 17, no. 2, p. 473, Jun 2020, doi: 10.14245/ns.2040058.029.c2.

[315] N. Muthiah, Y. U. Yolcu, N. Alan, N. Agarwal, D. K. Hamilton, and A. Ozpinar, "Evolution of polyetheretherketone (PEEK) and titanium interbody devices for spinal procedures: a comprehensive review of the literature," *Eur Spine J,* Jun 10 2022, doi: 10.1007/s00586-022-07272-1.

[316] M. Si, J. Guo, J. Hao, X. Zhao, C. A. Randall, and H. Wang, "Cold sintered composites consisting of PEEK and metal oxides with improved electrical properties via the hybrid interfaces," *Composites Part B: Engineering,* vol. 226, 2021, doi: https://doi.org/10.1016/j.compositesb.2021.109349.

[317] S. Olenik, H. S. Lee, and F. Guder, "The future of near-field communication-based wireless sensing," *Nat Rev Mater,* vol. 6, no. 4, pp. 286-288, 2021, doi: 10.1038/s41578-021-00299-8.

[318] S. H. Zhou, I. D. McCarthy, A. H. McGregor, R. R. Coombs, and S. P. Hughes, "Geometrical dimensions of the lower lumbar vertebrae--analysis of data from digitised CT images," *Eur Spine J,* vol. 9, no. 3, pp. 242-8, Jun 2000, doi: 10.1007/s005860000140.

[319] Y. Wang, K. H. Low, H. L. J. Pang, K. Hoon, H., F. X. Che, and Y. S. Yong, "Modeling and simulation for a drop-impact analysis of multi-layered printed circuit boards," *Microelectronics Reliability,* vol. 46, pp. 558-573, 2006.

[320] M. A. Hopcroft, W. D. Nix, and T. W. Kenny, "What is the Young's Modulus of Silicon?," *Journal of Microelectromechanical Systems,* vol. 19, no. 2, pp. 229-238, 2010.

[321] *Standard Test Methods for Tensile, Compressive, and Flexural Creep and Creep-Rupture of Plastics*, ASTM D2990, ASTM, 2009.

[322] E. Behrbalk, O. Uri, R. M. Parks, R. Musson, R. C. Soh, and B. M. Boszczyk, "Fusion and subsidence rate of stand alone anterior lumbar interbody fusion using PEEK cage with recombinant human bone morphogenetic protein-2," *Eur Spine J,* vol. 22, no. 12, pp. 2869-75, Dec 2013, doi: 10.1007/s00586-013-2948-5.

[323] M. C. Kim, H. T. Chung, J. L. Cho, D. J. Kim, and N. S. Chung, "Subsidence of polyetheretherketone cage after minimally invasive transforaminal lumbar interbody fusion," *J Spinal Disord Tech,* vol. 26, no. 2, pp. 87-92, Apr 2013, doi: 10.1097/BSD.0b013e318237b9b1.

[324] S. Kang, M. Song, J. Kim, J. W. Lee, and J. Kim, "Near-Field Communication in Biomedical Applications," *Sensors,* vol. 21, 703, 2021, doi: https://doi.org/10.3390/s21030703.

[325] K. R. Venugopal and L. M. Patnaik, *Wireless Networks and Computational Intelligence*. Bangalore, 2012.

[326] P. Lathiya and J. Wang, "Near-Field Communications (NFC) for Wireless Power Transfer (WPT): An Overview," in *Wireless Power Transfer*, Z. M. Ed. London, 2021.

[327] A. H. Omre, "Bluetooth low energy: wireless connectivity for medical monitoring," *J Diabetes Sci Technol,* vol. 4, no. 2, pp. 457-63, Mar 1 2010, doi: 10.1177/193229681000400227.

[328] B. Pradhan, S. Bhattacharyya, and K. Pal, "IoT-Based Applications in Healthcare Devices," *J Healthc Eng,* vol. 2021, p. 6632599, 2021, doi: 10.1155/2021/6632599.

[329] A. Dementyev, S. Hodges, S. Taylor, and J. Smith, "Power consumption analysis of bluetooth low energy, ZigBee and ANT sensor nodes in a cyclic sleep scenario," in *2013 IEEE International Wireless Symposium (IWS)*, Beijing, China, 2013, pp. 1-4.

[330] K. Shahzad and B. Oelmann, "A comparative study of in-sensor processing vs. raw data transmission using ZigBee, BLE and Wi-Fi for data intensive monitoring applications," in *2014 11th International Symposium on Wireless Communications Systems (ISWCS)*, Barcelona, Spain, 2014, pp. 519-524.

[331] S. Yoo, J. Lee, H. Joo, S. H. Sunwoo, S. Kim, and D. H. Kim, "Wireless Power Transfer and Telemetry for Implantable Bioelectronics," *Adv Healthc Mater,* vol. 10, no. 17, p. e2100614, Sep 2021, doi: 10.1002/adhm.202100614.

[332] Z. Cao *et al.*, "Near-Field Communication Sensors," *Sensors (Basel),* vol. 19, no. 18, Sep 12 2019, doi: 10.3390/s19183947.

[333] B. Lee, B. Kim, F. J. Harackiewicz, B. Mun, and H. Lee, "NFC Antenna Design for Low-Permeability Ferromagnetic Material," *IEEE Antennas and Wireless Propagation Letters,* vol. 13, pp. 59-62, 2014, doi: 10.1109/LAWP.2013.2296307.

[334] H. Saghlatoon, R. M. Boroujeni, M. M. Honari, and P. Mousavi, "Low-Cost Inkjet Printed Passive Booster for Increasing the Magnetic Coupling in Proximity of Metal Object for NFC Systems," *IEEE Microwave and Wireless Components Letters,* vol. 26, no. 12, pp. 996-998, 2016, doi: 10.1109/LMWC.2016.2623243.

[335] V. Coskun, B. Ozdenizci, and K. Ok, "The Survey on Near Field Communication," (in eng), *Sensors (Basel),* vol. 15, no. 6, pp. 13348-405, Jun 5 2015, doi: 10.3390/s150613348.

[336] Y. S. Lin *et al.*, "Impact of Pacemaker Lead Characteristics on Pacemaker Related Infection and Heart Perforation: A Nationwide Population-Based Cohort Study," *PLoS One,* vol. 10, no. 6, p. e0128320, 2015, doi: 10.1371/journal.pone.0128320.

[337] R. M. Fish and L. A. Geddes, "Conduction of electrical current to and through the human body: a review," (in eng), *Eplasty,* vol. 9, p. e44, Oct 12 2009.

[338] M. Sautter, N. Sautter, and F. G. Shellock, "Near field communication (NFC) device: Evaluation of MRI issues," *Magnetic Resonance Imaging,* vol. 92, pp. 82-87, 2022/10/01/ 2022, doi: https://doi.org/10.1016/j.mri.2022.06.002.

[339] C. Y. Kim *et al.*, "Soft subdermal implant capable of wireless battery charging and programmable controls for applications in optogenetics," *Nature Communications,* vol. 12, no. 1, p. 535, 2021/01/22 2021, doi: 10.1038/s41467-020-20803-y.

[340] D. F. Almeida *et al.*, "Fully automatic segmentation of femurs with medullary canal definition in high and in low resolution CT scans," *Medical Engineering & Physics,* vol. 38, no. 12, pp. 1474-1480, 2016/12/01/ 2016, doi: https://doi.org/10.1016/j.medengphy.2016.09.019.

[341] R. A. Zeineldin, M. E. Karar, J. Coburger, C. R. Wirtz, and O. Burgert, "DeepSeg: deep neural network framework for automatic brain tumor segmentation using magnetic resonance FLAIR images," *International journal of computer assisted radiology and surgery,* vol. 15, no. 6, pp. 909-920, 2020.

[342] R. A. Zeineldin *et al.*, "Explainability of deep neural networks for MRI analysis of brain tumors," *International Journal of Computer Assisted Radiology and Surgery,* vol. 17, no. 9, pp. 1673-1683, 2022/09/01 2022, doi: 10.1007/s11548-022-02619-x.

[343] N. Mangado, G. Piella, J. Noailly, J. Pons-Prats, and M. A. Ballester, "Analysis of Uncertainty and Variability in Finite Element Computational Models for Biomedical Engineering: Characterization and Propagation," *Front Bioeng Biotechnol,* vol. 4, p. 85, 2016, doi: 10.3389/fbioe.2016.00085.

[344] S. K. Easley, S. Pal, P. R. Tomaszewski, A. J. Petrella, P. J. Rullkoetter, and P. J. Laz, "Finite element-based probabilistic analysis tool for orthopaedic applications," *Comput Methods Programs Biomed,* vol. 85, no. 1, pp. 32-40, Jan 2007, doi: 10.1016/j.cmpb.2006.09.013.

[345] C. A. Myers, C. K. Fitzpatrick, D. N. Huff, P. J. Laz, and P. J. Rullkoetter, "Development and calibration of a probabilistic finite element hip capsule

representation," *Comput Methods Biomech Biomed Engin,* vol. 23, no. 11, pp. 755-764, Aug 2020, doi: 10.1080/10255842.2020.1764543.

[346] M. Schmidt, D. Pohle, and T. Rechtenwald, "Selective Laser Sintering of PEEK," *CIRP Annals,* vol. 56, no. 1, pp. 205-208, 2007/01/01/ 2007, doi: https://doi.org/10.1016/j.cirp.2007.05.097.

[347] L. A. Chavez *et al.*, "Low-temperature selective laser sintering 3D printing of PEEK-Nylon blends: Impact of thermal post-processing on mechanical properties and thermal stability," *Journal of Applied Polymer Science,* vol. 139, no. 23, p. 52290, 2022, doi: https://doi.org/10.1002/app.52290.

[348] X. Zhao, P. Li, K. Xiao, X. Meng, L. Han, and C. Yu, "Sensor Drift Compensation Based on the Improved LSTM and SVM Multi-Class Ensemble Learning Models," (in eng), *Sensors (Basel),* vol. 19, no. 18, Sep 5 2019, doi: 10.3390/s19183844.

[349] K. Chen and Z. Zhao, "Analysis of the Double-Layer Printed Spiral Coil for Wireless Power Transfer," *IEEE Journal of Emerging and Selected Topics in Power Electronics,* vol. 1, no. 2, pp. 114-121, 2013, doi: 10.1109/JESTPE.2013.2272696.

[350] W.-S. Lee, D.-Z. Kim, and J.-W. Yu, "Multi-functional high-isolation dual antenna for controllable wireless charging and NFC communication," *Electronics Letters,* vol. 50, no. 13, pp. 912-913, 2014, doi: https://doi.org/10.1049/el.2014.0858.